Interfacial phenomena in micro- and nanofluidics:
nanobubbles, cavitation, and wetting

Bram M. Borkent

Interfacial phenomena in micro- and nanofluidics: nanobubbles, cavitation, and wetting

Bram M. Borkent

Interfacial phenomena in micro- and nanofluidics: nanobubbles, cavitation, and wetting

Bram M. Borkent

Nederlandse titel:
Grensvlakverschijnselen in micro- and nanofluidics: nanobelletjes, cavitatie, en bevochtiging

ISBN 978-90-365-2870-2

INTERFACIAL PHENOMENA IN MICRO- AND NANOFLUIDICS:
NANOBUBBLES, CAVITATION, AND WETTING

PROEFSCHRIFT

ter verkrijging van
de graad van doctor aan de Universiteit Twente,
op gezag van de rector magnificus,
prof. dr. H. Brinksma,
volgens besluit van het College voor Promoties
in het openbaar te verdedigen
op vrijdag 2 oktober 2009 om 15.00 uur

door

Bram Matthias Borkent

geboren op 1 juli 1981

te Apeldoorn

Dit proefschrift is goedgekeurd door de promotor:
Prof. dr. rer. nat. Detlef Lohse

Contents

1

Interfacial phenomena in micro- and nanofluidics: an introduction

1.1 Motivations to study micro- and nanofluidics

Water in contact with hydrophobic surfaces*, shows fascinating behavior on different length scales: local density fluctuations on the molecular scale [1, 2], effective slip lengths [3] and long-range hydrophobic forces on the nanoscopic scale [4, 5], and - in case of textured surfaces - complete water repellency on the macroscopic scale [6], to mention just a few examples.

Despite the different length scales involved, the origin of those interesting phenomena mainly stems from (sub)microscopic details at the liquid-solid or liquid-gas interface. A recent, but already classic example is the experiment of a glass ball which is thrown in water: surface details on the order of just $1\,\mathrm{nm}^\dagger$ (i.e. the presence of a single molecular layer) make all the difference in the world between a tiny "plop" or a spectacular water splash on the macro-scale [7]. Therefore, understanding interfacial details at *small* length scales has become of primary importance to understand the sometimes *large-scale* behaviors which they lead to. These and other surprising phenomena have been triggering fluid physicists in recent years to study the behavior of fluids on micro- and nanoscopic length scales, i.e. the field of micro- and nanofluidics.

The fascination is enhanced by the emerging possibilities provided by current advances in technology: High-speed camera's, atomic force microscopes, clean rooms,

---

*Hydrophobic literally means "water fearing".

†To give some idea: a human hair is $8 \cdot 10^4$ nm thick and grows ~ 5 nm per second.

1

techniques to structure and image surfaces on the nanoscale, etc. They all open new routes to discover and characterize physical phenomena which were previously out of reach, and this thesis provides some illustrative examples.

Small-scale fluid phenomena can also be utilized in various ways, which brings us to the third stimulus to study micro- and nanofluidics: the ongoing miniaturization in industries. Various companies, producing e.g. semiconductor surfaces, labs-on-a-chip, ink jet printers, drug delivery systems, purification membranes, etc. are down scaling and optimizing their products. At some point in this process, a detailed understanding of liquids or bubbles in contact with solid surfaces on small length scales is required. This knowledge is often facilitated thanks to the efforts of scientists.

From a more fundamental point of view, micro- and nanofluidics attract scientific interest, as one may wonder whether the classic laws of fluid mechanics, which are based on a continuum picture, still hold on such small length scales. As an example, it has been argued that the no-slip hydrodynamic boundary condition - a more than 200 year old dogma - should be modified when the liquid flows over a hydrophobic solid wall [3].

All these considerations together, both practical and fundamental, are the primary motivations of this thesis.

1.2   Guide through the thesis

The studies presented in this thesis consider water in contact with a hydrophobic surface on the micro- and nanoscale, with some gas or vapor phase involved. Nevertheless, it is possible to divide the studies (and this thesis) into three parts or categories with increasing length scale and (geometric) complexity; see Table 1.1 for a schematic overview.

1.2.1   Part I - Nanobubbles at the solid-liquid interface

Water in contact with a smooth surface

The first and perhaps simplest configuration one may think of is the static situation of water in contact with an (atomically) smooth surface. One would not expect much surprises here (apart from possible structuring effects of the water close to the surface). Placing water on such a surface yields a spherical cap-shaped droplet shape, with radius R, which makes contact with the solid wall at an equilibrium angle θ_Y, which is usually termed Young's angle. At this contact angle the droplet-substrate system has minimized its total free energy associated with all its interfaces at constant temperature and droplet volume. The global thermodynamic derivation was first
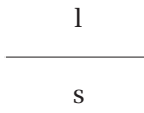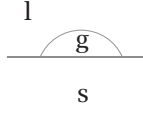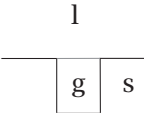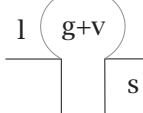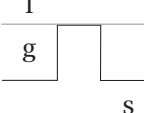
Part	System	Observation	Dimension	Chapter
I	l / s	l / g / s	$10-100\,\mathrm{nm}$	2, 3, 4
II	l / g s	l g+v / s	$100-1000\,\mathrm{nm}$	4, 5, 6, 7
III	l g / s	l / s	$1-10\mu\mathrm{m}$	8

Table 1.1: Overview of the systems studied in this thesis, together with the primary observations, typical lateral length scales, and Chapters in which the corresponding findings are reported. The abbreviations l,s,g, and v denote liquid, solid, gas, and vapor, respectively.

done by Gibbs in 1880 [8, 9], and yields

$$\cos\theta_Y = \frac{\sigma_{sv} - \sigma_{sl}}{\sigma_{lv}} \tag{1.1}$$

and

$$p_l - p_v = \frac{2\sigma_{lv}}{R} \quad, \tag{1.2}$$

in which σ represents the interfacial energy between phases s, l, and v, denoting the solid, liquid, and vapor phase, respectively. The terms p_l and p_v are the liquid and vapor pressure, respectively. The reader may have recognized here the famous Young's equation (Eq. 1.1) and Laplace's equation (Eq. 1.2), named after the scientists who first derived them in resp. 1805 [10] and 1806 [11].

Bubbles in contact with a smooth surface

Let us now consider the inverse case of a vapor bubble at the liquid-solid interface (which we will term "surface bubble"). Equations 1.1 and 1.2 do not change principally, except the sign of the curvature of the bubble, i.e. $p_l - p_v = -2\sigma_{lv}/R$, which is $p_v - p_l = 2\sigma_{lv}/R$. One can readily show that this situation cannot exist

in thermal equilibrium: the bubble either grows without bounds, or it collapses [12]. Let's try to overcome the instability by adding some gas to the water vapor, to get $p_g + p_v - p_l = 2\sigma_{lv}/R$. Unfortunately, at atmospheric pressure p_{atm} (and in fact at any pressure) the system still cannot be in thermodynamic equilibrium. Henry's law dictates that the amount of gas dissolved in the liquid in contact with a gas at a partial pressure p_g is $c = K(T)p_g$, with c the gas concentration and $K(T)$ a temperature-dependent constant. Far away from the bubble, where the liquid is in contact with the ambient air, the liquid pressure p_l is in equilibrium with $p_v + p_{atm}$ (assuming that hydrostatic effects can be neglected and the liquid-interface is flat), and the liquid is saturated at $c_s = K(T)(p_l - p_v)$. However, close to the bubble surface $c = K(T)p_g > c_s$, since $p_g > p_l - p_v$. Hence, a concentration gradient exists in the liquid and the bubble will dissolve. For bubbles with $10\,\text{nm} < R < 100\,\text{nm}$ dissolution times of 1 to $100\,\mu\text{s}$ can be calculated [13, 14]. Notice that this analysis was originally derived for a free gas bubble in the liquid, but if the bubble interface is not pinned to the solid surface, there is no reason why it should not apply to spherical-cap shaped surface bubbles. Hence, we conclude that surface bubbles cannot be in thermal equilibrium: either they grow (in supersaturated liquids) or dissolve in (sub)saturated liquids. On the nanoscale, such bubbles (called "surface nanobubbles") should be extremely short-lived with lifetimes of a few μs.

Observation of out-of-equilibrium surface bubbles

A simple kitchen-experiment may perfectly illustrate the out-of-equilibrium behavior of gas bubbles on the macroscale. Fill a glass cup with normal tap water and after a few minutes one can see bubbles appearing at the glass surface. Initially the bubbles grow, until at some point they will start to shrink and finally the surface bubbles disappear: clearly, they are not in stable equilibrium at all times (see Fig. 1.1). Tap water is kept at a few bars overpressure in the water supplies and therefore it is slightly oversaturated with gas at atmospheric pressure. During the filling process of the glass cup, microscopic surface defects can entrap air and form favorable sites for the oversaturated gas to 'precipitate'. As a consequence, spherical cap-shaped bubbles become visible at the glass surface[‡]. If the pinning forces at the triple contact line of the bubble are larger than the upward buoyancy forces, the bubble will be fixed at its position on the glass surface. In time, the partial gas pressure in the liquid equilibrates with the atmospheric pressure through the flat liquid-gas interface at the top of the liquid column. At some point, therefore, the oversaturation vanishes and the bubbles cannot grow anymore. Instead, they start to dissolve due to surface tension.

[‡]An accelerated process of this type occurs in carbonated beverages, like beer, champagne and Spa Barisart (Spa Red), in which the gas oversaturation is much larger than in tap water.
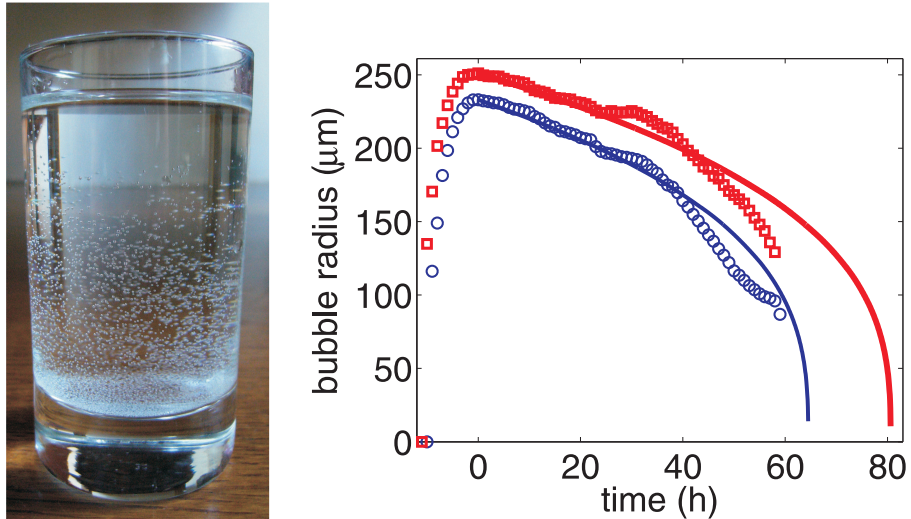
Figure 1.1: In freshly tapped water gaseous microbubbles form at the glass-water interface (left). Initially, the water is slightly oversaturated with gas and the bubbles grow, but once the solution becomes gas saturated the bubbles shrink due to surface tension. The sizes of a two bubbles, extracted from photographs taken each hour, are displayed in the right image. The lines are theoretical fits based on Eq. 34 of Epstein and Plesset [13], including the $\ln(2)$ correction factor to account for the presence of the wall. The value for the surface tension of the water is taken as 0.035 N/m, resulting from surface-active contaminants in the water (soap, salts, etc.)

Observation of stable surface nanobubbles

On the nanoscale, a dramatically different observation can be made: spherically cap-shaped gas bubbles, with typical radii of curvature of ~ 100 nm, which are stable for hours, or even days. Another awkward finding is the anomalously large contact angle which surface nanobubbles make with the solid wall (through the water), which is not in agreement with the macroscopic value (θ_Y). These observations lead to various fundamental questions: What prevents the bubble from rapid dissolution? What is the value of surface tension at these length scales? What is the pressure inside the nanobubble? How does gas behave in such confined systems, where the shortest length scale (nanobubble height) is comparable to the mean free path of a gas molecule? How are nanobubbles formed? etc. etc. Currently, a completely satisfying picture to these questions is not available. Apart from these fundamental aspects, surface nanobubbles attract interest due to their potential impact in several fields of applications. In particular, they are potential candidates to explain various phenomena associated with the liquid-solid interface, such as liquid slippage at walls [3, 15],

the anomalous attraction of hydrophobic surfaces [16, 17][§], and the formation of
nanometer-sized vaterite tubes in electrolysis-induced crystal growth [19]. Also in
immersion lithography[¶] one may encounter defects caused by surface nanobubbles,
although this has not been reported yet.

The aim of Part I of this thesis is to contribute to the scientific discussion regarding
the two main puzzles related to surface nanobubbles: their long term stability and
incredibly large contact angles, which were already identified in 2000 [18, 20]. The
nanobubble dimensions used in the scientific discourse are usually obtained through
atomic force microscopy in tapping mode (AFM-TM). Since nanobubbles are soft en-
tities and AFM-TM is an invasive technique, it is not *a priori* clear how the method
of detection influences the detected shape of the nanobubbles. This basic question,
which in fact should precede quantitative statements on nanobubble stability, will be
addressed in detail in *Chapter 2*. In addition, we will study how the contact angle de-
pends on the nanobubble size, which addresses another debated point. Furthermore,
we focus on the role played by contamination, as this will turn out to be a crucial
factor.

After characterizing geometrical dimensions of *individual* nanobubbles, *Chapter 3*
will focus on statistical properties of nanobubble *populations*, which allows us to
identify nanobubble characteristics which might be useful to understand and describe
nanobubble stability. In *Chapter 4* the central question is whether we are able to grow
surface nanobubbles to visible size due to a huge tensile stress in the liquid. This pro-
cess, called cavitation, needs pre-existing nanoscale gas pockets (cavitation nuclei) to
grow bubbles from, and in principle there is no reason why surface nanobubbles are
no suitable candidates for this purpose. If we succeed, we will have a new mechanism
to make nanobubbles visible. The growth of bubbles from micro- and nanoscopic gas
pockets in the liquid will be treated in more detail in part II of this thesis.

1.2.2   Part II - Cavitation from nanoscopic gas pockets

Water in contact with a structured surface: the case of a pit

The second and third configuration studied in this thesis is water in contact with a
structured surface. Let's first consider a surface decorated with pits, as depicted in
the second row of Table 1.1 and studied in part II of this thesis. The free-standing pits
can entrap air when the substrate is immersed in the water, provided that $\theta_Y > 90°$.
This follows from a simple analysis: a pit with arbitrary perimeter p and vertical
walls will stay dry when the energy gain ($\sigma_{sg} p \, dx$) to advance the wetting front by

---

[§]In fact, "bridging of submicroscopic bubbles" were inferred from these experiments, long before
surface nanobubbles were directly imaged by atomic force microscopes in tapping mode [18].

[¶]Popular method in the semiconductor industry which uses water in between a hydrophobic substrate
(wafer) and the lens system to miniaturize mask projections.

an amount dx into the pit is smaller than the energy loss ($\sigma_{sl}p\,dx$). This condition leads to $\sigma_{sg} < \sigma_{sl}$, i.e. $\cos\theta_Y = (\sigma_{sg} - \sigma_{sl})/\sigma_{lg} < 0$, which is equal to $\theta_Y > 90°$. Notice, that the energy gain obtained for wetting the bottom of the pit is not taken into account, as this information is usually not "known" by the liquid meniscus at the pit mouth. As a consequence, a gas-filled pit covered by a liquid meniscus can be in a meta-stable state, with its total free energy larger than it is in the completely wetted situation. The transition from the meta-stable to the fully wetted state occurs at a so-called 'critical value', at which energy gain and loss cancel out. Consider, for example, a cylindrical pit with radius $a = 250\,\text{nm}$ and $\theta_Y = 95°$, then the system is in a meta-stable state if $d < d_c = -a(\cos\theta_Y + 1)/2\cos\theta_Y = 1.3\,\mu\text{m}$ (!), while $\theta_Y = 110°$ yields $d_c = 240\,\text{nm}$. In case $d = 2a$ (as in *Chapter 5*), the dewetted state is meta-stable for contact angles $-a/(2d + a) = -1/5 > \cos\theta_Y > 0$. In other words, if one wishes a stable gas-filled cylindrical pit with $d = 2a$, one should have $\theta_Y > 101.5°$. In the aforementioned analysis, we have neglected the effect of a liquid meniscus which can be curved towards the bottom of the pit (in case $\theta > 90°$), yielding a negative radius of curvature, which decreases the total pressure in the pit contributing to its stability [12, 21].

A similar analysis can be applied to other geometries, such as pillars (the inverse configuration of pits) which is further described in Part III and *Chapter 8*.

Unstable bubble growth: cavitation

After this rough treatment regarding gas entrapment in (microscopic) cavities, we proceed to the study of rapid unstable bubble growth emerging from such gas pockets. This can be achieved with a tensile stress in the liquid, created by hydrodynamic or acoustic means, so that the equilibrium between expanding and collapsing forces acting on a pre-existing gas pocket is broken in favor of the expanding forces. The water around the gas pocket will vaporize leading to the formation of a large gas-vapor bubble which can be orders of magnitude larger than the original gas pocket. This process is called cavitation and was first termed in literature in 1895 by Barnaby and Thornycroft [22], who found that bubble clouds around ship propellers can dramatically reduce the propellers thrust. The existence of sub-microscopic gas pockets in the liquid was originally suggested in 1944 by Harvey *et al.* [23] and received some qualitative support during the years. A particularly noticeable experiment was done by Liebermann in 1957 [21], where he first observed a surface bubble going into solution by diffusion, then he reduced the liquid pressure to $0.25\,\text{atm}$ and observed growth of a bubble from the very same location where the original bubble had disappeared. Consequently, he postulated "the presence of a permanent submicroscopic bubble, stable against solution because of the presence of a hydrophobic surface". A direct observation and control of these tiny gas pockets has never been achieved. In *Chapter 5*, however, we will show that one can control the size of such submi-

croscopic bubbles down to a few nm in resolution. Moreover, the liquid pressure threshold at which nucleation occurs is a well-defined function of the nucleus size, as Atchley & Prosperetti formulated in 1989 [12]. They made the following statement: "Until a better feeling can be gained for the characteristics of the population of these nuclei, our results do not seem to be able to be turned into quantitative predictions of experimental cavitation thresholds." The perfect control on nuclei sizes, however, allows us to verify the predictions of Atchley & Prosperetti quantitatively in *Chapter 5*.

What happens with a cavitation bubble after its rapid growth? Since the pressure in a cavitation bubble is essentially the vapor pressure (which is far below the atmospheric pressure) the bubble will violently collapse as soon as the liquid pressure is restored to its atmospheric value. The bubble collapse can be so strong that a shock wave and even a short light pulse can be emitted (sonoluminescence). If the liquid phase around the bubble is not radially symmetric (i.e. in the presence of a wall), the bubble cannot collapse spherically, but will form a high-speed liquid jet directed towards the neighboring surface. The impact of this liquid jet can lead to serious surface erosion, so that tiny cavitation bubbles are collectively able to erode a complete ship propeller. Nowadays, ship propellers (and other parts of the ship) and turbines have been optimized to avoid surface erosion by cavitation as much as possible, but the prevention of damage and acoustic noise is still an active field of research.

In particle-laden waters the erosive effects of cavitation bubbles are still more severe than expected, as is for instance experienced by the dredging industry. A possible explanation for this phenomenon will be provided in *Chapter 6* where we study how microparticles can achieve huge translational momentum due to cavitation bubbles. In addition, we will show in *Chapter 7* that cavitation studies in particle suspensions can be carried out very reproducibly, in contrast to previous experiences.

Fortunately, the destructive nature of cavitation bubbles can also be exploited, e.g. for cleaning jewelry and semiconducting chips in ultrasonic or megasonic baths, respectively, or to destroy kidney stones in the human body. Cleaning, erosion and sound production caused by oscillating and collapsing cavitation bubbles form the main reasons why cavitation still attracts so much scientific and industrial interest today.

1.2.3   Part III - Wetting a superhydrophobic surface

Water in contact with a structured surface: the case of pillars

The last part of this thesis considers water in contact with a substrate decorated with pillars, see the last row of Table 1.1. This configuration is essentially the inverse of the one considered in the previous section: the pits are replaced by pillars. Again, one can wonder whether the water will wet the full structure or not. If not, i.e. in

the dewetted state, the water droplet rests entirely on the apex of the pillars ("Fakir droplet"). Since the associated interfacial energies are changed, Young's equation needs to be modified. The term σ_{sl} in Eq. 1.1 is replaced by $f\sigma_{sl} + (1-f)\sigma_{lv}$, with f the surface fraction of the wetted surface, and σ_{sv} changes into $f\sigma_{sv}$. This yields

$$\cos\theta_{CB} = f\cos\theta_Y - 1 + f \quad , \tag{1.3}$$

which is called the Cassie-Baxter equation [24]. If f goes to zero, the equilibrium angle with the substrate θ_{CB} reaches values close to 180°, i.e. the droplet becomes completely spherical and experiences extremely little contact (and hence friction) with the solid surface. In such cases the surface is called superhydrophobic. As an additional advantage repelled water droplets can take away small dirt particles while rolling off the surface, i.e. the surface is self-cleaning. This effect is called the "Lotus effect", after the most well-known example present in Nature: the Lotus leave [25]. Also animals utilize superhydrophobicity, e.g. blue swallows to fly in thick mist [26], water striders to walk on water [27], and butterflies to keep their fragile wings clean and dry [28].

In analogy with the previous section, the superhydrophobic state can exist in two thermodynamic states: stable and meta-stable. In the latter case, it is more favorable for the liquid to completely wet the complete structure, but it experiences an energy barrier to do so. A vertically advancing liquid front needs to 'pay' interfacial energy associated with wetting the side of the posts, before it 'receives' the interfacial energy gain at the bottom of the structure. This local energy barrier can be overcome by external forces, like acoustic vibrations or an externally applied load. However, it is also possible for the droplet to wet the superhydrophobic surface without external help in case of a little defect in the surface structure (e.g. a missing post or lower contact angle). If the little defect allows the liquid to wet the structure locally, the liquid front can now advance through the structure in the horizontal (instead of vertical) direction, which changes the associated energy balance. In *Chapter 8* we will show at which conditions it becomes favorable for the liquid front to advance horizontally through the microstructure and we will explain how it is possible that in some cases square-shaped wetted areas are observed, in stead of the usually encountered circular areas. After the wetting process, the superhydrophobic state has broken down. Consequently, the droplet has lost its frictionless movement and becomes pinned by the surface structure. This fully-wetted situation is called the "Wenzel" state and the corresponding macroscopic contact angle θ_W is described through Wenzel's equation [29]:

$$\cos\theta_W = r\cos\theta_Y \tag{1.4}$$

with $r = A_{real}/A_{proj}$ the ratio between actual and projected surface area. Again this equation follows from Eq. 1.1, by multiplying the interfacial energies associated with the solid by r, thus accounting for the additional solid surface area.

References

[1] P. Ball, "How to keep dry in water", Nature **423**, 25–26 (2003).

[2] S. Granick and S. C. Bae, "A curious antipathy for water", Science **322**, 1477–1478 (2008).

[3] E. Lauga, M. P. Brenner, and H. A. Stone, *Handbook of Experimental Fluid Dynamics* (Springer, New York) (2005).

[4] H. K. Christenson and P. M. Claesson, "Cavitation and the interaction between macroscopic hydrophobic surfaces", Science **239**, 390–392 (1988).

[5] H. Stevens, R. F. Considine, C. J. Drummond, R. A. Hayes, and P. Attard, "Effects of degassing on the long-range attractive force between hydrophobic surfaces in water", Langmuir **21**, 6399–6405 (2005).

[6] A. Lafuma and D. Quéré, "Superhydrophobic states", Nat. Mater. **2**, 457–460 (2003).

[7] C. Duez, C. Ybert, C. Clanet, and L. Bocquet, "Making a splash with water repellency", Nat. Phys. **3**, 180–183 (2007).

[8] J. W. Gibbs, *The Scientific Papers of J. Willard Gibbs* (OxBow Press, Woodbridge, Connecticut) (1993).

[9] P. Roura, "Thermodynamic derivations of the mechanical equilibrium conditions for fluid surfaces: Young's and Laplace's equations", Am. J. Phys. **73**, 1139–1147 (2005).

[10] T. Young, "An essay on the cohesion of fluids", Philos. Trans. R. Soc. London **95**, 65–87 (1805).

[11] P. S. Laplace, *Traité de Mécanique Céleste; Supplement au Dixième Livre, Sur l'Action Capillaire* (Courcier, Paris) (1806).

[12] A. A. Atchley and A. Prosperetti, "The crevice model of bubble nucleation", J. Acoust. Soc. Am. **86**, 1065–1084 (1989).

[13] P. S. Epstein and M. S. Plesset, "On the stability of gas bubbles in liquid-gas solutions", J. Chem. Phys. **18**, 1505 – 1509 (1950).

[14] S. Ljunggren and J. C. Eriksson, "The lifetime of a colloid-sized gas bubble in water and the cause of the hydrophobic attraction", Colloids Surf. A **129–130**, 151–155 (1997).

[15] A. Steinberger, C. Cottin-Bizonne, P. Kleimann, and E. Charlaix, "High friction on a bubble mattress", Nat. Mater. **6**, 665–668 (2007).

[16] J. L. Parker, P. M. Claesson, and P. Attard, "Bubbles, cavities, and the long-ranged attraction between hydrophobic surfaces", J. Phys. Chem. **98**, 8468–8480 (1994).

[17] O. I. Vinogradova, N. F. Bunkin, N. V. Churaev, O. A. Kiseleva, A. V. Lobeyev, and B. W. J. Ninham, "Submicrocavity structure of water between hydrophobic and hydrophilic walls as revealed by optical cavitation", J. Colloid Interface Sci. **173**, 443–447 (1995).

[18] N. Ishida, T. Inoue, M. Miyahara, and K. Higashitani, "Nano bubbles on a hydrophobic surface in water observed by tapping-mode atomic force microscopy", Langmuir **16**, 6377–6380 (2000).

[19] Y. Fan and R. Wang, "Submicrometer-sized vaterite tubes formed through nanobubble-templated crystal growth", Adv. Mater. **14**, 1857–1860 (2002).

[20] S. Lou, Z. Ouyang, Y. Zhang, X. Li, J. Hu, M. Li, and F. Yang, "Nanobubbles on solid surface imaged by atomic force microscopy", J. Vac. Sci. Technol. B **18**, 2573–2575 (2000).

[21] L. Liebermann, "Air bubbles in water", J. Appl. Phys. **28**, 205–211 (1957).

[22] S. Barnaby and S. J. Thornycroft, "Torpedo boat destroyers", P. I. Civil Eng. **122** (1895).

[23] E. N. Harvey, D. K. Barnes, W. D. McElroy, A. H. Whiteley, D. C. Pease, and K. W. Cooper, "Bubble formation in animals", J. Cell. Compar. Physl. **24**, 1–22 (1944).

[24] A. B. D. Cassie and S. Baxter, "Wettability of porous surfaces", Trans. Faraday Soc. **40**, 546–551 (1944).

[25] W. Barthlott and C. Neinhuis, "Purity of the sacred lotus, or escape from contamination in biological surfaces", Planta **202**, 1–8 (1997).

[26] A. Rijke, W. Jesser, S. Evans, and F. Bouwman, "Water repellency and feather structure of the Blue Swallow Hirundo atrocaerulea", Ostrich **71**, 143–145 (2000).

[27] X. F. Gao and L. Jiang, "Water-repellent legs of water striders", Nature **432**, 36 (2004).

[28] T. Wagner, C. Neinhuis, and W. Barthlott, "Wettability and contaminability of insect wings as a function of their surface sculptures", Acta Zool. **77**, 213–225 (1996).

[29] R. N. Wenzel, "Resistance of solid surfaces to wetting by water", Ind. Eng. Chem. **28**, 988–994 (1936).

Part I

Nanobubbles at the solid-liquid interface

2

On the shape of surface nanobubbles[‡][∗]

Previous AFM experiments on surface nanobubbles have suggested an anomalously large contact angle θ of the bubbles (typically ~160º measured through the water) and a possible size dependence θ(R). In this chapter we determine θ(R) for nanobubbles on smooth, highly orientated pyrolytic graphite (HOPG) with a variety of different cantilevers. It is found that θ(R) is constant within experimental error, down to bubbles as small as R=20 nm, and is equal to 119±4º. This result, which is the lowest contact angle for surface nanobubbles found so far, is very reproducible and independent of the cantilever type used, provided that the cantilever is clean and the HOPG surface is smooth. In contrast, we find that, for a particular set of cantilevers, the surface can become relatively rough due to precipitated matter from the cantilever onto the substrate, in which case larger nanoscopic contact angles (~150º) show up. In addition, we address the issue of the set-point dependence. Once the set-point ratio is below roughly 95%, the obtained nanobubble shape changes and depends on both nanobubble size and cantilever properties (spring constant, material, and shape).

2.1   Introduction

Water in contact with hydrophobic surfaces - the most frequently studied example of a non-wetting system - displays various intriguing but poorly understood properties. One of them are spherical cap-like soft domains at the solid-liquid interface, which are currently termed "surface nanobubbles". Since the first observations through atomic force microscopy (AFM) about a decade ago [1–5], ample evidence has been reported on their existence. Most of the AFM studies explored the formation mechanism of nanobubbles and their dependence on environmental changes. This yielded characteristics fitting with the interpretation of gas-filled nanobubbles: the features are spherically-shaped [6, 7], can merge together [6, 8], disappear in degassed water [9], re-appear when the liquid is locally oversaturated (e.g., through the exchange of two solvents [7, 10–14], liquid heating [10] or electrolysis [8, 15]). Although most of these studies were done with AFM in tapping mode, nanobubbles were also inferred from infrared spectroscopy [12, 14], neutron reflectometry [16], quartz crystal microbalance [17] and rapid shock-freeze cryofixation experiments [18].

Surface nanobubbles have been found on a variety of substrates*, with macroscopic contact angles (measured through the liquid) varying between $\sim 50^{\circ}$(Au) and 110° (hydrophobized Si), and roughnesses ranging from atomically smooth (HOPG) to rough on the nanometer-scale (e.g., 3.5 nm rms roughness on polyamide). In contrast, the observed contact angle of the nanobubbles with the substrates is always in the range 150-170°. Table 2.1 provides an overview of this contact angle discrepancy reported in literature so far.

The liquids in which surface nanobubbles have been found usually consist of ultrapure MilliQ water or DI water, with occasional additions of surfactants [7, 10], salts [7, 15] or acidic solutions [8]. The gas inside the nanobubbles generally comprise air, sometimes the bubbles are composed of single gases such as N_2 [8, 15], O_2 [15], or CO_2 [14]. It is found that these variations do not significantly change the magnitude of the nanoscopic contact angle.

How should the anomalously large contact angle of surface nanobubbles be interpreted? On one hand this result has been reproduced in various experiments, see Table 2.1. On the other hand, one would expect that for large enough bubbles (contact line radius $R \rightarrow \infty$) the nanoscopic contact angle will approach the macroscopic one. This, however, was never observed: the largest surface bubbles measured through AFM had R-values of several microns and radii of curvature R_c of several tens of microns, and still showed contact angles $\theta_{nb} > 160^{\circ}$ [7, 14] without a noticeable trend toward lower values. This raises a second and related issue as to whether one should expect the nanoscopic contact angle to be size-dependent. Although Zhang

---

*e.g., bare Si [19], hydrophobized Si [10, 11], polystyrene [6, 16, 20, 21], polyamide [11], gold [22, 23], and highly orientated pyrolitic graphite (HOPG) [1, 7–9, 13, 15]

Substrate	θ_m or θ_a / θ_r (°)	θ_{nb} (°)	Tip corr.	Ref.
HOPG	72±11	164±6	Y	[7]
HOPG	81±3 / 63±3	164±6	Y	[9]
Si (100) - OTS	110	150-170	N	[2]
Si (100) - OTS	108±5	168±9	Y	[7]
Si (100) - OTS	110±3	169±3	N	[24]
Si (100) - OTMS	112±3 / 101±3	174±1	N	[12, 14]
Si (100) - TMCS	74 / 67	150-157	N	[25]
Si (100) - PFDCS	105 / –	137-168	N	[10]
PS	97	170-177	N	[21]
PS	~90	168±10	N	[6]
Au(100)	40-60	166±2	Y	[23]

Table 2.1: Overview of contact angle discrepancy in surface nanobubble experiments with TM-AFM where both the static macroscopic contact angle θ_m (or: advancing contact angle θ_a / receding contact angle θ_r) and the contact angle as deduced from nanobubbles θ_{nb} are reported. Abbreviations of substrates: PS: polystyrene; OTS: octadecyltrichlorosilane; OTMS: octadecyltrimethylchlorosilane; TMCS: trimethylchlorosilane; PFDCS: 1H,1H,2H,2H-perfluorodecyldimethylchlorosilane. Note that the contact angles are not always corrected for the tip radius (see column 4 for yes=Y or no=N), in which case it is the apparent nanoscopic contact angle θ' which is reported.

et al. [14] were not able to detect such a relation, in contrast, other studies have reported a small decrease in contact angles with increasing nanobubble size, which was attributed to the presence of a line tension [19, 23, 25]. In one of these studies [25], the bubble shapes were not deconvoluted for the finite size of the cantilever tip, which hinders the extraction of line tension. Contact angles reported for surface nanodroplets - the inverse problem - measured by TM-AFM are either in good agreement with the macroscopic values [26, 27] or any discrepancies could be attributed to surface heterogeneities [28]. Note that theoretically, a line tension is expected to act on a length scale of $\sim \tau/\sigma \sim 10^{-11}\text{N}/10^{-1}\text{N/m} = 10^{-10}$ m [29], with τ the typical line tension and σ the liquid-air interfacial tension, which is well below the typical size of a surface nanobubble.

In the discussion on contact angle discrepancy and its possible size dependence, it has always been assumed that the actual topography of the gas-liquid (nanobubble) interface is obtained correctly by the vibrating cantilever tip. However, Zhang *et al.* [7] concluded that the cantilever tip most likely deforms (or penetrates) the bubble during imaging. How should the crucial premise that the actual shape of the nanobubble can be obtained by TM-AFM be verified? A possible way to approach this problem is to use cantilevers of different types to see whether their intrinsic properties such as tip radius, spring constant k, and local wetting properties (material), have an effect on the detected nanobubble shape. If the tip penetrates or deforms the bubble during imaging, then one would expect those properties play a role, and thus that different cantilevers will yield different nanobubble shapes.

In addition, tunable properties, such as the set-point ratio, free amplitude, and drive frequency of the cantilever, could play a role. From this list, only the effect of the set-point amplitude has been studied: Zhang *et al.* [7] found that a reproducible nanobubble shape is obtained when using a V-shaped Si_3N_4 cantilever (Veeco) with a spring constant $k = 0.079$ N/m for set-point ratios between 0.93 and 0.74. However, for imaging purposes, cantilevers that are a factor of > 4 stiffer are used in Ref. [7], and it is unclear how this affects the results. Yang *et al.* [13] showed that the recorded nanobubble shape is a subtle function of the set-point ratio in the case of a rectangular Si_3N_4 cantilever (MikroMasch) with $k = 3.8 \pm 1.8$ N/m: reducing the set-point ratio from 0.89 to 0.78 reduces the apparent nanobubble height with ~10%, whereas more drastic morphological changes are obtained for set-point ratios below 0.67. Apart from these studies, little is known.

The aim of this study is to obtain the contact angle of nanobubbles as a function of their size. As argued, a prerequisite for this measurement is, first, the validation of the assumption that the nanobubble shape is not affected by intrinsic cantilever properties and second, insight how the observed nanobubble shape depends on tunable properties such as the set-point ratio. To this end, we have measured nanobubbles present on HOPG using fifteen cantilevers of all kinds, displaying different materials, shapes,

and spring constants.

2.2 Materials and Methods

2.2.1 Substrate/water

As substrates Highly Ordered Pyrolytic Graphite (HOPG, Mikromasch grade ZYA) is used to ensure clean, atomically flat surfaces. Before each experiment, the dry, freshly cleaved (with adhesive tape) HOPG substrate is measured with AFM to ensure that the surface is clean and atomically smooth. Water is purified using a Milli-Q A10 system. To ensure gas saturated water, the liquid is allowed to equilibrate with atmospheric pressure for several hours. The macroscopic advancing contact angle θ_a of water with the HOPG substrate is 95°, and the receding contact angle is $\theta_r = 82^o$, as measured with an optical contact angle goniometer (OCA-15+, Data Physics, Germany) with built-in SCA-20 software.

2.2.2 Nanobubble formation by entrapment

To create nanobubbles, the cantilever is mounted in the holder (Fig. 7.1a) and immersed in a large water droplet deposited by a syringe (Fig. 7.1b). Second, the holder-cantilever assembly is turned upside down with the droplet hanging underneath the holder. The assembly is then quickly pressed onto the freshly cleaved HOPG surface, already mounted into the AFM head, allowing air to become entrapped between the droplet and the HOPG surface. See Fig. 7.1 for the accompanying sketches. We observed that the water droplet should be large enough in order to create nanobubbles by entrapment. Presumably, a small droplet is not able to trap air because of its larger curvature.

2.2.3 Atomic Force Microscopy (AFM)

Nanobubble measurements are performed on a Veeco Multimode equipped with a Nanoscope V controller, a low-noise head (Veeco), and a piezo scanner with vertical motor approach ("E scanner"). The cantilevers vary in manufacturing company (Veeco and Mikromasch), surface material (silicon, silicon nitride or gold), shape (rectangular or V-shaped), and spring constant. The following cantilever types have been used: Veeco NP-S Si_3N_4 V-shaped and MPP 22120 Si rectangular; Mikromasch NSC36 Si rectangular, NSC36 Si_3N_4 rectangular, CSC37 Au rectangular, CSC37 Si rectangular, and CSC37 Si_3N_4 rectangular. An overview of the cantilever properties used in this work is found in Table 2.2. Prior to each experiment the cantilever of interest is exposed to plasma for ~1 min (Harrick Plasma). The spring constant is determined in air using the thermal calibration method 'Thermal Tune' in the Nanoscope
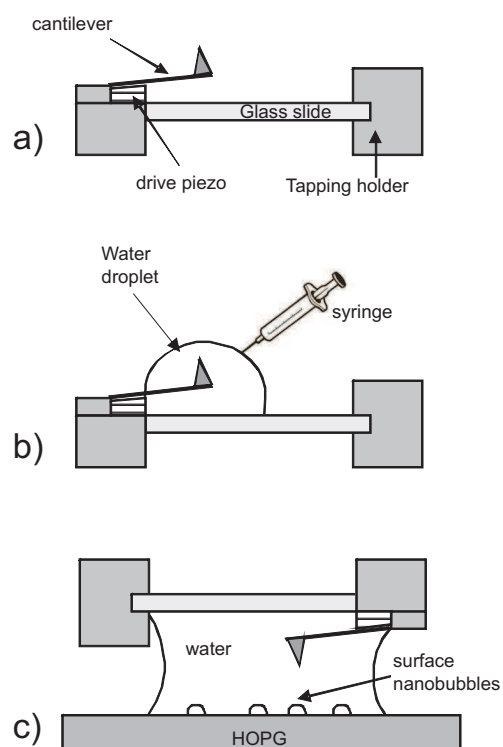
Figure 2.1: Sketch of the dry cantilever holder (a). To create nanobubbles, the cantilever is first immersed in a large water droplet deposited by a syringe (b), while secondly the holder-droplet assembly is turned upside down and pressed onto the HOPG substrate which is already mounted in the head of the AFM (c).

7.20 software [30]. The resonance frequency in liquid is determined with the same method at a distance of 100 nm above the sample surface for the correct characterization of the added mass of the system. The cantilever is acoustically driven with a frequency just below resonance (without Q-control). Acoustic driving of the cantilevers has been realized using a modified cantilever holder (Veeco Tapping holder air, MMMC), as first described in Ref. [31], which reduces spurious resonances characteristic of the conventional commercial liquid cell and increases the stability of the measurements. The height images are recorded at different amplitude set-point ratios $r_{sp} = A/A_0$, where A is the amplitude set-point during imaging and A_0 is the free amplitude of the cantilever. With the adjusted cantilever holder, the free amplitude is constant over a much longer period of time compared to the commercial liquid cell, allowing long-term imaging with a constant r_{sp}. To find the correct free amplitude, Amplitude Phase Distance (APD) curves are recorded before and after each recorded height image. Typically, $A_0 \sim 30\,\mathrm{mV}$ and deflection sensitivities are $\sim 40\,\mathrm{nm/V}$, resulting in values of $1\,\mathrm{nm} < A_0 < 1.5\,\mathrm{nm}$. Hence, the total amplitude of the cantilever, $A_{tot} = A_0 + A_d$, is kept around $1 - 2\,\mathrm{nm}$. Here, A_d is the amplitude of the piezo driving the cantilever base and can be determined through Eq. 2a of Ref. [32]. This low value of A_{tot} is feasible because of the low-noise head, the controller, and the special liquid cell and is probably much smaller than the one used in most other previous studies (cf. Ref [6]), however, we are not able to check this because of the lack of reported experimental details.

The images obtained are in most cases $2 \times 2\,\mathrm{\mu m}^2$ in size with a resolution of 512×512 pixels^2. Typical scan rates are $1\,\mathrm{Hz}$ (corresponding to a tip velocity of $4\,\mathrm{\mu m/s}$).

2.2.4 Image analysis

The obtained height images are processed and analyzed using digital image analysis software. First, the images are subjected to second-order flattening (excluding the bubbles) and leveled such that the HOPG surface represents zero height ($0\,\mathrm{nm}$). This allows for the identification of individual nanobubbles using a height-threshold (typically $\sim 4\,\mathrm{nm}$). In the next step a 3D fit is applied to each nanobubble separately (to those data points that are above the height threshold), thereby taking into account all information of the recorded nanobubble profile. This results in the apparent radius of curvature R_c' of the nanobubble and its position with respect to the substrate surface. From these parameters, the other relevant geometrical parameters follow: height h, apparent contact line radius R', and apparent contact angle θ' of the nanobubble, see Fig. 2.2a.
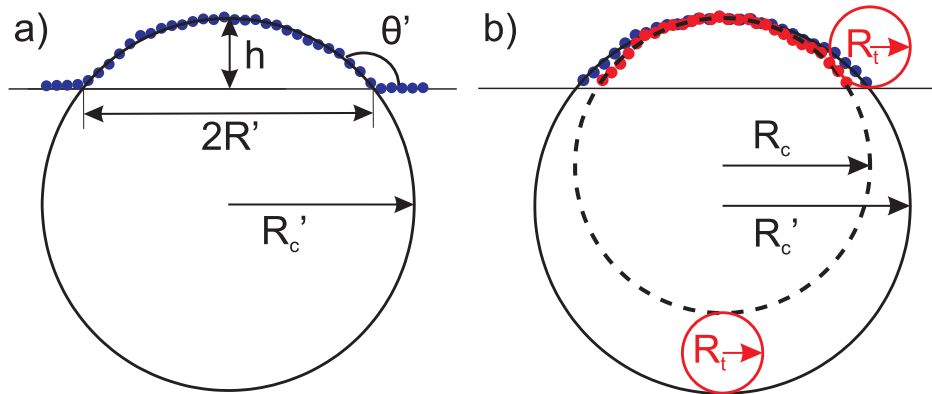
Figure 2.2: a) Cross-sectional datapoints (circles) along the scanning direction of a nanobubble present in Fig. 2.4 with height h=26.2 nm and apparent radius R'=54.6 nm (without tip radius correction). Note that the bubble resides on a smooth surface and remains spherically shaped when touching the surface, i.e., it does not form a noticeable foot at the triple-contact line. The 3D spherical fit (solid line) gives the apparent radius of curvature of $R'_c = 70$ nm for the bubble. When the position of the substrate (horizontal line) is known, the other relevant geometrical parameters follow. The apparent contact angle θ' is taken through the water. b) The same bubble showing raw and deconvoluted cross-sectional datapoints (blue and red circles, respectively) together with their respective spherical fits R'_c and $R_c = 55.0$ nm. Alternatively, R_c can be obtained using the tip radius R_t (in this case, $R_t = 15$ nm) through $R_c = R'_c - R_t$.

2.2.5 Tip correction

The topography image of the solid-liquid interface as obtained by the cantilever tip is a combination of the substrate morphology and the shape of the cantilever tip and therefore needs to be corrected for the tip shape [33]. In the case of a spherical cap-shaped object and a spherical tip apex, tip deconvolution simply implies that $R_c = R'_c - R_t$, with R_t being the tip radius [19]. Assuming that the bubble height h is not affected by the tip shape (see Fig. 2.2b) R and θ can be calculated. Note that it is also assumed that the bubble is only probed by the spherical tip apex and not by the tip side walls. This is correct insofar as the bubble makes an angle with the solid wall (through the water) of $\theta_{cutoff} > 90° +$half-cone angle of the tip. For the cantilevers used in this chapter $\theta_{cutoff} = 110°$ (Mikromasch) and $\theta_{cutoff} = 125°$ (Veeco). For the former cantilever it always holds $\theta > \theta_{cutoff}$ whereas for the latter we only take those datapoints into consideration for which this condition is fulfilled. Instead of applying the correction after the 3D fit, alternatively one can also first deconvolute the individual datapoints and then apply the spherical fit. We checked that this gives no noticeable difference in the corrected radius of curvature as compared to that of the first method, see Fig. 2.2b. Hence, it is save to apply the simple correction $R_c = R'_c - R_t$. Notice that this implies $dR_c = dR_t$, which is further translated into ΔR and $\Delta\theta$ by $\Delta R = \frac{\partial R(h,R_c)}{\partial R_c}\Delta R_c$ and $\Delta\theta = \frac{\partial \theta(h,R_c)}{\partial R_c}\Delta R_c$. These relations are used to estimate the error in our measurements.

The tip radius R_t has been determined in two ways: using high resolution SEM imaging (HR- SEM Zeiss LEO 1550 equipped with NORAN EDS and WDS) and using the measured profile of a (multiple) step on the substrate. From the SEM images, the tip radius R_t^{SEM} was determined by applying a circular fit to the imaged tip apex (Fig. 2.3a). In the second method, a step profile of the substrate is averaged along the direction of the (multi)step (to filter out any noise) and interpolated and then a circular fit is applied yielding R_t^{step} (Fig. 2.3b). We have checked the reproducibility of R_t^{step} by using as many steps as possible (typically $2-5$). The tip radii obtained with these two methods are shown in Table 2.2. The average of both values (if possible) is the tip radius R_t for which our data has been corrected. The experimental error of the tip radius dR_t is anticipated in a worst-case scenario by adding the two error values determined in the two methods, $dR_t = dR_t^{SEM} + dR_t^{step}$. In some cases, only one of the two methods could be used because of a broken tip (which became broken after taking the recordings) or the lack of a sufficiently large step. If neither of the two methods could be used, the tip correction is not applied; consequently, those data are not presented in graphs where tip-corrected data are shown.
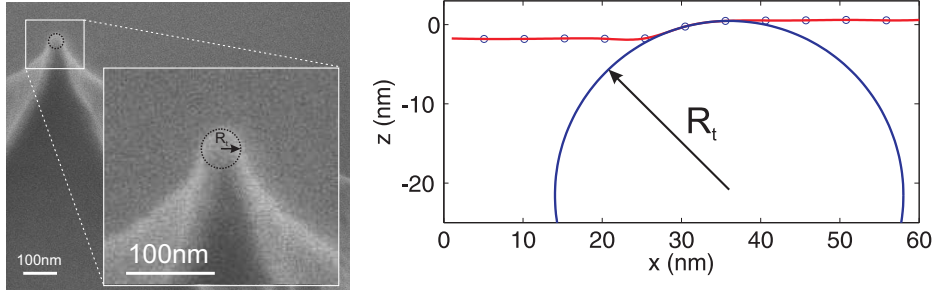
Figure 2.3: SEM picture of Veeco NP-S Si_3N_4 cantilever tip (left) and circular fit to the measured profile of a step edge in the HOPG (right).

2.3 Results and Discussions

Previous experimental studies showed that no nanobubbles are formed on HOPG unless the water is temporally supersaturated, e.g., through the exchange of two liquids in which the second liquid has a lower gas solubility than the first [7, 13]. Here, we show that there is an even simpler method to form nanobubbles on HOPG, that requires neither an explicit oversaturation of the liquid nor the flushing of one liquid with the other but involves just the deposition of a large water droplet on the HOPG substrate [11]. For further description and supporting sketches, see Figure 7.1. After this uncomplicated procedure, images of surface nanobubbles could be obtained through AFM in tapping mode.

2.3.1 Properties of nanobubbles formed by droplet deposition

A typical result of the water-solid interface is depicted in Fig. 2.4 and shows several distinctive features: the bubbles show up as spherical caps, consequently allowing them to be fitted by a spherical cap. Second, the number density of the nanobubbles is relatively low, which allows good analysis of individual bubbles. Because we did not create the bubbles with the help of a forced gas oversaturation, it is also expected that the number densities are relatively low compared to cases were strong gas oversaturation is used (e.g., in Refs. [7, 10, 11]). Also notice that there are more bubbles residing on the lower side of the HOPG step than on the upper side, in contrast with the observations in Ref. [13]. A step presumably hinders the air flow while it is escaping in between the substrate and the approaching droplet, and thus some air may become entrapped at this location. Some bubbles are not located at steps, but reside on apparently smooth HOPG plateaux. Third, the bubbles have various sizes, which allows the determination of $\theta(R)$ from a single image. Notice that this feature is not
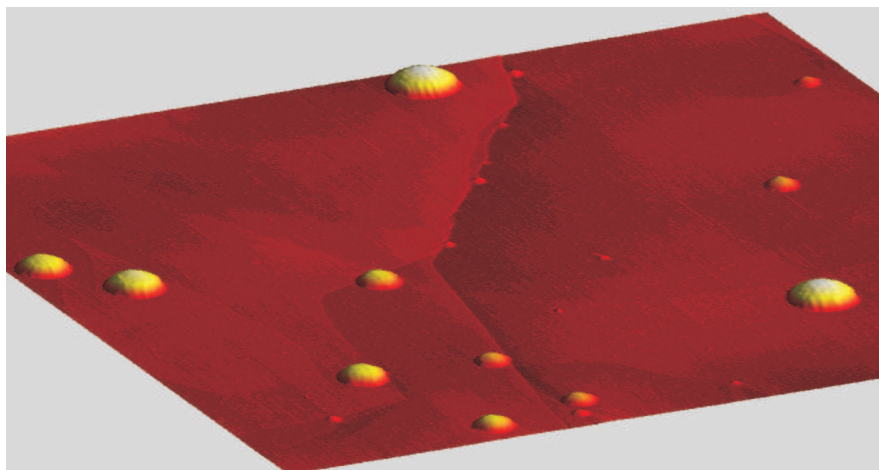
Figure 2.4: Typical 3D image of surface nanobubbles present on a HOPG surface immersed in water. The size of the image is $2000 \times 2000 \times 40 \, \text{nm}^3$ and is shown on scale. The nanobubbles show up as perfect spherical caps and have various sizes. They reside both at step edges and on atomically flat terraces. Apart from the step edges, the HOPG surface appears to be very smooth. The picture is taken with cantilever 11 in Table 2.2 and is shown in 2D in Fig. 2.5 (second from the top in the right column). No tip correction has been applied.

always the case: in dense surface nanobubble populations, a preferred nanobubble size can show up [6, 34].

2.3.2 Rough and smooth surfaces

To examine whether $\theta(R)$ is dependent on the cantilever properties, experiments are carried out with fifteen different cantilevers, displaying various shapes, materials, and spring constants. Table 2.2 provides an overview of the cantilevers used and their respective properties. Remarkably, all experiments can be divided into two significantly different classes. In the first class (A) the nanobubbles are present on relatively *rough* HOPG surfaces, while in the second class (B) the bubbles reside on relatively *smooth* HOPG surfaces. Figure 2.5 presents height images of eight different experiments and illustrates the categorization based on the roughness present on the HOPG.

In the left column, nanobubbles are residing on rough substrates (class A), and the middle column depicts nanobubbles on atomically smooth surfaces (class B). Corresponding line scans of the substrates illustrate the difference in surface roughness
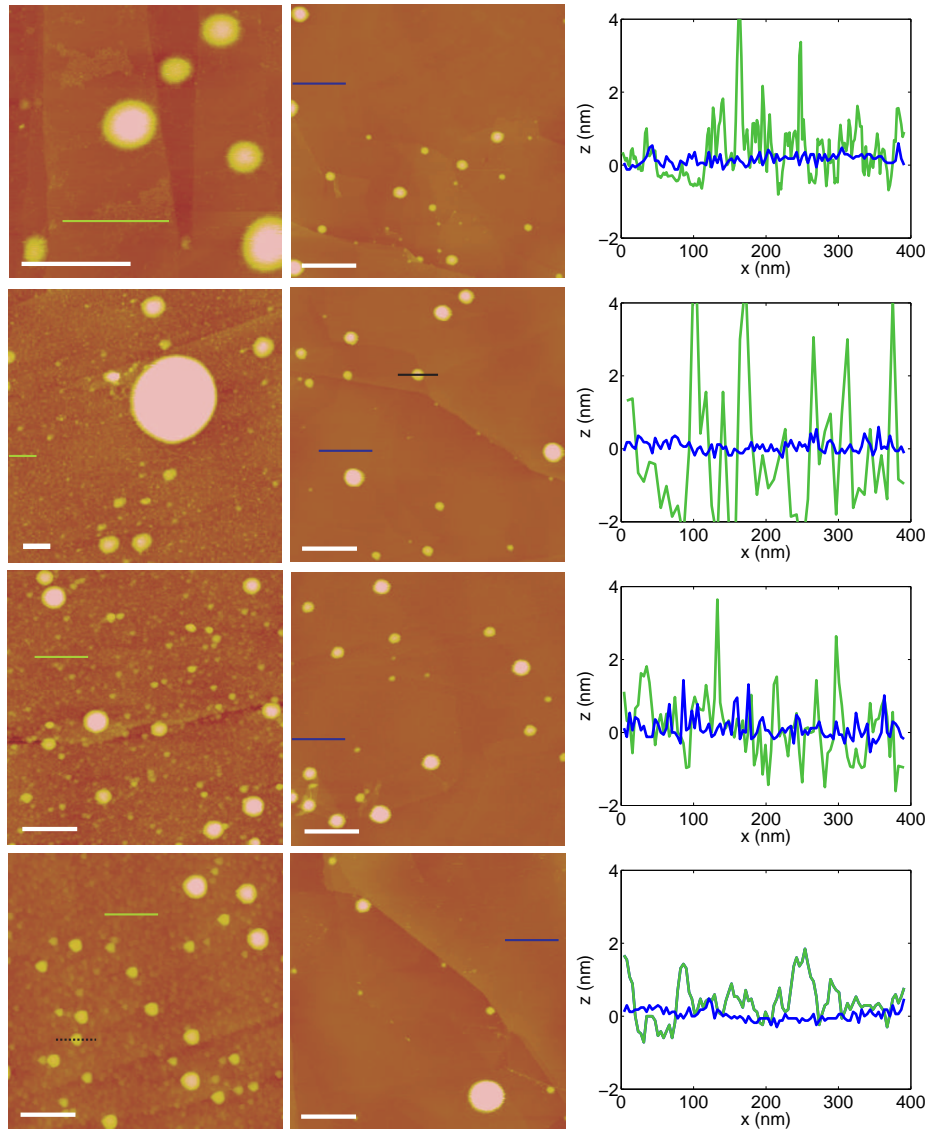
Figure 2.5: AFM height images of eight different experiments. All experiments could be divided into two categories: Images having *rough* background surfaces (left column) or with *smooth* background surfaces (middle column). The white scale bar is 400 nm in length and the color-coded height scale is 50 nm for all images. To show the difference in surface roughness, typical line scans of 400 nm are taken in both the left (green line) and middle (blue line) images and are displayed in the graphs in the right column. Two line scans of a bubble (black dashed resp. solid line) in contact with an apparently rough or smooth surface are compared in Fig. 2.6. Cantilevers used in these images correspond to nos. 1, 4, 6, and 7 (top to bottom, left column) and 10, 11, 13, and 15 (top to bottom, middle column) of Table 2.2.

(right column).

A quantitative distinction of roughness can be made by comparing the rms values of nanobubble-free areas in the pictures, which gives $z_{rms} = 0.6 - 2.6$ nm for the rough and $z_{rms} = 0.2 - 0.3$ nm for the smooth surfaces present in Fig. 2.5. Another useful measure is the surface area difference a, which is the difference between actual surface area A_{actual} and projected surface area A_{proj} with respect to A_{proj} in percentage:

$$a = \frac{A_{actual} - A_{proj}}{A_{proj}} \cdot 100\% \quad . \tag{2.1}$$

The pictures in the left column of Fig. 2.5 show $0.78\% < a < 5.64\%$, and the middle column pictures represent $0.12\% < a < 0.47\%$. In this way, all fifteen experiments can be categorized, see Table 2.2: eight experiments were carried out with cantilevers 1-8 (class A) and show surfaces which are relatively rough (i.e., the nanobubble-free background surface has rms-values > 0.6 nm and $a > 0.7\%$) whereas the other seven experiments display HOPG surfaces which are relatively smooth (i.e., the nanobubble-free background surface has rms values < 0.3 nm and $a < 0.7\%$) and correspond to cantilevers 9-15.

2.3.3 Large and small contact angles

The AFM images, of which some are depicted in Fig. 2.5, allow us to extract the contact angles of the bubbles, which is our quantity of interest. We find that the contact angle of two bubbles of equal apparent widths are dramatically different provided that they are residing on substrates of different classes (i.e., rough or smooth). Fig. 2.6 illustrates the result using two line scans of equally sized bubbles present either on a relatively rough substrate (dashed line) or on a smooth substrate (continuous line). What determines the difference? Besides the difference in substrate roughness, the bubbles have also been measured by cantilevers of different types (nr. 7 and 11 of Table 2.2). Therefore, we need to compare all bubbles obtained in all experiments, to give a final answer to the question what determines the difference in contact angle. This will be done in a subsequent section, however, first we will consider possible origins of the observed roughness, because this will turn out to be a crucial factor.

2.3.4 Contaminated and clean cantilevers

After the AFM experiments, the cantilevers are imaged by high-resolution SEM in order to obtain their tip radii. Interestingly, the SEM images can be divided into *the same* two classes. Cantilevers with which nanobubbles on rough surfaces have been measured (class A) are notably contaminated and show distinct staining all over the surface (Fig. 2.7 left). The structures look different from dust particles, which are more irregularly shaped. Furthermore, it is known that dark spots on
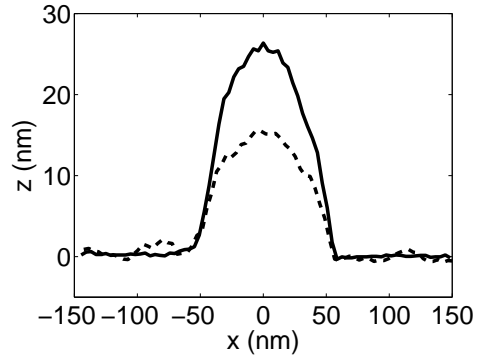
Figure 2.6: Linescans of two bubbles in contact with either an apparently rough substrate (dashed line, taken from the bottom left picture of Fig. 2.5) or a relatively smooth substrate (continuous line, taken from second picture in the middle column of Fig. 2.5). The apparent widths of both bubbles are similar, but their heights are markedly different, translating into different contact angles.
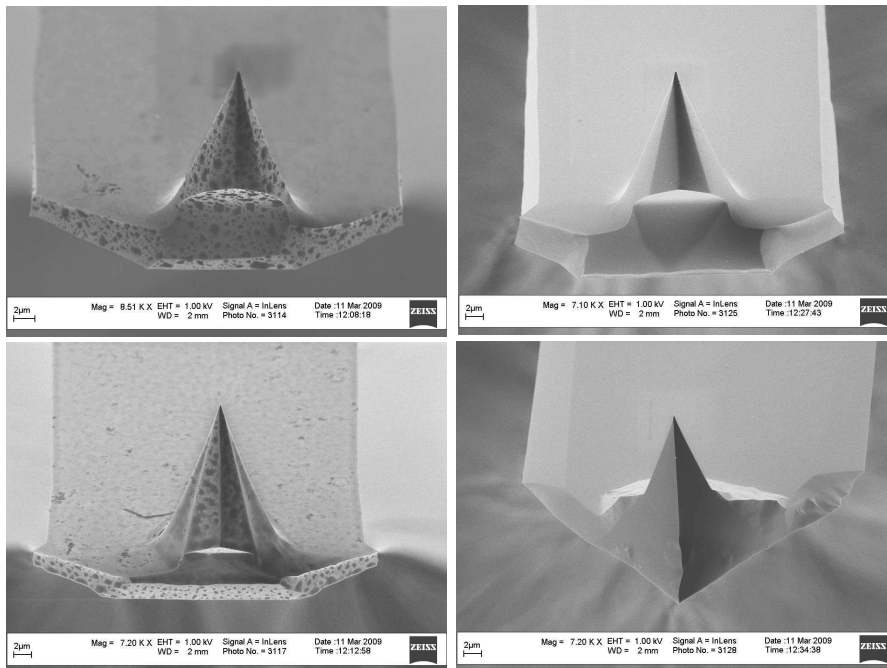
Figure 2.7: SEM images of cantilevers after use. Some cantilevers are stained (left), but others are completely smooth (right). The cantilevers correspond to nos. 1 and 7 (left) and 10 and 12 (right) in Table 2.2.

(semi)conducting surfaces in SEM images presumably indicate organic contamination, e.g., siloxane oil. In contrast, cantilevers with which the smooth surfaces had been measured (class B) look perfectly clean and smooth in the SEM images (Fig. 2.7 right).

2.3.5   Origin of contamination

All cantilevers are imaged simultaneously, which excludes the SEM chamber itself of being the source of contamination. We have also imaged new (unused) cantilevers from the same batches as the used cantilevers, and they are as clean or contaminated as the ones which were imaged after use. This indicates that the contamination is not measurement-induced but originates from the packaging material. Interestingly, MM cantilevers from class A were stored in their gel packages for longer periods of time (months) than MM cantilevers from class B (weeks). Veeco cantilevers did not show the strange contamination, even if they are stored in gel packages for several years, most likely due to a protective seal on top of the gel package. Our result is in line with previous observations of organic contamination on cantilevers arising from the packaging material [35, 36].

2.3.6   Origin of rough surfaces

For all fifteen experiments described here, the same experimental preparation procedure has been strictly followed. We checked via AFM that all HOPG surfaces are atomically smooth by preparation. One day the substrates remained atomically smooth in the experiment, but on another day (using another cantilever) the surfaces appeared to be much rougher. Sometimes, smooth and rough substrates were obtained on a single day in which nothing was changed, except the cantilever. We determined that other possible sources (water, substrate, handling material, or air) did not affect this result. Most importantly, we always find striking agreement between the observation of nanobubbles residing on rough substrates and the cantilevers that were used being contaminated. However, cantilevers with which smooth substrates have been measured are always clean in the SEM images. The most likely interpretation is that the contamination originally present on the cantilever (and presumably the whole chip) precipitates after immersion in the water on the HOPG surface, resulting in the observation of nanobubbles on relatively bumpy surfaces. This impression is underlined by some experimental cases, in which we could observe the growth of rough features in time indicating a precipitation process of an unwanted material.
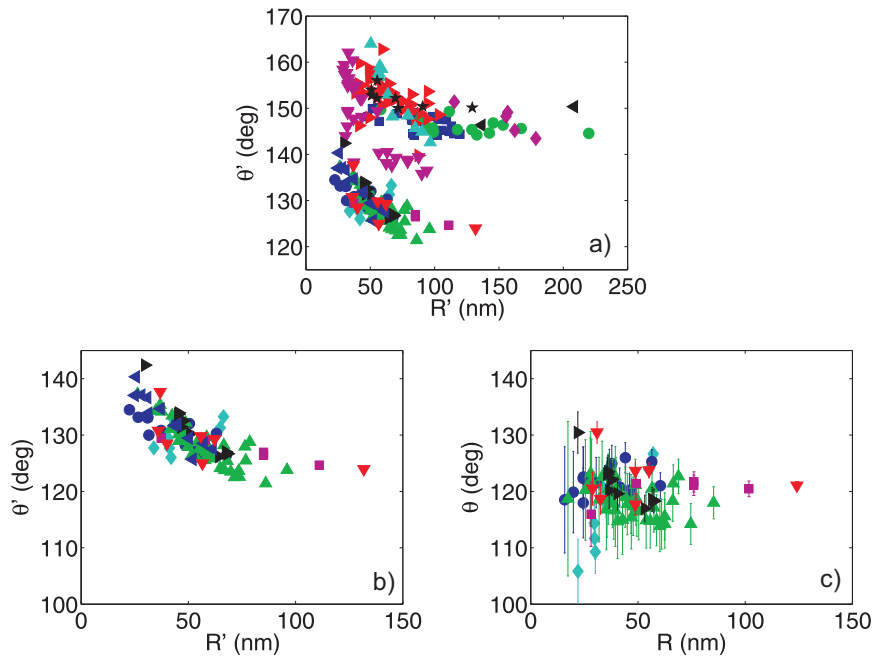
Figure 2.8: Contact angles as deduced from the imaged nanobubbles as a function of their size R. Each symbol refers to a particular cantilever, see Table 2.2. Only images obtained with the largest possible set-point ratio (typically ∼ 95%) are used. a) Apparent contact angle θ'(not tip-corrected) as a function of R' for all fifteen cantilevers. b) Same data corresponding to 'clean' experiments only, i.e., cantilevers 9-15 in Table 2.2 (class B) - note the different scale on the θ' axis. c) Tip-corrected data of class B experiments including errorbars.

2.3.7 Contact angle as function of size

Now we can address the main question of this work: How does the contact angle depend on the nanobubble size? Fig. 2.8a shows the apparent contact angle θ' as function of the apparent nanobubble size R' for all fifteen experiments, measured with the largest possible set-point ratio (typically $\sim 95\%$). Each symbol refers to a particular cantilever, see Table 2.2. As touched upon before, two separated regimes are clearly visible: a cloud of large contact angles in the range $145^{\circ} - 165^{\circ}$, which is similar in magnitude to those reported in the literature (see Table 2.1), and another cloud with $120^{\circ} < \theta' < 140^{\circ}$, i.e., much smaller (apparent) contact angles than previously observed. Strikingly, the cloud with the large contact angles contains all datapoints measured by cantilevers 1-8 (class A), corresponding to the rough substrates and the contaminated cantilevers. Similarly, the relatively small contact angles are obtained by cantilevers 9-15 (class B), i.e., the experiments with apparently smooth surfaces and clean cantilevers. Hence, the unwanted roughness, which is probably cantilever-induced contamination, increases the local contact angle of surface nanobubbles. We notice that the apparent roughness itself is not sufficient to explain the dramatic contact angle increase, i.e., through Wenzel's equation [37] $\cos\theta = r\cos\theta_m$. This indicates that the contamination is hydrophobic in nature. Second, the datapoints are not scattered but collapse on top of each other, despite differences in material, shape, and spring constants of the cantilevers. This could indicate that at large enough set-point ratios the vibrating cantilever tip during imaging hardly penetrates into the nanobubble. If it did, then the depth of penetration would depend on the cantilevers' local wetting properties, spring constant, and tip radius of curvature, and thus the nanobubble shape would be cantilever-dependent, but this is not observed. The good collapse of data points, especially of the lower cloud (class B, Fig. 2.8b), also means that the shape of surface nanobubbles can be reproducibly obtained on different days and with different cantilevers, provided that imaging conditions are identical. The spread in θ' in the upper cloud is larger than in the lower cloud, in line with the idea of contact angle hysteresis being larger on rough and chemical inhomogeneous surfaces [37]. Third, the apparent dependence of θ' on R' is an effect caused by the finite size of the tip. After application of the tip radius correction, the dependence of θ on R vanishes: θ is constant within the experimental error over a wide range of sizes (Fig. 2.8c). The error bars originate from the experimental tip radius determination, which has an error ΔR_t and translates into errors ΔR_c, ΔR, and $\Delta\theta$, as described earlier in this chapter. The mean contact angle of the 85 data points present in Fig. 2.8c is $\bar{\theta} = 119 \pm 4^{\circ}$. This is significantly below commonly reported values of $\sim 160^{\circ}$ [2, 6, 7, 9, 10, 12, 14, 21, 23, 25] and the lowest contact angle of surface nanobubbles reported so far. Alternatively, the contact angle can be determined from the plots of R_c vs R and R vs h, which both show linear relationships (Fig. 2.9a and b) and negligible offsets. Because $\cos(\theta - 90) = R/R_c$, the
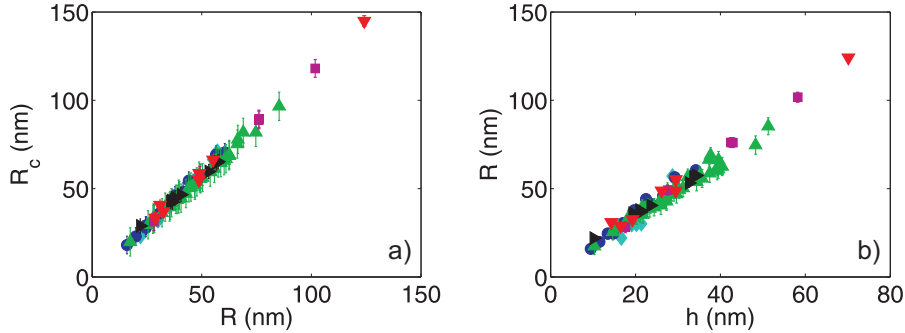
Figure 2.9: Plots of radius of curvature R_c vs radius R (a) and radius R vs height h (b) of class B experiments. Both plots show a linear relationship and go through the origin. The slope can be used to determine the contact angle θ.

linear relationship $R_c = \alpha R$ gives $\theta = \cos^{-1}(1/\alpha) + 90 = 119.4^o$, with $\alpha = 1.1478$ as result of a linear fit. Similarly, $\cos(\theta - 90) = 2hR/(h^2 + R^2)$ can be rewritten using $R = \beta h$ into $\theta = \cos^{-1}(2\beta/(1 + \beta^2)) + 90 = 117.7^o$ with $\beta = 1.6546$ as the fitted slope. Both values are within the statistical error range of $\overline{\theta} = 119 \pm 4^o$. The constant value of θ implies that the line tension is consistent with zero within the precision of our experiments [†].

2.3.8 Radius of curvature as function of size

The plot of R_c vs R (Fig. 2.9a) reveals another important characteristic of surface nanobubbles: $R_c \to 0$ as $R \to 0$, leading to a divergence in the Laplace pressure $p_\sigma = 2\sigma/R_c$, with σ being the water-air interfacial tension. Even a ten-fold reduction in surface tension (e.g., due to surface-active solutes or a local supersaturation [38]) still gives an excess pressure of 7.2 bars inside a nanobubble of $R_c = 20$ nm and should lead to rapid dissolution of the bubble [39, 40]. This puzzling result is a direct consequence of θ being constant. Therefore, there must be a stabilization mechanism that keeps the bubble stable over periods of days. It may be surface contamination on the bubble, blocking the gas outflux, as suggested in Refs. [41, 42] and recently by Ducker [43], but further work regarding this issue is necessary.

2.3.9 set-point dependence

Finally, we address the influence of the set-point ratio on the detected (i.e., not the actual) shape of the bubble. The set-point ratio r_{sp} is the ratio of the set-point ampli-

---

[†]A least-square fit to $\cos \theta$ vs $1/R$ yields $\tau = +1.1 \cdot 10^{-11}$ N, while manual fits (as done in Fig.5d of Ref. [19]) give $-3.2 \cdot 10^{-10} < \tau < -1.9 \cdot 10^{-10}$ N.

Class No.	Symbol	Type	Mat.	k (N/m)	R_t^{spec}	R_t^{SEM}	R_t^{step}	R_t	α (%)	z_{rms} (nm)
A										
1	■	MM NSC36♯	Si	1.6	10	26±4	29±9	...	5.64	0.94
2	▼	MM NSC36	Si	2.4	10	...	...	...	2.00	0.93
3	●	MM NSC36	Si₃N₄	1.98	20	25±4	...	...	1.15	0.70
4	◆	MM CSC37	Si	0.98	10	...	...	...	3.99	2.56
5	▲	MM CSC37	Si	0.86	10	33±5	...	...	0.74	0.99
6	▶	MM CSC37	Si₃N₄	0.63	20	23±4	...	...	5.12	1.08
7	◀	MM NSC36♯	Si₃N₄	2.33	20	35±7	...	...	0.78	0.64
8	★	MM CSC37	Si₃N₄	0.71	20	...	...	...	7.96	2.26
B										
9	◆	V NP-S	Si₃N₄	0.68	20	N.A.	20±3	20±3	0.42	0.28
10	●	MM CSC37♯	Au	1.14	50	17±3	10±2	13.5±5	0.47	0.26
11	◀	MM CSC37	Au	0.69	50	22±5	16±3	19±8	0.26	0.20
12	■	V MPP 22120 rect.♯	Si	0.68	10	15±2	19±3	17±5	a	a
13	▲	V NP-S [b]	Si₃N₄	0.27	10	20±4	N.A.	20±4	0.26	0.22
14	▼	MM NSC36	Si	4.8	10	N.A.	N.A.	N.A.	0.71	0.29
15	▶	V MPP 22120 rect.	Si	0.61	10	N.A.	14±3	14±3	0.12	0.19

Table 2.2: Characterization of the cantilevers investigated in this study. 'MM' denotes cantilevers produced by MikroMasch, which are rectangular in shape. 'V' stands for cantilevers from Veeco, which are V-shaped (default) or rectangular-shaped ("rect."). The values of the cantilever tip radius (in nm) are given as specified by the manufacturer R_t^{spec}, as measured by SEM imaging R_t^{SEM}, as deduced from the measured profile of HOPG steps R_t^{step}, and as the mean of the two former values R_t, respectively. R_t is the value used to correct the data. The two right columns depict the roughness of the substrates measured by the cantilevers, quantified by the surface area difference α and the rms value of the surface height z. SEM images of cantilevers marked with a flat ([b]) or sharp symbol (♯) are shown in Fig. 2.3 and Fig. 2.7 respectively. The colored symbols refer to Fig. 2.8 and 2.9.

---

[a]No reliable background data due to too large gain.
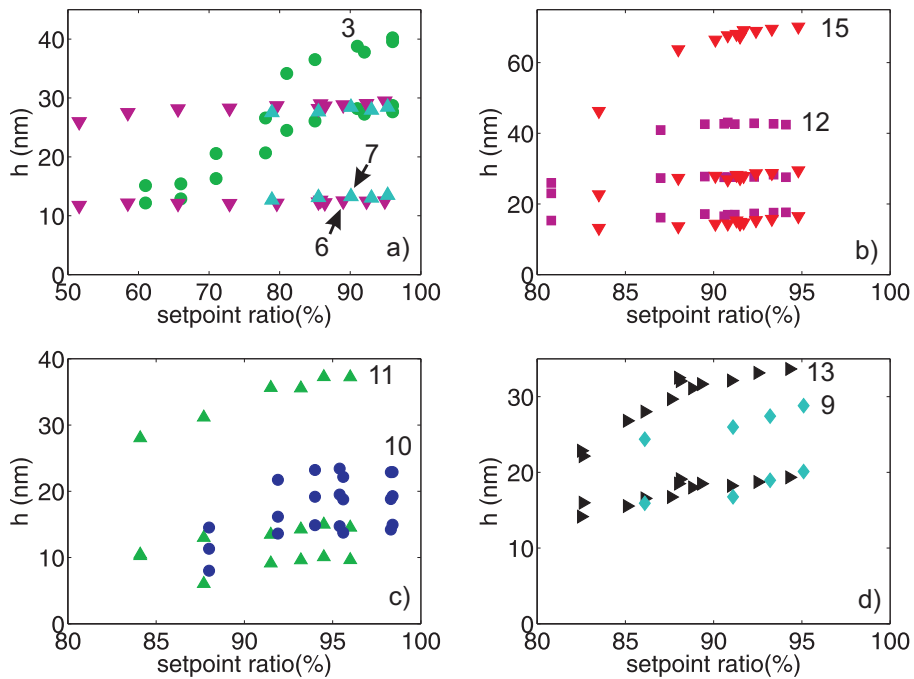
Figure 2.10: Nanobubble shape, parameterized by the height, as a function of the set-point ratio. Image a) depicts bubbles measured by cantilevers from class A, b)-d) shows bubbles from class B. The symbols and corresponding numbers refer to the cantilevers listed in Table 2.2. For each cantilever, the set-point dependence of two or three bubbles is depicted.

tude A to the free amplitude A_0 of the oscillating cantilever. As such, it is a measure of the force that the cantilever exerts on the substrate. For solid materials, the detected topography does not change with decreasing r_{sp}, but for soft and deformable surfaces such as surface nanobubbles, it generally does [13]. It is known that the detected surface nanobubble shape changes dramatically for $r_{sp} < 67\%$ [13], while for $r_{sp} > 67\%$ little to no changes are observed [7, 13]. Here, we show that the observed nanobubble shape can already be deformed at much larger set-point ratios and in a way that depends on the cleanliness of the system, the size of the probed nanobubble, and the specifications of the cantilever.

Not unexpectedly, the set-point dependence of the bubbles present on rough substrates (probed by the 'contaminated' cantilevers 1-8) is irreproducible: cantilevers of the same type sometimes measure a constant nanobubble shape down to $r_{sp} = 50\%$, whereas other times the detected bubble shape changes dramatically for set-point values $r_{sp} < 90\%$ (see Fig. 2.10a). This strange behavior cannot be explained by the different spring constants involved because stiff cantilevers sometimes show a weaker set-point dependence (or no set-point dependence at all), compared to that of soft cantilevers, opposite to the expectation (Fig. 2.10a). We attribute this conspicuous behavior to the uncontrolled presence of contamination, which may not only pin the triple contact line but could also form a skin or a surfactant layer on the nanobubble, thereby changing its response to external forces.

In contrast, clean cantilevers - which probed nanobubbles on smooth surfaces - always show that the observed bubble shape is set-point-dependent. For cantilevers of the same type and spring constant, this dependence is even quantitatively reproducible. For instance, in the case of two rectangular Veeco Si (MPP 22120) cantilevers with comparable spring constants (0.61 and 0.68 N/m), bubbles of equal size show a very similar dependence on the set-point ratio, see Fig. 2.10b. Interestingly, the plot also shows that both cantilevers at relatively low set-point ratios deform the largest bubble to a larger extent than the smallest nanobubbles. This effect also shows up in Fig. 2.10c (green upward-facing triangles) and Fig. 2.10d (black right-facing triangles). These results could be an indication that larger nanobubbles are more easily deformable/penetratable than smaller ones, possibly because of the larger curvature of the menisci or a lower Laplace pressure inside larger bubbles. In Fig. 2.10c two MM Au (CSC37) cantilevers are used. For $r_{sp} > 94\%$, the shape is identical for different set-point ratios, which shows that the nanobubble shape can be essentially set-point-independent provided that a large enough set-point ratio is chosen. This is also reflected in the corresponding linescans at different set-point ratios depicted in Fig. 2.11. However, both cantilevers also show that for $r_{sp} < 94\%$ the detected shape is dramatically altered, with larger deviations in nanobubble size inflicted by the stiffer cantilever. Notice that the changes in morphology are different (in a quantitative sense) compared to Fig. 2.10b, although in both cases spring constants of
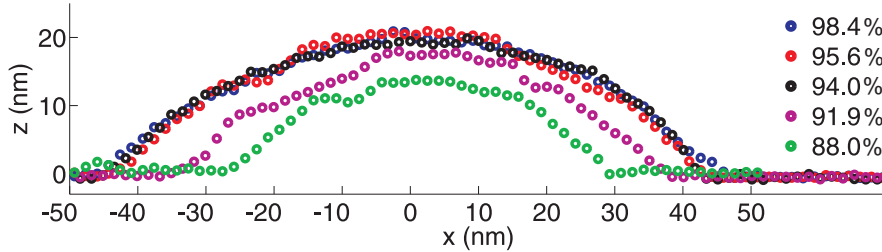
Figure 2.11: Linescans of the bubble topography as measured with different set-point ratios (see legend), using cantilever 10 (MM Au, k=1.14 N/m, class B).

k~0.68 N/m are used. Clearly, more factors are influencing the set-point-dependent bubble shape than the cantilever spring constant. Fig. 2.10d is a similar plot for two Veeco NP-S Si_3N_4 cantilevers and shows that for bubbles of equal size the set-point dependence is roughly similar, although here the cantilever spring constants are different (0.27 and 0.68 N/m).

It is not possible to make all $h - r_{sp}$-curves collapse on top of each other, not even for bubbles of identical sizes. For all cantilevers, it applies that below $r_{sp} \sim 95\%$ the detected nanobubble shape is a subtle function of the set-point ratio, and depends on more variables than the spring constant only. Presumably, the tip radius and the local wetting properties play key roles in the way in which the cantilever tip probes the bubble. Force spectroscopy is a more suitable method of studying this problem and will be the subject of a forthcoming study.

2.4 Discussion & Conclusion

We have performed a detailed study regarding the question of how the contact angle of surface nanobubbles changes with size. The nanoscopic contact angle of surface nanobubbles has been deduced from spherical cap-shaped surface nanobubbles found at the HOPG-water interface. The bubbles were detected by a Veeco AFM system in tapping mode using very small (total) amplitudes of $1 - 2$ nm and large set-point ratios ($> 95\%$). To rule out the possibility that the observed nanobubble shape is cantilever-dependent, experiments were carried out with fifteen different cantilevers, displaying different spring constants, shapes, materials (wetting properties), and tip radii of curvature.

We conclude that the contact angle of nanobubbles on atomically smooth surfaces such as HOPG strongly depends on spatial inhomogeneities in the AFM pictures. Data corresponding to an apparent roughness of $z_{rms} > 0.6$ nm and $a > 0.7\%$ display contact angles of order $150°$. For the data with a lower apparent surface roughness

($z_{\mathrm{rms}} < 0.3$ nm and $\alpha < 0.7\%$), which reflect as much as possible the ideal situation of nanobubbles on clean HOPG, we found here contact angles of $119 \pm 4^{\circ}$ despite the different cantilevers involved. Importantly, we found no noticeable $\theta(R)$ dependence within the experimental error.

The increased roughness and the different surface chemistry involved, leading to increased contact angles, originates from contamination. Cantilevers concerned with the experiments on seemingly relatively rough HOPG showed distinct contamination, presumably of an organic type. The origin of the contamination most likely comes from the gel package in which the cantilevers were stored. In contrast, cantilevers involved in the experiments with relatively smooth HOPG did not show any source of contamination.

Although the nanoscopic contact angle of 119° is considerably lower than has hitherto been reported, it is still $\sim 24 \pm 4^{\circ}$ larger than the (macroscopic) advancing contact angle. We speculate that this discrepancy still might originate from the presence of organic material (hydrocarbons) on the subnanometer lengthscale, as is also recently suggested in Ref. [43]. After all, we have shown in this study that contamination clearly increases the nanoscopic contact angle, whereas it is also known that ultrapure water-air interfaces and freshly cleaved HOPG easily collect airborne contaminant molecules.

This reasoning implies that if one is able to eliminate contaminants completely, then the nanoscopic contact angle can be further reduced to obtain Young's angle. Thus, from the two main issues associated with surface nanobubbles - extremely large contact angles and long-term stability - only one remains. The observation of an R-independent contact angle implies that $\lim_{R \to 0} R_c = 0$. Hence, some stability mechanism, such as the gas passage blocking mechanism caused by surfactants/contaminants as proposed recently [43], has to be identified in order to understand the long lifetime of surface nanobubbles, but also nonequilibrium mechanisms as suggested by [44] cannot be excluded.

Another future line of research concerns the complex tip-bubble interaction, which - as we have shown - depends not only on the cantilevers' spring constant, but also on the nanobubble curvature and most likely also on local wetting properties of the probing cantilever. Also, directly measuring the contamination-dependent surface tension of the nanobubble becomes feasible.

References

[1] S. Lou, Z. Ouyang, Y. Zhang, X. Li, J. Hu, M. Li, and F. Yang, "Nanobubbles on solid surface imaged by atomic force microscopy", J. Vac. Sci. Technol. B **18**, 2573–2575 (2000).

[2] N. Ishida, T. Inoue, M. Miyahara, and K. Higashitani, "Nano bubbles on a hydrophobic surface in water observed by tapping-mode atomic force microscopy", Langmuir **16**, 6377–6380 (2000).

[3] G. E. Yakubov, H.-J. Butt, and O. I. Vinogradova, "Interaction forces between hydrophobic surfaces. attractive jump as an indication of formation of "stable" submicrocavities", J. Phys. Chem. B **104**, 3407–3410 (2000).

[4] A. Carambassis, L. C. Jonker, P. Attard, and M. W. Rutland, "Forces measured between hydrophobic surfaces due to a submicroscopic bridging bubble", Phys. Rev. Lett. **80**, 5357–5360 (1998).

[5] J. W. G. Tyrrell and P. Attard, "Images of nanobubbles on hydrophobic surfaces and their interactions", Phys. Rev. Lett. **87**, 176104 (2001).

[6] A. C. Simonsen, P. L. Hansen, and B. Klösgen, "Nanobubbles give evidence of incomplete wetting at a hydrophobic interface", J. Colloid Interf. Sci. **273**, 291–299 (2004).

[7] X. H. Zhang, N. Maeda, and V. S. J. Craig, "Physical properties of nanobubbles on hydrophobic surfaces in water and aqueous solutions", Langmuir **22**, 5025–5035 (2006).

[8] L. Zhang, Y. Zhang, X. Zhang, Z. Li, G. Shen, M. Ye, C. Fan, H. Fang, and J. Hu, "Electrochemically controlled formation and growth of hydrogen nanobubbles", Langmuir **22**, 8109–8113 (2006).

[9] X. H. Zhang, G. Li, N. Maeda, and J. Hu, "Removal of induced nanobubbles from water/graphite interfaces by partial degassing", Langmuir **22**, 9238–9243 (2006).

[10] S. Yang, S. M. Dammer, N. Bremond, H. J. W. Zandvliet, E. S. Kooij, and D. Lohse, "Characterization of nanobubbles on hydrophobic surfaces in water", Langmuir **23**, 7072–7077 (2007).

[11] B. M. Borkent, S. M. Dammer, H. Schönherr, G. J. Vancso, and D. Lohse, "Superstability of surface nanobubbles", Phys. Rev. Lett. **98**, 204502 (2007).

[12] X. H. Zhang, A. Khan, and W. A. Ducker, "A nanoscale gas state", Phys. Rev. Lett. **98**, 136101 (2007).

[13] S. Yang, E. S. Kooij, B. Poelsema, D. Lohse, and H. J. W. Zandvliet, "Correlation between geometry and nanobubble distribution on hopg surface", EPL **81**, 64006 (2008).

[14] X. H. Zhang, A. Quinn, and W. A. Ducker, "Nanobubbles at the interface between water and a hydrophobic solid", Langmuir **24**, 4756–4764 (2008).

[15] S. Yang, P. Tsai, E. S. Kooij, A. Prosperetti, H. J. W. Zandvliet, and D. Lohse, "Electrolytically generated nanobubbles on highly orientated pyrolytic graphite surface", Langmuir **25**, 1466–1474 (2009).

[16] R. Steitz, T. Gutberlet, T. Hauss, B. Klösgen, R. Krastev, S. Schemmel, A. C. Simonsen, and G. H. Findenegg, "Nanobubbles and their precursor layer at the interface of water against a hydrophobic substrate", Langmuir **19**, 2409–2418 (2003).

[17] X. H. Zhang, "Quartz crystal microbalance study of the interfacial nanobubbles", Phys. Chem. Chem. Phys. **10**, 6842–6848 (2008).

[18] M. Switkes and J. W. Ruberti, "Rapid cryofixation/freeze fracture for the study of nanobubbles at solidliquid interfaces", Appl. Phys. Lett. **84**, 4759 (2004).

[19] N. Kameda, N. Sogoshi, and S. Nakabayashi, "Nitrogen nanobubbles and butane nanodroplets at si(100)", Surf. Sci. **602**, 1579–1584 (2008).

[20] O. I. Vinogradova, G. E. Yakubov, and H.-J. Butt, "Forces between polystyrene surfaces in waterelectrolyte solutions: Long-range attraction of two types?", J. Chem. Phys. **114**, 8124–8131 (2001).

[21] A. Agrawal, J. Park, D. Y. Ryu, P. T. Hammond, T. P. Russell, and G. H. McKinley, "Controlling the location and spatial extent of nanobubbles using hydrophobically nanopatterned surface", Nano Lett. **5**, 1751–1756 (2005).

[22] M. Holmberg, A. Kühle, J. Garnæs, K. A. Mørch, and A. Boisen, "Nanobubble trouble on gold surfaces", Langmuir **19**, 10510–10513 (2003).

[23] N. Kameda and S. Nakabayashi, "Size-induced sign inversion of line tension in nanobubbles at a solid/liquid interface", Chem. Phys. Lett **461**, 122–126 (2008).

[24] A. Agrawal and G. H. McKinley, "Nanobubble formation at the solid-liquid interface studied by atomic force microscopy", in *Mater. Res. Soc. Symp. Proc. Vol. 899E* (2006).

[25] J. Yang, J. Duan, D. Fornasiero, and J. Ralston, "Very small bubble formation at the solid-water interface", J. Phys. Chem. B **107**, 6139–6147 (2003).

[26] F. Mugele, T. Becker, R. Nikopoulos, M. Kohonen, and S. Herminghaus, "Capillarity at the nanoscale: an afm view", J. Adhesion Sci. Technol. **16**, 951–964 (2002).

[27] X. H. Zhang and W. Ducker, "Interfacial oil droplets", Langmuir **24**, 110–115 (2008).

[28] A. Checco, P. Guenoun, and J. Daillant, "Nonlinear dependence of the contact angle of nanodroplets on contact line curvature", Phys. Rev. Lett. **91**, 186101 (2003).

[29] L. Schimmele, M. Napiorkowski, and S. Dietrich, "Conceptual aspects of line tensions", J. Chem. Phys **127**, 164715 (2007).

[30] J. L. Hutter and J. Bechhoefer, "Calibration of atomic-force microscope tips", Rev. Sci. Instrum. **64**, 1868–1873 (1993).

[31] A. Maali, C. Hurth, T. Cohen-Bouhacina, G. Couturier, and J. P. Aime, "Improved acoustic excitation of atomic force microscope cantilevers in liquids", Appl. Phys. Lett. **88**, 163504 (2006).

[32] S. de Beer, D. van den Ende, and F. Mugele, "Atomic force microscopy cantilever dynamics in liquid in the presence of tip sample interaction", Appl. Phys. Lett. **93**, 253106 (2008).

[33] K. A. Ramirez-Aguilar and K. L. Rowlen, "Tip characterization from afm images of nanometric spherical particles", Langmuir **14**, 2562–2566 (1998).

[34] B. M. Borkent, H. Schönherr, G. Le Caër, B. Dollet, and D. Lohse, "Preferred sizes and ordering in surface nanobubble populations", Phys. Rev. E. (submitted), URL `http://arxiv.org/abs/0906.0486`.

[35] Y. Lo, N. D. Huefner, W. S. Chan, P. Dryden, B. Hagenhoff, and T. P. Beebe, "Organic and inorganic contamination on commercial afm cantilevers", Langmuir **15**, 6522–6526 (1999).

[36] E. Bonaccurso and G. Gillies, "Revealing contamination on afm cantilevers by microdrops and microbubbles", Langmuir **20**, 11824–11827 (2004).

[37] P.-G. de Gennes, F. Brochard-Wyart, and D. Quéré, *Capillarity and Wetting Phenomena: Drops, Bubbles, Pearls, Waves* (Springer, New York) (2003).

[38] P. Attard, "personal communication", (Leiden, June 2008).

[39] P. S. Epstein and M. S. Plesset, "On the stability of gas bubbles in liquid-gas solutions", J. Chem. Phys. **18**, 1505 – 1509 (1950).

[40] S. Ljunggren and J. C. Eriksson, "The lifetime of a colloid-sized gas bubble in water and the cause of the hydrophobic attraction", Colloids Surf. A **129–130**, 151–155 (1997).

[41] B. D. Johnson and R. C. Cooke, "Generation of stabilized microbubbles in sea-water", Science **213**, 209–211 (1974).

[42] E. Dressaire, R. Bee, D. C. Bell, A. Lips, and H. A. Stone, "Interfacial polygonal nanopatterning of stable microbubbles", Science **320**, 1198–1201 (2008).

[43] W. Ducker, "Contact angle and stability of interfacial nanobubbles", Langmuir **25**, 8907–8910 (2009).

[44] M. P. Brenner and D. Lohse, "Dynamic equilibrium mechanism for surface nanobubble stabilization", Phys. Rev. Lett. **101**, 214505 (2008).

3

Preferred sizes and ordering in surface nanobubble populations[‡]

In the previous chapter, we studied geometrical properties of individual nanobubbles. In this chapter we focus our attention on statistical properties of nanobubble populations. For this purpose, two types of homogeneous surface nanobubble populations, created by different means, are analyzed statistically on both their sizes and spatial positions. In the first type (created by droplet-deposition, case A) the bubble size R is found to be distributed according to a generalized gamma law with a preferred radius $R^* =20$ nm. The radial distribution function shows a preferred spacing at $\sim 5.5\ R^*$. These characteristics do not show up in comparable Monte-Carlo simulations of random packings of hard disks with the same size distribution and the same density, suggesting a structuring effect in the nanobubble formation process. The nanobubble size distribution of the second population type (created by ethanol-water exchange, case B) is a mixture of two clearly separated distributions, hence, with two preferred radii. The local ordering is less significant, due to the looser packing of the nanobubbles.

3.1   Introduction

The first atomic force microscopy (AFM) observations of spherical cap-like soft domains at the solid-liquid interface [1–5], later termed "surface nanobubbles", identified two typical, yet poorly understood, nanobubble characteristics: long-term stability and huge nanoscopic contact angles (on the water side). Later experiments confirmed these puzzling features of surface nanobubbles, and focused on verifying their gaseous nature by correlating the nanobubble densities with the gas concentration in the liquid [6–8]. Recently, the gas content of the bubbles was identified explicitly by infrared spectroscopy measurements in combination with AFM [9, 10]. Other studies investigated the effect of surface active solutes [8, 11], salts [11], substrate morphology [12], or electrolysis [13, 14] on the appearance, stability, and shape of surface nanobubbles. While the number of experiments supporting the notion that the observed structures are indeed surface nanobubbles, is increasing [15–22], no consensus has been reached concerning the mechanism which stabilizes the bubbles (see [23] and references therein). Understanding this phenomenon might lead to new insights of the behavior of gases or water at the nanoscale. Secondly, this knowledge could be utilized in technologies e.g. to produce stable nanoscopic bubbles as ultrasound contrast agents, or to produce nanochannels covered with densely packed nanobubbles in order to reduce the hydrodynamic drag in microfluidic devices [24]. Others have used nanobubbles in the design of catalytic nanomotors [25] and also as template to manufacture nanostructures [26]. In other situations, such as immersion lithography, one needs to avoid the presence of surface nanobubbles (as they might cause imaging defects), in which case it is crucial to understand how stable nanobubbles can be removed.

Regarding the stability of nanobubbles, one of the hypotheses has been recently put forward in [23] and is based on a non-stationary equilibrium between a gas outflux (through the gas-liquid interface) and a gas influx (at the three-phase contact line), and predicts a preferred nanobubble radius as a function of gas concentration and contact angle.

In this paper we want to test the prediction [23] of a preferred radius (of the contact area with the surface) R^* and its dependence on the gas concentration. Our good bubble statistics allow us to extract statistical properties of the whole nanobubble population. The analysis shows not only a preferred radius, but also a preferred spacing between the bubbles, suggesting a structuring mechanism between individual bubbles.

3.2 Materials and methods

As substrates small pieces diced from a Si(100) wafer are used, which are subsequently cleaned, coated with a monolayer of 1H,1H,2H,2H-perfluorodecyldimethylchlorosilane and analyzed following the procedure described previously [19]. The rms roughness is 0.36 nm (measured by AFM on $1 \times 1 \mu m^2$) and the static macroscopic contact angle is typically around 92°. The substrates are then mounted in an atomic force microscope (VEECO/Digital Instruments (DI) multimode) equipped with a NanoScope IIIa controller (DI, Santa Barbara, CA) and measured in tapping mode in water using a DI liquid cell and V-shaped Si_3N_4 cantilevers, with spring constants of $0.3 - 0.5 N/m$ (Nanoprobes, DI). The amplitude setpoint was chosen as high as possible, typically $> 90\%$. The size of the nanobubbles is extracted from the raw AFM topography images by application of a height-threshold [14], which yields the location and radius R of each nanobubble. The results are corrected for the finite size of the tip ($R_{tip} = 20$ nm), as done elsewhere [21]. We note that the tip correction does not affect the conclusions of this paper qualitatively.

The populations of surface nanobubbles are created in two different ways: in case A, a drop of gas-equilibrated Milli-Q water is put on the substrate, while in case B a finite, temporal local gas oversaturation (by flushing ethanol away with water [1, 8, 11, 19]) is employed to explicitly stimulate nanobubble formation. In both cases two typical images are selected which were suitable for further statistical analysis (see Fig. 3.1).

3.3 Quantification of nanobubble size distributions

In Case A (Fig. 3.1 top frames) a dense coverage of relatively small and rather uniformly sized nanobubbles is observed. This observation is not evident as not all labs find the 'spontaneous' occurrence of nanobubbles (see for instance the remark in Ref. [10] and references therein). Only incidently, some larger nanobubbles are visible, which are present next to a bubble-free area. Presumably, smaller nanobubbles have merged to these larger objects. A mixed population of both small and large nanobubbles can be created when a forced local oversaturation is applied temporally [11], as shown in Fig. 3.1 (bottom frames, cases B1 and B2, resp.). After the local gas-oversaturation, the bulk gas concentration is restored to its equilibrium value. In addition, the bubbles have been exposed to a single shockwave, as described in [19]. We noticed that the large nanobubbles did not vanish or shrink during the course of the experiment (i.e. within a few hours).

The experimental probability size distributions $P(D)$ present in case A and B are shown in Fig. 3.2. The bubble sizes clearly show a maximum at a particular diameter value, which we denote as the preferred diameter $D^*(= 2R^*)$. In case B there are even two peaks, corresponding to two preferred radii. To obtain the value of D^*
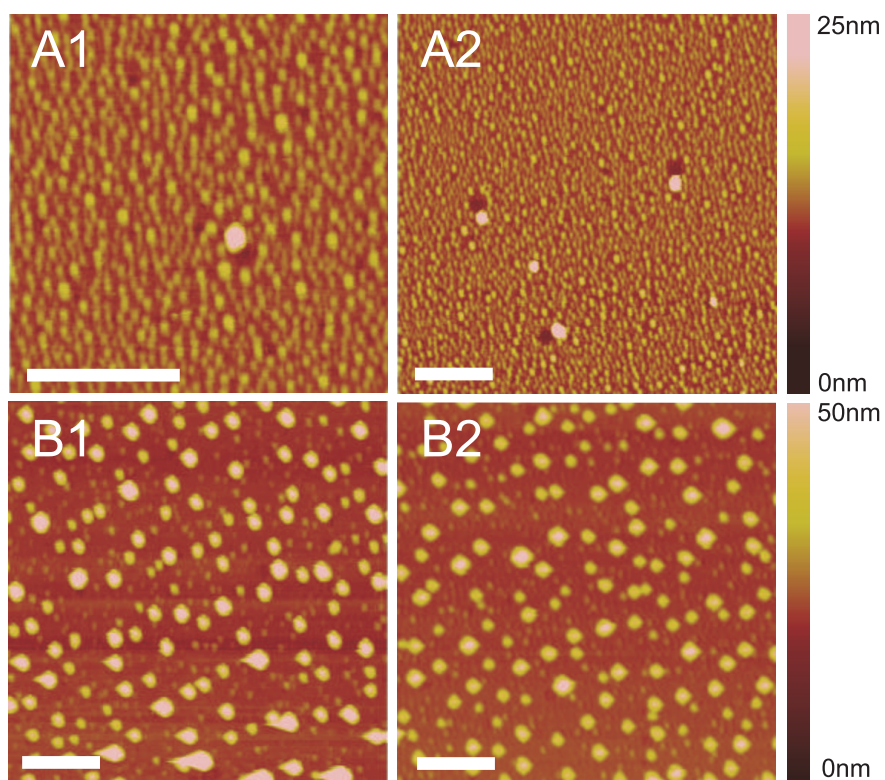
Figure 3.1: AFM topography images of the solid-liquid interface of the substrates. In cases A1 and A2 gas-equilibrated MilliQ-water was put on the substrate without explicit use of local oversaturation. In cases B1 and B2 the result is shown after a local and temporal oversaturation has been applied. Each scale bar corresponds to 1μm.

the experimental size histograms were fitted with a generalized gamma distribution (GG) [27] in case A and with a mixture of a GG and a Gaussian distribution in case B. In Case A the GG distribution which best fits the experimental results (Fig. 3.2) is

$$P_A(D) = \frac{\theta_A \beta_A^{1+\epsilon_A}}{\Gamma\left(\frac{1+\epsilon_A}{\theta_A}\right)} D^{\epsilon_A} \exp\{-(\beta_A D)^{\theta_A}\} \quad , \tag{3.1}$$

where $\Gamma(x)$ is Euler's gamma function, and β_A and θ_A are shape parameters which are fitted, yielding $\beta_A = (1.73 \pm 0.07) \cdot 10^{-2}\,\text{nm}^{-1}$ and $\theta_A = 2.37 \pm 0.17$. As the value of ϵ_A was found to be very close to 1, it was fixed to 1. The maximum (or the mode) of $P_A(D)$ is formed at $D_A^* = 1/\beta_A \theta_A^{1/\theta_A} = 40 \pm 2$ nm and the mean diameter $\langle D \rangle_A = 47 \pm 2$ nm. The standard deviation of the size distribution is $\sigma_A = 23 \pm 2$ nm. In case B the total probability distribution could be fitted with a mixture of a GG distribution with the same form as that of $P_A(D)$ and of a Gaussian distribution:

$$P_B(D) = \alpha \frac{\theta_B \beta_B^2}{\Gamma(2/\theta_B)} D \exp\{-(\beta_B D)^{\theta_B}\} + \frac{1-\alpha}{\sigma_{B,2}\sqrt{2\pi}} \exp\left(-\frac{(D - D_{B,2}^*)^2}{2\sigma_{B,2}^2}\right). \tag{3.2}$$

As in case A, the exponent of D was found to be close to 1 and fixed to that value. The fitted parameters are then $\alpha = 0.69 \pm 0.04$, $\beta_B = (1.20 \pm 0.07) \cdot 10^{-2}\,\text{nm}^{-1}$, $\theta_B = 2.8 \pm 0.3$, $D_{B,2}^* = \langle D \rangle_{B,2} = 224 \pm 9$ nm, and $\sigma_{B,2} = 48 \pm 7$ nm. The characteristics of the small nanobubbles are then $D_{B,1}^* = 58 \pm 4$ nm, $\langle D \rangle_{B,1} = 64 \pm 4$ nm and $\sigma_{B,1} = 29 \pm 4$ nm.

The observation of two co-existing but clearly separated sets of bubbles has not been reported or predicted before. The larger nanobubbles are created during the temporal gas oversaturation in the water during the exchange process, in agreement with previous observations [11], while we hypothesize that the smaller ones are formed once the saturated conditions are restored. Notice that the smaller set of bubbles in case B is fairly similar to the population in case A in both the shape of $P(D)$, as well as the order of magnitude of the respective maxima (40 ± 2 nm and 58 ± 4 nm, resp.). Remarkably, these maxima are close to the experimental result of Simonsen *et al.* [17], who found a normal distribution of sizes with $D^* = 66$ nm under identical lab conditions (i.e. gas-equilibrated Milli-Q water put on surfaces with a static contact angle 90°).

Notice that the tendency of surface nanobubbles to reside with a preference in size is also reflected by the nanobubbles present in the 'clean' cases of Chapter 2, see Fig. 3.3, despite differences in number densities and surface characteristics.
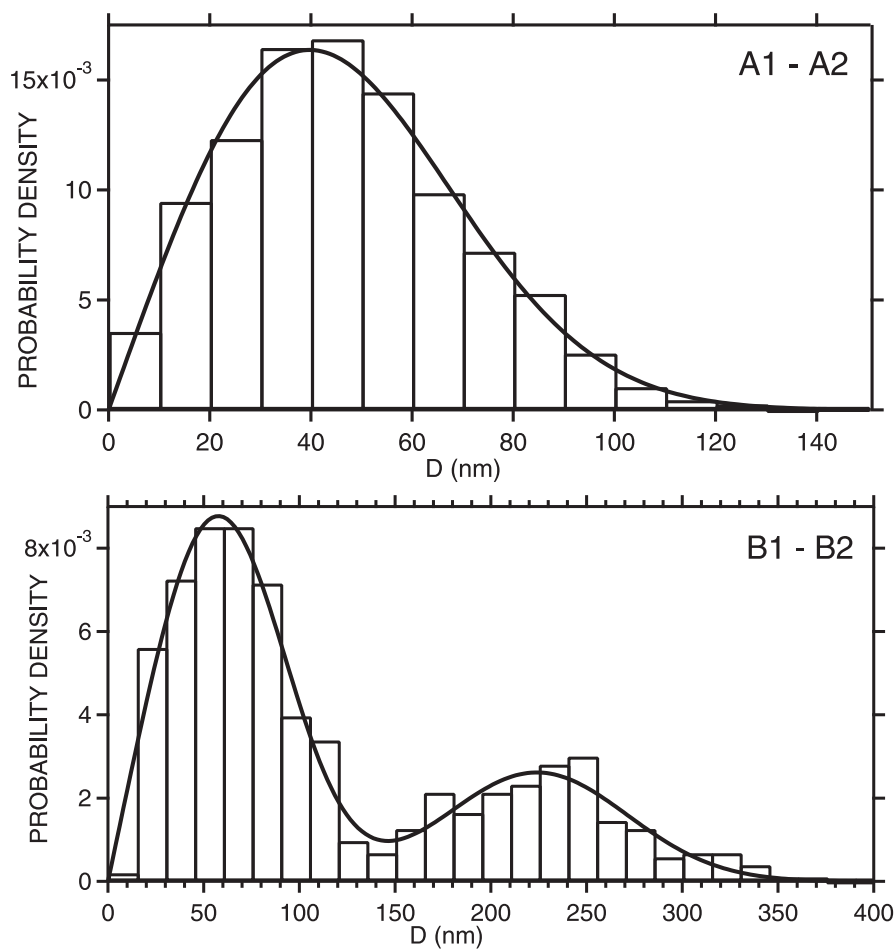
Figure 3.2: Probability distribution of the nanobubble diameter D in both case A (top) and case B (bottom). Each case is represented by two unique images (1 and 2, resp.), of which the total size distribution is shown. The bars depict experimental data, the lines show the best-fitted probability distribution.
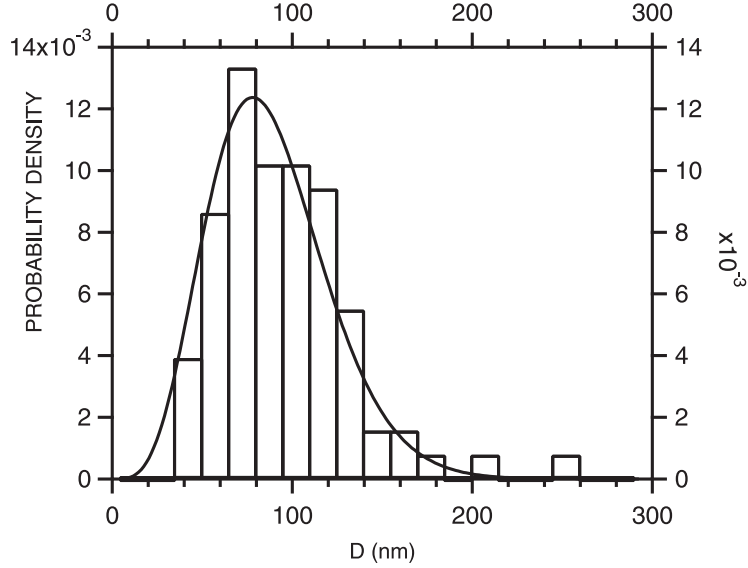
Figure 3.3: Probability distribution of the nanobubble diameter D in the 'clean' cases of Chapter 2, based on 85 nanobubbles. The line is a fit according to a generalized gamma law (Eq. 3.1), with fitting parameters $\epsilon = 3.78$, $\beta = 0.0234\,\text{nm}^{-1}$, and $\theta = 1.52$ yielding a preferred diameter $D^* = 1/\beta(\epsilon/\theta)^{1/\theta} = 78\,\text{nm}$ and mean diameter $\langle D \rangle = 88\,\text{nm}$ with standard deviation $\sigma = 33\,\text{nm}$.

3.4 Quantification of spatial ordering

The homogeneity of the nanobubble coverage depicted in Fig. 3.1 suggests local structuring of the bubbles. To test this idea quantitatively, Monte-Carlo (MC) simulated configurations of a random packing of hard-disks with the same size distribution and density as in the experiments are employed. For case A2, the nanobubble center positions in both experiment and MC-simulated configuration are depicted in Fig. 3.4, which shows that the experimental positions are much more structured than the simulated bubble positions. This effect is further shown by the radial distribution function $g(r)$, which quantifies the probability of finding a bubble at a radial distance r from another bubble, and the nearest neighbor distribution function $D_{NN}(r)$, which gives the probability of finding a nearest neighbor of a nanobubble at a distance less than or equal to r [28]. In all cases, the MC plots are calculated from a single simulation. Statistical convergence has been checked by calculating averages over ten different simulated configurations (data not shown), which confirms all conclusions we can draw for a single simulation. The plots of $g(r)$ and $D_{NN}(r)$ are depicted in Fig. 3.5 and Fig. 3.6, respectively, for both the experimental and MC-simulated positions. In addition, the figures show the distributions for a Poisson point process (where neither
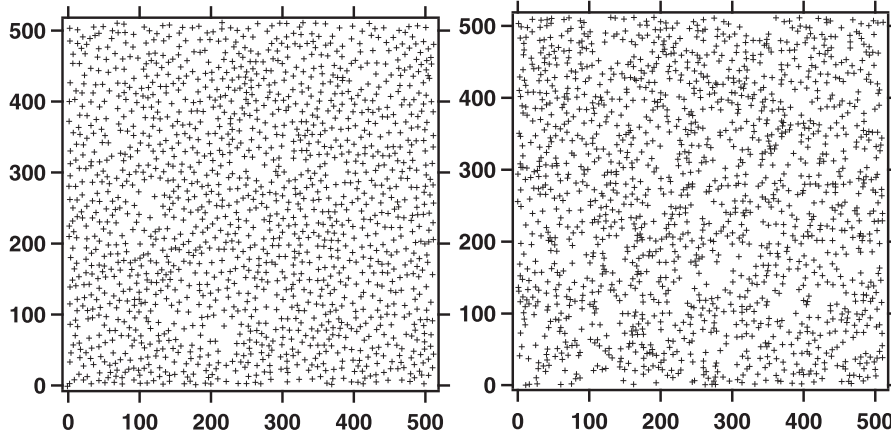
Figure 3.4: Positions of the nanobubbles in case A2 (left) vs. Monte-Carlo simulated configurations of a random packing of hard-disks with the same size distribution and density as experiment A2 (right). The experimental positions show much more structure than the simulated bubbles.

steric nor repulsive interaction is present), and a determinantal point process with a very soft repulsion between the points *.

For case A1 and A2 the experimental curves in Fig. 3.5 show a significant peak in $g(r)$ at $r \sim 5\langle R \rangle \sim 5.5R^*$ while, interestingly, this peak is absent in the corresponding MC-simulated configuration and the determinantal point process. This shows that there is a preferred spacing between the bubbles present in both case A1 and A2, which is not only steric and stronger than the 'soft' repulsion represented by the determinantal point process. The regularity of the bubble positions in case A1 and A2 is also shown in the plots of $D_{NN}(r)$ (Fig. 3.6): the experimental curves are on the right-hand side of the MC-curves. Notice that the $D_{NN}(r)$ curves of the MC simulated cases A1 and A2 (red lines) are close to those given by the determinantal point process (dash-dotted lines) although in the MC-simulated configurations hard disks are used without any mutual interaction apart from the hard-core repulsive potential. The similarity is not seen when the MC-simulated configuration utilizes a single disk size. Hence, the effect of the size distribution looks like an effective soft repulsion.

In contrast, for cases B1 and B2 no significant difference is observed between experiments and MC-simulated configurations, in both $g(r)$ and $D_{NN}(r)$. The reason could be that the statistics is too poor: case A counted three times as many bubbles as case B. Another, more likely reason could be that the number densities in case B are

---

*The latter process is a universal 2D point process with explicit expressions of correlation functions of any order (see [29, 30] and references therein). The points are more regularly distributed than they are for a Poisson point process.
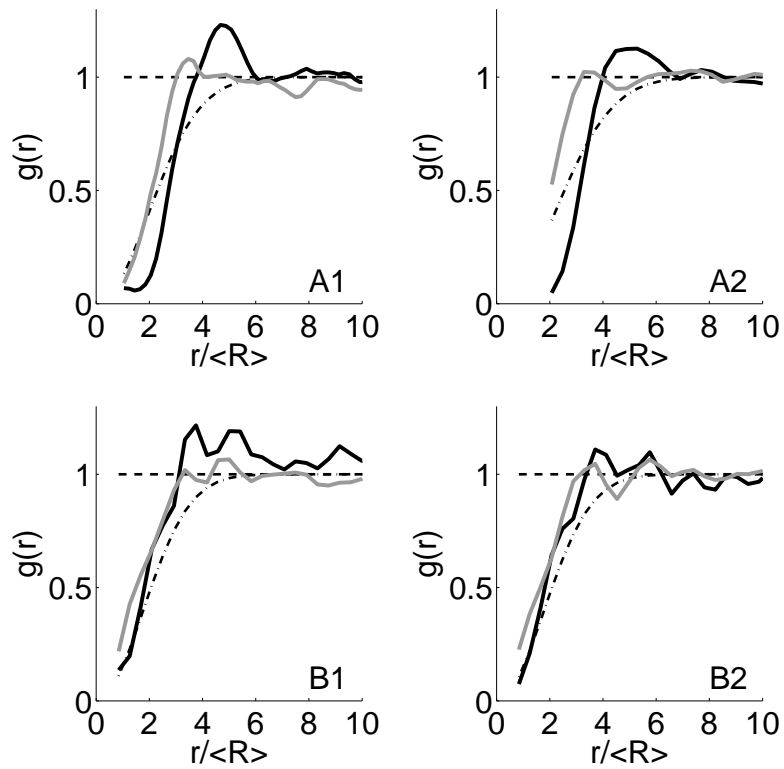
Figure 3.5: Radial distribution functions $g(r)$ as a function of r normalized by the mean radius $\langle R \rangle$ for case A (top) and case B (bottom). Black line: experiment; gray line: Monte-Carlo simulated configuration of a random packing of hard-disks with the same size distribution and density as the associated experiments; dashed line: Poisson point process; dash-dotted line: determinantal point process.
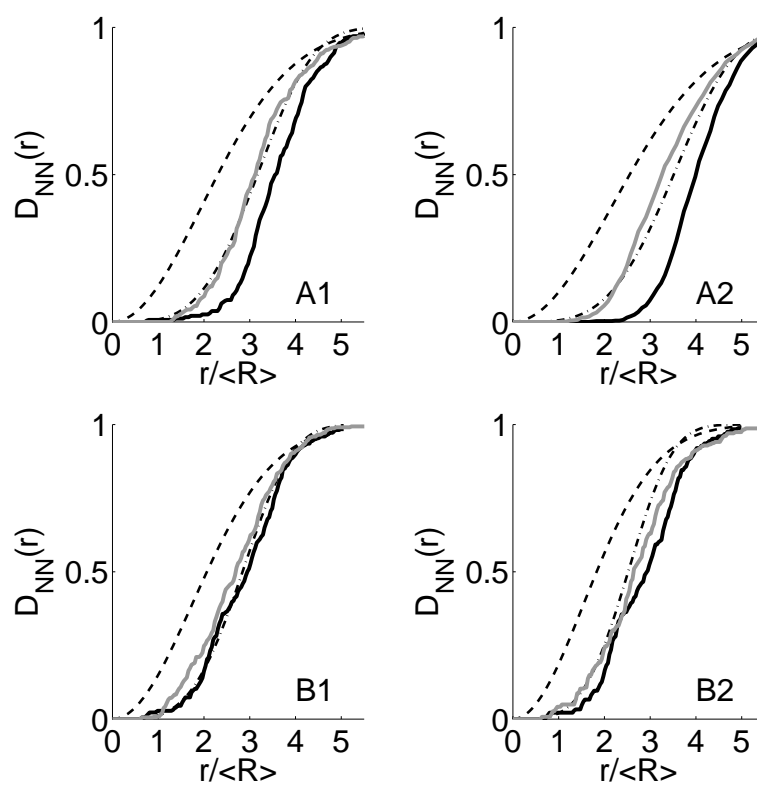
Figure 3.6: Nearest neighbor distributions $D_{NN}(r)$ for the four cases A1–B2. The legend is the same as in Fig. 3.5.

too low for structuring effects to be present. In case B1 and B2 the number density was 13.8 per μm^2 on average, while in case A1 and A2 this was 70.7 per μm^2, more than a factor of five difference.

3.5 Conclusion

In summary, it is demonstrated for two types of surface nanobubble populations that nanobubbles (i) show a preference in size, and (ii) show a preference in spacing. The first observation shows up in both cases, while the second observation only shows up when the number densities are large enough. In case A the size distribution is found to be distributed according to a generalized gamma law. A very similar size distribution is present in case B, where in addition a larger set of normal-distributed nanobubbles is present, which were created most likely during the temporal gas-oversaturation in the water. These findings are consistent with the hypothesis of a uniform stabilizing mechanism leading to a preferred radius, as put forward in [23]. Comparisons with MC-simulated configurations show that densely packed nanobubbles do not reside randomly, but choose a position were it is easiest for them to be: away from each others vicinity. The physical mechanism responsible for this effect could be the limited availability of gas in the vicinity of an already formed nanobubble, prohibiting the nucleation of other nanobubbles nearby. Alternatively, nanobubbles could be formed instantaneously from the breakup of a homogeneous gas film into individual bubbles, analogous to the break-up of thin liquid films into surface patterns [31]. Thirdly, the ordering effect could result from a short-range repulsive force, e.g. due to surface charges. Although the preference in size seems to be a reproducible feature of surface nanobubble populations, the experimental factors determining their sizes need more quantitative control in order to unravel the precise formation mechanism of nanobubbles and their mutual interplay at the nanoscale.

References

[1] S. Lou, Z. Ouyang, Y. Zhang, X. Li, J. Hu, M. Li, and F. Yang, "Nanobubbles on solid surface imaged by atomic force microscopy", J. Vac. Sci. Technol. B **18**, 2573–2575 (2000).

[2] N. Ishida, T. Inoue, M. Miyahara, and K. Higashitani, "Nano bubbles on a hydrophobic surface in water observed by tapping-mode atomic force microscopy", Langmuir **16**, 6377–6380 (2000).

[3] G. E. Yakubov, H.-J. Butt, and O. I. Vinogradova, "Interaction forces between hydrophobic surfaces. attractive jump as an indication of formation of "stable" submicrocavities", J. Phys. Chem. B **104**, 3407–3410 (2000).

[4] A. Carambassis, L. C. Jonker, P. Attard, and M. W. Rutland, "Forces measured between hydrophobic surfaces due to a submicroscopic bridging bubble", Phys. Rev. Lett. **80**, 5357–5360 (1998).

[5] J. W. G. Tyrrell and P. Attard, "Images of nanobubbles on hydrophobic surfaces and their interactions", Phys. Rev. Lett. **87**, 176104 (2001).

[6] X. H. Zhang, X. D. Zhang, S. T. Lou, Z. X. Zhang, J. L. Sun, and J. Hu, "Degassing and temperature effects on the formation of nanobubbles at the mica/water interface", Langmuir **20**, 3813–3815 (2004).

[7] X. H. Zhang, G. Li, N. Maeda, and J. Hu, "Removal of induced nanobubbles from water/graphite interfaces by partial degassing", Langmuir **22**, 9238–9243 (2006).

[8] S. Yang, S. M. Dammer, N. Bremond, H. J. W. Zandvliet, E. S. Kooij, and D. Lohse, "Characterization of nanobubbles on hydrophobic surfaces in water", Langmuir **23**, 7072–7077 (2007).

[9] X. H. Zhang, A. Khan, and W. A. Ducker, "A nanoscale gas state", Phys. Rev. Lett. **98**, 136101 (2007).

[10] X. H. Zhang, A. Quinn, and W. A. Ducker, "Nanobubbles at the interface between water and a hydrophobic solid", Langmuir **24**, 4756–4764 (2008).

[11] X. H. Zhang, N. Maeda, and V. S. J. Craig, "Physical properties of nanobubbles on hydrophobic surfaces in water and aqueous solutions", Langmuir **22**, 5025–5035 (2006).

[12] S. Yang, E. S. Kooij, B. Poelsema, D. Lohse, and H. J. W. Zandvliet, "Correlation between geometry and nanobubble distribution on hopg surface", EPL **81**, 64006 (2008).

[13] L. Zhang, Y. Zhang, X. Zhang, Z. Li, G. Shen, M. Ye, C. Fan, H. Fang, and J. Hu, "Electrochemically controlled formation and growth of hydrogen nanobubbles", Langmuir **22**, 8109–8113 (2006).

[14] S. Yang, P. Tsai, E. S. Kooij, A. Prosperetti, H. J. W. Zandvliet, and D. Lohse, "Electrolytically generated nanobubbles on highly oriented pyrolytic graphite surface", Langmuir **25**, 1466–1474 (2009).

[15] R. Steitz, T. Gutberlet, T. Hauss, B. Klösgen, R. Krastev, S. Schemmel, A. C. Simonsen, and G. H. Findenegg, "Nanobubbles and their precursor layer at the interface of water against a hydrophobic substrate", Langmuir **19**, 2409–2418 (2003).

[16] M. Switkes and J. W. Ruberti, "Rapid cryofixation/freeze fracture for the study of nanobubbles at solidliquid interfaces", Appl. Phys. Lett. **84**, 4759 (2004).

[17] A. C. Simonsen, P. L. Hansen, and B. Klösgen, "Nanobubbles give evidence of incomplete wetting at a hydrophobic interface", J. Colloid Interf. Sci. **273**, 291–299 (2004).

[18] A. Agrawal, J. Park, D. Y. Ryu, P. T. Hammond, T. P. Russell, and G. H. McKinley, "Controlling the location and spatial extent of nanobubbles using hydrophobically nanopatterned surface", Nano Lett. **5**, 1751–1756 (2005).

[19] B. M. Borkent, S. M. Dammer, H. Schönherr, G. J. Vancso, and D. Lohse, "Superstability of surface nanobubbles", Phys. Rev. Lett. **98**, 204502 (2007).

[20] N. Kameda, N. Sogoshi, and S. Nakabayashi, "Nitrogen nanobubbles and butane nanodroplets at si(100)", Surf. Sci. **602**, 1579–1584 (2008).

[21] N. Kameda and S. Nakabayashi, "Size-induced sign inversion of line tension in nanobubbles at a solid/liquid interface", Chem. Phys. Lett. **461**, 122–126 (2008).

[22] Y. Nam and Y. S. Ju, "Bubble nucleation on hydrophobic islands provides evidence to anomalously high contact angles of nanobubbles", Appl. Phys. Lett. **93**, 103115 (2008).

[23] M. P. Brenner and D. Lohse, "Dynamic equilibrium mechanism for surface nanobubble stabilization", Phys. Rev. Lett. **101**, 214505 (2008).

[24] A. Steinberger, C. Cottin-Bizonne, P. Kleimann, and E. Charlaix, "High friction on a bubble mattress", Nat. Mater. **6**, 665–668 (2007).

[25] W. F. Paxton, K. C. Kistler, C. C. Olmeda, A. Sen, S. K. S. Angelo, Y. Cao, T. E. Mallouk, P. E. Lammert, and V. H. Crespi, "Catalytic nanomotors: Autonomous movement of striped nanorods", J. Am. Chem. Soc. **126**, 13424 (2004).

[26] Y. Fan and R. Wang, "Submicrometer-sized vaterite tubes formed through nanobubble-templated crystal growth", Adv. Mater. **14**, 1857–1860 (2002).

[27] E. W. Stacy, "Generalization of gamma distribution", Ann. Math. Stats. **33**, 1187–1192 (1961).

[28] D. Stoyan, W. Kendall, and J. Mecke, *Stochastic Geometry and Its Applications*, second edition (Wiley, New York) (1995).

[29] G. Le Caër and R. Delannay, "The administrative divisions of mainland france as 2d random cellular structures", J. Phys. I France **3**, 1770–1800 (1993).

[30] A. Scardicchio, C. E. Zachary, and S. Torquato, "Statistical properties of deter-
     minantal point processes in high-dimensional euclidean spaces", Phys. Rev. E
     79, 041108 (2009).

[31] M. Bestehorn and K. Neuffer, "Surface patterns of laterally extended thin liquid
     films in three dimensions", Phys. Rev. Lett. **87**, 046101 (2001).

4

Superstability of surface nanobubbles[‡]

After the characterization of nanobubble shapes and populations in the previous chapters, this chapter investigates how surface nanobubbles react to external forces, like a rapid pressure reduction in the liquid. Therefore, shock wave induced cavitation experiments and atomic force microscopy measurements of flat polyamide and hydrophobized silicon surfaces immersed in water are performed. It is shown that surface nanobubbles, present on these surfaces, do not act as nucleation sites for cavitation bubbles, in contrast to the expectation. This implies that surface nanobubbles are not just stable under ambient conditions but also under enormous reduction of the liquid pressure down to -6 MPa. We denote this feature as superstability.

4.1   Introduction

In recent years, numerous experiments revealed the existence of nanoscopic soft domains at the liquid-solid interface, see [1–10] and references therein. Most experiments employ atomic force microscopy (AFM) [1–8], but other techniques [9, 10] have been used as well. The most consistent interpretation of these experiments is that the soft domains, which resemble spherical caps with heights of the order of 10 nm and diameters of the order of 100 nm, are so-called surface nanobubbles, i.e., nanoscale gas bubbles located at the liquid-solid interface. This claim is, for instance, supported by the fact that nanobubbles can be merged by the tip of an AFM to form a larger bubble [2], or by the fact that they disappear upon degassing of the liquid [6, 7, 9], or by the gas concentration dependence of their density [8].

Surface nanobubbles are puzzling objects. First, they should not exist: according to the experimental data these bubbles have a radius of curvature R of the order of 100 nm, and therefore (due to a large Laplace pressure inside of the bubbles) they should dissolve on timescales far below a second [11, 12]. In marked contrast the experiments show that nanobubbles are stable for hours. Second, they are potential candidates to explain various phenomena associated with the liquid-solid interface, such as liquid slippage at walls [13–15] or the anomalous attraction of hydrophobic surfaces [1] in water. In addition, heterogeneous cavitation usually starts from gaseous nuclei at solid surfaces (see [16] and references therein), and surface nanobubbles are suggested as potential inception sites [3, 7, 17]. However, apart from convincing experimental evidence for the existence and stability of nanobubbles, still little is known. For instance, why are they apparently stable or how do they react to environmental changes?

In this chapter it is shown that surface nanobubbles, contrary to the expectation, do *not* act as nucleation sites for shock wave induced cavitation on surfaces, where a large tensile stress is created in the water. Hence, yet another puzzle is added to the nanobubble paradox: They are not only stable under ambient conditions but also under enormous reduction of the water pressure down to −6 MPa. We denote this phenomenon as *superstability*.

To demonstrate the superstability of surface nanobubbles we combine cavitation experiments and AFM measurements. More precisely, cavitation experiments (similar to [17–19]) with different hydrophobic substrates submerged in water are performed: a shock wave generates a large tensile stress (≈ -6 MPa) in the water which leads to cavitation of bubbles at the substrates. The size of the cavitation bubbles is of the order of several hundred μm. Thus, though the bubbles originate from smaller nuclei, they can be visualized by optical means. In addition, AFM-measurements of the same substrates in water at ambient conditions are performed to proof and quantify the existence of stable nanobubbles on these substrates. Combining the cavitation

and AFM experiments allows to study the relation between cavitation activity and nanobubbles. An analogous strategy has been used previously [18] to perfectly correlate the appearance of surface bubbles in cavitation experiments to the existence of gas-filled microcavities (i.e., microbubbles) of diameter of $2 - 4 \, \mu$m which had been etched into the surface. Is there a similar connection between cavitation on smooth unstructured surfaces and surface nanobubbles?

4.2 Theoretical estimation

In other words: to what extent must the liquid pressure p_L be reduced to grow a nanoscale bubble to a visible size, i.e., above microns)? A first estimate is obtained from the criterion that unstable growth of a bubble occurs when p_L falls below the critical pressure $p_L^c = p_0 - p_B$, with the ambient static pressure p_0 and the Blake threshold p_B [20, 21]. The hemispherical dynamics of a surface bubble under rapid decrease of the liquid pressure is close to that of a free bubble with the same radius of curvature [19]. Therefore, though surface nanobubbles are spherical caps rather than free spherical bubbles, one may obtain a reasonable estimate by the assumption of a spherical bubble. Assuming a nanoscale bubble with radius $R = 100$ nm and $p_0 = 1$ atm one arrives at $p_L^c \approx -0.55$ MPa which is exceeded in the experiments by more than an order of magnitude, see Fig. 4.1. Moreover, we solved the Rayleigh-Plesset equation [20, 21] (which describes the dynamics of a spherical bubble under variations of the liquid pressure) numerically for a gas bubble with the measured liquid pressure reduction as driving force. This calculation yields that bubbles down to a radius of curvature $R = 10$ nm should grow to visible bubbles during the experiments. Hence, theoretically it should be no problem to nucleate a surface nanobubble to visible size, but is this reflected in the experiments?

4.3 Experiment

The setup for the cavitation experiments is similar to that used in [17–19]. A shock wave generator (Piezoson 100, Richard Wolf GmbH) consisting of piezoceramic elements mounted on a spherical cap generates a pressure signal in the water, consisting of a high pressure front followed by a large tensile stress, see Fig. 4.1. The substrate of interest is processed and handled inside a filtered flow bench (HERAsafe KS Safety Cabinet Class II, Kendro) and placed inside of a sterile flask (EasyFlask 75 cm^2, Nunc) filled with pure water (Milli-Q Synthesis A10, Millipore), ensuring cleanroom conditions throughout the experiment. The flask is placed inside the water tank such that the shock wave is focussed onto the substrate. The pressure signal at this position is recorded with a fibre optic probe hydrophone. The cavitation event is
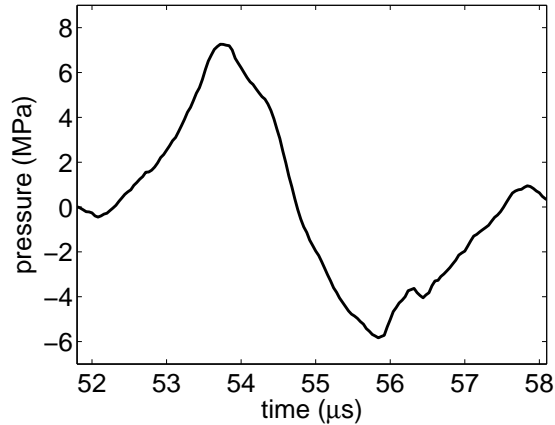
Figure 4.1: Pressure signal from the shock wave generator recorded inside of the protective flask with the fibre optic probe hydrophone close to the surface of the chip. The line depicts the low pass filtered signal averaged over five recordings. Triggering the shock wave generator corresponds to time $t = 0$.

photographed by a CCD camera (Flowmaster, LaVision) through a long-distance microscope (Model K2, Infinity). The major difference between the present setup and that of [17–19] is the maintenance of cleanroom conditions by use of the protective flask. Compared to Fig. 2 of Ref. [17] less than 1% cavitation activity on the surface is observed when cleanroom conditions are preserved, indicating that contaminations play a dominant role for cavitation experiments under ambient lab conditions.

The AFM data are acquired on a VEECO/Digital Instruments (DI) multimode AFM equipped with a NanoScope IIIa controller (DI, Santa Barbara, CA) in tapping mode in water using a DI liquid cell and V-shaped Si_3N_4 cantilevers (Nanoprobes, DI). The data shown for case D) are obtained after mounting the sample into the AFM while keeping the sample surface covered by water at all times, as described previously [22].

Corresponding to different kinds of substrates and/or different procedures of substrate preparation, we present results associated with four different kinds of probes, labeled A) − D). Probes A) and B) use smooth polyamide surfaces as solid substrate. Polyamide is heated and molded between silicon and atomically smooth mica. The mica is removed when the polyamide is cooled down to room temperature, leaving a relatively smooth polyamide surface with a root mean square (rms) roughness of 3.5 nm (measured by AFM on $1 \times 1\,\mu m^2$) and a static contact angle of $80°$. Besides large smooth areas of many mm^2 the production process also creates several microscopic cracks in the surface. In case A) these polyamide surfaces are used in the experiments without further treatment. In case B) the substrate is first covered by

ethanol which is then flushed away by water. This ethanol-water exchange has been reported to induce the formation of surface nanobubbles, see [5, 8] and references therein. Besides the explanation suggested in [5] we note that also the exothermic mixing [23] of ethanol and water might induce the formation of nanobubbles, since a temperature increase favors the formation of nanobubbles [8]. In the cavitation experiments a drop of ethanol is placed on the substrate such that it is completely covered by ethanol before it is submerged in water. Then the substrate is moved inside the protective flask for a minute to replace the miscible ethanol by water *. In the AFM experiment for case B) a liquid cell is used.

Probes C) and D) use pieces of smooth hydrophobized silicon as the substrate. A Si(100) wafer is diced into chips ($1 \times 1 \, cm^2$) which are immersed for 15 minutes in a (5:1) Piranha cleaning mixture. Hereafter, the chips are hydrophobized by chemical vapor deposition of 1H,1H,2H,2H-perfluorodecyldimethylchlorosilane (PFDCS) [17], yielding a rms value of $\approx 0.36 \, nm$ (measured by AFM on $1 \times 1 \, \mu m^2$), a coating thickness $\approx 2.6 \, nm$ (measured by ellipsometry), and an advancing contact angle $\approx 100°$. Note that the silane-film is not able to move; it is a stable self-assembled monolayer covalently bonded to the underlying substrate. Before immersion in water the probes are rinsed with ethanol and blown dry with argon gas [17]. Case D) additionally applies the *ex situ* ethanol-water exchange as described above.

In each of the cases A)$-$C) substrates of the respective type are produced in an identical manner. One substrate is used in the cavitation experiments and one in the AFM measurements. Note that we checked that the observed cavitation activity and nanobubble density were reproducible among substrates of the same kind. Furthermore, in case D) the *same* substrate is used in both experiments. After the cavitation experiment (exposure to a single shock wave) the substrate is transported in water to the AFM, where it is mounted without exposure to air, whereafter the water-solid interface is imaged as it appears after the cavitation experiments.

4.4   Results and Discussion

Do substrates with a high nanobubble density show a large cavitation activity? Fig. 4.2 illustrates the experimental results. The left panel shows typical recordings of the cavitation experiments for the cases A)$-$D). The right panel shows the corresponding AFM-measurements of the substrate surfaces immersed in water. Though the substrates have relatively large contact angles and the water pressure drops down to $\approx -6 \, MPa$ during the experiments there is hardly any cavitation on the smooth substrates A)$-$D). Note that the cavitation bubbles in A) originate exclusively from

---

*We verified that our *ex situ* ethanol-water exchange generates surface nanobubbles, by placing the processed substrate in the AFM while keeping water on its surface. Then the substrate was AFM-scanned and many surface nanobubbles (> 10 per μm^2) were observed.
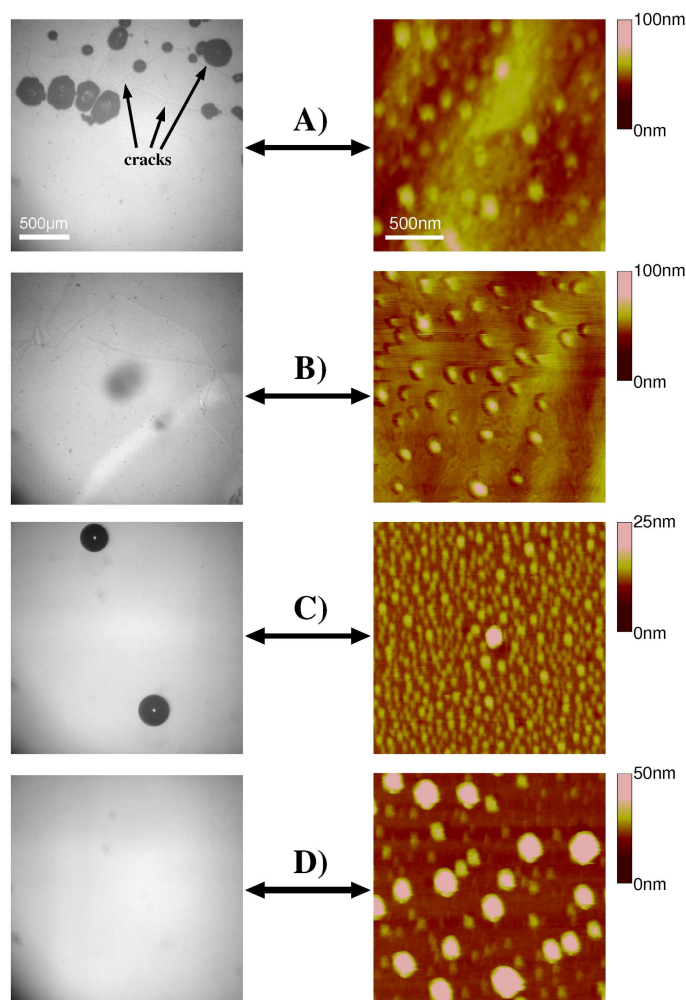
Figure 4.2: Cavitation activity (left), and corresponding nanobubble density (right) imaged by AFM (topography images) for various probes. The length scales given in A) also refer to B) − D). – A) and B): polyamide substrates, B) after ethanol-water exchange. C) and D): hydrophobized silicon substrates, D) after ethanol-water exchange. There is hardly any cavitation though the substrates are densely covered by surface nanobubbles. Note that the cavitation bubbles in A) emerge exclusively from microscopic cracks in the surface, whereas the whole substrate is covered by nanobubbles. The cavitation bubbles in C) presumably originate from surface contaminations. In D) it is shown that nanobubbles are still stably present *after* the cavitation experiments.

microscopic cracks in the surface, as can be seen in Fig. 4.2A). Applying the ethanol-water exchange, these microcracks do not lead to surface cavitation, see Fig. 4.2B). Contrary to the cavitation experiments, the AFM measurements show that all substrates are densely covered by surface nanobubbles, with number densities between 10 and 80 bubbles per μm^2. The sizes range from 3 to 40 nm in height and 60 to 300 nm in diameter. Several standard tests were performed (not shown) to ensure that the structures seen in the AFM images are indeed surface nanobubbles. Force-volume measurements [1, 3, 5] and tip manipulation of the bubbles [2] are in accordance with previous studies. Furthermore, nanobubbles are not present when the substrates are immersed in ethanol, in agreement with [8]. Successive cycles of ethanol-water and water-ethanol exchange resulted in pictures without (in ethanol) and with nanobubbles (in water). Finally, when degassed ethanol is exchanged by degassed water, nanobubbles are *not* induced.

Thus the combination of the cavitation and the AFM experiments yields the remarkable result that the surface nanobubbles do not cavitate, in spite of the enormous tensile stress they are exposed to. This contradicts the expectation that the experimental pressure signal should be able to cavitate bubbles with an initial radius of curvature down to 8 nm. Case D) explicitly shows that nanobubbles are still present *after* [†] the cavitation experiments, and that there is no cavitation activity at the surface induced by the shockwave. While it is already puzzling that surface nanobubbles are stable under ambient conditions, it is even more puzzling that they still exist after the passage of a shock wave with a large tensile stress down to $\approx -6\,MPa$. We denote this as *superstability*.

One may wonder what actually is happening with the surface nanobubbles when the shock wave is passing by. With the present technology it is impossible to AFM-image the nanobubbles (which takes order of minutes) during the shock wave passage (which is order of μs). Therefore, evidence can only be indirect.

One may also question whether the nanobubbles survive the compression wave (with typical time scale $\tau \approx 1\,\mu s$ so that the nanobubbles respond quasi-statically). During the compression phase, gas may diffuse into the neighboring liquid around the bubble. With a typical diffusion constant of $D \approx 10^{-9} m^2/s$ we get as typical diffusion length scale $\sqrt{\tau D} \approx 100\,nm$. Hence the liquid close to the remaining void (100 nm) will become supersaturated with gas. However, during the negative pressure phase, i.e., during the expansion of the bubble, all this gas will be recollected by the bubble, as has been shown in Ref. [24] (for micrometer bubbles).

[†]Strictly speaking, we cannot exclude that surface nanobubbles re-form prior to the AFM measurements (within minutes), after the cavitation had originally removed them.

4.5 Conclusion

In summary, it is demonstrated that in standard shock wave induced cavitation experiments surface nanobubbles do *not* act as nucleation sites. Cavitation bubbles originate from contaminations or from microscopic structures such as microcracks or microcrevices [18, 19], rather than from surface nanobubbles which densely populate the immersed substrates. This implies that surface nanobubbles are unexpectedly stable under large tensile stresses.

References

[1] J. W. G. Tyrrell and P. Attard, "Images of nanobubbles on hydrophobic surfaces and their interactions", Phys. Rev. Lett. **87**, 176104 (2001).

[2] A. C. Simonsen, P. L. Hansen, and B. Klösgen, "Nanobubbles give evidence of incomplete wetting at a hydrophobic interface", J. Colloid Interf. Sci. **273**, 291–299 (2004).

[3] M. Holmberg, A. Kühle, J. Garnæs, K. A. Mørch, and A. Boisen, "Nanobubble trouble on gold surfaces", Langmuir **19**, 10510–10513 (2003).

[4] A. Agrawal, J. Park, D. Y. Ryu, P. T. Hammond, T. P. Russell, and G. H. McKinley, "Controlling the location and spatial extent of nanobubbles using hydrophobically nanopatterned surface", Nano Lett. **5**, 1751–1756 (2005).

[5] X. H. Zhang, N. Maeda, and V. S. J. Craig, "Physical properties of nanobubbles on hydrophobic surfaces in water and aqueous solutions", Langmuir **22**, 5025–5035 (2006).

[6] L. Zhang, Y. Zhang, X. Zhang, Z. Li, G. Shen, M. Ye, C. Fan, H. Fang, and J. Hu, "Electrochemically controlled formation and growth of hydrogen nanobubbles", Langmuir **22**, 8109–8113 (2006).

[7] X. H. Zhang, G. Li, N. Maeda, and J. Hu, "Removal of induced nanobubbles from water/graphite interfaces by partial degassing", Langmuir **22**, 9238–9243 (2006).

[8] S. Yang, S. M. Dammer, N. Bremond, H. J. W. Zandvliet, E. S. Kooij, and D. Lohse, "Characterization of nanobubbles on hydrophobic surfaces in water", Langmuir **23**, 7072–7077 (2007).

[9] M. Switkes and J. W. Ruberti, "Rapid cryofixation/freeze fracture for the study of nanobubbles at solidliquid interfaces", Appl. Phys. Lett. **84**, 4759 (2004).

[10] R. Steitz, T. Gutberlet, T. Hauss, B. Klösgen, R. Krastev, S. Schemmel, A. C. Simonsen, and G. H. Findenegg, "Nanobubbles and their precursor layer at the interface of water against a hydrophobic substrate", Langmuir **19**, 2409–2418 (2003).

[11] P. S. Epstein and M. S. Plesset, "On the stability of gas bubbles in liquid-gas solutions", J. Chem. Phys. **18**, 1505 – 1509 (1950).

[12] S. Ljunggren and J. C. Eriksson, "The lifetime of a colloid-sized gas bubble in water and the cause of the hydrophobic attraction", Colloids Surf. A **129–130**, 151–155 (1997).

[13] E. Lauga and M. P. Brenner, "Dynamic mechanisms for apparent slip on hydrophobic surfaces", Phys. Rev. E **70**, 026311 (2004).

[14] E. Lauga, M. P. Brenner, and H. A. Stone, *Handbook of Experimental Fluid Dynamics* (Springer, New York) (2005).

[15] C. Neto, D. R. Evans, E. Bonaccurso, H.-J. Butt, and V. S. J. Craig, "Boundary slip in newtonian liquids: a review of experimental studies", Rep. Prog. Phys. **68**, 2859–2897 (2005).

[16] A. A. Atchley and A. Prosperetti, "The crevice model of bubble nucleation", J. Acoust. Soc. Am. **86**, 1065–1084 (1989).

[17] N. Bremond, M. Arora, C. D. Ohl, and D. Lohse, "Cavitation on surfaces", J. Phys.: Condens. Matter **17**, S3603–S3608 (2005).

[18] N. Bremond, M. Arora, C. D. Ohl, and D. Lohse, "Controlled multibubble surface cavitation", Phys. Rev. Lett. **96**, 224501 (2006).

[19] N. Bremond, M. Arora, S. M. Dammer, and D. Lohse, "Interaction of cavitation bubbles on a wall", Phys. Fluids. **18**, 121505 (2006).

[20] C. E. Brennen, *Cavitation and Bubble Dynamics* (Oxford University Press, New York) (1995).

[21] T. G. Leighton, *The Acoustic Bubble* (Cambridge University Press, Cambridge) (1994).

[22] K. Morigaki, H. Schönherr, C. W. Frank, and W. Knoll, "Photolithographic polymerization of diacetylene-containing phospholipid bilayers studied by multimode atomic force microscopy", Langmuir **19**, 6994 (2003).

[23] S. Coffey, ed., *Rodd's chemistry of carbon compounds 2nd edition, vol 1, part B* (Elsevier, Amsterdam) (1965).

[24] S. Hilgenfeldt, D. Lohse, and M. P. Brenner, "Phase diagrams for sonolumi-
     nescing bubbles", Phys. Fluids **8**, 2808 (1996).

Part II

Cavitation from nanoscopic gas pockets

5

Nucleation threshold and deactivation mechanisms of nanoscopic cavitation nuclei[‡][*]

In the previous chapter we found that surface nanobubbles do not act as nucleation sites in shock-wave induced cavitation experiments. In contrast, we will show in this chapter that nanobubbles of similar lateral and volumetric dimensions do *nucleate when they are trapped in well-defined nanoscopic pits. The corresponding acoustic nucleation thresholds are determined experimentally by decreasing the minimum pressure in the liquid stepwise. The results are quantitatively in good agreement with the theoretical predictions developed within the crevice theory by Atchley & Prosperetti [J. Acoust. Soc. Am.* **86**, *1065-1084 (1989)]. In addition, we provide the mechanism which explains the deactivation of cavitation nuclei: gas diffusion together with an aspherical bubble collapse. Finally, we present superhydrophobic nuclei which cannot be deactivated, unless with a high-speed liquid jet directed into the pit.*

5.1   Introduction

Water can be ruptured at much smaller tensile stresses than theoretically is expected [1]. The reason for this discrepancy could be the existence of small inhomogeneities in the liquid, which may exist even when special care on the cleanliness of the water has been taken [2]. The inhomogeneities, whatever their origin might be, have received the generic name "cavitation nuclei", while the bubble generation produced in this way is termed heterogeneous nucleation. Cavitation nuclei are generally long-lived and it is believed that they consist at least in part of a volume of gas [3]. This observation excludes the possibility of the inhomogeneities being free spherical gas bubbles, as these are unstable. To account for stable gaseous cavitation nuclei, two types are distinguished in the literature: bubbles stabilized by a skin (see Ref. [3] and references therein) and bubbles trapped inside a surface defect ("crevice model") [4–9].

The principle of the crevice model dates back to 1944 [4] and has found extensive qualitative experimental evidence over the years. Greenspan and Tschiegg [10], for example, reported that removing particles larger than $0.2 \mu m$ in diameter increased the tensile strength of water to about 200 bar (see also Refs. [2, 11]). Others found that the addition of suspended particles lowers the nucleation threshold [12–17], while pre-experimental pressurization of water increases the nucleation threshold [5, 18]. Although these findings are in line with the general idea of the crevice model, none of the experiments could quantitatively verify the theoretical crevice model as developed by Atchley & Prosperetti [8] in 1989. One of the reasons is that their predictions are valid for a single cavity of a well-defined shape, while in practice the liquid usually contains a wide variety of nuclei of different sizes and shapes. Even in ultrapure water with a controlled number of microparticles, the sizes of the nuclei present on the microparticles can exhibit size variations yielding a wide range of thresholds [18]. A step forward was achieved by Bremond *et al.* who were able to create monodisperse cavitation nuclei by trapping gas inside cylindrical holes of well-defined shape etched in silicon surfaces using standard lithography techniques [19–21]. Not only was the position and size of the nuclei perfectly controlled, but the nucleation event itself was also highly reproducible, so that it could be followed in time with stroboscopic methods without the need of expensive high-speed cameras.

Both conditions, the reproducibility of the experiment and the monodispersity of the nuclei present at fixed positions, are important ingredients of this chapter. Here, we have downscaled the micropits of Bremond *et al.* two orders of magnitude, so that it becomes possible to experimentally verify the theoretical predictions made in the framework of the crevice model. This is the first aim of this chapter. Secondly, we explore the mechanisms leading to the deactivation of nuclei after a single nucleation event. In addition, we show that superhydrophobic cavitation nuclei can nucleate hundreds of times, without being deactivated. Our observations and interpretations have implications for an increased understanding of the behavior of cavitation nuclei

down to length scales of a few tens of nm ("surface nanobubbles") [22].

5.2 Brief theoretical description

A comprehensive description and development of the crevice model can be found in the paper of Atchley & Prosperetti [8] with extensions to any axisymmetric geometry, including cylindrical cavities, given by Chappell & Payne [23]. In both papers, the authors predict the various nucleation thresholds as function of crevice shape, gas tension, and receding contact angle. Atchley & Prosperetti argue that a true nucleation event must be the result of the loss of mechanical stability of the nucleus, and calculated the threshold for two situations: the first threshold denotes the pressure at which the nucleus *inside* a crevice begins its unstable growth, and is the lowest pressure value belonging to a bubble reaching either the critical radius of curvature R_c, or the receding radius of curvature R_R, i.e. the radius of curvature at which the receding contact angle θ_R is reached. The second threshold is equivalent in definition, but holds for the bubble growing *outside* of the crevice mouth. The lower value of the first and second nucleation threshold is the one for which the bubble grows explosively out of the cavity. For the case of a bubble trapped in a cavity with volume V_c with its interface at the crevice mouth, the (second) nucleation threshold is given by

$$p_L + \frac{2\sigma}{R} = p_v + \frac{V_0 p_{g,0}}{V_c + (\pi/3)g(\theta)R^3}, \tag{5.1}$$

with p_L the liquid pressure, p_v the vapor pressure, V_0 the initial volume of the gas, $p_{g,0}$ the initial gas pressure in the bubble, σ the liquid-gas surface tension, and $(\pi/3)g(\theta)R^3$ the volume of the spherical-cap-shaped bubble with radius R as it expands above the cavity [8] (see Fig. 5.1). Here, $g(\theta) = \left(2 + (2 + \sin^2\theta)\cos\theta\right)$ is a geometric function depending on the contact angle θ. The right-hand side of Eq. 5.1 represents the expanding forces caused by the vapor and gas pressure, $p_v + p_g$, respectively, while the left-hand side represents the collapsing forces due to the liquid pressure and surface tension, respectively. Eq. 5.1 implies that, for nucleation to occur, the expanding forces should exceed the collapsing forces (condition 1). Secondly, this condition should persist for increasing R, i.e. $d(p_g + p_v)/dR > d(p_L + 2\sigma/R)/dR$ (condition 2).

Let us now consider the case - which we will examine experimentally - of a cylindrical cavity with radius r_c and depth d_c, under the assumption that the initial gas-liquid interface at the crevice mouth is approximately flat (i.e. we assume a negligible effect of the hydrostatic pressure and gas-saturated water), so that we can write $V_0 = V_c = \pi r_c^2 d_c$. For $\theta_R \geqslant \pi/2$ the nucleation threshold is the pressure needed to pull the bubble beyond its minimum radius while it expands from the cavity, i.e.
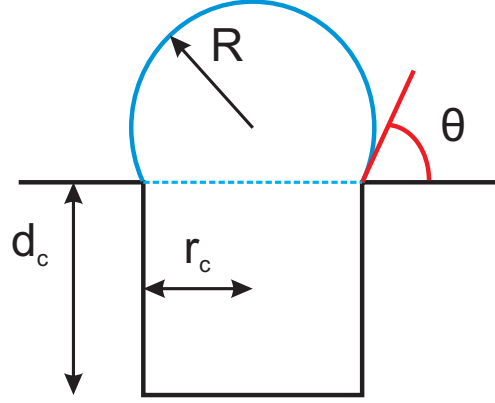
Figure 5.1: Cylindrical cavity with its dimensions. The initial gas-liquid interface is flat (dashed line), while the expanding bubble has a radius of curvature R and contact angle θ with the flat surface.

$R_{min} = R_R = r_c / \sin \theta_R$. Now, Eq. 5.1 can be rewritten as

$$p_L = p_v + \frac{3 p_{g,0}}{3 + (r_c/d_c) g(\theta_R)/\sin^3 \theta_R} - \frac{2\sigma \sin \theta_R}{r_c}. \qquad (5.2)$$

This prediction will be verified experimentally in this chapter. At the point $R = R_{min} = R_R$ the bubble experiences the maximum collapsing force. Any further reduction of the liquid pressure will make the bubble expand, thus reducing the surface tension pressure, and the bubble will grow explosively with the contact angle fixed at θ_R. Equations 5.1 and 5.2 are illustrated in Fig. 5.2, for an air bubble trapped in a cylindrical pit with dimensions $r_c = 250$ nm and $d_c = 500$ nm and with $p_{g,0} = 10^5$ Pa $- p_v$, $p_v = 73 \cdot 10^2$ Pa and $\theta_R = 100°$. The graph shows the expanding and the collapsing forces for two cases: 1) $p_L = -0.20$ MPa (Blake threshold [24, 25] for a free bubble with $R_0 = r_c$) and 2) $p_L = -0.486$ MPa (prediction of Eq. 5.2). From this plot it is readily seen that the expanding pressure in the second case is always larger than the collapsing pressure, and that $d(p_g + p_v)/dR > d(p_L + 2\sigma/R)/dR$.

For $\theta_R < \pi/2$ the nucleation threshold is much more complicated to calculate. At $R = R_{min} = r_c$ the collapsing force due to surface tension is indeed maximum, but now $d(p_g + p_v)/dR < d(p_L + 2\sigma/R)/dR$ and therefore $p_L(R_{min})$ cannot be the nucleation threshold. Also $p_L(R_R)$ is not the correct threshold, as this gives a stable equilibrium in the upper branch of the compressive force curve. Instead, the threshold needs to be found by numerically solving $d(p_g + p_v)/dR = d(p_L + 2\sigma/R)/dR$, which is an implicit equation as the contact angle depends on the radius R, through $\sin \theta = r_c/R$, as long as the receding contact angle has not yet been reached.

In the prediction of p_L the gas term is significant for cavities down to a few hundred
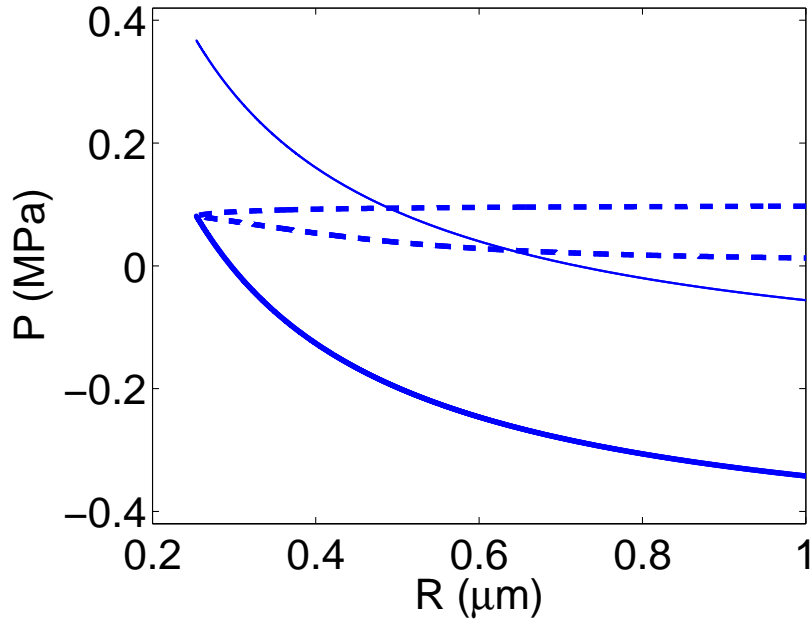
Figure 5.2: Graph of the expanding forces (right-hand side of Eq. 5.1, dashed line) and the collapsing forces (left-hand side of Eq. 5.1, solid lines) for a bubble expanding from a cylindrical pit with $r_c = 250\,$nm, $d_c = 500\,$nm, $p_{g,0} = 10^5\,$Pa $- p_v$, $p_v = 73 \cdot 10^2\,$Pa and $\theta_R = 100^\circ$. The expanding forces (dashed line) show two branches corresponding to the possible solutions of R. The upper branch reflects the initially flat bubble during its first expansion phase: R decreases from $R = R_\infty$ to $R = R_R$; the lower branch shows the solutions for the bubble expanding during its second phase: R increases from $R = R_R$ to larger sizes. The collapsing forces are shown for two cases: 1) $p_L = -0.20\,$MPa (thin solid line) and 2) $p_L = -0.486\,$MPa (thick solid line). For case 1, the expanding forces dominate over the collapsing forces and the bubble will expand, until at $R = 0.49\mu$m a stable equilibrium is reached. No nucleation will occur in this case. In case 2 the expanding forces are larger than the collapsing forces for all possible solutions of R, and as a result the bubble will grow explosively.

nm in radius and will therefore be taken into account in the present analysis.

5.3   Materials & methods

5.3.1   Experimental setup

The experimental setup to investigate the nucleation behavior of bubbles trapped in well-defined cavities is similar to that used by Bremond *et al.* [19–21] and sketched in Fig. 5.3. Cavitation is induced by a focused shock wave generator (Piezoson 100, Richard Wolf GmbH) consisting of piezoelectric elements mounted on a spherical cap at the bottom of the liquid bath, which is filled with 1 liter of air-saturated water (Milli-Q Synthesis A10, Millipore). The cavitation activity is recorded optically with a CCD camera (Flowmaster, LaVision) through a long-distance microscope (Model K2, Infinity). Illumination is provided by a flash lamp in reflection mode. The liquid pressure p_L is obtained with the help of a calibrated glass fiber hydrophone (FOPH 500, RP Acoustics). The pressure is derived by measuring the reflected intensity of the laser beam at the fiber tip, which depends on the density of the water as affected by the local pressure [26]. At the acoustic focus the pressure signal is typically characterized by a pressure peak (duration $\sim 1\,\mu s$) followed by a negative pressure phase ($\sim 5\mu s$). The intensity of the pressure pulse can be varied in twenty discrete steps. Since the smallest possible pressure decrease at the acoustic focus $\min(p_L) = -3.2\,\mathrm{MPa}$ is already too large for our purpose, the samples are translated horizontally (away from the acoustic focus) along the line of sight, until the pressure signal is sufficiently weak that nucleation does not occur at the smallest pressure drop, but only at larger pressure decreases. The hydrophone tip (diameter: $100\,\mu m$) is positioned $\sim 0.1\,\mathrm{mm}$ in front of the chip surface, at an angle with the vertical plane of $10 - 20°$. We took care of the close proximity between tip and surface by checking: 1) that the hydrophone tip end was not touching the chip surface (as this gave noisy data); 2) that the tip was in the optical focus of the camera (differences of 0.1 mm could be detected by comparing sharpness of the pictures). The corresponding pressure signals are recorded using a low pass filter (cutoff frequency 2.2 MHz) and averaged over 25 recordings to reduce the noise. A typical recording of the averaged pressure signal obtained 25 mm out of focus is shown in Fig. 5.4 and corresponds to the experiment with the sample containing pits of 246 nm in radius.

5.3.2   Samples with nanopits

The substrates of interest are silicon pieces of $5 \times 5\,\mathrm{mm}^2$ diced from a Si(100) wafer. The nanoscopic cylindrical pits are directly etched into the substrate by a focused ion beam (FIB) in a 6×6 square pattern, with $200\,\mu m$ distance between the pits.

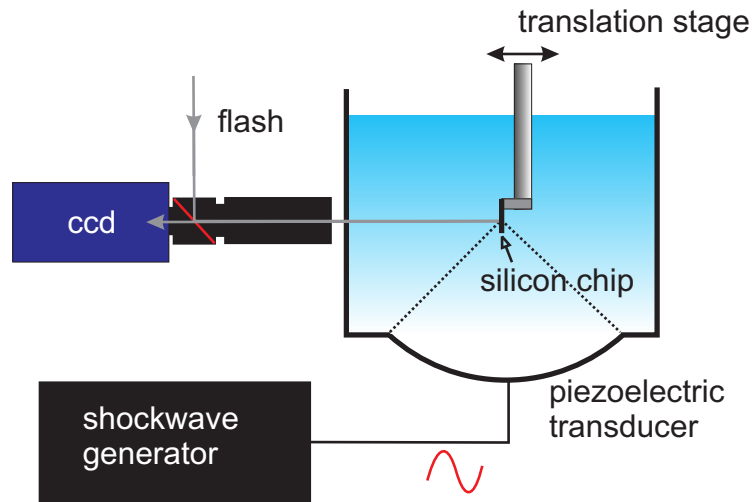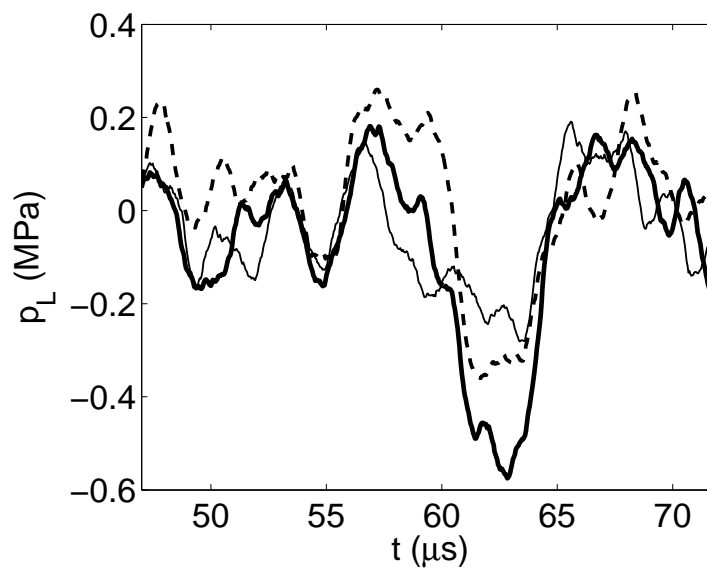Figure 5.3: Sketch of the experimental setup.

Figure 5.4: Three pressure signals with increasing strength recorded at the chip surface 25 mm out of focus, corresponding to the experiment with sample B (r_c = 246 nm). Each line is the mean of 25 recordings. From these signals the minimum pressure can be extracted: -0.24 MPa (thin solid line), -0.35 MPa (dashed line) and -0.54 MPa (thick solid line)

The resulting $1 \times 1\,\mathrm{mm}^2$ pattern is located at the center of the chip. In order to facilitate detailed imaging by atomic force microscopy (AFM) and scanning electron microscopy (SEM) identical pits are etched near the chip corner. Four samples (A-D) were studied with the following dimensions (determined with SEM) of the nanopits: A) $r_c = 495\,\mathrm{nm}$; B) $r_c = 246\,\mathrm{nm}$; C) $r_c = 53\,\mathrm{nm}$; D) $r_c = 50 - 60\,\mathrm{nm}$. In sample A-C the pattern consisted of uniformly sized pits, with depth $d_c = 2r_c$, while in sample D each column of pits had different depths (75, 100, 200, 300, 500, and 1000 nm), which influenced the radial pit size per column by a few nm (50, 50, 50, 55, 57, and 60 nm resp.); see Fig. 5.5 for the corresponding SEM pictures. Notice that r_c has been measured precisely with SEM, while d_c could not be measured and should therefore be regarded as an indicative value of the depth. In contrast to r_c, the exact depth of the pits (which only determines the initial gas volume) does not matter too much for the overall bubble dynamics, provided that the radius r_c is small enough, which is the case in our experiments. After production the samples were cleaned ultrasonically in ethanol (15 minutes), followed by an oxygen plasma (5 min.), a chemical cleaning step using a fresh (5:1) Piranha mixture (30 min.) and again an ultrasonic bath in ethanol (15 min.). This yielded clean and completely wetting substrates, which were characterized by a smoothly dewetting contact line (if not, the whole process was repeated). Subsequently, the samples were hydrophobized with 1-H,1-H,2-H,2H-perfluorodecyltrichlorosilane following Ref. [27]. The advancing and receding contact angles on the surface were $\theta_a = 124^\mathrm{o}$ and $\theta_r = 100^\mathrm{o}$. After immersion in water it was confirmed with AFM in tapping mode that a horizontal gas-liquid meniscus was present at the mouth of the pits.

5.4   Results

5.4.1   Nucleation from gas-filled nanopits

To see whether it is possible to nucleate bubbles from nanopits as small as 53 nm in radius, samples A-C were immersed in the liquid bath allowing air to be entrapped in the pits. In successive experiments the samples were put at the acoustic focus of the shock wave generator and subjected to a pressure pulse with $p_m = \min(p_L) = -3.2\,\mathrm{MPa}$. This value is sufficiently below the nucleation thresholds of the three samples, i.e. $-0.23\,\mathrm{MPa}$, $-0.48\,\mathrm{MPa}$, and $-2.59\,\mathrm{MPa}$ respectively (see Eq. 5.2), to expect nucleation of bubbles from the nanopits. The camera and flash were triggered a few μs after passage of the negative part of the shock wave to capture the expanding bubbles at maximum sizes. The result is depicted in Fig. 5.6 for the samples A-C, respectively. Sample A and B showed almost perfect bubble patterns, with each bubble corresponding to the position of the nanoscopic cavitation nucleus. In each experiment, the cavitation nuclei had to be 're-activated' (filled with air again), since it was not possible to nucleate bubbles a second time without taking the sample out
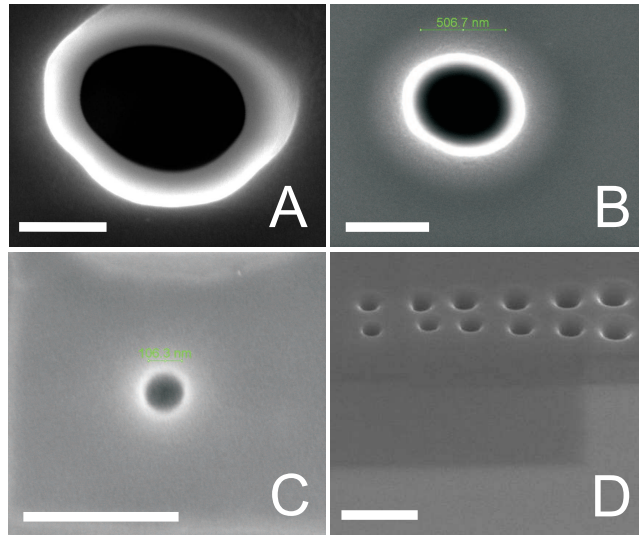
Figure 5.5: SEM images of samples A-D, respectively. The bars in each picture denote 500 nm. The ellipsoidal shapes for sample A and B are due to drift in the SEM chamber, i.e. the pits have circular cross-sections in reality.

of the water first [20]. With sample C a maximum amount of 34 bubbles could be nucleated in the first experiment, implying that it is indeed possible to nucleate bubbles from such small cavities. While sample A and B showed perfect reproducibility, the number of bubbles nucleating from sample C declined dramatically in later experiments, even when the negative pressure amplitude was increased to -7 MPa. Presumably, small contaminant molecules had decreased the contact angle locally, leading to completely wetted nanopits. To test this possibility, the old hydrophobic coating was stripped off with an oxygen plasma and the sample was hydrophobized again through the cleaning and coating steps described before. This process indeed re-activated part of the nuclei (~ 80% of the pits) though the number of bubbles declined again in successive experiments.

5.4.2 Determination of the experimental nucleation threshold

The experimental nucleation threshold of the nanosized cavities can be obtained by moving the samples to a position in the liquid bath where the pressure drop p_m is sufficiently small that no nucleation occurs. By lowering p_m stepwise the cavities will nucleate at a certain negative pressure amplitude which is the experimental nucleation threshold. To observe the bubbles optically, it is not sufficient for the negative pressure to be low enough, but it should also last long enough in time. A lower limit
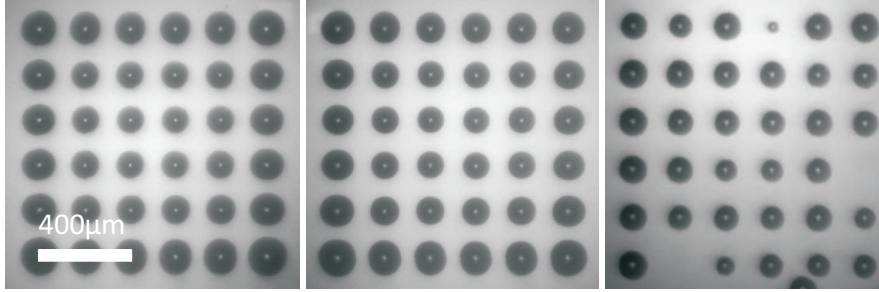
Figure 5.6: Cavitation bubbles nucleated from cylindrical pits with radius $r_c = 495$ nm (left), $r_c = 246$ nm (middle) and $r_c = 53$ nm (right), and depth $d_c = 2r_c$ for a pressure pulse with $p_m = -3.2$ MPa.

to the time Δt the bubble needs to grow to visible size is estimated, by first estimating the critical size $R_{c,o}$ to be optically observable. We take $R_{c,o} \sim 3$ image pixels = 3 pix $\times$ 2.9 μm /pix = 8.7 μm. Now, using [21, 28] $\dot{R} = \left(\frac{2}{3} \frac{p_v - p_m}{\rho} \right)^{1/2}$ with ρ the liquid density and $\dot{R}$ the bubble wall velocity, it follows that $\Delta t = R_{c,o}/\dot{R} = 0.9\,\mu$s (sample A), 0.6 μs (sample B) and $\sim 0.3\,\mu$s (sample C and D). The minimum pressure level which lasts Δt is the negative pressure amplitude p_m of interest. Note that the difference with the absolute minimum pressure level is in most cases only a few percent, much smaller than the typical statistical error, which is ~ 0.2 MPa in the cases of sample A and B, and $\sim 0.4 - 0.6$ MPa in the case of sample C.

Let us first consider the case of sample B ($r_c = 246$ nm, $d_c = 2r_c$). The sample was put 25 mm out of the acoustic focus, and three pressure pulses with increasing strength (Fig. 5.4) were applied successively, without taking the sample out of the water. A typical result is shown in Fig. 5.7. With the first pulse ($p_m = -0.24$ MPa) no cavitation bubbles could be observed (Fig. 5.7a). The second pressure pulse ($p_m = -0.35$ MPa), resulted in a few nucleated bubbles (always in the top rows of the pattern), but the majority of the nuclei in the pattern still did not cavitate (Fig. 5.7b). The third pressure pulse, with $p_m = -0.54$ MPa, was able to nucleate all remaining nuclei (Fig. 5.7c). Note that the nuclei which nucleated with the second pulse could not be nucleated with the stronger third pulse, implying that the nuclei can be used only once. Nuclei which were not nucleated during the second pulse, however, survived and were nucleated with the stronger third pulse. The experiment was repeated eight times with reproducible results (Table 5.1): on average 0, 10, and 26 bubbles were counted for the three applied pressure pulses, respectively. When the third pulse ($p_m = -0.54$ MPa) was applied without the other two preceding ones, the full pattern became visible (Fig. 5.7d). Since the majority of the pits nucleated at $p_m = -0.54$ MPa it is reasonable to assume that this pressure amplitude is

p_m (MPa)	Amount of bubbles in exp. 1-8								mean
	1	2	3	4	5	6	7	8	
-0.24	0	0	0	0	0	0	0	0	0
-0.35	11	9	8	15	10	8	8	7	10
-0.54	23	27	28	19	25	27	27	29	26

Table 5.1: Results of eight experiments with sample B ($r_c = 246$ nm, $d_c = 2r_c$). In each experiment the minimum pressure p_m is decreased in three successive steps. The majority of the pits nucleates at $p_m = -0.54$ MPa.

above the experimental nucleation threshold for sample B, while the weaker pulse ($p_m = -0.35$ MPa) is (just) below the experimental nucleation threshold.

Since it was always the top row of pits plus some part of the second top row that nucleated at an apparently less negative p_m, it could very well be that there was a pressure variation along the chip surface in the vertical direction (i.e. direction of wave propagation), so that the most negative pressure occurred at the top row of the pits. In Fig. 5.7c and d we can indeed see that bubbles become slightly larger in the vertical direction, indicating a more negative pressure along this direction. With our setup we have not been able to measure a difference in pressure between top and bottom location of the pattern.

A similar experiment was carried out with sample A ($r_c = 495$ nm, $d_c = 2r_c$, Fig. 5.8). Again the sample was subjected to three successive pressure signals of decreasing negative pressure without being taken out of the water. For the lowest pressure amplitude ($p_m = -0.20$ MPa) no cavitation bubbles could be detected optically (Fig. 5.8a). A larger amplitude of $p_m = -0.23$ MPa yielded 14 bubbles of different sizes, with some of them barely visible (Fig. 5.8b), while a further reduction of the liquid pressure ($p_m = -0.34$ MPa) resulted in no visible bubbles at all (Fig. 5.8c). What happened with the remaining $36 - 14 = 22$ pits? As the lowest negative pressure was not able to nucleate them, they must already have been nucleated during the first two pulses, i.e. the nucleation took place below optical resolution. This is possible as the resolution of our optical detection is limited and the pressure pulse in this case is relatively weak (i.e. $\dot{R}$ is small). Therefore, in contrast with case B, we are not able to measure the pressure for which nucleation does *not* take place. When the third pulse ($p_m = -0.34$ MPa) was applied without the other two preceding pulses, the full pattern became visible (Fig. 5.8d). Hence, this is the pressure level for which we are sure that nucleation of the full pattern takes place.

Finally, sample D was studied, which consists of nanopits with 50 nm $\leqslant r_c \leqslant 60$ nm and varying depths. Just like sample C, the shallow pits on sample D nucleated only a few times, and could not be nucleated in later experiments. Fortunately, two columns with the deepest pits ($d_c = 500$ nm & $r_c = 57$ nm, and $d_c = 1000$ nm & $r_c = 60$ nm)
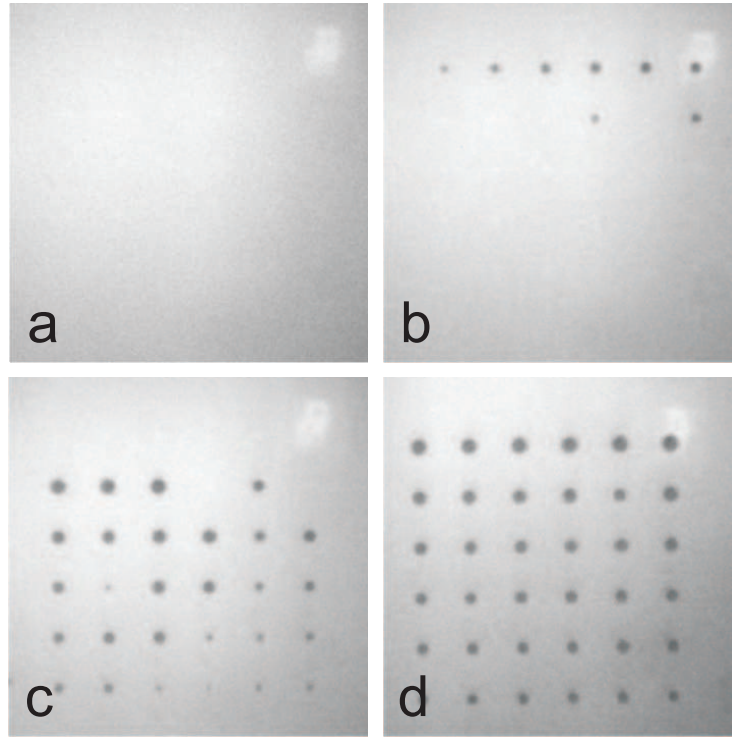
Figure 5.7: Cavitation bubbles emerging from 6×6 cylindrical pits with $r_c = 246\,nm$ (sample B), for three successively applied pressure pulses: a) $p_m = -0.24\,MPa$; b) $p_m = -0.35\,MPa$; c) $p_m = -0.54\,MPa$. The full pattern develops when $p_m = -0.54\,MPa$ is applied without the other two preceding pulses (d).

could be nucleated repeatedly, and the nucleation threshold could be measured for these pits. The experiment was very similar to the ones described before, but now the sample was $12\,mm$ away from the acoustic focus. A typical experimental result is depicted in Fig. 5.9. First, a pressure pulse with $p_m = -2.3\,MPa$ was applied and 1 pit from the right column ($r_c = 60\,nm$) was nucleated. A stronger second pulse ($p_m = -2.6\,MPa$) was able to nucleate the remaining 5 pits from this column, though other pits in the sample did not nucleate, as they were smaller. Reducing the negative pressure further ($p_m = -3.0\,MPa$) resulted in the nucleation of the left column of pits with $r_c = 57\,nm$. Hence, a small variation in pit sizes of just a few nm is reflected in a different nucleation threshold. It is also observed that the pits did not nucleate a second time, despite their huge aspect ratios.
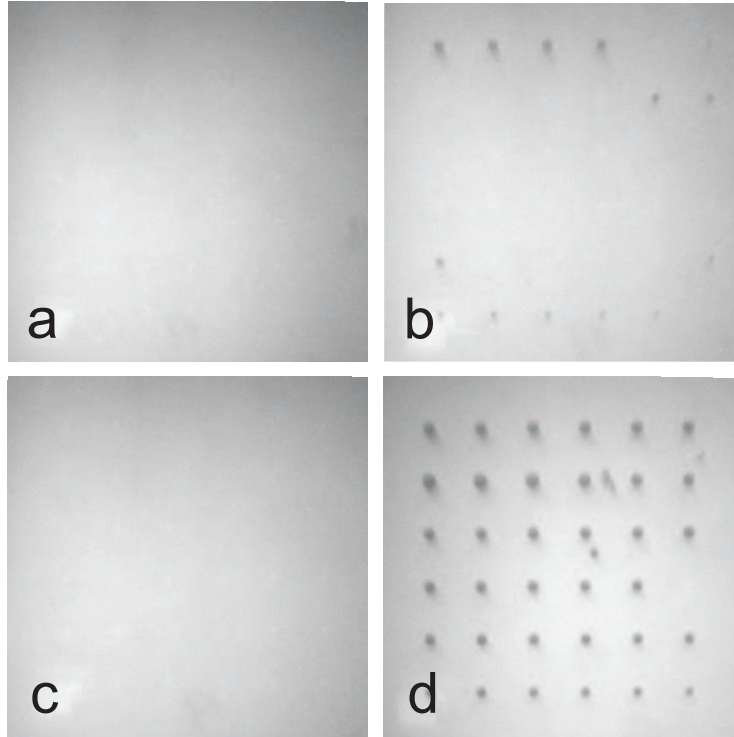
Figure 5.8: Cavitation bubbles emerging from 6×6 cylindrical pits with $r_c = 495$ nm (sample A), for three successively applied pressure pulses: a) $p_m = -0.20$ MPa; b) $p_m = -0.23$ MPa; c) $p_m = -0.34$ MPa. The full pattern develops when $p_m = -0.34$ MPa is applied without the other two preceding pulses (d).

5.4.3 Comparison with theoretical prediction

How do the experimental results compare with theoretical predictions? In Fig. 5.10 the theoretical nucleation threshold (line), based on Eq. 5.2, is plotted as a function of the pit radius r_c together with the experimental results (symbols). We used $d_c = 2r_c$ as is the case in sample A and B. Note that for the pits present in sample D the gas pressure term is negligible: the difference between $d_c = 2r_c$ and $d_c = 20r_c$ changes the theoretical prediction for pits of $r_c = 50$ nm $< 1\%$. The experimental data points at which full nucleation was detected for samples A, B and D are depicted by crosses, while the experimental pressures where nucleation of the full pattern (just) did not happen are marked with circles. The inset shows the experimental results for sample D including typical error bars depicting the standard deviation of the pressure recordings.

We observe a striking quantitative agreement between theory and experiment for all
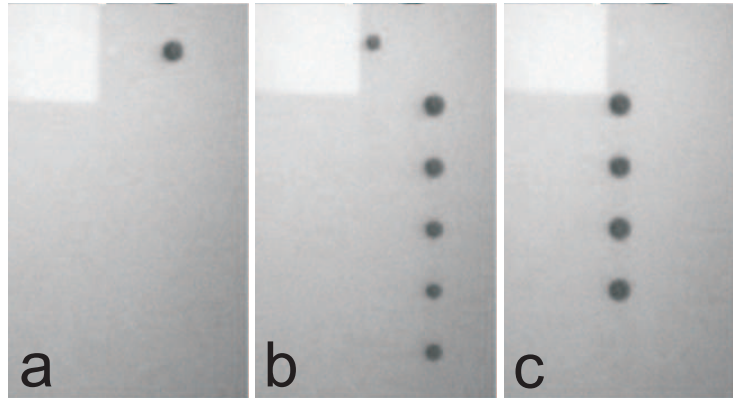
Figure 5.9: Cavitation bubbles emerging from 2×6 cylindrical pits (sample D) with $r_c = 57\,\text{nm}$, $d_c = 500\,\text{nm}$ (left column) and $r_c = 60\,\text{nm}$, $d_c = 1000\,\text{nm}$ (right column), for three successively applied pressure pulses: a) $p_m = -2.3\,\text{MPa}$; b) $p_m = -2.6\,\text{MPa}$; c) $p_m = -3.0\,\text{MPa}$.

samples. Pressure amplitudes for which nucleation was first detected are below the line marking the nucleation threshold. Pressure amplitudes for which nucleation did not occur are either above this line, i.e. in the regime where nucleation is not expected, or the line is within experimental errorbars. For sample D it was observed that the nucleation threshold strongly depends on the size of the pits: pit radii just a few nm smaller resulted in a significantly lower nucleation threshold, in agreement with the steep slope of $p_m(r_c)$ around these values.

5.4.4 Deactivation of cavitation nuclei

It is well known that artificial nucleation sites in boiling continue to be active for a long time, emitting many bubbles [29]. Similarly, the microscopic wall cracks and scratches in a glass full of beer or champagne are seen to emit bubbles for a very long time [30]. Even in cavitation studies on bare hydrophobic substrates, bubbles trapped in localized defects could be nucleated more than a hundred times [19]. Thus, there is something special in the deactivation of nuclei observed here which makes this situation different from the others. What is the physical mechanism responsible for the deactivation of the nuclei?

The main mechanism responsible for the deactivation of nuclei is encountered during the collapse phase of the bubble, where a wall-directed jet is formed. In the case of a single bubble (or weak interaction among bubbles) the jet momentum is expected to be directed mostly normal to the wall [31, 32]. When bubble-bubble interaction is non-negligible, on the other hand, the jet momentum may be deflected away from the
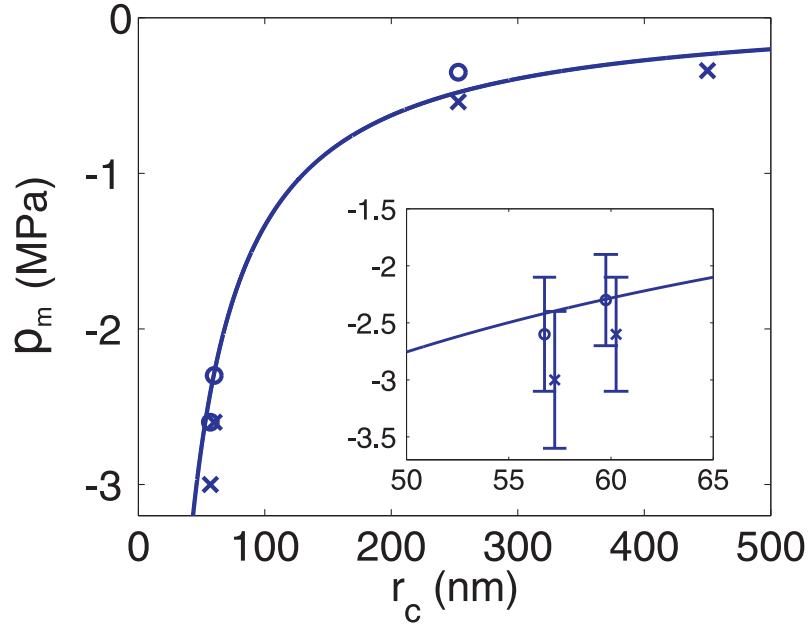
Figure 5.10: Nucleation threshold as function of the pit radius for both theory (line) and experiment (symbols, crosses: nucleation, circles: no nucleation). The inset shows a zoom in with errorbars. For visibility overlapping points are shifted ± 0.25 nm with respect to each other.

normal [21].

In order to shed light on this proposed deactivation mechanism, numerical simulations were carried out to elucidate the shape of the air-liquid interface during the bubble collapse. For this we used the boundary-integral method described in Ref. [33] based on a potential flow description of the liquid dynamics. The liquid-solid angle was prescribed to be $\theta_a = 124°$ which corresponds to the experimentally determined advancing contact angle of water on the substrates. At the starting point of the simulations the bubble was assumed to be a segment of a sphere with a radius significantly larger than the cavity radius r_c, see Fig. 5.11 (a). The pressure inside the bubble was assumed to be uniform, satisfying the adiabatic relation $p_0/V_0^{1.4} = p_{bub}/V_{bub}^{1.4}$ with the initial pressure p_0 and V_0 the volume of the crevice, and p_{bub} and V_{bub} the instantaneous pressure and volume of the bubble, respectively. After release the bubble begins to shrink rapidly due to both surface tension and the low internal pressure. Eventually it evolves into an almost cylindrical shape as illustrated in Fig. 5.11 (c). This air cylinder collapses radially and finally closes in a single point on the axis of symmetry, leaving a small air bubble entrapped above the pinch-off point,

see Fig. 5.11 (d). Towards pinch-off the liquid rushing radially inwards has to accelerate more and more to satisfy the requirement of mass conservation. When the advancing liquid front reaches the axis of symmetry a high pressure develops and the flow is deflected up and down to form two fast, needle-like water jets. The continuing collapse of the air cavity below and above the pinch-off point provides additional momentum to the two jets[34]. The downward jet protrudes deeply into the cavity until it hits the bottom of the cavity as illustrated in Fig. 5.11 (e)-(f). For simplicity we neglected the upper bubble here which is expected to have only negligible influence on the downward jet. Upon reaching the bottom the impacting jet would form a violent, non-axisymmetric splash which cannot be captured by our numerical technique. Nevertheless, one can easily imagine the continuation of the process: as more and more liquid enters the cavity through the jet, the cavity is flooded with liquid, making a second nucleation impossible. We checked that the jet mechanism is present for pits in the size range studied here ($50\,\mathrm{nm} < r_c < 500\,\mathrm{nm}$) and is independent of the initial bubble size, pit depth, and contact angle.

The previous explanation is not applicable to the case of strong mutual interaction between the bubbles, when the jet tends to be deflected away from the wall-normal [21], although the nuclei are still observed to be de-activated after emission of the first bubble. We estimated that within the typical lifetime of the bubble (typically $t_b \sim 10\mu s$), the gas molecules have ample time to fill the bubble volume to reach a uniform gas pressure. The gas transport is probably a combination of convection and diffusion, although the latter mechanism alone would already be sufficient to move all the gas: The typical diffusion length scale is $\sim \sqrt{Dt_b} = 10\mu m$, using the diffusion coefficient $D \sim 10^{-5}\mathrm{m^2/s}$. In the cases studied here the pits are $< 1\mu m$ deep, i.e. much smaller than the typical diffusion length scale. Also, the volume of a typical bubble is $10^5 - 10^7$ larger than the volume of the nanopits, allowing the majority of the gas to move from the pit into the bubble *. During collapse, the interaction between bubbles breaks the bubble in such a way that a large gas-vapor bubble goes away from the sample, and only a tiny fraction ($< 0.001\%$) of the initial gas remains in the pit, which therefore remains essentially full of vapor and is easily filled by the liquid. Suppose that during this filling process a tiny amount of gas remains in the pit. The contact angle being larger than $90°$ would force the meniscus to be curved towards the gas and consequently the bubble would grow by diffusion. We estimated that the waiting time in between two successive shots (in our case: 15 s) would then be enough to refill the pits completely with gas by diffusion, and a second nucleation event should then be possible. Since we never have observed a second nucleation, we conclude that the pits have to be filled with liquid completely during bubble collapse. These conclusions agree with our experimental results. In the cases A-D we observed

---

*Notice that this estimation does not take into account the confinement of the nanopits and their large aspect ratios (case D), which may lead to lower values of the diffusion coefficient.
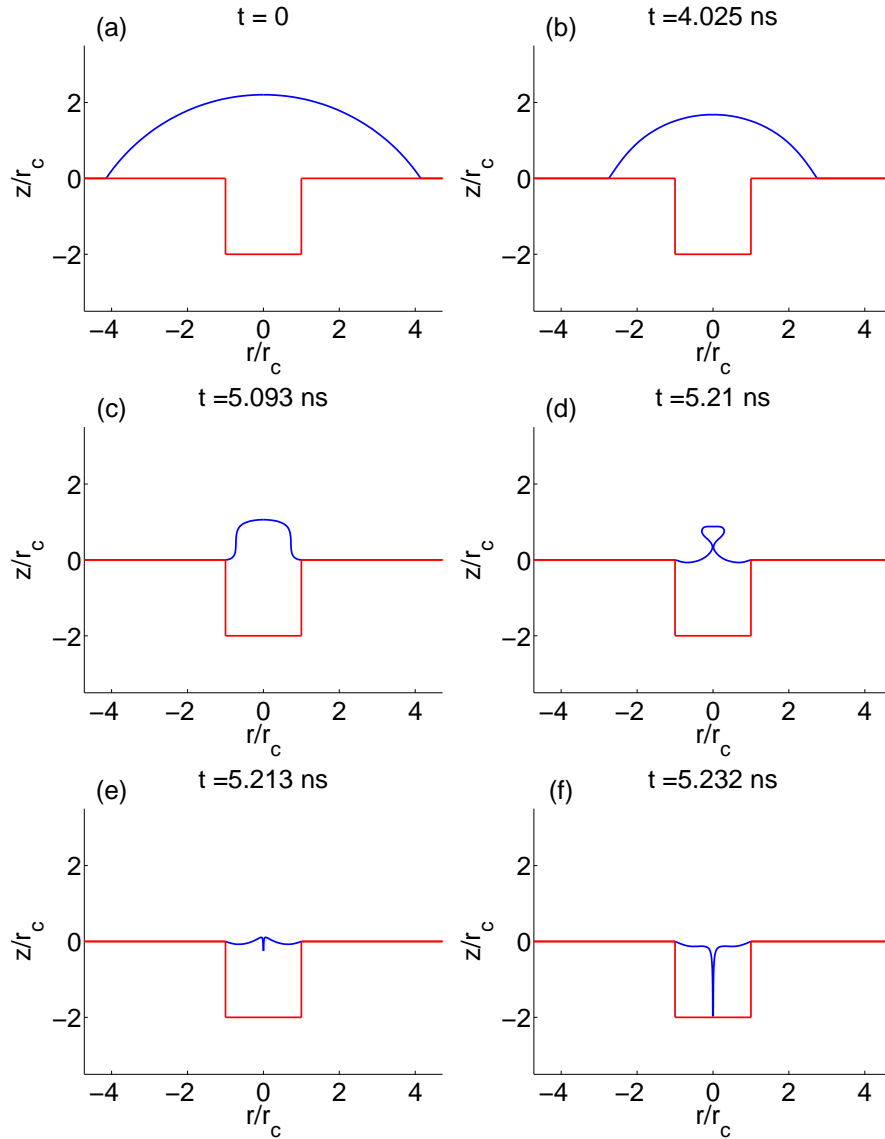
Figure 5.11: (a) Initial configuration for a spherical bubble (blue) with radius $5r_c$ on top of the cavity (red). The (advancing) contact angle is $\theta = 124°$. Due to the low pressure inside the cavity the bubble starts to collapse (b) evolving into an almost cylindrical shape (c), which eventually closes on the axis of symmetry in a single point (d). From the pinch-off location a downward jet protrudes into the cavity (e) eventually hitting the cavity bottom (f). Here it would cause a splash filling the cavity with liquid.

no differences between strong (Fig. 5.6) and weak (Figs. 5.7, 5.8 & 5.9) bubble interaction: in both situations the pits were emptied after one nucleation event, in line with the explanations provided here.

This situation can be compared with the previously mentioned continuous and long-lived emission of bubbles in carbonated beverages and the related phenomena observed with enhanced surfaces frequently used in boiling heat transfer [35, 36]. In none of these cases the bubbles collapse and therefore the primary mechanism for the filling up and consequent de-activation of the pits is present.

5.4.5   Superhydrophobic nuclei

To show the importance of the liquid jet into the pits, experiments using superhydrophobic nuclei are illustrative. Cylindrical pits, etched in Si(100) with a diameter of 4 μm, were created with a superhydrophobic bottom layer (see Fig. 5.12), consisting of hydrophobic pillars of ~ 100 nm in diameter (created through a black silicon etching process [37] and a hydrophobic fluoro-carbon top layer). The combination of hydrophobicity with roughness is known to create superhydrophobicity [38] with typical contact angles > 160º. When the bubbles were strongly interacting (leading to wall-parallel jets), we observed that the pits remained active nucleation sites even after hundreds of shots (see Fig. 5.12). On the contrary, in the case of a single bubble (wall-normal jet) we observed that the micropits were deactivated after a few nucleation events. To explain this striking difference one really has to take the direction of the liquid jet into account. Apparently, the wall-parallel jet is not able to wet the superhydrophobic bottom of the pits, while the vigorous, ultra-thin jet directed towards the superhydrophobic bottom layer presumably pushes the liquid from the dewetted into the wetted state. From other work it is indeed known that a force may be re-
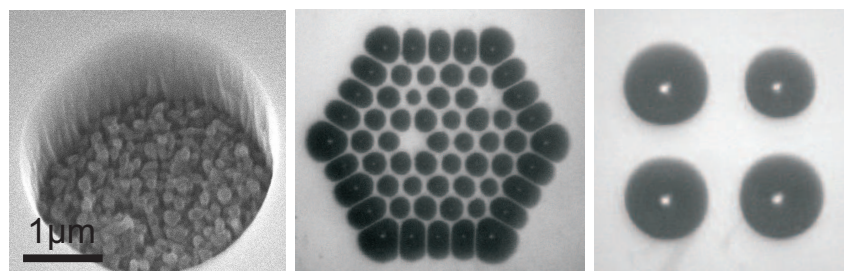
Figure 5.12: A superhydrophobic pit (left) can be nucleated hundreds of times, provided that the liquid jet in the bubble collapse phase is not directed into the pit. Center: a hexagonal pattern of superhydrophobic pits (100 μm in between the pits) after 230 nucleation events shows only 2 defects. Right: a square pattern (300 μm in between the pits) is completely intact after 100 shots.

quired to overcome the energy barrier associated with this wetting transition [39]. Once in the wetted state, the superhydrophobic pit is deactivated and cannot be nucleated again, apart of course from drying the whole sample.

5.5 Conclusion

In conclusion, Atchley & Propseretti's 1989 crevice model of cavitation nuclei is experimentally verified using nanoscopic well-defined nuclei. Advanced etching techniques allowed us to create cylindrical pits down to 50 nm in radius with high accuracy in both their size, depth and mutual position. Upon immersion in water, the hydrophobic nanopits trapped air and served as nucleation sites. Stepwise lowering of the acoustic minimum pressure allowed us to determine the nucleation threshold at which the pits start to cavitate. We found that the experimental results are in very good agreement with the theoretical predictions. This implies that in shock wave experiments the size of cavitation nuclei can be determined by measuring the pressure at which they start to nucleate, provided that either the cavity geometry is known, so that one can incorporate the effect of the expanding gas from the pit, or that the gas content of the pit can be neglected, which is roughly the case for $r_c < 200$ nm (in case $d_c = r_c$).

Cavitation nuclei were deactivated after a single nucleation event, despite differences in width, depth and aspect ratios of the pits. The two mechanisms contributing to this effect are diffusion of gas out of the pit during the lifetime of the bubble and the subsequent aspherical collapse of the bubble. Numerical simulations show that in the case of weak bubble-bubble interaction, a sharp wall-normal liquid jet is formed which hits the bottom of the cavities, thus vigorously wetting the pits. Superhydrophobic nuclei can only be wetted thanks to this wall-normal jet. For strong bubble-bubble interactions with wall-parallel jets, superhydrophobic pits remain active nucleation sites, even after hundreds of nucleation events, in contrast to standard hydrophobic pits. In systems were one wants to control the number of cavitation nuclei which do not deactivate, superhydrophobic pits may find applications.

References

[1] F. Caupin and E. Herbert, "Cavitation in water: a review", C. R. Physique **7**, 1000–1017 (2006).

[2] E. Herbert, S. Balibar, and F. Caupin, "Cavitation pressure in water", Phys. Rev. E **74**, 041603 (2006).

[3] K. A. Mørch, "Reflections on cavitation nuclei in water", Phys. Fluids **19**, 072104 (2007).

[4] E. N. Harvey, D. K. Barnes, W. D. McElroy, A. H. Whiteley, D. C. Pease, and K. W. Cooper, "Bubble formation in animals", J. Cell. Compar. Physl. **24**, 1–22 (1944).

[5] M. Strasberg, "Onset of ultrasonic cavitation in tap water", J. Acoust. Soc. Am. **31**, 163–176 (1959).

[6] R. E. Apfel, "The role of impurities in cavitation-threshold determination", J. Acoust. Soc. Am. **48**, 1179–1186 (1970).

[7] L. A. Crum, "Tensile strength of water", Nature **278**, 148–149 (1979).

[8] A. A. Atchley and A. Prosperetti, "The crevice model of bubble nucleation", J. Acoust. Soc. Am. **86**, 1065–1084 (1989).

[9] K. A. Mørch, "Cavitation nuclei and bubble formation – a dynamic liquid-solid interface problem", J. Fluids Eng. **122**, 494–498 (2000).

[10] M. Greenspan and C. E. Tschiegg, "Radiation-induced acoustic cavitation: Apparatus and some results", J. Res. Natl. Bur. Stand., Sect. C **71**, 299–312 (1967).

[11] L. J. Briggs, "Limiting negative pressure of water", J. Appl. Phys. **21**, 721 (1950).

[12] R. A. Roy, S. I. Madanshetty, and R. E. Apfel, "An acoustic backscattering technique for the detection of transient cavitation produced by microsecond pulses of ultrasound", J. Acoust. Soc. Am. **87**, 2451–2458 (1989).

[13] S. I. Madanshetty and R. E. Apfel, "Acoustic microcavitation: Enhancement and applications", J. Acoust. Soc. Am. **90**, 1508–1514 (1991).

[14] S. I. Madanshetty, R. A. Roy, and R. E. Apfel, "Acoustic microcavitation: its active and passive acoustic detection", J. Acoust. Soc. Am. **90**, 1515–1526 (1991).

[15] S. I. Madanshetty, "A conceptual modeal for acoustic microcavitation", J. Acoust. Soc. Am. **98**, 2681–2689 (1995).

[16] C. X. Deng, Q. Xu, R. E. Apfel, and C. K. Holland, "Inertial cavitation produced by pulsed ultrasound in controlled host media", J. Acoust. Soc. Am. **100**, 1199–1208 (1996).

[17] H. B. Marschall, K. A. Mørch, A. P. Keller, and M. Kjeldsen, "Cavitation inception by almost spherical solid particles in water", Phys. Fluids **15**, 545–553 (2003).

[18] B. M. Borkent, M. Arora, and C. D. Ohl, "Reproducible cavitation activity in water-particle suspensions", J. Acoust. Soc. Am. **121**, 1406–1412 (2007).

[19] N. Bremond, M. Arora, C. D. Ohl, and D. Lohse, "Cavitation on surfaces", J. Phys.: Condens. Matter **17**, S3603–S3608 (2005).

[20] N. Bremond, M. Arora, C. D. Ohl, and D. Lohse, "Controlled multibubble surface cavitation", Phys. Rev. Lett. **96**, 224501 (2006).

[21] N. Bremond, M. Arora, S. M. Dammer, and D. Lohse, "Interaction of cavitation bubbles on a wall", Phys. Fluids. **18**, 121505 (2006).

[22] B. M. Borkent, S. M. Dammer, H. Schönherr, G. J. Vancso, and D. Lohse, "Superstability of surface nanobubbles", Phys. Rev. Lett. **98**, 204502 (2007).

[23] M. A. Chappell and S. J. Paine, "The effect of cavity geometry on the nucleation of bubbles from cavities", J. Acoust. Soc. Am. **121**, 853–862 (2007).

[24] C. E. Brennen, *Cavitation and Bubble Dynamics* (Oxford University Press, New York) (1995).

[25] T. G. Leighton, *The Acoustic Bubble* (Cambridge University Press, Cambridge) (1994).

[26] J. Staudenraus and W. Eisenmenger, "Fiberoptic probe hydrophone for ultrasonic and shock-wave measurements in water", Ultrasonics **31**, 267 (1993).

[27] T. M. Mayer, M. P. de Boer, N. D. Shinn, P. J. Clews, and T. A. Michalske, "Chemical vapor deposition of fluoroalkylsilane monolayer films for adhesion control in microelectromechanical systems", J. Vac. Sci. Technol. B **18**, 2433–2440 (2000).

[28] M. S. Plesset and A. Prosperetti, "Bubble dynamics and cavitation", Annu. Rev. Fluid Mech. **9**, 145 (1977).

[29] V. K. Dhir, "Boiling heat transfer", Ann. Rev. Fluid Mech. **30**, 365–401 (1998).

[30] G. Liger-Belair, G. Polidorib, and P. Jeandeta, "Recent advances in the science of champagne bubbles", Chem. Soc. Rev. **37**, 2490–2511 (2008).

[31] T. B. Benjamin and A. T. Ellis, "The collapse of cavitation bubbles and the pressure thereby produced against solid boundaries", Philos. Trans. R. Soc. London, Ser. A **260**, 221 (1966).

[32] M. S. Plesset and R. B. Chapman, "Collapse of an initially spherical vapor cavity in the neighborhood of a solid boundary", J. Fluid Mech. **47**, 283 (1966).

[33] R. Bergmann, D. van der Meer, S. Gekle, A. van der Bos, and D. Lohse, "Controlled impact of a disc on a water surface: Cavity dynamics", J. Fluid Mech. **633**, 381–409 (2009).

[34] S. Gekle, J. M. Gordillo, D. van der Meer, and D. Lohse, "High-speed jet formation after solid object impact", Phys. Rev. Lett. **102**, 034502 (2009).

[35] A. D. Messina and E. L. Park, "Effects of precise arrays of pits on nucleate boiling", Int. J. Heat Mass Transfer **24**, 141–145 (1981).

[36] Y. Qi, J. F. Klausner, and R. Mei, "Role of surface structure in heterogeneous nucleation", Int. J. Heat Mass Transfer **47**, 3097–3107 (2004).

[37] H. Jansen, M. de Boer, R. Legtenberg, and M. Elwenspoek, "The black silicon method: a universal method for determining the parameter setting of a fluorine-based reactive ion etcher in deep silicon trench etching with profile control", J. Micromech. Microeng. **5**, 115–120 (1995).

[38] D. Quéré, "Surface chemistry - fakir droplets", Nat. Mater. **1**, 14–15 (2003).

[39] N. A. Patankar, "Transition between superhydrophobic states on rough surfaces", Langmuir **20**, 7097–7102 (2004).

6

The acceleration of solid particles subjected to cavitation nucleation[‡]

The cavity-particle dynamics at cavitation inception on the surface of spherical particles suspended in water and exposed to a strong tensile stress wave is experimentally studied with high-speed photography. Particles, which serve as nucleation sites for cavitation bubbles, are set into a fast translatory motion during the explosive growth of the cavity. They reach velocities of $\sim 40\,\mathrm{m\,s}^{-1}$ and even higher. When the volume growth of the cavity slows down, the particle detaches from the cavity through a process of neck-breaking, and the particle is shot away. The experimental observations are simulated with (i) a spherical cavity model and (ii) with an axisymmetric boundary element method (BEM). The input for both models is a pressure pulse, which is obtained from the observed radial cavity dynamics during an individual experiment. The model then allows us to calculate the resulting particle trajectory. The cavity shapes obtained from the BEM calculations compare well with the photographs until neck formation occurs. In several cases we observed inception at two or more locations on a single particle. Moreover, after collapse of the primary cavity, a second inception was often observed. Finally, an example is presented to demonstrate the potential application of the cavity-particle system as a particle cannon, e.g. in the context of drug delivery into tissue.

91

6.1   Introduction

The tensile strength of a liquid is the stress it can resist before it ruptures. For pure water, homogeneous nucleation theory predicts a threshold of $-140\,\mathrm{MPa}$ at $25\,^\circ\mathrm{C}$ before cavities form. Although this high threshold has been verified for pristine water trapped in minerals [1, 2], ultimate thresholds being a factor 10 smaller are reported even in very pure water. Harvey et al. [3] attributed the measured low tensile strength of plain water to cavitation nuclei, stabilized in crevices at solid surfaces, and Atchley & Prosperetti [4] developed a quantitative model for the bubble dynamics in crevices. Subsequent investigations [5–10] have supported the basic character of cavitation nuclei as interfacial voids, though not necessarily located at crevices. Recently Arora, Ohl & Mørch [11] documented the inception process on corrugated spherical polystyrene particles. Their high-speed photo sequences showed that when subjected to a tensile stress wave, solid particles with diameters in the $30-150\,\mu\mathrm{m}$ range nucleated cavities which grew to sizes much larger than the particles themselves. The particles were observed to move away at high speed, typically in the $10\,\mathrm{m\,s^{-1}}$ range, from the cavities they themselves nucleated. The connection between the cavity and the nucleating particle was broken within about $10\,\mu\mathrm{s}$, and thereafter the detached particle was translated independent of the cavity. Though it is well known that normal liquids contain large numbers of small particles, and that they are of importance for cavitation inception [12], the complex sequence of events at inception may explain the difficulties experienced over the years in understanding the phenomenon. The present work is motivated by the demand for a deeper analysis of this basic mechanism of cavitation inception, experimentally as well as theoretically. Arora *et al.* [11] triggered their cavitation events by the negative phase of the pressure pulse from a lithotripter, and recorded them with photographic equipment that allowed only two frames to be captured in each experimental run. Though the principal features of the process were clear, details of the dynamics were not revealed, and the theory presented requires adjustment in order to give quantitatively correct particle motion data for comparison with experiments. Such analysis may contribute to explaining, for example, the finding that particle-laden flows cause accelerated surface erosion [13, 14] at low pressure/cavitation conditions, way beyond the added effects of simple particle erosion and cavitation erosion. It has been suggested that particles are propelled towards solid surfaces by the jetting mechanism of collapsing cavitation bubbles, thus causing erosion on impact. However, experiments with particles positioned close to a spark-induced cavitation bubble showed little motion during its expansion and collapse [15]. Therefore, it is inferred that particles cannot just be propelled by cavity-induced flow onto a solid wall, such that they cause wear at collision. In contrast, we find that particle acceleration to considerable speed is achieved when cavities are nucleated and grow from the surface of particles exposed to tensile stress, thus offering a possible mechanism of wear. In the present work,

we first present the experimental set-up for initiating and recording cavitation on suspended particles. In contrast to the earlier works, we now record the dynamics with much higher temporal resolution. We have 128 consecutive frames in high-speed recordings at up to a million frames per second to study the inception in detail. Then we present characteristic examples of cavitation events on a particle, and distinguish three different dynamic regimes. Two theoretical models based on potential theory are presented, one with direct calculations of the particle. cavity interaction using the pressure gradient along the particle surface, the other using the boundary-element method. Both models are able to predict very well the phenomena observed in the experiments.

6.2 Experimental setup

The experimental setup is shown in Fig. 6.1. Dry polystyrene particles (polystyrene-2% divinylbenzene, with a diameter distribution $30 - 150\,\mu m$ and of density $\rho_p = 1.05 \times 10^3\,kg\,m^{-3}$) of spherical shape and with nano-scale surface roughness [10, 11, 16, 17] were suspended in partly degassed water from a Milli-Q waterpurification system, contained in a sterile flask (75 ml Nunc EasyFlask, Nunclon). The closed flask, containing $\sim 1 \times 10^4$ particles, was submerged into a basin with approximately 50 l of de-mineralized water. A waterproof magnetic stirrer (Telemodul 90407, Variomag) drove a glass-encapsulated magnet within the flask to prevent sedimentation of the particles. In the selection of particles, we noticed that their size matters. Spherical polyamide particles of a density the same as the polystyrene particles, but of a diameter of only $20\,\mu m$, could not be propelled away by cavitation nucleation. We argue that this is an effect of their limited size, causing drag to dominate. In addition, the pressure drop across their surface is relatively small and the particles are not able to acquire enough momentum. Heterogeneous cavitation on the particles was excited with a focused wave from a slightly modified commercial shock-wave lithotripter (Piezolith 3000, Richard-Wolf GmbH, Knittlingen, Germany). The transducer consisted of two active layers, each with hundreds of piezoelectric ceramics arranged in a hexagonal pattern and wired in parallel, on the front and back sides, respectively, of a spherically shaped shell. The clinical device has a fixed delay between the two layers, which ensures that the pressure waves emitted from both layers superimpose constructively. However, in our setup we could control both layers individually in time and driving voltage. If not mentioned otherwise, only the frontal transducer was operated, and at a discharge voltage of 5 kV. The transducer had a diameter of 251 mm and an opening angle of 94°. In Fig. 6.2, a typical pressure recording is shown, as obtained with a calibrated glass fibre hydrophone (FOPH-500, RP Acoustics). It was positioned inside the flask, close to the acoustic focus, which was marked with two crossed beams from laser diodes. The Milli-Q water in the flask did not con-

tain particles and it therefore showed low cavitation activity. The travelling time of the pressure wave from the surface of the frontal transducer to the acoustic focus was $\sim 136\,\mu s$ which was important for the time-delay used for the flashlight and camera. The wave path via the closest reflecting object (the wall of the flask) to the acoustic focus corresponded to a delay of $\sim 7\,\mu s$, but as any tensile stress pulse, that was strong enough to cause cavitation served our purpose, reflections were in principle without importance. In the recorded lithotripter pulse (Fig. 6.2) the pressure first rose to a positive peak pressure of about $10\,MPa$, and then it dropped to $-6\,MPa$. The pressure varied strongly with the spatial position owing to the narrow focal width, being only $1.8\,mm$ at half of the maximum pressure amplitude. The period of tensile stress was responsible for the creation of cavitation bubbles when the particles were seeded into the water. In experiments with particles, the local pressure at the focal region differs from that shown in Fig. 6.2 owing to the expansion and collapse of neighbouring cavities. A shortening of the tensile stress pulse occurs at high cavitation activity when many cavities form [18–20]. Additionally, when cavitation sets in, the pressure measurements obtained with a fibreoptic hydrophone vary considerably from shot to shot owing to the statistical nature of the bubble dynamics in the whole cavitation zone. Zijlstra & Ohl [21] found that the pressure fluctuations are real, and caused by acoustic transients emitted from nearby cavitation bubbles. Owing to the statistical nature of the local pressure during cavitation, only a typical pressure pulse measurement in a non-cavitating liquid (i.e. without particles) is presented. It was impossible to record the pressure at exactly the position of the particle being observed to cavitate, as all the particles were moving freely, and we had no control over their positions or of which ones would cause cavitation in the experiment. Even if we did try, we had measured at best a pressure that was not necessarily the far-field pressure in a 'Rayleigh sense', but just a local pressure. Further, the probe itself would have disturbed the event being studied. Thus, we could not expect that a measured pressure would be representative of the observed bubble expansion. Instead we have used the observed cavity dynamics as our local pressure probe. It is this dynamics that governs the specific particle motion being recorded in the experiment, and which we aim to calculate. This is probably the only way to obtain the 'far-field pressure' of an observed cavity. The technique is applicable only with a sufficiently high resolution both in time and space. Microscopic imaging of particles and cavitation bubbles from a distance of $40\,mm$ was done with a long-working-distance objective (K2, C4 objective, Infinity, USA) illuminated with a continuous light source from behind. For recording of the fast dynamics with a sufficient number of frames, we used the rotating mirror camera Brandaris-128 equipped with 128 light-sensitive image sensors which were read out digitally [22]. Although the camera can be operated with up to 25 million frames per second we used up to $10^6\,\text{frames s}^{-1}$ only, to gain longer recording times. After each experiment, the images were transferred to a computer and corrected for slight

misalignments of the individual sensors, using digital image-processing routines. Finally, a movie with 128 frames, each of 475×346 pixels and with a resolution of $5.7\,\mu\text{m}\,\text{pixel}^{-1}$, was stored. In the experimental procedure, the camera was operated as the master device, which triggered the shock-wave generator $136\,\mu\text{s}$ before the first frame of the sequence was to be recorded. Within this time interval the pressure wave travelled from the surface of the transducer to the centre of the flask. Not every experimental run led to a movie with particles in focus because the particles were randomly mixed in the flask. By adjusting the particle concentration, we obtained one or more particles imaged in focus in about a third of the experiments. Altogether, 51 recordings with a single pressure pulse and 105 recordings with two shock waves at different delay settings were found to be suited for further analysis. Because the particle motion is not limited to the image plane, the measured positions are only projections onto the image plane, and thus the experimentally determined velocities are lower bounds. Yet, the focal depth of the long-distance microscope of $\sim 50\,\mu\text{m}$ causes a blurring of particles leaving the focal plane. The typical travel distance of particles being imaged in focus during their entire motion is $300\,\mu\text{m} - 400\,\mu\text{m}$, and thus much larger than the focal depth. In two of the three cases presented in this chapter, we can consider the motion to be fairly close to the image plane. Finally, the sizes of the objects of interest (the particle and the cavity) are determined as follows. The contour of the object of interest is identified manually with 5 points. Through these points a circular fit is calculated, giving the corresponding area and hence the radius of the object. Comparing the calculated size of the particle in all the frames, which should be constant, we find that the absolute error in the experimental data is less than $3\,\mu\text{m}$.

6.3 Experimental observations

A typical and instructive recording that shows cavitation inception on a particle of radius $R_p = 68\,\mu\text{m}$ is presented in Fig. 6.3. In the first frame, the tensile stress pulse has arrived, and from time $t = 1.0\,\mu\text{s}$ to $t = 2.9\,\mu\text{s}$ a cavity grows from a point on the particle surface with a radial expansion velocity of about $70\,\text{m}\,\text{s}^{-1}$. Its radius reaches a maximum of $203\,\mu\text{m}$ and it becomes approximately spherical, but it only partly entrains the particle. In the following frames the remarkable dynamics is revealed ($t = 2.9 - 10.8\,\mu\text{s}$): the particle moves away from the cavity wall, shaping first a neck which connects it to the cavity, but eventually the neck breaks. The particle velocity, v_p, comes up to a maximum of $37\,\text{m}\,\text{s}^{-1}$ at $t = 2.9\,\mu\text{s}$, and then drops to $15\,\text{m}\,\text{s}^{-1}$ at $t = 10.8\,\mu\text{s}$. From this time, the particle moves along independently, completely free of the cavity, which shrinks and reaches a minimum size at $t = 19.6\,\mu\text{s}$ (not shown). Then the cavity re-expands while its centre moves slightly in the direction opposite that of the particle, and it develops a protrusion directed away from the particle. Most
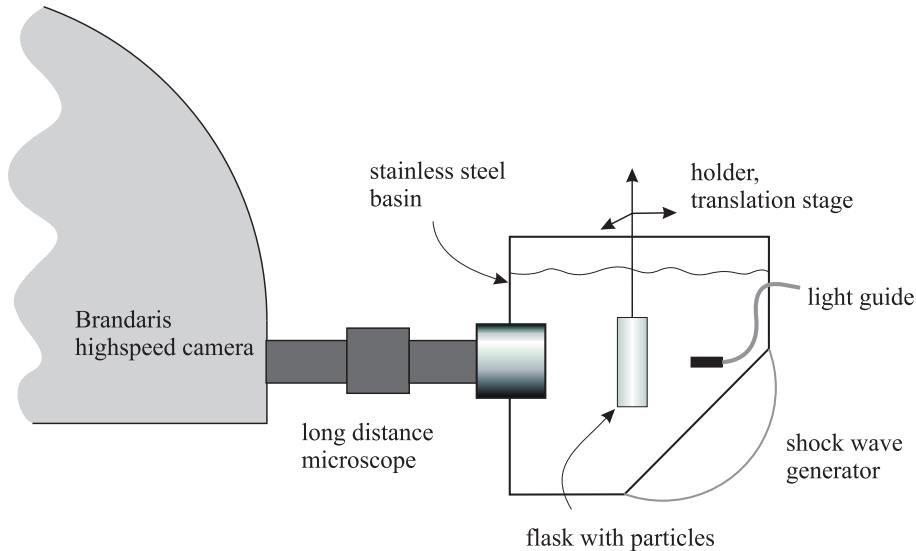
Figure 6.1: Sketch of the experimental setup. The particles are suspended in a flask which can be positioned in the water basin with a three-axis translation stage. The pressure wave is generated with the shock wave generator from a commercial lithotripter. A light guide serves as back illumination for the high-speed camera, which is connected to a long distance microscope observing the particles. The thickness of the flask is 20 mm and the distance between the glass surface protecting the long distance microscope and the flask is ~ 30 mm. The water level is about 100 mm above the acoustic focus.

probably, the protrusion is caused by a liquid jet flow through the centre of the cavity, deforming the opposite cavity surface on impact. From $t = 22.5\,\mu s$ to $34.3\,\mu s$ a new attached cavity grows on the downstream side of the particle. This is primarily interesting from an inception point of view because in our experiments the first and primary cavity develops from a nucleus of strongly negative critical pressure (-2 to -3 MPa), while the secondary cavity develops unexpectedly, and at a pressure close to zero. We can separate the dynamics depicted in Fig. 6.3 into three regimes.

(i) Explosive bubble growth on the particle ($t = 0 - 4.9\,\mu s$).

(ii) Neck formation and detachment of the particle ($t = 4.9 - 10.8\,\mu s$).

(iii) Collapse and re-expansion of the cavity, and growth of a secondary attached cavity from the particle.

The ejection of the particle from the cavity is due to momentum being imparted to it by the pressure drop that arises across it when a sufficient tensile stress in the liquid causes cavitation inception at the particle surface. The surface area of the particle in contact with the cavity then experiences the vapour pressure, while at inception
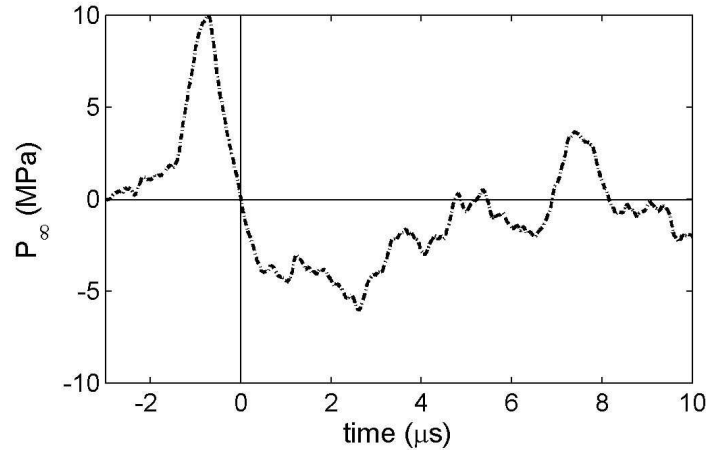
Figure 6.2: Typical pressure profile in water without particles seeded into the liquid, measured in a single experiment as a function of time. The measured negative part lasts roughly 5 µs and reaches a value of about −6 MPa. When particles are present cavitation occurs during the negative part of the pressure pulse, i.e. for t > 0, and it affects the pulse shape. A pressure profile with a longer temporal duration of 40 µs is presented in [11].

and just after inception the opposite side is exposed to a pressure governed by the tensile stress of the lithotripter pulse. Hence the particle is accelerated away from the position of cavity nucleation. When the tensile stress in the pulse relaxes and the pressure becomes positive, the cavity growth decelerates, and eventually the cavity shrinks and collapses. In contrast, the particle continues to move with the velocity gained, it separates from the cavity, and moves on until viscous forces stop its motion.

6.3.1 Single and multiple cavity events

In 40 of the 51 recordings with a single pressure pulse, the growth of a single cavity on the particle is observed. In the remaining 11 experiments, we find two or more cavities growing explosively from a single particle. Figure 6.4 depicts such a case of multiple cavitation inception occurring on two particles in the field of view during the initial 8 µs. On inspection of the images, four exploding cavitation bubbles can be distinguished on the lower right particle in Fig. 6.4 at 8.2 µs. The liquid space separating the two uppermost cavities on this particle remains visible until t = 4.1 µs. At t = 5.1 µs, it disappears, but at its former position a swelling of the merging cavity surfaces starts, and in the successive frames a bulge grows. The arrows in Fig. 6.4
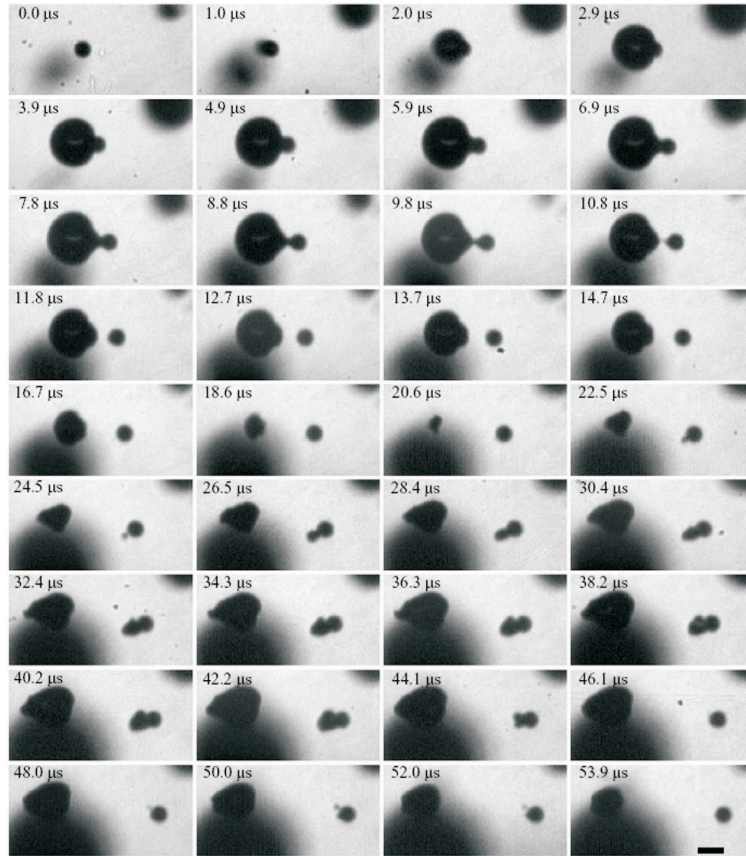
Figure 6.3: Example of a cavitation event on a particle and the successive dynamics. In the first frame, t = 0, an isolated particle is visible. A cavitation bubble expanding on the left-hand side of the particle becomes visible at t = 1 μs and grows explosively. As the growth decelerates (t = 4.9 μs), the particle moves away from the cavity and forms a neck which breaks around t = 10.8 μs. During the detachment process, the cavity develops a mushroom shape, and collapses between t = 18.6 μs and t = 20.6 μs. Moreover, the volume center of the cavity shifts slightly to the left. The re-expanding cavity obtains a funnel-like shape, which indicates that a liquid jet has developed during the cavity collapse. A secondary attached cavity on the particle becomes visible at t = 20.6 μs and grows in the following frames into a void of size comparable to that of the particle. The black bar in the last frame has a length of 200 μm. Two additional out-of-focus cavitation events are recorded in this series, too. They are visible as blurred shadows, one in the upper right-hand corner and the other as a dark fuzzy object just below the in-focus cavity.
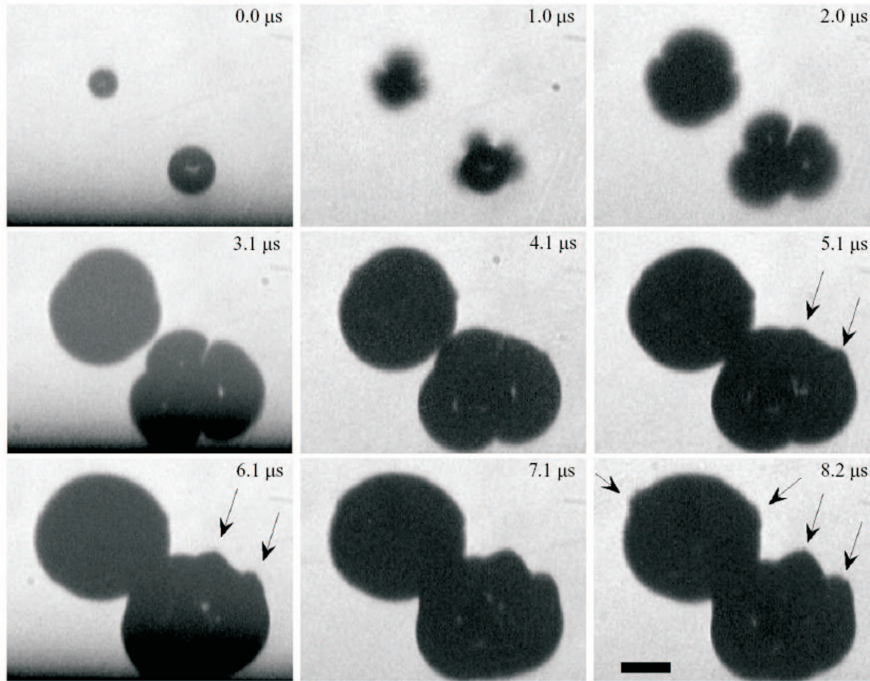
Figure 6.4: Multiple cavitation inception sites are found on particles in about 20% of the experimental runs. Here, two particles which both show multiple cavity growth on their surface are depicted. When the cavities merge (between 4.1 μs and 5.1 μs) swelling of the gas-liquid interface occurs, which is indicated with arrows. The scale bar in the last frame is 200 μm in length.

point at former liquid films between cavities, which have transformed into swelling interfaces. The upper left particle in Fig. 6.4 also seems to develop four cavities at t = 1.0 μs. The three lower ones merge without the process being visible, while the upper one clearly merges with the lower ones at t = 4.1 μs. From the geometry it seems that after the merging, the bulge is located circumferentially. Thus, the two bulges marked with the uppermost arrows in Fig. 6.4 result from the merging of a cavity with a system of neighbouring cavities. The swelling of an interface has been reported as an indication for coalescence in experiments by Lal & Menon [23], and in numerical simulations by Rungsiyaphornrat *et al.* [24].

6.3.2   Non-depletion of cavitation nuclei

Can cavitation bubbles be nucleated multiple times from the same particle? Though the depletion of cavitation activity has been observed by Borkent *et al.* [16] (see also Chapter 7), where they show that cavitation nuclei become finally used up when repetitive pulses are applied, this does not necessarily mean that particles cannot nucleate multiple times. To test this experimentally we exposed particles to two successive shock waves within a sufficiently short interval of time. We found that a time interval of $200\,\mu$s allowed the cavitation dynamics from the first tensile wave to cease, so that no visible cavities remained. Yet, particles accelerated by cavitation inception at the first wave had still not left the field of view. The design of the shock wave source allowed both piezoelectric layers to be triggered independently. Here, the frontal layer was used for the first shock wave, and the back layer for the second. When the camera was operated at framing rates below $0.30 \times 10^6\,\mathrm{frames\,s^{-1}}$ the cavitation dynamics from both shock waves could be captured in a single recording. From a total number of 92 recordings showing cavitation activity on a particle at exposure to the first shock wave, 23 recordings revealed cavitation activity again on the same particle after the second shock-wave exposure. Thirty-four recordings showed no second cavitation event on the particle, whereas in the remaining cases it was impossible to see what happened, owing to particles moving out of the screen, motion blurring, or cavitation bubbles that were too large. An example of two-fold cavitation activity on the same particle is depicted in Fig. 6.5 where the camera was operated at a framing rate of $0.28 \times 10^6\,\mathrm{frames\,s^{-1}}$. Close to $\mathrm{t} = 0.0\,\mu$s the negative part of the shock wave impacts the particle imaged in focus, and makes a cavity grow on its surface. At $\mathrm{t} = 7.4\,\mu$s, the particle splits from the cavitation bubble, leaving a short neck, and the particle moves upward with a small tilt to the left. During the detachment process, an elongated attached cavity develops, and it collapses around $\mathrm{t} = 44\,\mu$s, approximately concurrently with the main cavitation bubble. Around $152\,\mu$s later ($\mathrm{t} = 196.3\,\mu$s), the slowed down particle is imaged at the upper central part of the frame just prior to excitation with the second shock wave. At $\mathrm{t} = 200\,\mu$s, a second cavitation bubble is in development on the particle and causes it to move, at this time to the left. This demonstrates that a particle can serve multiple times as a cavitation nucleus. When at the first cavitation event the particle separates from the cavity and the neck gently closes, a cavitation nucleus may be left on its surface. Such a nucleus explains that in a number of cases a secondary attached cavity is observed to develop on the particle surface at low tensile stress, and it may form the site of inception when the next lithotripter pulse arrives, the direction of cavity growth being dependent on a possible particle rotation. However, even in the absence of such a nucleus, there may still be gaseous voids left on the particle surface which did not reach critical size when exposed to the first tensile pulse. The second pulse is weaker than the first as it is emitted from the back layer of the lithotripter, but the tensile stress field it sets

up also depends on the cluster formation, and it may still be strong enough to cause a second primary cavitation event from the same particle within the short time allowed between the pulses. It should be noticed that the different directions of particle motion at exposure to successive waves emphasize that the motion is independent of the path of the acoustic wave, and is determined by the random position of nuclei on the particle. Further, we find that a stronger cavitation activity is set up by the second shock wave, e.g. the frame at t = 229.6 μs (Fig. 6.5) is to a large extent covered by bubbles. The large number of cavities in the bulk of the water at the top and bottom of the frame at t = 200 μs is most probably caused by gas nuclei produced at disintegration of the first cavitation bubbles at their collapse. During cavity expansion, more gas diffuses into the bubble than is transported back into the liquid during its collapse. Thereby, a cavity leaves one or more gaseous nuclei. We can estimate the amount of gas collected in a cavity during a lifetime of ~ 40 μs to be 1.1×10^{-12} g, assuming that the cavity reaches a maximum radius of 200 μm in air-saturated water. It is equivalent to a gas bubble of 6 μm equilibrium radius. For the derivation of the gas-uptake equation, see the Appendix of Arora, Junge & Ohl [25]. An air bubble of radius 6 μm dissolves within approximately 1.2 s in gas-saturated water; see for example [26–28]. However, the cavitation bubble may fragment at collapse [29], which reduces the time of dissolution. From the frame at t = 200 μs, we can coarsely estimate the number of visible fragments to be about 50, which have survived the time interval of 156 μs between the first cavity collapse and the arrival of the second tensile stress wave. During this time, only gas bubble nuclei of radius up to 0.15 μm go into solution, whereas the surviving nuclei have a mean volume corresponding to radii of about 1.7 μm. Thus, with the second wave, gas bubbles originally below the imaging resolution can be made visible.

6.4 Potential flow models

6.4.1 Introduction and comparison of the two models

The growth of a supercritical cavitation bubble on a planar wall is essentially hemispherical, and is modelled well by potential flow theory [30, 31]. The wall acts as a mirror and thus the situation is equivalent to that of a spherically symmetric cavity. During supercritical expansion, surface tension and compressibility of water, as well as viscous effects, can be ignored. Following the same philosophy, the flow field around a cavity expanding from a particle can be modelled as a potential flow. Within the first (crucial) microsecond after nucleation, the cavity has already developed beyond supercritical size, but it is still small compared to the size of the particle and it grows hemispherically. Later on, the cavity becomes much larger than the particle, and it approaches a spherical shape. Hence, with the cavity following spherical bubble dynamics, potential theory can be used throughout the whole growth
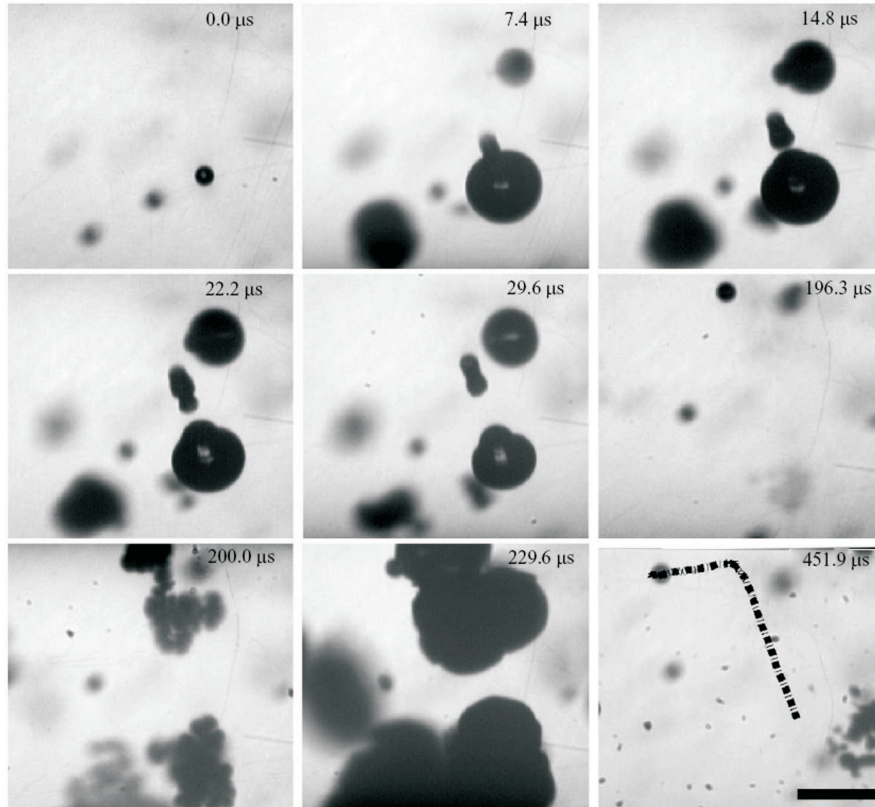
Figure 6.5: Experiment demonstrating that a particle being exposed twice to a shock wave can nucleate a cavitation bubble on its surface in both events. Here, a tensile stress wave excites cavitation at t = 0 and at t = 200 μs. The trajectory of the particle is indicated in the last frame (t = 451 μs) with the dashed black line. Note the different directions of motion induced at the successive cavitation events. The scale bar in the last frame is 500 μm in length. The lithotripter pulse motion is downwards in a direction 45° out of the photo-plane.

process. Based on the same potential flow principles, two models of increasing complexity will now be presented. Potential theory is described by Laplace's equation, $\nabla^2\Phi = 0$, where Φ is the velocity potential. In Model 1, the initial cavity considered (the cavitation nucleus) is already larger than the critical cavity, and it is assumed to be a small spherical vapour void with its centre attached to the particle, such that it resembles a hemispherical cavity. At exposure to a tensile stress pulse, it expands radially from its location of nucleation, while remaining in contact with the particle (unless it grows to swallow it). As it grows beyond the size of the particle, it embraces it more or less. A semi-analytical expression of the particle motion is derived.

Model 2 uses the axisymmetric formulation of the boundary-integral method and thus accounts for the strong deformation of the bubble observed in the experiments. For ease of calculation, the cavitation nucleus is here assumed to be a spherical cavity of radius as in Model 1, positioned in very close proximity to the particle surface. The basic equations that the two models have in common are given below. In both models the local pressure, $p(\mathbf{x}, t)$, can be calculated with the unsteady Bernoulli equation, i.e.

$$\rho \frac{\partial \Phi(\mathbf{x}, t)}{\partial t} + \frac{1}{2}\rho |\mathbf{u}(\mathbf{x}, t)|^2 + p(\mathbf{x}, t) = p_\infty(t) \quad . \tag{6.1}$$

Here, $\mathbf{u}$ is the local fluid velocity, $\mathbf{u} = \nabla \Phi$, $\mathbf{x}$ is the position vector, t is time, and ρ is the liquid density. The pressure on the right-hand side of Eq. 6.1, $p_\infty(t)$, is set up by the applied pressure pulse and is a function of time only, not of space. Owing to the very short time scales considered, the effect of gravity can be neglected in Eq. 6.1. At the end of this section, it is explained how $p_\infty(t)$ was extracted from the experimental data. In Model 2, Eq. 6.1 is used to calculate the pressure distribution on the wetted surface of the particle. The non-wetted part is subjected to the pressure inside the cavity, p_c, but as this pressure as well as the surface tension σ are significant only until just after the critical conditions for the equilibrium cavitation nucleus are exceeded [32], they are of no importance for the particle acceleration, and they are neglected, thus $p_c = 0$ and $\sigma = 0$. The force balance of the particle is obtained by integrating the pressure distribution on the particle surface, and by applying Newton's second law:

$$\mathbf{F} = \int_S p\mathbf{n}dS = m_p \mathbf{a}_p \quad , \tag{6.2}$$

where S is the surface of the particle, $\mathbf{a}_p$ its acceleration, and $m_p = 4\pi R_p^3 \rho_p / 3$ its mass. Note that there is no need to account for the added mass, since this effect is automatically incorporated in the surface integral of Eq. 6.2 (see Lamb [33], pp. 160). In Eq. 6.2, $\mathbf{n}$ represents the normal vector at the particle surface. The effect of viscous drag on the particle can be included by addition of an effective drag force to (2). During cavity growth, drag is assumed to be negligible as compared to the strong acceleration force, but for the particle motion after cavity-particle detachment it is important, and it is included, see § 6.4.4 for a detailed discussion. Provided only a single cavity is nucleated, the problem can be considered as axisymmetric. The velocity $\mathbf{u}_p$ and position $\mathbf{x}_p$ of the particle follows from the acceleration $\mathbf{a}_p$ by integration. At the moment the cavity first appears, $\mathbf{x}_p$ and $\mathbf{u}_p$ are zero. We define this time as $t = 0$, and proceed stepwise by applying the changing far field pressure and the corresponding cavity governed velocity parameters to (1) to determine $p(\mathbf{x}, t)$, which is used in Model 1 (the spherical bubble model, described in § 6.4.2) as well as in Model 2 (BEM, see § 6.4.3). Then we calculate the force on the particle and its acceleration from Eq. 6.2, and derive its velocity and displacement by

integration. Note that in Gracewski, Miao & Dalecki [34] comparable models are used to describe bubble-particle interaction. However, in their work, the particle is fixed and of comparable or larger size than the cavities. At first, it seemed reasonable to use the pressure profile measured without particles, i.e. the profile depicted in Fig. 6.2, as $p_\infty(t)$. However, when doing so the maximum cavity radii obtained were much larger than those observed in the experiments. The explanation of this observation is that neighbouring cavities alter the local pressure around a cavity (see for example [21, 35]). Unfortunately, the local pressure cannot be measured directly, as described in § 6.2. How do we then obtain the pressure profile that leads to the cavity dynamics we observe experimentally? We obtain it from the observed dynamics of the cavity radius $R_c(t)$, i.e. we employ the bubble as a local pressure sensor. Particle-generated cavities grow almost spherically in the half-space of liquid which does not include the particle, and the momentary radius of a given cavity is determined from this part of the cavity. Now we can estimate the far-field pressure $p_\infty(t)$ which the cavity has experienced from the Rayleigh-Plesset equation [36]

$$\frac{-p_\infty(t) + p_c}{\rho} = \frac{3}{2}\left(\frac{dR_c}{dt}\right)^2 + R_c\frac{d^2R_c}{dt^2} \quad . \tag{6.3}$$

The pressure p_c inside the explosively expanding cavity is essentially the vapour pressure, which is small compared to the magnitude of $p_\infty(t)$. Thus we again set $p_c = 0$. A smooth representation of the bubble radii which is required for the temporal derivatives, is obtained by spline interpolation of the measured cavity radius-time traces. After differentiating them twice, the pressure $p_\infty(t)$ can be calculated from Eq. 6.3.

6.4.2   Model 1: spherical bubble model

In Model 1, we start from an initial spherical cavitation nucleus of radius $R_{c,0} = 1\,\mu m$, with its centre on the particle surface, and let it expand spherically, i.e. the distortion from sphericity observed in the experiments is neglected. The initial centre of the cavity is assumed to be stationary. This can be justified at least for the cavity expansion phase, in which its added mass increases rapidly. Thus, we assume a velocity potential as for a spherical cavity undergoing radial expansion

$$\Phi = -\frac{R_c^2}{r}\frac{dR_c}{dt} \quad . \tag{6.4}$$

The radial velocity at position r from the cavity centre is given by

$$|\mathbf{u}| = \frac{R_c^2}{r^2}\frac{dR_c}{dt} \quad . \tag{6.5}$$
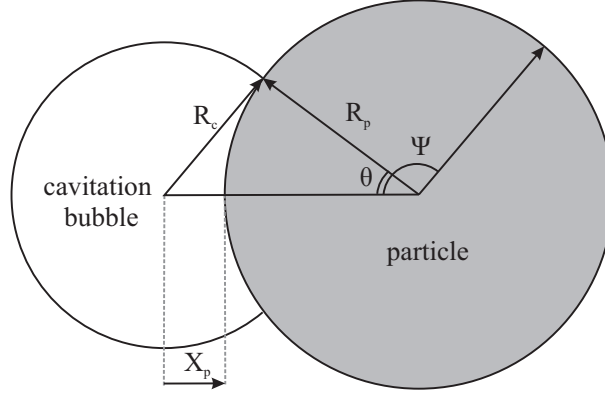
Figure 6.6: Sketch of the geometry for Model 1: a spherical cavitation bubble growing on a particle. The angle θ separates the non-wetted and wetted surface areas, and ψ identifies positions on the wetted surface. The coordinate of the particle displacement is X_p.

Here, r is the radial distance measured from the stationary centre of the cavity. Using Eq. 6.1 and Eq. 6.3, the pressure $p_\infty(t)$ can be eliminated. Now the local pressure $p(r, t)$ anywhere in the liquid is expressed in terms of the cavity radius and its temporal derivatives by

$$p(r, t) = \left(2 \left(\frac{dR_c}{dt} \right)^2 + R_c \frac{d^2 R_c}{dt^2} \right) \left(\left(\frac{R_c}{r} \right) - 1 \right) - \frac{1}{2} \left(\frac{dR_c}{dt} \right)^2 \left(\left(\frac{R_c}{r} \right)^4 - 1 \right) .$$

(6.6)

In Eq. 6.6, the pressure becomes 0 when r approaches R_c, and $p_\infty(t)$ when r goes to infinity. To evaluate the force integral in Eq. 6.2, the pressure on the surface of the particle has to be described. The part of it covered by the cavity ($\phi < \theta$, see Fig. 6.6) is subjected to the pressure $p_c \approx 0$, while the pressure distribution acting on the remaining wetted particle surface area ($\theta < \phi < \pi$) is approximated by the pressure field of Eq. 6.6. For calculations of the particle motion, the values of R_c and its derivatives are used, as obtained from the experimentally observed cavity radii after they are processed with the spline interpolation mentioned in § 6.4.1. Equations 6.2-6.6 for Model 1 are solved numerically to determine the particle motion. This scheme is followed until cavity collapse; thereafter the particle motion is supposed to be influenced only by viscous drag, see § 6.4.4.

6.4.3   Model 2: axisymmetric boundary-element method (BEM)

Model 2 is able to describe the deformation of the cavity during its expansion. The pressure p on the particle described by the unsteady Bernoulli equation, Eq. 6.1, is written for convenience in terms of the material derivative using $\mathbf{u} \cdot \nabla \Phi = \mathbf{u} \cdot \mathbf{u}$, thus

$$p(\mathbf{x},t) = p_\infty(t) - \rho \frac{D\Phi(\mathbf{x},t)}{Dt} + \frac{1}{2}\rho|\mathbf{u}(\mathbf{x},t)|^2 \quad . \tag{6.7}$$

This notation allows for a simpler implementation of the algorithm to obtain the potentials on the cavity surface from the previous time steps. The pressure $p_\infty(t)$ in Eq. 6.7 is calculated from the experimental cavity radius as mentioned in § 6.4.1. We note that although the bubble dynamics is modelled axisymmetrically, the driving pressure $p_\infty(t)$ is derived from a spherically expanding bubble model. The validity of this approach is outlined in the Appendix. An elegant method for solving potential flow problems is the boundary-element method (BEM). It makes use of the fact that when either the potentials or their normal derivatives (the normal velocity in this case) are known on all boundaries of the problem at a given time, the whole flow field is determined. It has the further advantage that only boundary elements, here the moving particle and the growing cavity, need to be specified. Thus, there is no need to create a mesh for the whole fluid domain. For the problem under consideration, the following BEM-equation (see for example [37]) is used:

$$c(\mathbf{x}_0)\Phi(\mathbf{x}_0) + \int_{S+C} \Phi(\mathbf{x}) \frac{\partial G(\mathbf{x}_0,\mathbf{x})}{\partial n} dS = \int_{S+C} G(\mathbf{x}_0,\mathbf{x}) \frac{\partial \Phi(\mathbf{x})}{\partial n} dS \quad . \tag{6.8}$$

Here, $\mathbf{x}_0$ points to a node describing either the cavity or the particle surface. The variable $c(\mathbf{x}_0)$ is the solid angle, G is the Green function, and $\partial/\partial n = \mathbf{n} \cdot \nabla$. The integration in Eq. 6.8 must be done on both objects, the cavity surface 'C' and the particle surface 'S'. At every new time step, the potential is updated on the cavity surface 'C' with the rephrased Bernoulli equation Eq. 6.1

$$\rho \frac{D\Phi}{Dt} = \frac{1}{2}\rho|\mathbf{u}|^2 + p_\infty(t) \quad . \tag{6.9}$$

Again, we assume the pressure inside the cavity to be $p_c = 0$, see § 6.4.2. The normal derivative of the potential, i.e. the normal velocity, on the particle is obtained through:

$$\frac{\partial \Phi}{\partial n} = \mathbf{n} \cdot \mathbf{u}_p \quad . \tag{6.10}$$

Still the potential on the particle surface and the normal velocity on the cavity have to be determined. The numerical scheme divides the cavity and particle surfaces into linear elements connected by nodes (51 nodes on the cavity and 51 nodes on the particle). The nodes are distributed equidistantly on the surface of the bubble and the

particle. Following the standard procedure in BEM Eq. 6.8 is rewritten into a matrix equation relating the potential and its normal derivative at each node to all other ones (see [38] for more details). The matrix equation is solved for $\partial\Phi/\partial n$ on the cavity and Φ on the particle. This method is described in more detail in [24, 39, 40]. With Eq. 6.7, the pressure on the surface of the particle can be calculated, while Eq. 6.2 gives the force. The velocity and the position of the particle are then obtained by integration. Finally, the cavity surface position is obtained from $\partial\Phi/\partial n$ In order to prevent unphysical behaviour and numerical instabilities, the minimum distance between the cavity-nodes and the particle-nodes is limited to the inter-node distance on the particle surface. When this happens, the pressure on the particle is set to $p = p_c = 0$ for the evaluation of the force with Eq. 6.2. The initial cavity is taken to be a full sphere of radius $R_{c,0} = 1\,\mu m$ (corresponding roughly to the inter-node distance on the particle). The sensitivity to the choice of $R_{c,0}$ has been tested and even a value of $R_{c,0} = 10\,\mu m$ gives results that differ by less than a few per cent. In the calculations, we use the initial expansion rate $dR_c/dt = 0$ and $p_\infty(t) = 0$. Although these initial conditions are a simplified version of the physics involved, they do not influence the numerical results for the experimental conditions, see § 6.5.1.

6.4.4 Viscous effects

The drag force has been neglected during the first stages of particle acceleration because the pressure force acting on the particle is much larger. However, as the particle moves away from the bubble, viscous forces slow down the particle and eventually it comes at rest. Usually, viscous effects are taken into account by introducing the drag force and the Basset history force [41]. The latter is neglected for simplicity. The former is written as:

$$\mathbf{F}_d = \frac{1}{2}\rho\pi R_p{}^2 C_d(Re)|\mathbf{u}_p - \mathbf{u}|(\mathbf{u}_p - \mathbf{u}) \quad, \tag{6.11}$$

where $C_d(Re)$ is the Reynolds number dependent drag coefficient. The Reynolds number is based on the particle diameter and the relative velocity, $\mathbf{u}_p - \mathbf{u}$. The drag coefficient C_d is approximated [41] by the following expressions

$$Cd = \frac{24}{Re}(1 + 0.15 \times Re^{0.687}) \quad, 200 < Re < 800, \tag{6.12}$$

$$Cd = 0.44, Re > 800 \quad. \tag{6.13}$$

After the particle has been ejected from the bubble, the Reynolds number reaches values of 2000 to 5000 for the three cases studied in §§ 6.5.2–6.5.4. To account for viscous drag after the detachment of the particle from the cavity surface, Eq. 6.2 is replaced by

$$\mathbf{F} = \int_S p\mathbf{n}dS - \mathbf{F}_d = m_p\mathbf{a}_p \quad . \tag{6.14}$$

6.5   Comparison of experiments with simulations

6.5.1   Preliminary remarks

We have compared the observed particle motion in three cavitation experiments with simulated particle motions based on the two models presented above. As explained in § 6.4.1, the pressure that drives the cavity dynamics and the particle motion can be evaluated only from the experimental radius vs. time curve of the cavity, because more direct local pressure measurements are not possible, and thus the evaluation of $p_\infty(t)$ is based on the idealized conditions of the Rayleigh.Plesset equation. The three measured cavity radii (the cavity remains almost spherical outside the region with the particle) are shown in Fig. 6.7. The last frame without a visible cavity is used as the starting point $t = 0$ for the simulations of $p_\infty(t)$, and the initial position of the point on the particle surface from which the cavity develops is taken as $x_p = 0$, see Fig. 6.6. The pressure profiles $p_\infty(t)$ calculated from the $R_c(t)$ curves are shown in Fig. 6.8. We notice that all cases show $dp/dt = 0$ at $t = 0$, which misrepresents what actually happens during the inception period. However, it is a consequence of the initial boundary conditions for the spline interpolation which are chosen to be $dR/dt = 0$ at $t = 0$, because the cavity is initially at rest, and $R(t = 0) = R_0$. Furthermore, we remark that the observed pressure profiles are very different from each other, and we ascribe this to differences between the cavity clusters generated in the individual experiments. We also notice that in the Cases A and B, the calculated maximum tensile stress is notably higher than that measured for a lithotripter pulse without cavitation. In this context, it should be noted that owing to the assumption of incompressible flow, the maximum tensile stress, calculated from Eq. 6.1, is overestimated, see also the discussion on compressibility effects in bubbly clouds in Hamilton *et al.* [42]. However, during the fast initial cavity growth which is decisive for the particle acceleration, only a small volume of liquid relaxes, and therefore the assumption of incompressibility is acceptable. With the BEM model, the simulations are stopped just before the final stage of cavity collapse. To reflect the slowing down of the particle motion owing to the drag force, the simulations with the spherical cavity model are continued beyond the cavity collapse. In previous experiments [11] we found that cavitation inception occurs in the focal region once the tensile stress exceeds a certain limit. Actually, a value of $p_\infty(t) < -2.5\,\text{MPa}$ (corresponding to a critical cavity radius of $\sim 50\,\text{nm}$) was necessary to initiate cavitation. However, we do not know the critical stress for each individual cavitation event observed in the current photographic series. Inception occurs within one frame interval, i.e. between
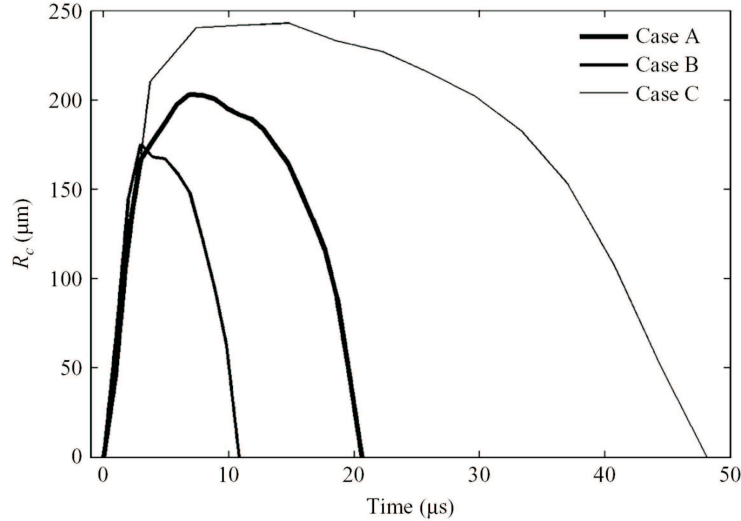
Figure 6.7: Experimentally determined cavity radii as a function of time for Cases A, B and C. Here, Case A corresponds to a particle of $R_p = 68\,\mu m$ and maximum cavity radius $R_c^{max} = 203\,\mu m$, Case B to $R_p = 30\,\mu m$ and $R_c^{max} = 175\,\mu m$, and Case C to $R_p = 62\,\mu m$ and $R_c^{max} = 243\,\mu m$.

the last picture without a cavity and the first one with a visible cavity. The use of $p_\infty(t = 0) = 0$ as the cavitation threshold introduces an error, but it is small because it takes only about 200 ns for the pressure to drop from a slightly positive pressure level to one below $-2.5\,MPa$ (see Fig. 6.2), and the frame intervals are at least $\sim 1\,\mu s$. By varying $p_\infty(t = 0)$ between 0 and $-5\,MPa$ we found a negligible effect on the particle trajectory, demonstrating the robustness of the approach.

6.5.2 Case A: particle radius $68\,\mu m$, max. cavity radius $203\,\mu m$

Case A, shown in Fig. 6.3 (and discussed in § 6.3 depicts cavitation on a polystyrene particle of radius $R_p = 68\,\mu m$ recorded at a framing rate of 1.02 million frames s^{-1}. The initial growth of the cavity radius R_c is very rapid, reaching $120\,\mu m$ in only $2\,\mu s$ (Case A, Fig. 6.7). The framing rate is sufficient to give a reliable growth rate. The cavity acquires its maximum size $R_c^{max} = 203\,\mu m$ in $7.8\,\mu s$, then it starts collapsing, but less violently than the initial growth. The pressure profile used for calculations with both models is given in Fig. 6.8. The maximum negative pressure is about $-11\,MPa$, i.e. notably lower than the value of $-7\,MPa$ measured in water without particles (Fig. 6.2), as discussed before (§ 6.5.1). Subsequently, the pressure rises steeply and becomes positive again at $t = 2.0\,\mu s$, i.e. notably earlier than the pressure measured in the absence of particles, see Fig. 6.2. It reaches a maximum positive
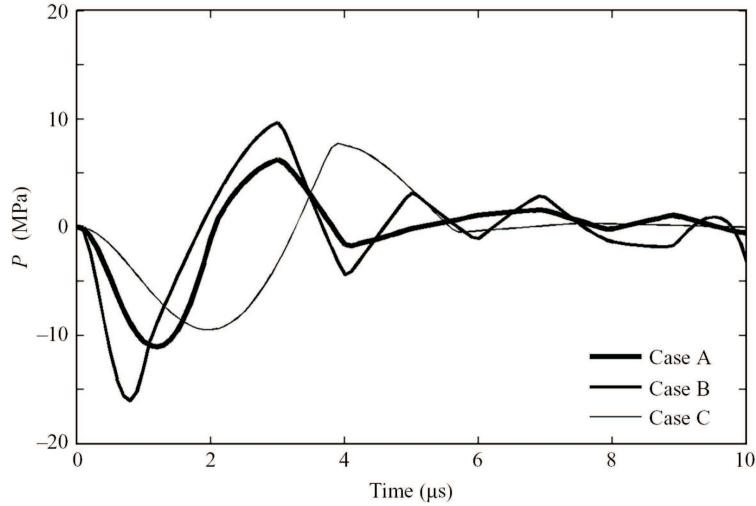
Figure 6.8: Calculated pressures $p_\infty(t)$ deduced from the experimental cavity radii as shown in Fig. 6.7 for Cases A, B and C.

value of $\sim 6\,\mathrm{MPa}$ before it drops, oscillating towards $0.1\,\mathrm{MPa}$. In Fig. 6.9 the particle position and velocity vs. time curves found experimentally are shown together with those simulated with Models 1 and 2. It is apparent that viscous effects are important when the particle has detached from the cavity, and the agreement between experiment and simulation when these effects are included shows that the above calculation of the drag is adequate. Also, the linear position vs. time relationships obtained in the simulations without the viscous effects after detachment demonstrate that the cavity dynamics ceases to influence the motion of the particle. The S-shape of the particle displacement vs. time curve is a result of positive acceleration of the particle during the period of tensile stress in the liquid and negative acceleration when the pressure rises and becomes positive for $t > 2\,\mu s$. During positive particle acceleration, the cavity grows from a small size, and the drop of pressure across the particle is very high. Therefore the particle acquires a high kinetic energy. During the subsequent negative acceleration, the cavity is large and the adverse pressure drop is smaller, which allows the particle to retain a considerable kinetic energy. Thus, at particle detachment the particle velocity u_p has the value of $\sim 14\,\mathrm{m\,s^{-1}}$. Model 1 predicts a maximum velocity of $\sim 40\,\mathrm{m\,s^{-1}}$, which agrees well with the experimental observations. Thus, the spherical cavity model captures the main features of the experimentally observed particle motion driven by the initial rapid growth of the cavitation bubble. However, the changes of the cavity shape are not accounted for by this simple model. For this, the boundary-element method is required. In the BEM simulation (Model 2), the spherical cavitation nucleus is subjected to the same pressure profile as used for Model

1 (Case A of Fig. 6.8). With Eq. 6.2, the force acting on the particle is calculated, and by integration, its velocity and position are found. In Fig. 6.10, the calculated cavity shapes and particle positions are plotted on top of selected frames from the experiment (Fig. 6.3). The outlines of the particle and the cavity obtained from the simulations are depicted with a solid grey and a white dashed line, respectively. At $t = 0\,\mu$s, cavitation inception is indicated by a small dot immediately to the left of the particle. Subsequently, the cavity starts growing and partly wraps the particle from $t = 1.0\,\mu$s to $t = 5.9\,\mu$s. At the same time, the particle is accelerated away from the cavity. On the particle surface in contact with the cavity the pressure is close to 0, while on the opposite side it is still strongly negative. We find good agreement between the experiment and the BEM calculated cavity shape and the positions of the cavity and particle until the neck formation is initiated, starting for $t > 5.9\,\mu$s in Fig. 6.10. In the experiment the righthand cavity surface, which is attached to the particle, is stretched and elongates into a thin neck at $t = 9.8\,\mu$s, until detachment from the particle. The BEM simulations do not reveal this cavity dynamics, because the liquidgasparticle contact condition is omitted, see §6.4.3. Thus, it is not surprising that differences in the cavity shape between simulation and experiment occur from shortly before the necking and during the collapse of the neck, i.e. in the time interval from $t = 5.9\,\mu$s to $11.8\,\mu$s. However, the basic cavity deformation during growth, related to the cavity-particle interaction is well reproduced in the simulation. From this time, the particle moves away from the cavity at slowly decreasing speed. The neck-breaking initiates a surface wave on the cavity, which results in the typical 'mushroom' shape observed in Fig. 6.3, e.g. at $t = 14.7\,\mu$s. In the experiment, the cavity collapses at $\sim 20.6\,\mu$s, but at this time the particle is already relatively far from the cavity which does not seem to influence the particle motion any more. When the particle starts to move away from the cavity, the radial velocity and the pressure gradient in the liquid are small, but the particle motion through the liquid causes a loss of kinetic energy by friction. An additional source of energy loss is the creation of the neck. In general, the surface energy $E_n = 2\pi r_n \sigma l_n$, where r_n is the neck radius, σ the coefficient of surface tension, and l_n the length of the neck, is negligible for the particle sizes considered in this study. However, for smaller particles, the surface energy can become comparable with the kinetic energy. For particles below $\sim 100\,$nm, all of the kinetic energy will be required in order to create the surface, assuming $l_n = R_p$, $r_n = R_p$, $\sigma = 0.06\,\mathrm{N\,m^{-1}}$, and $u_p = 40\,\mathrm{m\,s^{-1}}$.

6.5.3 Case B: particle radius $30\,\mu$m, max. cavity radius $175\,\mu$m

Another case of polystyrene particle acceleration is depicted in Fig. 6.11. The motion of the particle of $R_p = 30\,\mu$m is visible in each frame, and a cavity develops (Fig. 6.7, Case B), reaching a maximum radius of $R_c^{\mathrm{max}} = 175\,\mu$m, owing to the tensile stress in its far field. As in Case A, a framing rate of 1.02 million frames$\,\mathrm{s^{-1}}$ was used, i.e.

Figure 6.9: Comparison of the experimental Case A, $R_p = 68\,\mu$m with simulations from both models. The particle positions are compared in (a) and the velocities of the particle in (b). The experimentally determined values are indicated with crosses, while the lines are the results from the models. The spherical bubble model (Model 1) simulations are drawn as solid lines and the axisymmetric BEM simulations (Model 2) are drawn with dashed-dotted lines. Computational results including viscous friction (from the moment of detachment) are drawn with thick lines, and those neglecting viscosity with thin lines.

sufficient to give a reliable initial cavity growth rate and pressure profile (Fig. 6.8, Case B). Experimentally, the cavity collapses $10.8\,\mu$s after it has been created. Thus, the collapse time is much shorter than in Case A because the trailing positive pressure pulse arrives earlier and it is stronger. We notice that in the simulation with Model 1, the particle becomes engulfed by the cavity in the time interval from $t = 1\,\mu$s to $t = 3\,\mu$s, which leads to a zero force and thus to a constant particle velocity in this interval of time. This does not occur for Model 2. Consequently, the maximum velocities calculated from the two models differ substantially. The BEM model apparently overestimates the displacement of the particle, even when viscous drag is included.
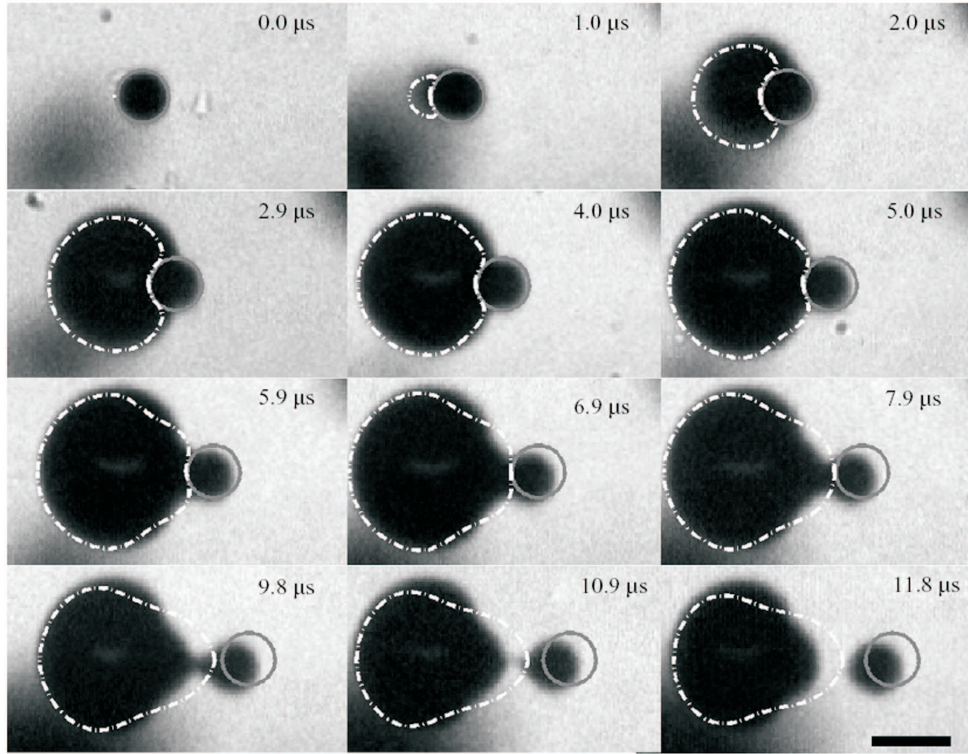
Figure 6.10: The cavity shapes (dash-dotted curves) and particle positions (grey solid lines) obtained by BEM calculations compared with the corresponding high-speed recordings (Case A). The cavity is taken to be nucleated at $t = 0\,\mu s$. At $t = 2.9\,\mu s$, the cavity partly wraps the particle, and at $t = 7.8\,\mu s$, a neck is created. Good agreement between the BEM calculations and the experiment is found until $t = 5.9\,\mu s$. After this time, and in particular after detachment of the particle from the cavity at $t = 10.8\,\mu s$, clear deviations are found in the cavity shape; presumably because the attachment of the cavity to the particle surface is not modelled in the BEM calculations. The scale bar shown is $200\,\mu m$.

However, the increase of the particle blurriness recorded experimentally suggests that an out-of-plane motion of the particle occurred. This indicates that the particle velocity is higher than the one we calculate assuming in-plane motion.

6.5.4 Case C: particle radius $62\,\mu m$, max. cavity radius $243\,\mu m$

Figure 6.12 shows the dynamics of a particle of radius $62\,\mu m$ set up during the growth of a cavity to a maximum radius of $R_c^{max} = 243\,\mu m$ and with a lifetime of $48\,\mu s$
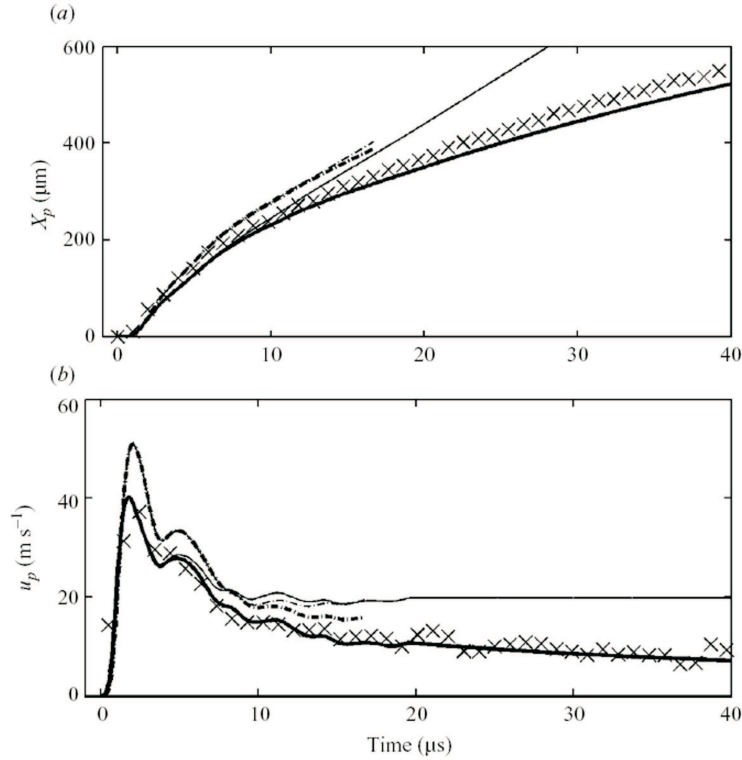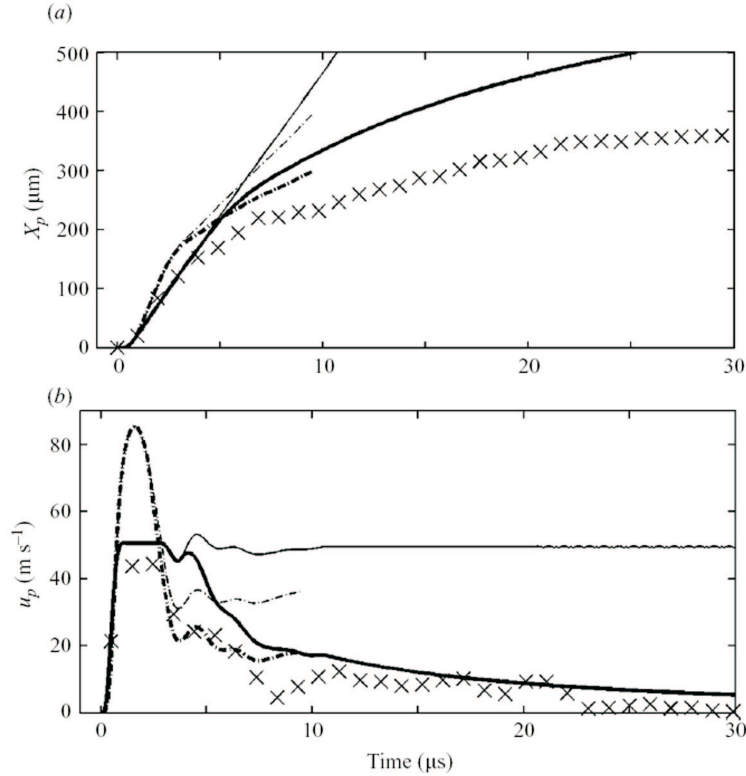
Figure 6.11: Comparison of the experimental Case B, $R_p = 30\,\mu$m with simulations from both models. The particle positions are compared in (a) and the velocities of the particle in (b). The experimentally determined values are indicated with crosses, while the lines are the results from the models. The spherical bubble model (Model 1) simulations are drawn as solid lines and the axisymmetric BEM simulations (Model 2) with dashed-dotted lines. Computational results including viscous friction are drawn with thick lines, and those neglecting viscosity with thin lines.

(Fig. 6.7, Case C), recorded at a framing rate of 0.27 million frames s^{-1}. The calculated pressure profile is shown in Fig. 6.8. Until inception, we can assume that the pressure pulses are reproducible and well represented by Fig. 6.2, but after inception the pressure depends on the development of the cavity cluster, and the rate of change of the pressure varies from experiment to experiment. However, the dynamics of the particle motion is well simulated by both models, when the effect of viscous drag is taken into consideration.
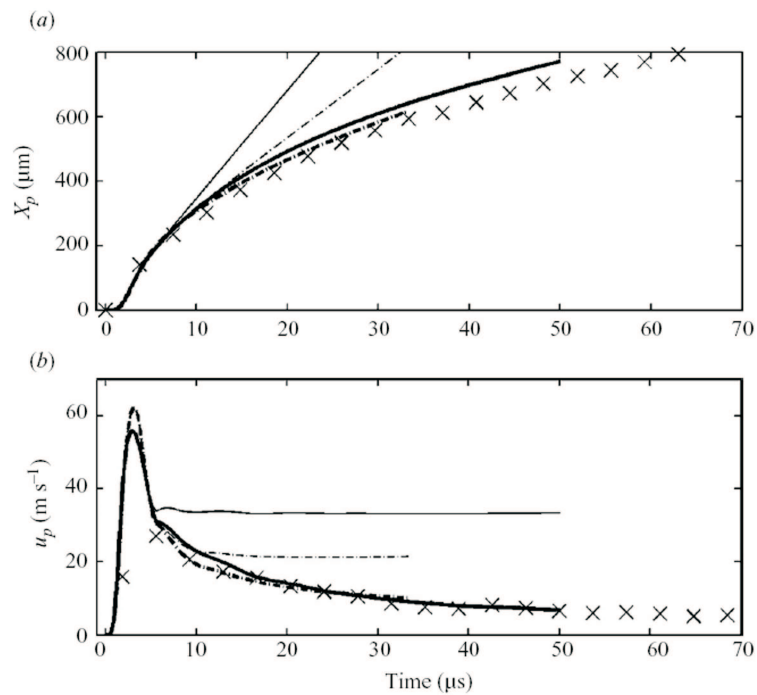
Figure 6.12: Comparison of the experimental Case C, $R_p = 62\,\mu m$ with simulations from both models. The particle positions are compared in (a) and the velocities of the particle in (b). The experimentally determined values are indicated with crosses, while the lines are the results from the models. The spherical bubble model (Model 1) simulations are drawn as solid lines and the axisymmetric BEM (Model 2) simulations with dashed-dotted lines. Computational results including viscous friction are drawn with thick lines, and those neglecting viscosity with thin lines.
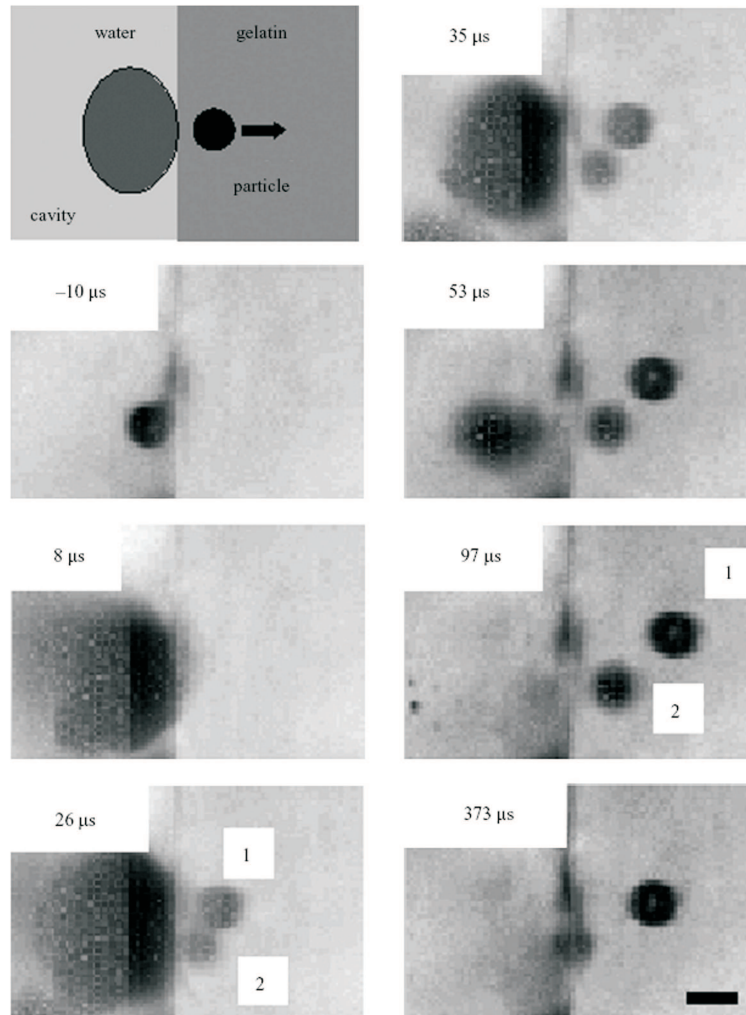
Figure 6.13: Particle injection into gelatin induced by cavitation. The first picture shows the fluid environment. The water-gelatin interface is located along the vertical centreline of the frame. At $t \sim 10\,\mu s$, a particle of radius $\sim 50\,\mu m$ is initially located in the water, touching the gelatin. This particle (denoted 1 in the frames taken at $t = 26\,\mu s$ and $t = 97\,\mu s$) holds a cavitation nucleus that explodes, and the particle is shot into the gelatin. The process is shown in the subsequent frames. A second particle (denoted 2, radius about $40\,\mu m$) is accelerated from some distance and under an angle from below. It penetrates into the gelatin shortly before $t = 26\,\mu s$. Particle 1 stays entrained after the cavitation activity has ceased ($t = 373\,\mu s$) whereas particle 2 is repelled from the elastic material. The maximum radius of the cavity propelling particle 1 is almost $200\,\mu m$. The scale bar in the last frame is $100\,\mu m$ in length.

6.6 Injection into elastic material

The very strong particle acceleration due to the explosive cavity expansion suggests that it might be possible to inject particles into a bulk elastic material by this technique. To achieve entrainment of particles into a material, the threshold strain of its elastic plastic transition has to be overcome. We choose gelatin (3% vol. concentration) as the receiving bulk material together with the polystyrene particles. For the experiment, a microscope slide is covered with a layer of gelatin, approximately 2 mm thick and submerged in water with suspended particles. The cavity and particle dynamics are recorded with a setup similar to that depicted in Fig. 6.1; only a different highspeed framing camera is used (Photron APX, Photron Ltd, Marlow, Bucks, UK). An experiment showing implantation of a particle into gelatin is depicted in Fig. 6.13. In the first frame the geometry is sketched: water at the left hand side and gelatine at the right hand side. The frames in this figure are selected from a highspeed series taken at 125000 frames s^{-1}. The time of recording is given relative to the moment of cavitation inception. A particle adhering to the water/gelatin interface is depicted in Fig. 6.13, $t = -10 \mu s$. A cavity has formed 8 μs after inception on the surface of the particle, and it develops in the water environment only. The particle detaches from this cavity between the frames at 8 μs and at 26 μs and propels towards the right into the gelatin (particle 1 in Fig. 6.13, 26 μs). Particle 2 is shot into the gelatin close to particle 1 from another cavity not visible in the recorded section, but located in the bulk phase of the fluid below to the left. The visible cavity collapses between 53 μs and 97 μs (Fig. 6.13). Particle 1 continues to penetrate deeper into the material (∼ 350 μm) whereas particle 2 resides around 100 μm below the water-gelatin interface. Later, particle 1 is slightly pushed back, but remains inside the gelatin; in contrast, particle 2 is ejected back into the liquid, see $t = 373 \mu s$, Fig. 6.13. The reason for the difference in penetration is presumably the difference of the momentum of the particles. Not only is particle 1 larger, it is also accelerated directly from the interface, whereas particle 2 travels through water before it hits the interface, and therefore presumably has a slower impact velocity. This experiment demonstrates that particles close to an elastic interface can be implanted in the substance by cavitation activity. Thus also particles containing drugs may be delivered from a liquid environment into tissue by non-invasive means. The method is also able to target a certain site within tissue by using a focused wave, a technique already used in kidney stone fragmentation (lithotripsy). Another medical application could be transdermal delivery of pharmaceuticals. Here, the particles serving as drug vehicles are brought on top of the skin and become exposed to the tensile wave through a coupling medium.

6.7   Conclusions

Cavitation bubbles expanding from suspended particles cause rapid particle acceleration. The pressure difference across the particle during the expansion of the cavity results in a net force that accelerates the particle. When the cavity reaches its maximum size, part of it remains attached to the particle for some time ('necking'). When the cavity finally collapses, the particle is already quite far away and the final cavity dynamics has little influence on the dynamics of the particle. The results show that the spherical cavity model (Model 1) and the BEM simulations (Model 2) are both consistent with the experimental data obtained. The cavity shapes calculated by the axisymmetric BEM agree well with the experiments until neck formation sets in. At later times, the calculated cavity shapes differ from the experimental ones presumably owing to the neglect of the cavity-particle contact condition in these simulations. Further studies are required to show how the particle velocities depend on applied pressure (i.e. maximum bubble size), particle diameter, particle density, particle shape, etc. The feasibility of cavitation-induced particle implantation in a gelatine phantom has been demonstrated which might open up a new working principle to implant particles into tissue, e.g. for drug delivery. We could think of biodegradable particles serving as drug containers carrying cavitation nuclei which allow them to be implanted into cells. This method, when used with a focused extracorporeal acoustic source, would have the additional advantage of being local (order of $1\,\mathrm{cm}$ in width, and $10.15\,\mathrm{cm}$ in depth). Another potential lies in particle penetration through skin for transdermal drug delivery or vaccination.

6.8   Appendix: Is $p_\infty(t)$ suited for the description of the non-spherical cavity dynamics?

Equation 6.3 for the pressure $p_\infty(t)$ is derived under the assumption of purely radial symmetry (isotropy). However, the BEM model uses an axisymmetric formulation. In this Appendix, we discuss the validity of this approximation. The reference pressure $p_\infty(t)$ used in the numerical simulations is calculated from the experimental cavity radius (see §6.4.1). Clearly, far away from the bubble, isotropy is given, but it breaks down close to the bubble. At large distances, only the first-order source/sink terms are important; any higher-order terms, such as dipoles, will approach zero much more quickly. The true motion of the cavity will not of course be spherically symmetric, as part of the cavity surface is bounded by the particle. In order to check how well the assumption of the far-field pressure $p_\infty(t)$ in Eq. 6.1 works for describing the non-spherical dynamics, we compare in Fig. 6.14 the radial dynamics from the Case A experiment (interpolated to splines for a smooth representation, see § 6.4.1) with a volume-averaged radius extracted from the BEM (Model 2). Indeed,
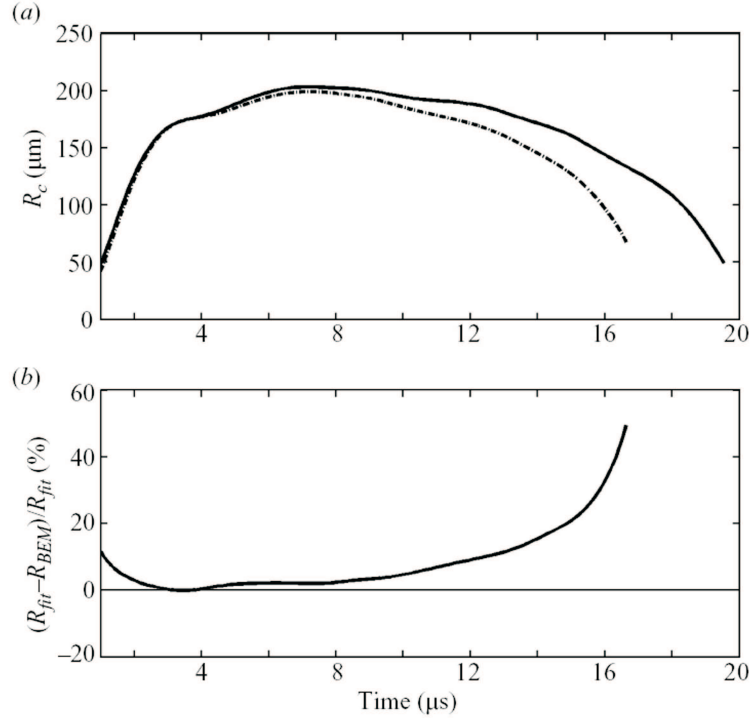
Figure 6.14: (a) The smooth representation of the cavity radius $R_c(t)$ from the experiment (solid line) is compared with the volume averaged radius from the BEM (dashed dotted line). (b) The relative deviation of these two curves is given in percent.

in the first few microseconds, some differences occur which we attribute to the particle.cavity interaction being predominant, until the cavity grows to a size larger than the particle. Thereafter, the pressure function $p_\infty(t)$ leads to a good calculation of the experimental cavity radius until collapse of the cavity. Fig. 6.14(b) reveals that the relative deviation between the radius obtained in the BEM simulation and in the experiment is below 10% most of the time, but it increases to 50% during the collapse phase. Another cause of the difference might lie in the limited number of experimental data points available during the initial bubble expansion. Here, small differences in the smooth representation between two measured radii caused by the fitting procedure can introduce a substantial error because a second temporal derivative of the cavity radius has to be employed in order to calculate $p_\infty(t)$. Finally we want to emphasize that on the time scales of the pressure recordings, the far-field pressure obtained through Eq. 6.3 does not display rapid local pressure changes which are probably present and generated from nearby collapsing bubbles (see [21]). However, it can be concluded from Klaseboer *et al.* [43, 44] that these pressure pulses are not

very intense, otherwise we would have observed jets in random directions.

References

[1] J. L. Green, D. J. Durben, G. H. Wolf, and C. A. Angell, "Water and solutions at negative pressure: Raman spectroscopy study to -80 megapascals", Science **249**, 649–652 (1990).

[2] Q. Zheng, D. J. Durben, G. H. Wolf, and C. A. Angell, "Liquids at large negative pressures: Water at the homogeneous nucleation limit", Science **254**, 829–832 (1991).

[3] E. N. Harvey, D. K. Barnes, W. D. McElroy, A. H. Whiteley, D. C. Pease, and K. W. Cooper, "Bubble formation in animals", J. Cell. Compar. Physl. **24**, 1–22 (1944).

[4] A. A. Atchley and A. Prosperetti, "The crevice model of bubble nucleation", J. Acoust. Soc. Am. **86**, 1065–1084 (1989).

[5] M. Greenspan and C. E. Tschiegg, "Radiation-induced acoustic cavitation: Apparatus and some results", J. Res. Natl. Bur. Stand., Sect. C **71**, 299–312 (1967).

[6] R. E. Apfel, "The role of impurities in cavitation-threshold determination", J. Acoust. Soc. Am. **48**, 1179–1186 (1970).

[7] S. I. Madanshetty, "A conceptual modeal for acoustic microcavitation", J. Acoust. Soc. Am. **98**, 2681–2689 (1995).

[8] K. A. Mørch, "Cavitation nuclei and bubble formation – a dynamic liquid-solid interface problem", J. Fluids Eng. **122**, 494–498 (2000).

[9] M. Holmberg, A. Kühle, J. Garnæs, K. A. Mørch, and A. Boisen, "Nanobubble trouble on gold surfaces", Langmuir **19**, 10510–10513 (2003).

[10] H. B. Marschall, K. A. Mørch, A. P. Keller, and M. Kjeldsen, "Cavitation inception by almost spherical solid particles in water", Phys. Fluids **15**, 545–553 (2003).

[11] M. Arora, C. D. Ohl, and K. A. Mørch, "Cavitation inception on microparticles: A self-propelled particle accelarator", Phys. Rev. Lett. **92**, 174501–1–4 (2004).

[12] L. A. Crum, "Tensile strength of water", Nature **278**, 148–149 (1979).

[13] J. Madadnia and I. Owen, "Accelerated surface erosion by cavitating particulate-laden flows", Wear **165**, 113–116 (1993).

[14] J. Madadnia and I. Owen, "Erosion in conical diffusers in particulate-laden cavitating flow", Intl. J. Multiphase Flow **21**, 1253–1257 (1995).

[15] W. K. Soh and B. Willis, "A flow visualization study on the movement of solid particles propelled by a collapsing cavitation bubble", Exp. Therm. Fluid Sci. **27**, 537–544 (2003).

[16] B. M. Borkent, M. Arora, and C. D. Ohl, "Reproducible cavitation activity in water-particle suspensions", J. Acoust. Soc. Am. **121**, 1406–1412 (2007).

[17] K. A. Mørch, "Reflections on cavitation nuclei in water", Phys. Fluids **19**, 072104 (2007).

[18] Y. A. Pishchalnikov, O. A. Sapozhnikov, and M. R. Bailey, "Cavitation selectively reduces the negative-pressure phase of lithotripter shock pulses", Ac. Res. Lett. Onl. **6**, 280–286 (2005).

[19] M. Liebler, T. Dreyer, and R. E. Riedlinger, "Nonlinear modelling of interactions between ultrasound propagation and cavitation bubbles", Acta Acust. **92**, 165–167 (2006).

[20] M. Arora, C. D. Ohl, and D. Lohse, "Effect of nuclei concentration on cavitation cluster dynamics", J. Acoust. Soc. Am. **121**, 3432–3436 (2007).

[21] A. Zijlstra and C. D. Ohl, "On fiber optic probe hydrophone measurements in a cavitating liquid", J. Acoust. Soc. Am. **123**, 29–32 (2008).

[22] C. T. Chin, C. Lanceé, J. Borsboom, F. Mastik, M. E. Frijlink, N. D. Jong, M. Versluis, and D. Lohse, "Brandaris 128: A digital 25 million frames per second camera with 128 highly sensitive frames", Rev. sci. instrum. **74**, 5026–5034 (2003).

[23] M. K. Lal and S. Menon, "Interaction of two underwater explosion bubbles", ASME Fluids Engng Div. Conf. **236**, 595–600 (1996).

[24] S. Rungsiyaphornrat, E. Klaseboer, B. C. Khoo, and K. S. Yeo, "The merging of two gaseous bubbles with an application to underwater explosions", Comput. Fluids **32**, 1049–1074 (2003).

[25] M. Arora, L. Junge, and C. D. Ohl, "Cavitation cluster dynamics in shock-wave lithotripsy: Part 1. free field", Ultrasound Med. Biol. **31**, 827–839 (2005).

[26] O. A. Sapozhnikov, V. A. Khokhlova, M. R. Bailey, J. C. Williams, J. A. McAteer, R. O. Cleveland, and L. A. Crum, "Effect of overpressure and pulse repetition frequency on cavitation in shock wave lithotripsy", J. Acoust. Soc. Am. **112**, 1183–1195 (2002).

[27] P. S. Epstein and M. S. Plesset, "On the stability of gas bubbles in liquid-gas solutions", J. Chem. Phys. **18**, 1505 – 1509 (1950).

[28] A. Eller and H. G. Flynn, "Rectified diffusion during nonlinear pulsations of cavitation bubbles", J. Acoust. Soc. Am. **37**, 493–503 (1963).

[29] C. E. Brennen, "Fission of collapsing cavitation bubbles", J. Fluid Mech. **472**, 153–166 (2002).

[30] N. Bremond, M. Arora, C. D. Ohl, and D. Lohse, "Controlled multibubble surface cavitation", Phys. Rev. Lett. **96**, 224501 (2006).

[31] N. Bremond, M. Arora, S. M. Dammer, and D. Lohse, "Interaction of cavitation bubbles on a wall", Phys. Fluids **18**, 121505 (2006).

[32] S. Hilgenfeldt, M. P. Brenner, S. Grossmann, and D. Lohse, "Analysis of rayleighplesset dynamics for sonoluminescing bubbles", J. Fluid Mech. **365**, 171–204 (1998).

[33] H. Lamb, ed., *Hydrodynamics, 6th edn.* (Cambridge University Press) (1932).

[34] S. M. Gracewski, H. Miao, and D. Dalecki, "Ultrasonic excitation of a bubble near a rigid or deformable sphere: implications for ultrasonically induced hemolysis", J. Acoust. Soc. Am. **117**, 1440–1447 (2005).

[35] M. Tanguay and T. Colonius, "Progress in modeling and simulation of shock wave lithotripsy (swl)", in *Fifth Intl Symp. on Cavitation* (2003).

[36] C. E. Brennen, *Cavitation and Bubble Dynamics* (Oxford University Press, New York) (1995).

[37] J. R. Blake and D. C. Gibson, "Cavitation bubbles near boundaries", Annu. Rev. Fluid Mech. **19**, 99–123 (1987).

[38] P. J. Harris, "A numerical method for predicting the motion of a bubble close to a moving rigid structure", Commun. Numer. Meth. Engng **9**, 81–86 (1993).

[39] Q. X. Wang, K. S. Yeo, B. C. Khoo, and K. Y. Lam, "Strong interaction between a buoyancy bubble and a free surface", Theoret. Comput. Fluid Dyn. **8**, 73–88 (1996).

[40] B. C. Khoo, E. Klaseboer, and K. C. Hung, "A collapsing bubble-induced micro-pump using the jetting effect", Sensors Actuators A **118**, 152–161 (2005).

[41] R. Clift, J. R. Grace, and M. E. Weber, *Bubbles, Drops and Particles* (Academic Press, Amsterdam) (1978).

[42] M. F. Hamilton, Y. A. Ilinskii, G. D. Meegan, and E. A. Zabolotskaya, "Interaction of bubbles in a cluster near a rigid surface", Acoust. Res. Lett. Online **6**, 207–213 (2005).

[43] E. Klaseboer, C. Turangan, S. W. Fong, T. G. Liu, K. C. Hung, and B. C. Khoo, "Simulations of pressure pulsebubble interaction using boundary element method", Comput. Meth. Appl. Engng **195**, 4287–4302 (2006).

[44] E. Klaseboer, S. W. Fong, C. Turangan, B. C. Khoo, A. J. Szeri, A. J. Calvisi, G. N. Sankin, and P. Zhong, "Interaction of lithotripter shockwaves with single inertial cavitation bubbles", J. Fluid Mech. **593**, 33–56 (2007).

7

Reproducible cavitation activity in water-particle suspensions[‡]

The study of cavitation inception in liquids rarely yields reproducible data, unless special control is taken on the cleanliness of the experimental environment. In this chapter, an experimental technique is demonstrated which allows repeatable measurements of cavitation activity in liquid-particle suspensions. In addition, the method is non-invasive: cavitation bubbles are generated using a shock-wave generator, and they are photographed using a digital camera. The cavitation activity is obtained after suitable image processing steps. From these measurements, the importance of the particle's surface structure and its chemical composition is revealed, with polystyrene and polyamide particles generating the highest yields. Further findings are that cavitation nuclei become depleted with an increasing number of experiments, and the existence of nuclei with varying negative pressure thresholds. Finally, a decrease of the cavitation yield is achieved by pre-pressurization of the suspension – indicating that the cavitation nuclei are gaseous.

125

7.1   Introduction

The discrepancy between the theoretical tensile strength of pure water and the much lower values reported in various cavitation experiments has been attributed to the presence of cavitation nuclei. Harvey *et.al.* [1] suggested that stable, minute gas nuclei are present in cavities on the solid surfaces of suspended particles, and that such cavities could act as nucleation sources. Greenspan and Tschiegg [2] reported that removing particles larger than $0.2 \mu m$ in diameter increased the tensile strength of water to about 200 bar. The hypothesis of Harvey *et al.* developed over several years into the so-called "crevice model" [3–7] which predicts the acoustic cavitation threshold required to nucleate a vapor cavity from a mote, and the threshold's dependency on bulk liquid properties and crevice attributes such as size, wettability and geometry.

The experiments [2, 3, 8] revealed that cavitation inception depends not only on various liquid properties but also on acoustic parameters such as pulse duration, frequency and the geometric form of the sound field, and (if present) the number of cavitation nuclei and their respective nuclei properties. The latter observation stimulated investigations into the role played by controlled amounts of impurities, such as suspended particles [9–14]. As a result of that work, it was recognized that the method used to determine whether a cavitation event has happened can play a crucial role in determining cavitation thresholds. In the majority of experiments an active detector is used [9–13] which consists of a focused transducer operated in pulse-echo mode, typically at 30 MHz (see for example Madanshetty *et al.* [10, 11] for details). However, this invasive method affects the cavitation process [11], for example the acoustic field can convect the particles into the cavitation zone through acoustic radiation forces, and high acoustic frequencies might set particles into oscillatory motion. The latter could stimulate the formation and subsequent merging of surface bubbles into microscale cavities, which has been termed acoustic coaxing [11, 12]. This hypothesis is also put forward in a more recent study in which a Keller-vortex flow system is used to induce cavitation on microparticles [14].

Cavitation experiments, when performed under uncontrolled lab conditions, are usually difficult to reproduce, see the comments of Strasberg in 1959 [3] for example. His data showed a "surprising" mean deviation of $10 - 15\%$ for $10 - 20$ measurements with unchanged experimental conditions. Madanshetty *et al.* [11] and Deng *et al.* [13] suggest that cavitation thresholds are strongly influenced by the cleanliness of the system. They both stress the importance of monitoring and accounting for fine details in the liquid preparation and handling. Thus great experimental care has to be taken to set up the nuclei environment in order to obtain repeatable cavitation measurements. Yet, cavitation thresholds measurements typically have a standard deviation of about 15%, which is regarded as good; see for example Atchley *et al.*[15]. In the present work the term reproducibility addresses the fact that the experimental results can be reproduced on different days and months with freshly prepared particle-

water suspensions. Thus, other groups should be able to repeat our experiments and obtain quantitative similar numbers – within the error margins – of cavitation activity. Given that most of the problems faced in cavitation experiments are related to the invasiveness of the cavitation detector and the cleanliness of the nuclei environment, we designed a method which overcomes both. In this study, we make use of a single acoustic cycle from a shock wave generator to nucleate cavitation bubbles in an ultra-clean environment. Since the shockwave passage takes only a few microseconds, the interaction of the acoustic signal with the cavitation bubbles is reduced to a minimum which distinguishes this approach from the ones presented in [2, 3, 8–10, 12, 13]. In addition, we detect cavitation bubbles optically, thus quantitative and non-invasive. With this method we showed previously that cavitation bubbles nucleate on the microparticles itself and, as a direct consequence, the particles are accelerated away with velocities up to tens of meters per second [16]. In contrast, we report here on the depletion of cavitation nuclei due to both the nucleation event itself and pre-pressurization of the particles. Finally, we report how new sets of cavitation nuclei can be activated by increasing the tensile stress in the liquid in a stepwise manner.

7.2 Materials and Methods

7.2.1 Experimental setup

Given that acoustic cavitation is usually observed through invasive means like active cavitation detectors, a more reliable non-invasive method seems necessary. In this chapter we present an optical (non-invasive) and simple system, which evolved from a prior experiment discussed in Arora *et al.*[16]. In principle, cavitation is induced by a focused shock wave source and is detected with a camera, see Fig.7.1. The shock wave source is attached at an angle of 45° in one of the walls of a large container filled with approximately 50 liters of partially degassed demineralized water ($\sim$ 3mg/l O_2 concentration at a temperature of approx. 20°C).

The probe suspension is contained within a polystyrene sterile flask (75 ml, Easy-Flask, Nunclon). This is positioned with its center aligned with the acoustic focus of the shock wave source using a xyz-translation stage. A watertight magnetic stirrer (Telemodul 90407, Variomag), located below the flask, is mixing the suspension in the flask homogeneously with a glass-coated magnet. Before submerging the flask in the basin its content is sealed with a foil (Parafilm, American National Can, Chicago). Here, care is taken that no air bubbles become entrapped.

Shock waves are generated by a focused piezoelectric source which is a slightly modified extracorporeal lithotripter (Piezolith 3000, Wolf GmbH). The strength of the applied tensile stress is set through the discharge voltage which is in the order of kV. A
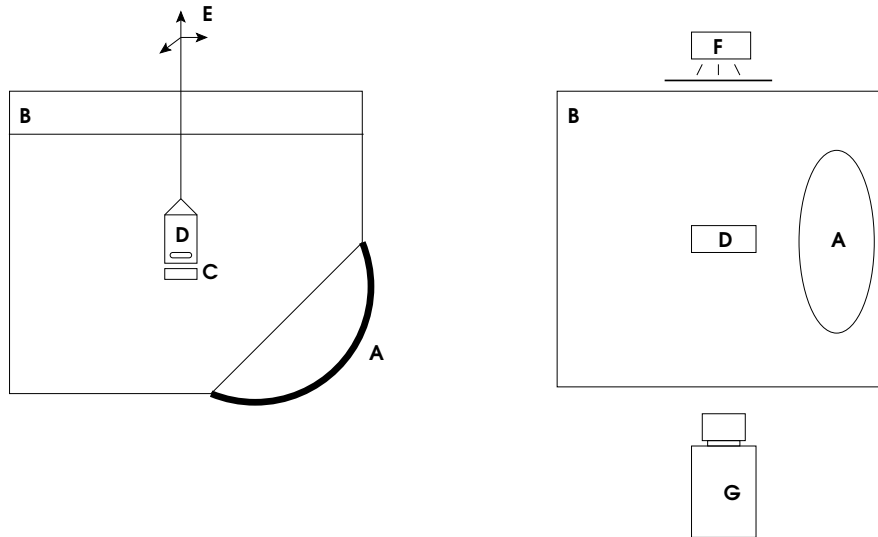
Figure 7.1: Side and top view (resp. left and right) of the experimental setup. A: shockwave generator, B: water tank, C: magnetic stirrer, D: flask with particle suspension, E: translation stage, F: flash light, G: camera.

typical pressure profile (5 kV discharge voltage) *inside* the polystyrene flask is shown in Fig. 7.2.

The pressure pulse has been recorded with a calibrated glass fiber hydrophone (FOPH-500, RP Acoustics) located inside the sealed flask and close to the acoustic focus point, which is marked by two crossing laser-diodes. The measurement shows that the travel time for the pressure wave from the front shell to the acoustic focus is approximately 136 µs. Once the acoustic wave arrives, a steep overpressure-peak (maximum of 100 bar, half-width of 1 µs) is followed by a more elongated tensile wave (minimum of −60 bar, 5 µs duration). During the latter period the threshold pressure (around −25 bar as obtained from experiments) is exceeded and cavitation bubbles are created (Fig. 7.3). If sufficient cavitation nuclei are present, an approximately cigar-like cavitation cluster is found [17].

Bearing in mind that each expanding and collapsing bubble is acting as an acoustic source, the shape of the pressure wave following the positive peak in Fig. 7.2 may vary strongly with cavitation activity [18].

The bubble activity is illuminated with a flash lamp (Strobolume 1540, General Radio) positioned behind a diffuser and photographed with a single frame from a digital charged-coupled device (CCD) camera (Pulnix TM-6710, Alzenau, Germany). The camera is equipped with a macro lens (Makro-Planar T*2.8/60, Carl Zeiss) and placed around 30 cm from the acoustic focus, which is just outside the water tank.
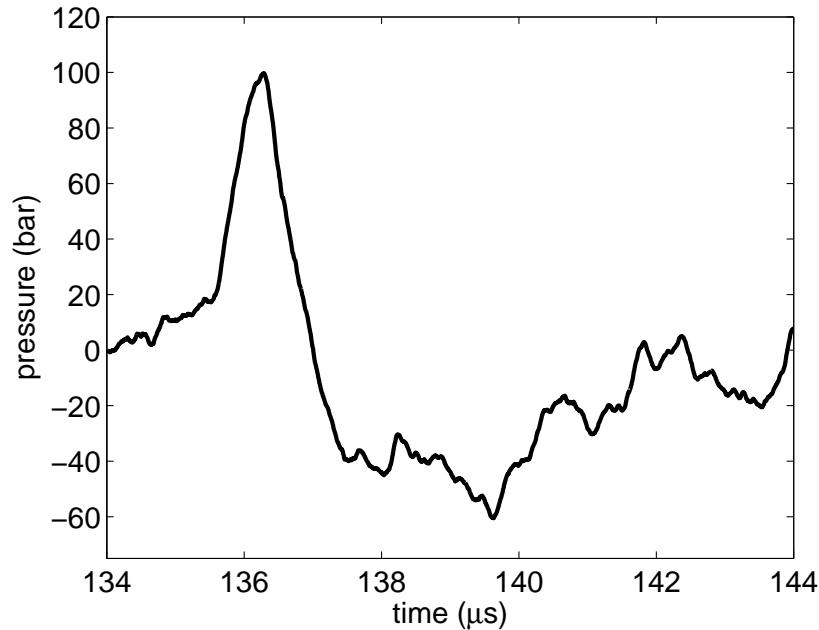
Figure 7.2: Pressure as a function of time as recorded inside the flask (without particles) with the fiber optic probe hydrophone FOPH-500 for a charging voltage of 5 kV. The time $t = 0$ corresponds to the start of the lithotripter pulse.

The devices are triggered with a home-made delay generator. The diffuse back-illumination provides a good contrast for detecting the bubbles; they are imaged as dark dishes (Fig. 7.3). The spatial resolution of the images obtained is 32.1 ± 0.1 μm per pixel, resulting in an image area of 15.4×20.6 mm^2. In this image a region of interest (ROI) is selected parallel to the direction of the shock wave propagation being $45°$ to the horizontal. Bubbles in this ROI are segmented, counted, and analyzed with standard image processing tools (Matlab, The Mathworks, Natick, MA, USA). To limit the analysis to bubbles within a certain depth range a threshold technique is applied on the bubble border. Bubbles imaged in focus possess a strong gray scale gradient at their edge, whereas the magnitude of the gradient decreases with distance from the image plane. By applying a threshold filter on the mean gradient of the bubble boundary the bubble counting algorithm is limited to bubbles within a certain distance from the image plane. The gray scale gradient has been measured with an artificial bubble object moved back and forth in the imaged volume. In this way the depth range in which bubbles are counted has been set to 8.0 mm.
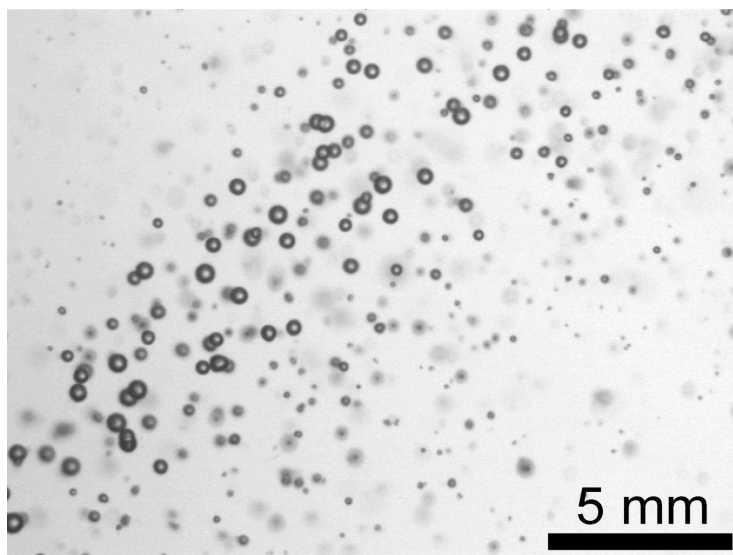
Figure 7.3: Typical bubble cloud which appears approx. 14 µs after passage of the tensile wave (Fig. 7.2) inside of the flask. Settings: 10^4 particles/75ml and 5 kV discharge voltage.

7.2.2 Liquid handling

Stock solutions of the particles were made in test tubes and their number densities were determined with a Neubauer cell-counting chamber under the microscope. The corresponding volume containing 10^4 particles was pipetted from the test tube with a micro-pipette into the sterile 75 ml flask. Then, the flasks are filled to their rim with Milli-Q water and sealed carefully. After placing the flask in the holder at the acoustic focus a shock wave is generated. The bubble activity is recorded approximately 14 µs after the passage of the tensile wave through the focus. To check for the water quality of the suspending liquid control experiments were conducted. Only if the flasks containing pure Milli-Q water showed less than 5 cavitation bubbles in the field of view the water was considered appropriately clean.

In the case of pre-pressurization (§ 7.3.3) the suspension was first introduced into a pressure chamber. This consists of a stainless steel cylinder having a maximum volume of 40 ml. The liquid in the cylinder is pressurized with a gas tight piston connected to the labs high pressure air supply. First, the liquid handling system is gently flushed with the suspension. Thereby, it was verified that most bubbles in this system are removed. Then, 40 ml of the suspension are sucked into the cylinder and pressurized with 3 or 5 bar absolute pressure for 15 minutes. In the control experiment all liquid handling steps were conducted in the same way with the exception of pressur-

izing the chamber. After 15 minutes the suspension was pushed smoothly out of the chamber into the flask and an additional volume of 35 ml of partly degassed Milli-Q water with no particles is gently added to fill up the flask, which is then sealed and put into the water tank.

7.2.3   Estimation of the cavitation yield

The cavitation yield, α, is defined as the percentage of particles in the acoustic volume which develop into cavitation bubbles, i.e.

$$\alpha = \frac{N_{bub}}{N_{particles}} \cdot 100\% \quad . \tag{7.1}$$

Here, N_{bub} is the number of imaged bubbles and $N_{particles}$ is the number of particles. The acoustic volume is the volume in the flask where the pressure becomes low enough such that cavitation bubbles become visible. Although the particles are distributed homogeneously in the flask, it is important to stress that the negative pressure amplitude varies strongly in space. Thus, not all of the particles in the acoustic volume can develop into cavitation bubbles. To estimate this acoustically active volume we sum up many images with bubble activity. This averaged image reveals that bubbles appear in an approximately cylindrical region with its central axis aligned with the acoustic pathway: The cylinder length is 14.2 ± 0.1 mm and its diameter is 7.3 ± 0.1 mm leading to an optically registered acoustic volume as 0.59 ± 0.02 cm^3. Clearly, these values vary with the applied acoustic pressure but here we limit to the case of 5 kV discharge voltage (corresponding to -60 bar peak tensile stress, see Fig. 7.2). With the number density of 133 particles/ml given and the assumption of a homogeneous distribution of particles, approx. 78 ± 3 particles are present in the optically registered acoustic volume. For instance, in the first shot of Fig. 7.6 66 bubbles were counted resulting into a cavitation yield of $\alpha = 85 \pm 3\%$. Thus, most of the particles serve as a cavitation nucleus.

7.3   Results

The key-request of the experiment was that a quantitative measure of cavitation activity of a controlled amount of particles could be obtained *in a reproducible way*. Reproducibility in cavitation experiments is a notorious problem since many factors may stimulate or impose nucleation, especially contamination. In the end, it was found that reliable quantitative data could be obtained by counting the number of bubbles produced by a controlled number of particles in a fixed volume at given shock wave settings, careful handling the liquids and ultra pure water conditions.
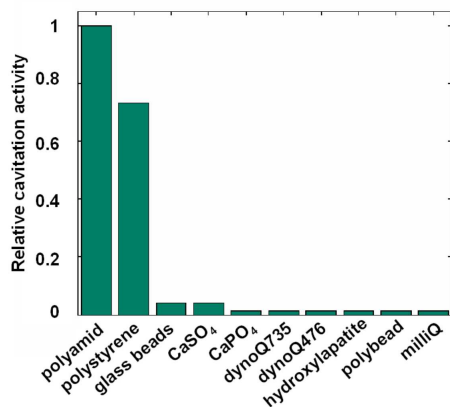
Figure 7.4: Relative cavitation activity for different particles suspended in Milli-Q water. The control with the plain suspension liquid gives a count of 0.01.

7.3.1 Cavitation activity of microparticles

First we investigated different types of particles from which we select one type for further quantitative studies. Figure 7.4 depicts the number of cavitation events per particle for the ones listed in table I.

Here 10^4 particles per flask, thus $1.3 \cdot 10^2$ per ml, have been prepared and the shock wave generator has been operated from $1-5$ kV discharge voltage with steps of 1 kV. (The pressure pulse corresponding to 5 kV discharge voltage is depicted in Fig. 7.2 and has a peak negative pressure of -60 bar.)

The total number of bubbles, nucleated in these five subsequent shots, is depicted in Fig. 7.4. Clearly, polyamide and polystyrene enhance cavitation significantly, while the other studied particles (either hydrophilic or covered with surfactants) show only cavitation activity similar to the plain liquid (Milli-Q water). Polyamide and polystrene particles differ from the other particles as both can be categorized as hydrophobic and rough-structured on the surface. Interestingly, polyamide particles show more cavitation activity than polystyrene. This is surprising since polystyrene (consisting of methyl-groups and phenyl-rings) can be assessed as more hydrophobic than polyamide (which contains many polar amide-groups) and secondly because the polystyrene particles have around 40 times as much surface area compared with the relatively small polyamide particle, where cavitation nuclei could be entrapped (provided that necessary conditions are satisfied). On the other hand, scanning electron microscopy (SEM) reveals that polyamide particles have a much rougher surface structure, at least on the microscale as compared to polystyrene (Fig. 7.5). Thus, the higher surface roughness of polyamide may facilitate the entrapment and stabilization

Particle name	Mean ⌀ (μm)	Features	Manufacturer (prod. nr.)
Hollow Glass Spheres (glass oxide)	11*	Hydrophilic, smooth surface	Potters Industries (110P8)
Polyamide Seeding Particles	20*	Hydrophobic, rough surface	Dantec Dynamics GmbH (80A4011)
Polystyrene-2%-divinylbenzene	80–150*	Hydrophobic, rough surface	Serva GmbH
Dynosphere Q735, from Ref. [14]	40	Hydrophilic, with hydroxyl groups	Dyno Particles AS, Norway (EXP-SS-42.3-RSH)
Dynosphere Q476, from Ref. [14]	3.0*	Hydrophilic, smooth surface	Dyno Particles AS, Norway (EXP-SA-3.2-RNI)
Polybead Polystyrene Microspheres	1.00*	Filled with water, surfactant on surface	Polysciences
Hydroxylapatite $(Ca_{10}(OH)_2(PO_4)_6)$	10–100	Biocompatible, slow-dissolving salt	Sigma Aldrich (289396)
β-tri-Calcium phosphate hydroxide $(Ca_3(PO_4))$	5–10	Slow-dissolving salt	Fluka (21218)
Calcium sulphate Dihydrate $(CaSO_4 \cdot H_2O)$	10–100	Slow-dissolving salt	Sigma Aldrich (255548)

Table 7.1: Characterization of the particles investigated in this study on cavitation activity. An (*) asterisk behind the mean diameter ⌀ indicates the manufacturers specification. In the other cases the particle sizes were determined with a microscope in the lab.

of gas pockets on the surface. The further studies are conducted with the polyamide particles.

### 7.3.2 Depletion of cavitation activity

Effect of repetitive tensile waves

In the next experiment the effect of multiple pressure waves on the cavitation activity was investigated. 10^4 polyamide particles were suspended in a flask, and 40 subsequent waves at 5 kV discharge voltage (-60 bar peak negative pressure) were applied. The experiment was repeated three times and the number of cavitation bubbles measured. From the average number of bubbles, the mean percentage of nucleated particles per shot was calculated as the cavitation yield, α, and is shown in Fig. 7.6. We find a decreasing number of cavitation events with a low variability between experiments, thus high reproducibility. Interestingly, it is found that the number of particles which can be nucleated decreases per shot. This can be explained that each particle has a limited number of nuclei which become finally used up. Additionally, the waiting time between two shots was varied from 10 s to 60 s for the circles and the squares in Fig. 7.6, respectively. No effect of this time interval is found on the cavitation yield. The dissolution time for the gaseous remains from cavitation bubbles can be estimated for bubbles reaching a maximum diameter of 400 µm during 40 µs in water saturated with air at room temperature. A bubble will thereby collect approx. $1.1 \cdot 10^{-12}$ g of air [17] which is equivalent to a bubble of 6 µm equilibrium radius. This sized bubbles dissolve again within 1.2 s, see for example [19] and [20]. Thus, a waiting time between two experiments of 10 s assures that gaseous remains from prior cavitation activity have dissolved.

Effect of tensile stress level

If one thinks of cavitation nuclei as becoming "used up" after nucleation, it is interesting to investigate what would happen when the discharge voltage (and thus the tensile stress) is increased stepwise. Are we able to activate a new population of nuclei by applying higher tensile stresses? To answer this question, an experiment similar to the previous one has been performed, but now beginning with a discharge voltage of 4 kV and after 20 shots followed by 20 shots of 5 kV. This was repeated three times and the result is plotted in Fig. 7.7.

During the first 20 shots the nuclei which can be activated with a 4 kV discharge voltage are growing into cavitation bubbles. The trend of decrease in the cavitation yield resembles the one as depicted in Fig. 7.6. However, if after 20 shots the acoustic tensile stress is increased, more bubbles become visible, hence, a new set of nuclei is triggered. With the higher tensile stress the number of bubbles again starts to decrease for successive shots.
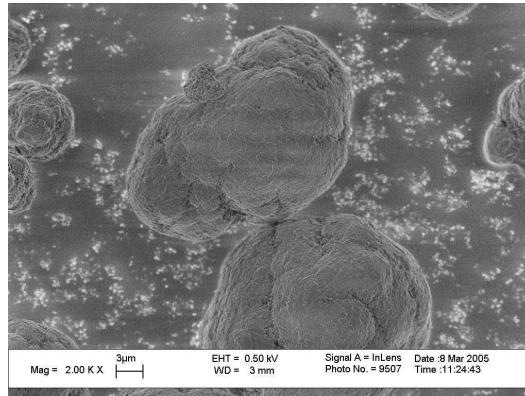
(a) polyamide particles
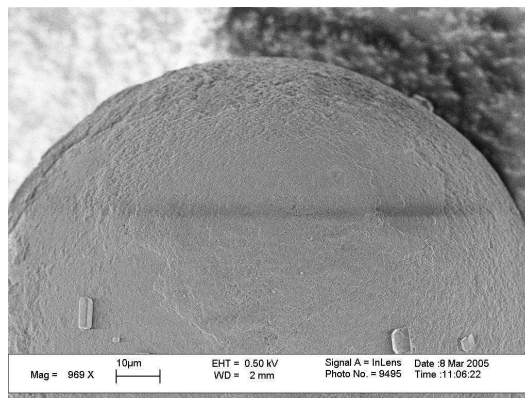
(b) polystyrene particles
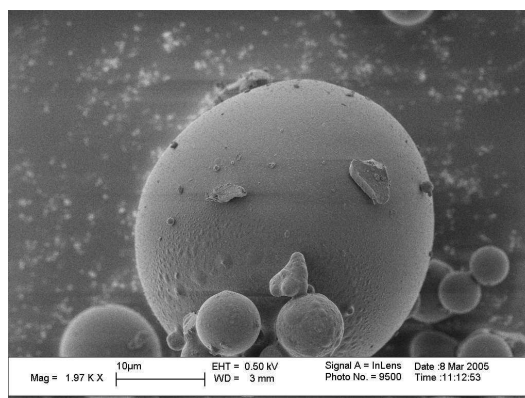
(c) glass spheres

Figure 7.5: SEM pictures of a) polyamide, b) polystyrene, and c) glass spheres. Further specifications in Table I.
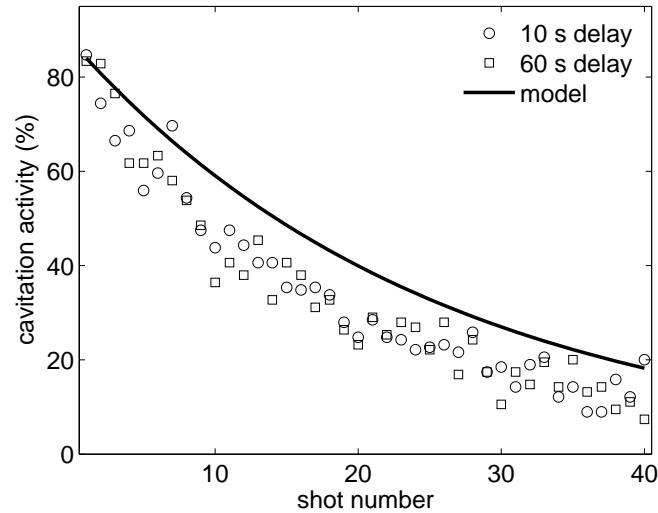
Figure 7.6: Cavitation activity given as the percentage of particles that lead to a cavitation event. Each data point is the mean of three experiments. The waiting time of 10 s (circles) and 60 s (squares) has no effect on the cavitation yield. The line shows the values as calculated by the model, Eq. (7.3), without fitting parameter.
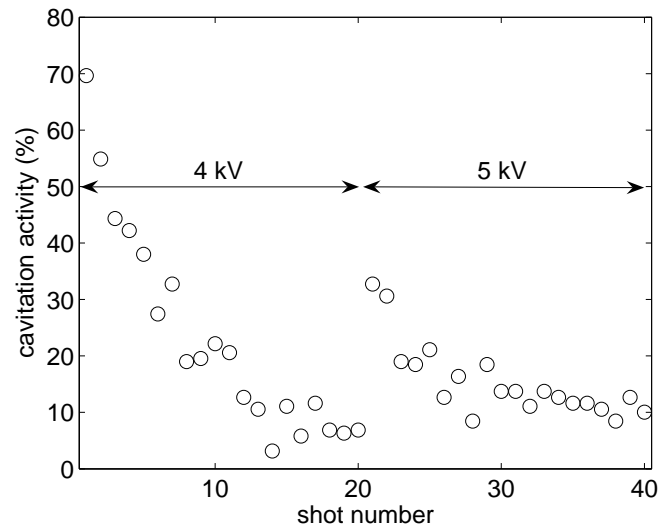
Figure 7.7: Cavitation activity for two different tensile stresses, 4 kV and 5 kV experiments resp. Each data-point is the mean of three experiments.

7.3.3 Pre-pressurization

The crevice model [6] predicts that a pressurization of the suspension will force the meniscus of the gaseous nuclei to a more convex shape, until it reaches the advancing contact angle. An increased or prolonged pressurization will move the meniscus of the interface towards the apex of the assumed conical crevice: the bubble shrinks and liquid moves into the crevice. Here, the question is addressed if pre-existing nuclei on the particles can be affected by pressurization of the suspension prior to the nucleation experiment. The effect of pre-pressurization of controlled water-particle-suspensions has not been investigated before, yet it was proposed by Deng *et al.* [13]. Interestingly, Strasberg found that cavitation is more difficult in tap water which is subjected temporary to a high pressure [3].

The liquid handling during the pressurization step is described in § 7.2.2. Two different pre-experimental pressurization levels are compared with the case with no pressurization but the same fluid handling steps in Fig. 7.8. Again, each experiment is repeated three times and the mean number of cavitation bubbles are plotted. The control case, circles in Fig. 7.8 shows the typical decrease of cavitation activity with shot number. A pre-pressurization of the suspension with 3 bar absolute pressure for 15 minutes leads to a significant decrease of cavitation (diamonds in Fig. 7.8). Cavitation activity is largely diminished with a pre-experimental treatment of the suspension with 5 bar overpressure, see squares in Fig. 7.8. Here, only about 20% of the bubbles are counted as compared to the control.

7.4 Discussion

7.4.1 Effect of exposure time

Interestingly, the particles (dynoQ735 and dynoQ476, see Fig. 7.4), which are from the same batch as the ones tested in Marschall *et al.* [14] did not show pronounced cavitation activity in response to the 60 bar peak negative pressure wave (Fig. 7.2). This is in considerable contrast to Keller's vortex-flow nozzle experiment as described in Ref. [14]. In that work a negative pressure of 0.87 bar was sufficient to induce cavitation with the particles. The obvious difference between the two experimental conditions is the exposure duration for the particles to the tensile stress. In the shock wave experiments particles are exposed only a few microseconds, whereas in the flow cavitation experiments the tensile stress lasts two orders of magnitude longer [21]. This difference suggests, that not only the tensile strength but also the duration of negative pressure exposure is critical for the nucleation process. Our hypothesis is that a longer exposure to tensile stress allows a dynamic rearrangement and possibly a coalescence of gaseous nuclei on the particle surface. These now larger nuclei posses a reduced cavitation threshold and thus explode at smaller abso-
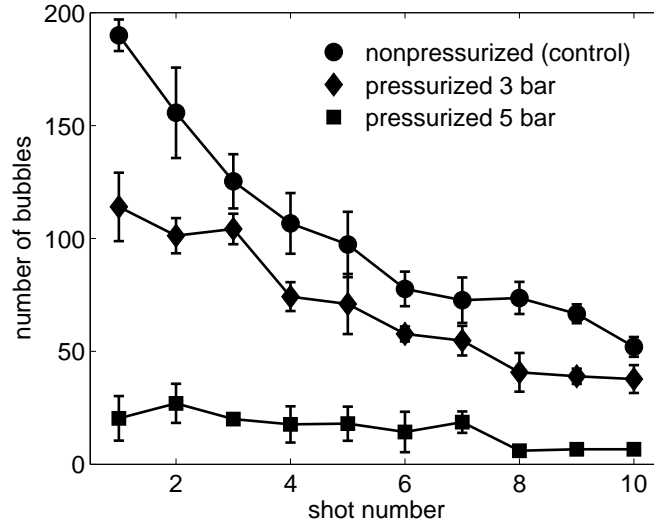
Figure 7.8: Temporal evolution of cavitation after pre-experimental pressurization. A decrease of cavitation of around 30% has been measured when shooting with 3kV-shots after pressurization with 3 bars (diamonds), compared to the non-pressurized scenario (circles). Pressurization with 5 bars (squares) leads to a cavitation reduction of more than 80%. Every datapoint is the mean of three experiments (bars depict standard deviation).

lute pressures.

7.4.2 Model

Assuming that each nucleus in the acoustic volume can grow into a cavitation bubble the observed number of bubbles, N_{bub}, should be equal to the number of nuclei present in the observed acoustic volume V_{ob}.

The number of nuclei in the observed acoustic volume is determined from

$$N_{bub} = \frac{V_{ob}}{V_{flask}} \cdot N_{nuclei} \quad , \tag{7.2}$$

where V_{flask}=75 ml is the total flask volume and N_{nuclei} the total number of nuclei available in the flask.

The observed acoustic volume is approximated from the experimental geometry with a cylinder, $V_{ob} = \pi r^2 l$ having a radius $r = 3.6$ mm and a length $l = 14.2$ mm. Initially (exposure number $n = 1$), the number of nuclei in the flask, N_{nuclei} is related to the number of particles $N_{particles}$ through the cavitation yield, thus $N_{nuclei} = N_{particles} \cdot$

α, where α is the cavitation yield. We assume that at later stages ($n > 1$) nuclei become used up due to cavitation, thus N_{nuclei} decreases with every shot by a factor of V_{tav}/V_{flask}. Here, V_{tav} is the total acoustic volume $\pi r^2 l_{flask}$, where $l_{flask} = 71$ mm is the length of the acoustic volume in the entire flask. Therefore, the decrease of cavitation nuclei as a function of the exposure number n is given by

$$N_{nuclei}^{n+1} = \left(1 - \frac{V_{tav}}{V_{flask}} \right) N_{nuclei}^{n} \quad . \tag{7.3}$$

Now the number of nucleated bubbles N_{bub} can be calculated from Eq.7.2. Here, all model parameters are determined from the experiment and no fitting parameters come into play. The model Eq.7.2 gives an exponential decrease in cavitation activity which resembles the trend in the experimental curve reasonably well. It is possible to obtain a very good fit to the measured decay and the model by changing the experimental parameters by no more than by 10%. Yet, we see the good agreement with the measured only data as an indication that indeed a particle is acting as one-time triggerable source of cavitation. This finding underlines the importance of the history of the suspension in cavitation studies, e.g. how many times it has been exposed to a rarefaction wave; and the golden rule of Robert Apfel [22]: "Know thy liquid!" applies.

7.5 Conclusion

A novel experimental approach to study cavitation inception within a well controlled environment has been presented. A flask filled with a suspension of clean water and an adjustable number of particles is exposed to a single shockwave-rarefaction wave cycle. At a peak negative pressure amplitude of 60 bar, hydrophobic and corrugated polymer particles facilitate cavitation inception, while smooth and hydrophilic particles do not enhance cavitation activity. In the case of polyamide, around 80 % of the particles nucleate after the passage of the first shockwave. For successive shockwaves, the number of cavitation bubbles decreases exponentially, which is shown by running a simple cavitation nucleation model. This exponential decrease suggests that particles have a limited number of nucleation sites which are consumed during the experiment. Therefore the level of cavitation activity reflects the history of the liquid. It was found also that more bubbles are observed with increasing negative pressure. This suggests that the nucleation sites on the particles have varying cavitation thresholds. Finally, it was observed that the cavitation yield decreases when the suspension is pre-pressurized suggesting that the cavitation nucleus is gaseous in origin.

References

[1] E. N. Harvey, D. K. Barnes, W. D. McElroy, A. H. Whiteley, D. C. Pease, and K. W. Cooper, "Bubble formation in animals", J. Cell. Comp. Physiol. **24**, 1–22 (1944).

[2] M. Greenspan and C. E. Tschiegg, "Radiation-induced acoustic cavitation: Apparatus and some results", J. Res. Natl. Bur. Stand., Sect. C **71**, 299–312 (1967).

[3] M. Strasberg, "Onset of ultrasonic cavitation in tap water", J. Acoust. Soc. Am. **31**, 163–176 (1959).

[4] R. E. Apfel, "The role of impurities in cavitation-threshold determination", J. Acoust. Soc. Am. **48**, 1179–1186 (1970).

[5] L. A. Crum, "Tensile strength of water", Nature **278**, 148–149 (1979).

[6] A. A. Atchley and A. Prosperetti, "The crevice model of bubble nucleation", J. Acoust. Soc. Am. **86**, 1065–1084 (1989).

[7] K. A. Mørch, "Cavitation nuclei and bubble formation – a dynamic liquid-solid interface problem", J. Fluids Eng. **122**, 494–498 (2000).

[8] W. J. Galloway, "An experimental study of acoustically induced cavitation in liquids", J. Acoust. Soc. Am. **26**, 849–857 (1954).

[9] R. A. Roy, S. I. Madanshetty, and R. E. Apfel, "An acoustic backscattering technique for the detection of transient cavitation produced by microsecond pulses of ultrasound", J. Acoust. Soc. Am. **87**, 2451–2458 (1989).

[10] S. I. Madanshetty and R. E. Apfel, "Acoustic microcavitation: Enhancement and applications", J. Acoust. Soc. Am. **90**, 1508–1514 (1991).

[11] S. I. Madanshetty, R. A. Roy, and R. E. Apfel, "Acoustic microcavitation: its active and passive acoustic detection", J. Acoust. Soc. Am. **90**, 1515–1526 (1991).

[12] S. I. Madanshetty, "A conceptual modeal for acoustic microcavitation", J. Acoust. Soc. Am. **98**, 2681–2689 (1995).

[13] C. X. Deng, Q. Xu, R. E. Apfel, and C. K. Holland, "Inertial cavitation produced by pulsed ultrasound in controlled host media", J. Acoust. Soc. Am. **100**, 1199–1208 (1996).

[14] H. B. Marschall, K. A. Mørch, A. P. Keller, and M. Kjeldsen, "Cavitation inception by almost spherical solid particles in water", Phys. Fluids **15**, 545–553 (2003).

[15] A. A. Atchley, L. A. Frizzell, R. E. Apfel, C. K. Holland, S. Madanshetty, and R. A. Roy, "Thresholds for cavitation produced in water by pulsed ultrasound", Ultrasonics **26**, 280–285 (1988).

[16] M. Arora, C. D. Ohl, and K. A. Mørch, "Cavitation inception on microparticles: A self-propelled particle accelarator", Phys. Rev. Lett. **92**, 174501–1–4 (2004).

[17] M. Arora, L. Junge, and C. D. Ohl, "Cavitation cluster dynamics in shock-wave lithotripsy: Part 1. free field", Ultrasound Med. Biol. **31**, 827–839 (2005).

[18] Y. A. Pishchalnikov, O. A. Sapozhnikov, and M. R. Bailey, "Cavitation selectively reduces the negative-pressure phase of lithotripter shock pulses", Ac. Res. Lett. Onl. **6**, 280–286 (2005).

[19] O. A. Sapozhnikov, V. A. Khokhlova, M. R. Bailey, J. C. Williams, J. A. McAteer, R. O. Cleveland, and L. A. Crum, "Effect of overpressure and pulse repetition frequency on cavitation in shock wave lithotripsy", J. Acoust. Soc. Am. **112**, 1183–1195 (2002).

[20] P. S. Epstein and M. S. Plesset, "On the stability of gas bubbles in liquid-gas solutions", J. Chem. Phys. **18**, 1505 – 1509 (1950).

[21] K. A. Mørch, "personal communication", (2006).

[22] R. E. Apfel, "Acoustic cavitation inception", Ultrasonics **22**, 167–173 (1984).

Part III

Wetting a superhydrophobic surface

8

Zipping wetting and the breakdown of superhydrophobicity[‡]

In some cases water droplets can completely wet micro-structured superhydrophobic surfaces. The dynamics of this rapid process is analyzed by ultra-high-speed imaging. Depending on the scales of the micro-structure, the wetting fronts propagate smoothly and circularly or – more interestingly – in a stepwise manner, leading to a growing square-shaped wetted area: entering a new row perpendicular to the direction of front propagation takes milliseconds, whereas once this has happened, the row itself fills in microseconds ("zipping"). Numerical simulations confirm this view and are in quantitative agreement with the experiments.

[‡]Based on:

Mauro Sbragaglia, Alisia M. Peters, Christophe Pirat, Bram M. Borkent, Rob G. H. Lammertink, Matthias Wessling, and Detlef Lohse, "Spontaneous breakdown of superhydrophobicity", Phys. Rev. Lett. **99**, 156001 (2007).

Christophe Pirat, Mauro Sbragaglia, Alisia M. Peters, Bram M. Borkent, Rob G. H. Lammertink, Matthias Wessling, and D. Lohse, "Multiple time scale dynamics in the breakdown of superhydrophobicity", Europhys. Lett. **81**,66002 (2008).

Alisia M. Peters, Christophe Pirat, Mauro Sbragaglia, Bram M. Borkent, Matthias Wessling, Detlef Lohse, Rob G. H. Lammertink, "Cassie-Baxter to Wenzel state wetting transition: scaling of the front velocity", Eur. Phys. J. E. (2009) 10.1140/epje/i2009-10489-3.

8.1   Introduction

When a liquid droplet is deposited on hydrophobic micro-structured materials, it can stay suspended with very high contact angles (typically 160° and beyond) and very low hydrodynamic resistance ("Lotus effect") [1–5]. This property makes such materials useful for a wide series of applications ranging from coatings and self-cleaning windows, to water-repellent textiles and microfluidics [6–8]. However, under certain conditions, this superhydrophobic situation ("Cassie-Baxter state" [9], hereafter CB) spontaneously breaks down [10, 11]: fluid enters in between the micro-structures and spreads, resulting into a smaller contact angle ("Wenzel state" [12], hereafter W), see Fig. 8.1.

In some situations this transition from the CB to the W state is highly desirable. An example is provided by heterogeneous porous catalysts, where superhydrophobicity is an unwanted effect as it reduces the contact area [13]. Understanding the mechanisms triggering the transition and characterizing its dynamical properties is crucial. The triggering mechanisms for the transitions are still widely debated in the literature [14, 15]. This is due to the presence of energy barriers encountered when passing
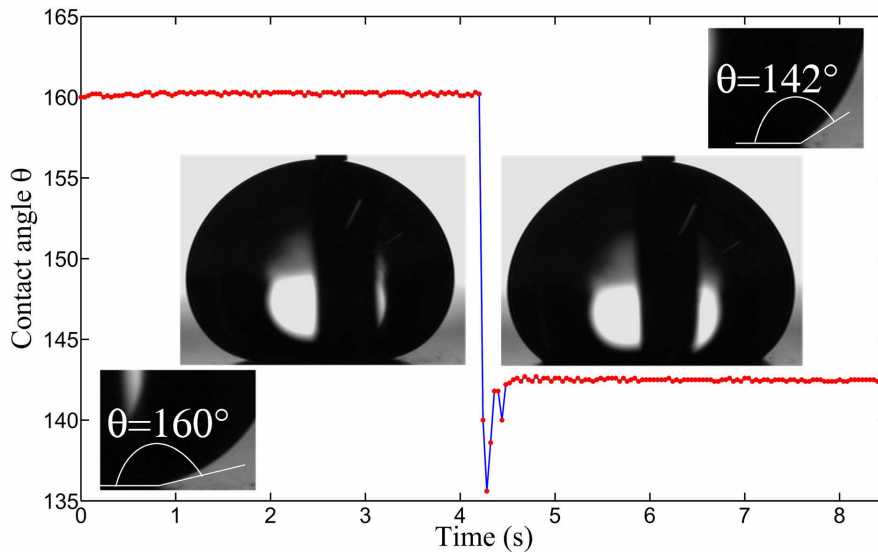

Figure 8.1: Transition from the (meta-)stable CB to the W state. A drop softly deposited on a micro-patterned surface can stay suspended with air pockets trapped in the grooves underneath the liquid (left). At some point the CB state spontaneously breaks down. The drop then homogeneously wets the substrate, resulting in a lower contact angle (right).

from CB to W that may strongly depend on the filling procedure. This means that even when the Wenzel state has lower energy (lower contact angle), the transition is not always spontaneous and has to be triggered, for example, by pressing on the drop [3] or by using an electric field [16]. However, under certain conditions, local spontaneous infiltrations can be achieved. Whether the liquid is able to then spread and fill the micro-structures depends of the surface patterning. In particular, when the surface roughness becomes comparable to an intrinsic value (critical value), a smooth filling is replaced by a step-like process in which rows of the structured surfaces fill through a zipping mechanism. The origin of this "zipping wetting" behavior will be addressed both experimentally, numerically and theoretically in § 8.3. Details of this anisotropic wetting process, with different time scales involved, is provided both experimentally and with the help of numerical simulations in § 8.4. Finally, the velocity of the wetting front is analyzed and rescaled as a function of pattern geometry and materials contact angle in § 8.5.

8.2 Materials and Methods

In the present study, patterns of micrometer-size pillars arranged on a square lattice are considered (Fig. 8.2). The sketch of the pattern (Fig. 8.2a) illustrates its geometrical parameters: pillar width w, pillar height h, gap size between the pillars a and wavelength $d = a + w$.

8.2.1 Preparation of the molds

The fabrication of highly precise and controllable micro-structured surfaces becomes possible through a micro-molding technique [17]. Molds are prepared in the cleanroom by standard photolithography and deep reactive ion etching on silicon wafers. Each mold contains fields (20 mm × 20 mm) filled with 5 μm wide square holes (w) in a regular square array with gap sizes between the holes (a) varying from 2 to 26 μm. Two mold types are defined in Table 8.1: mold type 1 is used as is for replicating Kraton^{TM} films, while mold type 2 is hydrophobized with a hydrophobic FOTS coating (1H,1H,2H,2H-perfluorooctyltrichlorosilane, Fluka Chemicals) enabling an easy release of thin PDMS films. The coating procedure is as follows: a silicon wafer is placed in a large petridish with a drop of FOTS next to the wafer. The covered petridish is placed in an oven for 2 hours at 120°C to evaporate the FOTS and to deposit the FOTS molecules onto the substrate. This is followed by an annealing step at 100°C for 1 hour, a washing step with with isopropanol (analysis grade, Merck), MilliQ water and again isopropanol and, finally, the samples are dried under a flow of nitrogen. The depth of the mold (equal to height h of the pillars) is varied. Four copies of mold type 1 are etched to different depths: 4.4, 10, 14 and 15.6 μm. The

Field	Mold 1(Kraton)	Mold 2 (PDMS)
1	2	16
2	5	18
3	8	20
4	11	22
5	14	24
6	17	26

Table 8.1: Gap sizes a of used molds [µm]

final depths of two copies of mold type 2 are 4.7 and 8µm. The result is a variety of combinations of gap sizes and pillar heights.

8.2.2   Preparation of the polymer films

All materials are used as received, i.e. without any further purification. Two types of polymers are used for casting micro-patterned films: Kraton^{TM} D-1102CS (a linear styrene-butadiene-styrene block copolymer with 29.5 wt% styrene, Kraton Polymers) and PDMS (polydimethylsiloxane, RTV 615 rubber component A and curing agent B, GE Bayer Silicones). The Kraton is dissolved in toluene (analysis grade, Merck) to make a 30 wt% solution, which is stirred overnight. The solution is then casted on an untreated mold (type 1) with a thickness of $200-300$µm. The toluene is allowed to evaporate overnight before releasing the micro-patterned film with ethanol (analysis grade, Merck). Films are dried and stored in a $30°C$ vacuum oven until use.
To obtain a PDMS mixture the rubber component A is mixed with the curing agent B (10:1 w/w) and degassed before use. The liquid is cast on a hydrophobized mold (type 2) with a thickness of 100-300µm and cured in an oven for 3 hours at $60°C$.

8.2.3   Characterization of the micropatterns

The geometrical sizes of the micropatterns are taken from scanning electron microscopy pictures (5 kV, JSM 5600LV, JEOL) of the polymer films, not from the molds, see Fig. 8.2b. Prior to imaging, the films are broken in liquid nitrogen and sputtered with a 30 nm gold layer (SCD 040, Balzers Union).
The contact angle (CA) for water on a pattern with $a=5$µm and $h=10$µm is typically $\theta \sim 160°$ in the metastable CB state and $\theta \sim 142°$ in the W state (Fig. 8.1), whereas CA for a smooth surface made of the same material is of $\theta_f \sim 100°$. CAs are measured with an optical contact angle measuring instrument (OCA 20, Dataphysics) by suspending a 6 µl drop on the surface. Notice that the measured CAs corresponding to the CB and W state are larger than the theoretically expected values
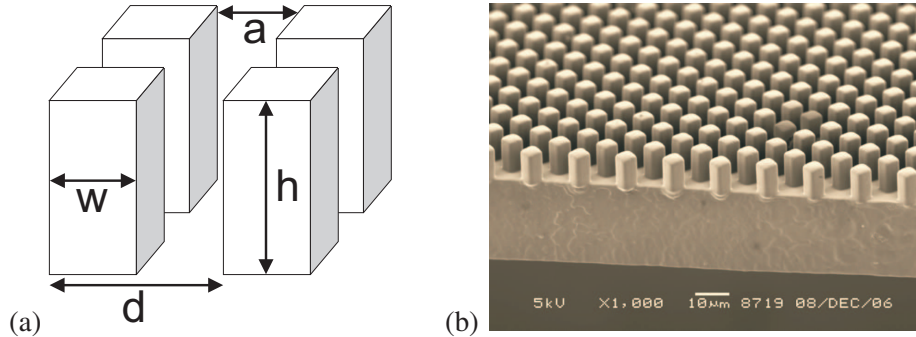
Figure 8.2: Sketch (a) and scanning electron microscopy (SEM) picture (b) of the micro-patterned substrate. The geometrical dimensions of the pattern are the pillar height $h = 10\mu m$, the pillar width $w = 5\mu m$ (both kept fixed for all experiments), and the gap width a, which is varied between $2\mu m$ and $17\mu m$. The wavelength d of the pattern is $d = a + w$. In (b) we have $a = 5\mu m$. Typical equilibrium contact angles for a smooth surface made up of the same material are $\theta \sim 100°$.

from the CB and W equations, $143°$ and $121°$ respectively. This is due to the system being in a metastable local energy minimum in both cases. One needs to apply a sufficient amount of energy (e.g. vibrations) to the droplet to bring it in its global energy minimum state, where the idealized CB and W equations apply [18].

The static contact angle for water on flat PDMS is $\sim 120°$ and on the micro-patterned PDMS between $157°$ and $161°$ (CB state). Each micro-patterned field is cut out and placed on a $170\mu m$ thick microscope slide before use.

8.2.4 Optical microscopy and high-speed imaging

Water droplets are softly deposited on the surface with a syringe pump (PHD 2000, Harvard Appartus GmbH, March-Hugstetten, Germany) at a low flow rate ($5\,\mu l/min$) from the outlet of a vertical thin tubing (outer diameter $0.158\,mm$). The outlet is set parallel to the flat film, $2\,mm$ above it. A typical droplet grows slowly and reaches the dry surface within a minute. Then the flow is stopped and a stable drop of contact area $\sim 1\,mm^2$ in the CB state is observed. Observations are performed from the bottom of the film with an inverted microscope (Axiovert 40 CFL, Carl Zeiss BV, Weesp, The Netherlands). Proper illumination is obtained with a fiber lamp (ILP-1, Olympus, Zoeterwoude, The Netherlands), combined with a high-speed charged coupled device camera (APX-RS, Photron Limited, UK). The large scale dynamics is captured with a $10\times$ magnification objective at 5 kfps. Smaller details are resolved at 50 kfps with an oil immersion Plan-Apochromat $100\times$ objective, of numerical aperture $NA = 1.4$, allowing for a few microns thick image plane. Focusing in the material

features is achieved with a piezoelectric objective-lens positioning system with re-
producibilitybelow 100 nm (MIPOS 500, Piezosystem Jena GmbH, Jena, Germany).
The translucent film is only $\sim$ 40 µm thick, allowing for high quality optical imaging
of the CB to W transition through its bottom.

8.2.5   Image processing

Submicron resolution is achieved with the help of a home-made image post-processing
technique. First a movie with region of interest 20 µm $\times$ 20 µm is decomposed in an
image sequence. For each image, the initially 117×117 pixels window undergoes a
$10\times$ oversampling up to 1170×1170 pixels. Next, a FFT bandpass filter consisting in
a twofold 2d Gaussian filtering in the Fourier space is applied. The low-pass compo-
nent acts as a small structure smoother, whereas the high-pass one corrects large scale
illumination inhomogeneities and increases contour contrast. Finally, adaptive inten-
sity threshold is properly applied and interface position detected. Attention should
be paid on the fact that this method is sensitive to illumination variations through the
image sequence, and may result from time to time in a slight shift of the detected
interface position. Moreover, shadowing caused by pillars yields an imprecise detec-
tion of the interface position in the vicinity of the pillars, although the main part is
accurately detected within 100 nm.

8.3   Origin of zipping wetting behavior

In this paragraph our aim is to characterize and analyze the dynamics of the sponta-
neous breakdown of superhydrophobicity in terms of geometry, wetting, liquid-gas
surface tension σ_{lg}, and the liquid viscosity η. For this purpose we make use of
Kraton micropatterns, with $h = 10$µm, $w = 5$µm and different gap widths a.

8.3.1   Experimental results

After depositing the drop on the surface, a spontaneous breakdown of the metastable
CB state starts usually within a minute. From a local infiltration point, a rapid spread-
ing (responsible for the lateral front, hereafter called "main front") develops through
the square lattice posts. The details of this local infiltration point are sensitively
dependent on the height (i.e. roughness): the higher the posts, the larger the time
needed to achieve that. This is probably due to the presence of some local energy
barrier [14, 15] whose value is increasing with surface roughness. In this way, for
large h, the infiltration threshold cannot be achieved spontaneously and some local
trigger mechanism is therefore necessary. Interestingly, kraton is subject to water
impregnation. This effect could be strong enough to lower the energy barrier and
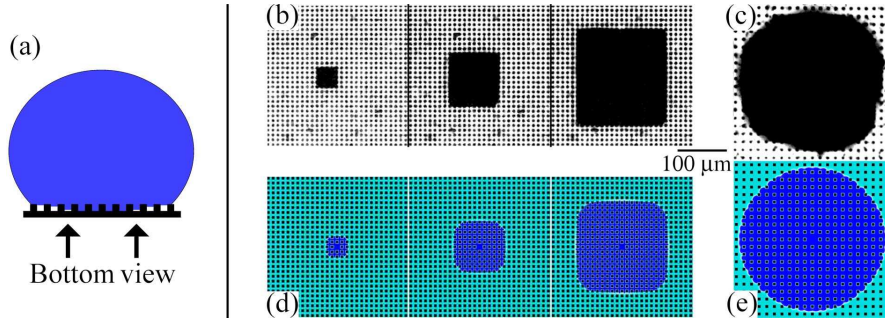
Figure 8.3: Bottom views of the front evolution of the transition, as sketched in (a). In (b) three snapshots for the case with $a = 5\mu m$ are shown, leading to square-shaped wetted area. In (c) it is $a = 11\mu m$, resulting in a circular wetted area. Figures (d) and (e) show the results of the corresponding numerical simulations with the Lattice Boltzmann method with $a = 5\mu m$ and $11\mu m$, respectively. The infiltration point has been centered in the figure but is not located in the center of the droplet's base: its dependence on local energy barriers can indeed produce uncertainty in its location.

thus trigger the transition. In Fig. 8.3 the large scale time evolution of the filling process is shown. After fluid sinks down at a certain point, a lateral spreading develops which sensitively depends on the parameters characterizing the micro-textured surface: while for large gap width $a = 11\mu m$ a round shape of the fully wetted area is emerging (Fig. 8.3c), at smaller $a = 5\mu m$ the propagating fronts reflect the structure of the underlying square lattice, leading to a square-shaped wetted area (Fig. 8.3b). At even smaller $a = 2\mu m$ we never observed any transition to the W state.

For the wetting cases, the velocity of front propagation drastically depends on the gap width a (see Fig. 8.4): For $a = 11\mu m$ we measure a mean velocity $v \sim 700\,mm/s$, two orders of magnitude faster than the case with $a = 5\mu m$, where $v \sim 7mm/s$. Moreover, in the latter case the front propagates in a stepwise manner (Fig. 8.4a) and fronts at different positions on the sample or in different directions show a remarkable variation in their velocity ("dispersion").

For the more striking case of the square-shaped wetted area ($a = 5\mu m$) we show details of the wetting dynamics in Fig. 8.5a. The front is here advancing from top to bottom and is slowing down while wetting occurs in a *zipping* manner: the timescale of the front for entering a new row is slow as already shown above (Fig. 8.4a), namely typically $d/v \sim 1.4\,ms$, the timescale for the filling of the once entered row itself is about two orders of magnitude faster, ~ 0.01 ms.
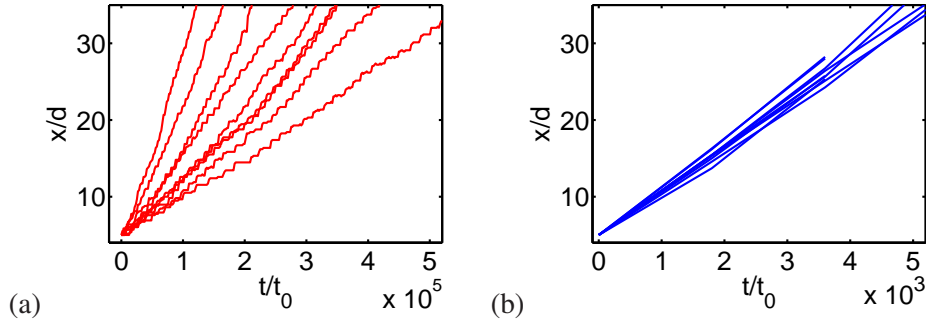
Figure 8.4: Wetting front evolution for micro-patterned surfaces with different gap-width a. We show a case where $a = 5\mu m$ (a) and a case where $a = 11\mu m$ (b). In both cases, nine different experiments were carried out with the same sample. The position of the front has been normalized with respect to the pattern wavelength $d = a + w$ and time has been made dimensionless with t_0 as in Eq. (8.4). Note the difference in front speeds v in the two cases: in the small wavelength case (left) a *critical slowing down* ($v \sim 7\,mm/s$) induces large dispersion and *zipping* is revealed. The large wavelength case (right) is less dispersed and much faster, reaching velocities of $v \sim 7 \cdot 10^2\,mm/s$.

8.3.2   Numerical results

In order to better reveal the physics of the wetting mechanism, numerical simulations are performed using a three-dimensional Lattice Boltzmann algorithm [19] for single component multiphase fluids. Wetting properties with surface tension are introduced as explained in [20, 21], leading to wetting angles comparable with those in the experiments. Geometrical structures are reproduced with the same aspect ratio as in the experiment. Similarly, in the large gap width case $a = 11\mu m$ (nearly) spherical wetted areas are observed (Fig. 8.3e), whereas in the case $a = 5\mu m$ we observe square-shaped wetted areas, see Fig. 8.3d. Also the zipping wetting behavior is reproduced in these simulations for $a = 5\mu m$ (see Fig. 8.5b). When repeating the simulations with a gap width $a = 2\mu m$, we do not observe any lateral infiltration of the substrate and the CB state remains stable, again, just as experimentally observed.

8.3.3   Theoretical interpretation of the results

How to explain the transition from CB to W? The energy of a droplet in equilibrium on a substrate is monotonically increasing with the effective contact angle [11]. As a result, when the CB effective contact angle is higher than the W one, we would argue that the CB droplet always collapses towards the W state. Anyhow, intermediate states with higher energy can be encountered [11]: they represent energy barriers
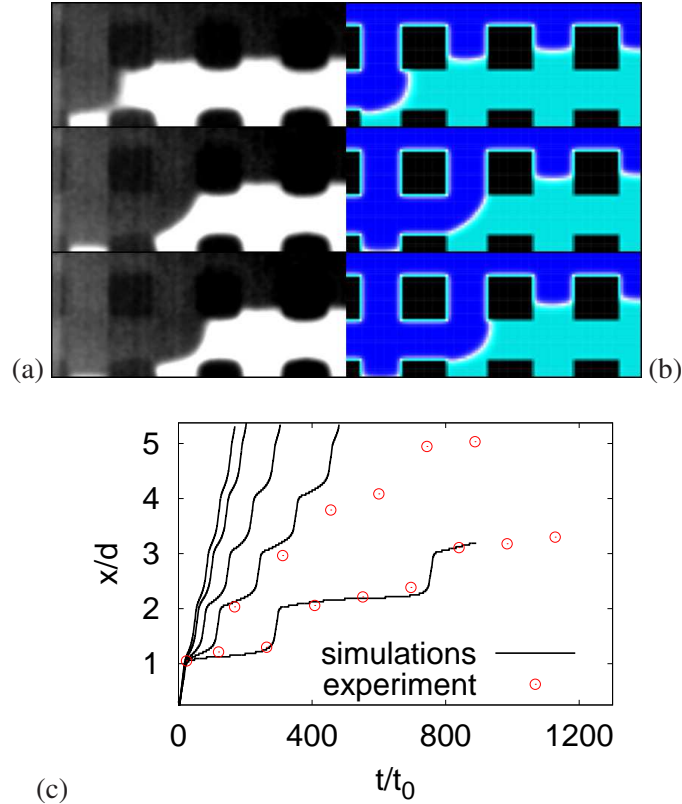
Figure 8.5: The lateral zipping mechanism (left to right) close to the critical point ($\theta \sim \theta_c$). (a) Snapshots of the zipping mechanism recorded in an experiment with $a = 5\mu m$ with the front propagation from top to bottom. (b) The results are also compared with snapshots from numerical simulations. (c) Numerical results for the front propagation (lines) in the lateral zipping process close to the critical point. From top to bottom we show the following cases: $\cos\theta/\cos\theta_c \sim 0.868, 0.890, 0.927, 0.945, 0.971$. The geometrical aspect ratio for the simulations is chosen to be the same as in the experiment with $a = 5\mu m$, whose typical outcomes are also reported ($\circ$).

to overcome and work has to be done in order to induce the transition [3, 11]. The bottom-view observations reveal that the micro-structured surface is not wetted all at once, but the infiltration starts locally. In our case, this happens spontaneously after a few seconds whereas in other cases (i.e. larger h) the infiltration can take longer and one may want to trigger it. Once the transition has started, how to theoretically understand the shape of the wetted area, the zipping, and the different involved timescales? For the dynamics of liquid moving in between the posts, both the free

surface and wall interactions play a role. A small advancing displacement $dx \ll a$ of the interface within the posts would take place in favour of a gain in surface energy due to the reduction of liquid-gas interface ($\sigma_{lg} a dx$) on the top of the pillars. This is a pulling mechanism for the transition that must be balanced with the energy loss to wet a small portion of hydrophobic wall ($\sigma_{lg}(2h+a)dx\cos\theta$, $\cos\theta < 0$). The overall energy gain is

$$dE_s = \sigma_{lg} a dx + \sigma_{lg}(2h+a)dx\cos\theta. \tag{8.1}$$

The limit $dE_s \to 0$ characterizes a critical contact angle θ_c for the wetting properties above which the liquid can spread horizontally through the posts. For square posts and square geometry it is equal to

$$\cos\theta_c = -1 + \frac{2h}{2h+a}. \tag{8.2}$$

Note that in this equation there is no reference to the width w of the posts because we describe the horizontal filling, different from a simultaneous vertical collapse [1, 11]. With this critical value, the energy gain (8.1) can be rewritten as

$$dE_s = \sigma_{lg} a dx \left(1 - \frac{\cos\theta}{\cos\theta_c}\right) \tag{8.3}$$

where for $\cos\theta < \cos\theta_c$ no favorable propagation is expected while in the other case, when $\cos\theta_c < \cos\theta < 0$, the propagation is energetically favored. For the two analyzed cases $a = 5\mu m$ and $11\mu m$ we obtain $\theta_c = 101.54°$ and $110.78°$, respectively. As $\theta = 100°$ for water on flat kraton, we thus understand that for gap widths smaller than $a = 4.2\mu m$ the propagation to the W state is energetically not possible.

We can also understand the critical slowing down of the front close to the critical angle θ_c (Fig. 8.4). Therefore we have to identify the relevant time scale τ for the system and quantify its fluctuations with respect to the geometry. To do so, we estimate the energy cost in terms of dissipation and compare it with the change in surface energy of Eq. (8.3). With the small dimensions under consideration, flows can be regarded as laminar and viscous dissipation is dominating as compared to flow inertia. A simple estimate for the rate of viscous dissipation per unit volume in a fluid with viscosity η is $\epsilon \approx \eta \dot{\gamma}^2$ [22], with $\dot{\gamma} \sim 1/\tau$ the characteristic shear rate. If we integrate it over the small volume $dV = ahdx$ and time lag τ, we obtain the viscous contribution for the energy as $dE_d \approx \epsilon \tau dV = \eta ahdx/\tau$. Balancing dE_s in Eq. (8.3) with dE_d, we deduce the time scale

$$\tau = \frac{t_0}{\left(1 - \frac{\cos\theta}{\cos\theta_c}\right)} \tag{8.4}$$

with $t_0 = \eta h/\sigma_{lg} \sim 10^{-7}$s for typical values of η, σ_{lg}, and $h = 10\mu$m. Equation (8.4) reveals the origin of the critical slowing down of the front propagation, its dispersion and the appearance of zipping: if $\theta \sim \theta_c$, the timescale τ of front propagation *diverges* as $\tau \sim 1/|\theta - \theta_c|$. Around this *critical point*, a small uncontrollable variation (imperfections of the microstructure, dust deposit) in the local wetting angle translates into a huge dispersion in the time scales, which is consistent with the experimental observation shown in Fig. 8.4a. A flat front is slowly allowed to proceed further, and entering a new row perpendicular to the direction of the front can take up to milliseconds, whereas once this has happened, the row itself is filled on a faster time scale (*zipping*). In this way a square-shaped propagating wetting pattern emerges (see the case with $a = 5\mu$m in Fig. 8.3b where $\theta_c \sim 101.54°$ and $\theta \sim 100°$).

On the contrary, when approaching the other limit $\cos\theta/\cos\theta_c \ll 1$ (as in Fig. 8.3c, where $\theta \sim 100°$ and $a = 11\mu$m, implying $\theta_c \sim 110.78°$) the dynamics becomes more and more determined by the time scale t_0 itself (see Fig. 8.4b) and the propagation through the posts is expected to be smooth. In this limit it is the pure pulling mechanism of surface tension in equation (8.3) that dominates the spreading dynamics and is prevalent over wall effects [23]. For this reason, the geometrical properties of the lattice do not emerge and the front assumes an almost circular shape.

8.4 Characterization of the zipping process

In §8.3 it has been pointed out that a critical slowing down of the wetting front (involved when θ_f becomes close to θ_c, Eq. 8.2) results in large dispersion of the measured front velocities, carried out from several experiments with the same sample, although in each case the front velocity remains almost constant during the filling. We also noticed that, although averaged front velocities vary from one experiment to the other close to the critical point, the main zipping wetting features persist, provided that experiments are performed close enough to the critical point. The question we address in this paragraph is: how can we characterize the dynamics during the invasion process?

8.4.1 Experimental results

To answer this question, we have performed large and small scale measurements using Kraton micropatterns (Fig. 8.2), with $a = 5\mu$m, $w = 5\mu$m, and $h = 10\mu$m. Figure 8.6a shows the main front position as a function of time in a typical experiment. When the filled area only extends over few pillars the dynamics undergoes a transitional regime, also observed in the numerical simulations. Afterwards, the front velocity is found to be $V_f = 2.3$ mm/s. Since V_f is almost constant and, at the same time, the square-shaped pattern remains, one may wonder how the zipping
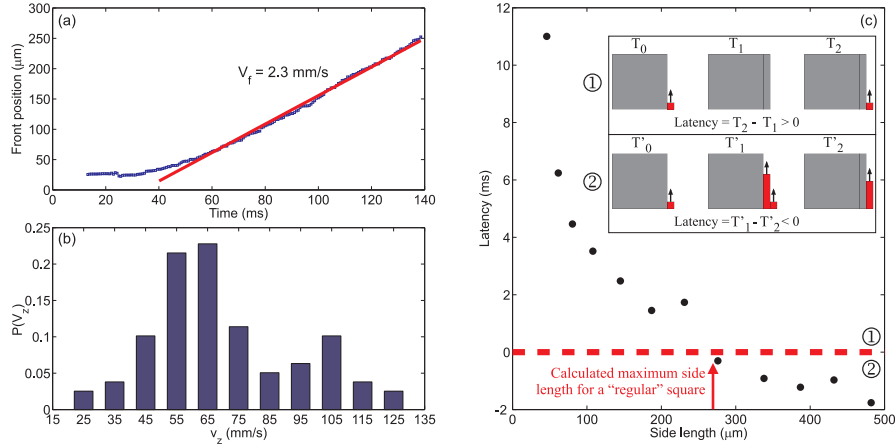
Figure 8.6: (a) Temporal evolution of the front position. Values have been averaged over the 4 sides of the square-shaped pattern, starting from its center. (b) Probability distribution of the zipping velocity V_z. (c) Measured latency as a function of the side length. The insets (1) and (2) sketch out how positive and negative latencies have been calculated, respectively (see text for details). The red dashed line shows $l_t = 0$. According to the theory, the latency becomes negative at a side length of $270\,\mu m$ (see arrow). As observed in the corresponding movie, beyond this value the pattern is not a perfect parallelepiped anymore.

process adjusts. Figure 8.6b shows the probability distribution of the zipping velocity V_z involved to fill a row, throughout the filling, processed over approximately 500 frames. Interestingly, it shows a bimodal distribution with a significant dispersion. One may speculate that the maximum of the probability distribution, located at $V_z^{max} = 62\,mm/s$, corresponds to the wetting dynamics for an ideal sample. The large dispersion can be attributed to surface inhomogeneities resulting in a surface energy lowering (caused by defects or impurities). Larger defects might be the cause of the second peak, located around $V_z = 105\,mm/s$.

Beyond the observed dispersion of the zipping velocity, it is worthwhile noticing that rows do not fill one by one continuously. A schematic picture of this is provided in the inset at Fig. 8.6(c). When the filled square is still small, a sideway row gets filled (at time T_1), and then the next row (at time T_2) after a latency time ($l_t = T_2 - T_1 > 0$). The latency is decreasing with increasing square size until it finally vanishes (at about $270\,\mu m$ square side length, (1) in Fig. 8.6(c)). Afterwards, a different scenario is observed. The new row is already started (at time T_1') before the former one has been completed (at time T_2'). In this case, we express the latency time as $l_t = T_1' - T_2' < 0$ ((2) in Fig. 8.6(c)). As a consequence, the filled area cannot be seen as a perfect parallelepiped any longer although the macroscopic square-like shape remains, con-

sidering that the filled surface gets larger. Moreover, the side length corresponding to $l_t = 0$ can simply be calculated from velocities by $V_z^{max}/V_f \times d = 270\,\mu m$, which is in good agreement with the length extrapolated in Fig. 8.6(c).

Details of the front advancing in between the posts are shown in Fig. 8.7a. The height is *a priori* not exactly known. The dynamics of the interface are captured in a plane close to the middle of the pillars. Based on the objective specifications, we estimate it to be at $z = 4 \pm 1\,\mu m$ from the base. The dynamics are processed from an experimental record chosen especially for its low V_z/V_f ratio to better reveal main and zipping front progressions at once. Thus, when averaged over $20\,\mu m$, the main front velocity is $V_f = 1.9\,mm/s$ and the zipping front velocity is $V_z = 10\,mm/s$. The figure enables a comprehensive picture of the complex dynamics in the 2d plane: position, curvature and velocity variation of the interface are easily accessible. Front and zipping interface positions as a function of time are quantitatively tracked in Fig. 8.7b along the straight lines passing through the middle of the 4 rows shown in Fig. 8.7a. First, the two perpendicular liquid-gas interfaces defined as main and zipping fronts spread between the pillars and reach almost simultaneously the edge. Next, they fastly merge, and the resulting interface straighten. Rectangles drawn in Fig. 8.7b highlight this stage. In rectangles labeled "1", main and zipping fronts are superimposed, indicating that the interface at an intersection is almost symmetric. In rectangles labeled "2", the merged front has reached a lower velocity and an asymmetry develops: V_z increases more than V_f. Afterwards, when the interface has reached the opposite post, it splits into 2 fronts that progress in main and zipping direction respectively, with drastically different velocities. The passage is made within $4\,ms$ for the main front whereas it is almost 2 orders of magnitude less for the zipping front. Here the interface is described in one plane, but since the filling is a 3d process, it is straightforward that several planes should be analyzed simultaneously. Unfortunately this cannot be achieved experimentally. Therefore, we have carried out numerical simulations to better reveal the 3d structure as well as the dynamics of the zipping mechanism.

8.4.2 Numerical results

For the numerical simulations presented here, we use a 3d lattice Boltzmann [19, 26, 27] model for single component multiphase flows whose details are discussed in [20, 21]. In all these mesoscale models [28], it is impossible to match all the physical parameters and preserve at the same time a feasible computation. Typically the width of the interface is too large and the liquid-gas density difference is unphysically small with respect to physical reality. As already noticed elsewhere [29, 30], this may affect the speed of the interface that, if directly proportional to the interface width and inversely proportional to the density difference, will move too quickly in the simulations when compared to an experiment. This must be taken into account
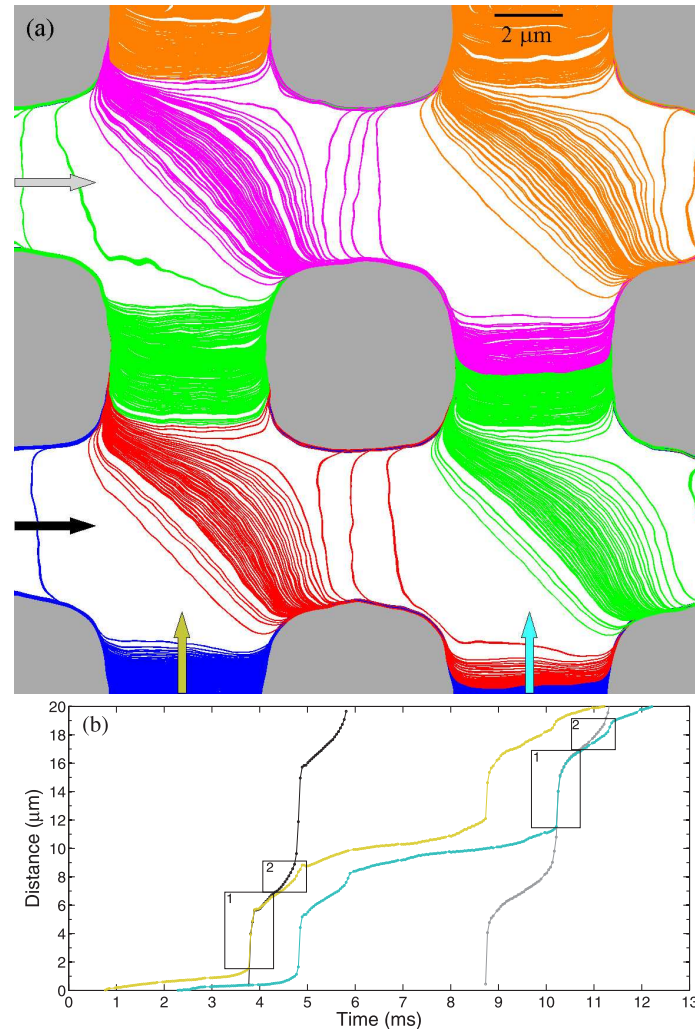
Figure 8.7: (a) Details of the zipping process in the experiment. Liquid-gas interface positions obtained every 20 μs are simultaneously drawn. The filling begins at bottom-left corner. The main front (responsible for the macroscopic square shape) is from bottom to top. The zipping front (in a row to be filled) is from left to right. Color changes after an interface has detached from a pillar; in chronological order: blue, red, green, pink, orange. (b) Interface position as a function of time along the 4 straight lines suggested by the arrows in (a). Curve and arrow colors match. Labeled rectangles correspond to different steps in the dynamics, as explained in the text. Notice that the balancing of capillary effects with viscous forces [24] in between the pillars should lead to an asymptotic Washburn-like behavior [25] for the front position rescaling as the square root of time. However, pillars are not wide enough and the system hardly reaches the stationary state of such a balance. We consequently observe a series of not stationary fillings whose main linear trend can be measured in the experiments (see also §8.3).
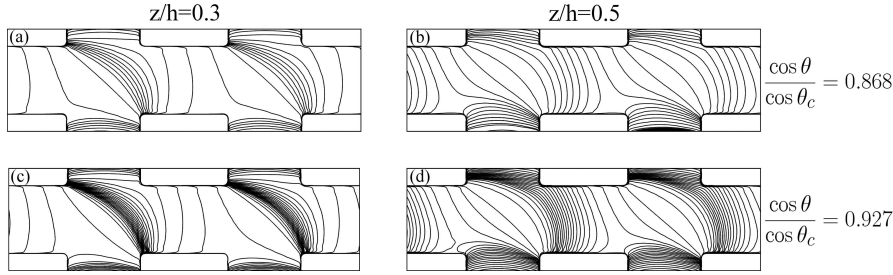
Figure 8.8: Numerical simulations reveal the details of the zipping mechanism. Two values of the wetting properties are used with respect to the critical angle given in Eq. (8.2): $\cos\theta/\cos\theta_c = 0.868$ ((a) and (b)) and $\cos\theta/\cos\theta_c = 0.927$ ((c) and (d)). The interface position is tracked as a function of time (from left to right) at a given height z ($z/h = 0.3$ for (a) and (c) and $z/h = 0.3$ for (b) and (d)) and all plots are equispaced with the same numerical time lag. When approaching the critical point ((c) and (d)), the zipping is experiencing a dynamical slowing down followed by a rapid merging process. The pulling mechanism provided by the liquid on the top of the pillars is inducing a complex 3d stretching that deforms the interface. An insight of this is provided by the cuts at different heights ($z/h = 0.5$ and $z/h = 0.3$). In particular, quantitative agreement is found with the experiments, assuming a height less than $h/2$ ($z/h = 0.3$ in (c)).

by renormalizing the time scale if one wants to reconstruct a correct pathway as a function of time [29, 30].

All the geometrical aspect ratios for the surface micro-structures can be adapted in order to match those typically studied in the experiments [31] and wall interactions with wetting properties are introduced as explained in [20, 21]. The initial condition consists of a liquid reservoir on the top of the pillars and an infiltration characterized by a flat front perturbed with an advanced liquid precursor, just as experimentally observed at the onset of zipping. In this way the liquid precursor induces a lateral motion that is continuously driven by the pulling mechanism of surface tension on the top of the pillars. After a small time transient, the properties of this numerical zipping motion show a remarkable independence on the initial condition details and are reported in Fig. 8.8 (zipping is advancing from left to right in these figures). Two wetting properties are shown, $\cos\theta/\cos\theta_c = 0.868$ ((a) and (b)) and $\cos\theta/\cos\theta_c = 0.927$ ((c) and (d)) and the interface contour is tracked in a two dimensional plane for two different heights, $z/h = 0.3$ ((a) and (c)) and $z/h = 0.5$ ((b) and (d)).
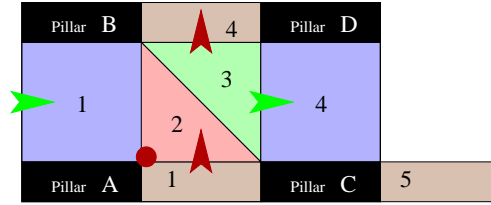
Figure 8.9: Sketch of the different steps in the zipping process. The numbered areas refer to the text. As in Figs. 8.7(a) and 8.8, the zipping front is from left to right (green arrows) and main front is from bottom to top (red arrows).

8.4.3 Description of the zipping process

The results presented in Figs. 8.7a and 8.8 reveal the complex structure of the zipping process, both from experimental and numerical viewpoints. Firstly the liquid precursor fastly merges with its neighbor and after that experiences a passage through the walls. It is observed that as one approaches the critical point the numerical pathway at the height $z/h = 0.3$ in Fig. 8.8c shares quantitative agreement with the experimental one.

Starting with the case $z/h = 0.3$, the successive steps of the zipping process are described as numbered in Fig. 8.9.

1- The pulling mechanism induced at the top of the pillars makes zipping and main front interfaces merge (red point at the corner of pillar A).

2- The liquid bridge suspended on the four pillars collapses at pillar A, producing a local top-to-bottom pulling mechanism. The dynamics is dominated by surface tension effects that tend to reduce the strongly curved surface of the merged interface, by drawing liquid from the top. Wall effects are negligible in this extremely fast process (within $20\,\mu s$ in the experiment): it is almost independent of the wetting properties (compare for example case (b) and (d) in Fig. 8.8).

3- Since the interface is straight, the pulling persists but the interface above is behind (late). Viscous dissipation dominates, making the front much slower (time scale is $\approx 1\,ms$ in the experiment). Moreover, the interface is still pinned on the edges of pillars B and C.

4- The interface reaches pillar D and splits into two parts and then the filling progresses. The dynamical details are influenced by wall interactions that cause a slowing down for the propagation. This is strongly pronounced especially when the wetting properties approach the critical point passing from (a) to (c) in fig. 8.8.

The pulling mechanism on the top of the pillars is stretching the interface, and obviously the closer to the top the stronger it is. Consequently, we choose a cut plan at $z/h = 0.5$ to evidence the change in the dynamics. If we compare with $z/h = 0.3$, the front is slower in region 2, but much faster in region 3 where the slowing down is not

observed (compare (c) to (d) in Fig. 8.8). Interestingly, this makes the liquid invade the gap between pillars C and D at $z/h = 0.5$ before than at $z/h = 0.3$. The resulting stretching overcomes the wall interactions that, being in the slightly hydrophobic regime ($\theta_f \sim 100°$), act to prevent a complete wetting of the boundaries (Figs. 8.7a and 8.8c).

One has to remember that liquid is present in area 5, causing the interface that bridges over pillars C and D to be more curved than the one over pillars B and D (the portion beyond these pillars in not filled). This induces a faster filling in the zipping direction (green arrows in Fig. 8.7) than in the main front direction (red arrows). The front velocity between pillars C and D is progressively increased while the interface along pillar C is deformed by a stronger pulling (Fig. 8.8d). It can be assumed that this effect is mainly at the base of the macroscopic square front and that the zipping velocity is quite sensitive to slight variations of the shape of the pillars top.

8.5 Scaling of the front velocity in CB to W transition

By placing the drop completely on an array of pillars the initiation time as well as the initial location strongly varies. To control the initiation point and time of the transition, the water drop is placed at the edge of the patterned area (Fig. 8.10). Initial spreading now occurs at the flat surface, which lowers the energy barrier for wetting the volume between the pillars. The figure shows three steps in time to illustrate the movement of the liquid in the zipping regime. For moderate values of the height, this procedure leads to similar front velocities as those obtained after a spontaneous infiltration by placing the drop completely on the pillars. To highlight the overlap between the two methods, the front velocities from §8.3 were compared to the results obtained for the same geometries in this paragraph. Quantitative overlap was found. For a Kraton film with $h = 10\mu m$ and $a = 11\mu m$, the initial method generated a front velocity of 0.7 ± 0.05 m/s [32], whereas the above described method produces a front velocity of 0.8 ± 0.29 m/s (both methods averaged more than 9 recordings). This strategy allows us to collect data, even for those micro-patterns where the Wenzel state could not be observed with the initial method as the time until transition was longer than the evaporation time of the drop.

During the wetting transition, the liquid-gas interface moving in between the pillar pattern is followed and its velocity determined from high-speed movies. This front velocity v_f depends on the type of substrate (water contact angle θ), pillar height h, and gap size a between the pillars. All averaged experimental data points are displayed in Fig. 8.11. At least 3 and up to 25 measurements were performed to generate each point (457 experiments in total).

The data show that all three control parameters (a, h, and θ) influence the front velocity significantly. The velocity increases with increasing gap size a. For the
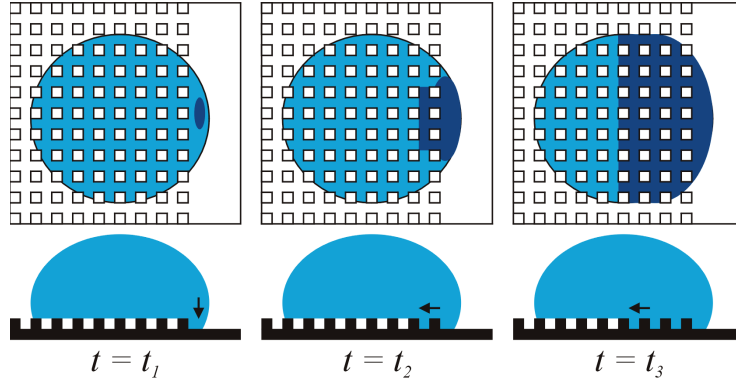
Figure 8.10: Three images illustrating the spreading of the liquid between the pillars in the zipping regime in time (bottom and side views, not to scale). Left: the base of a drop hangs over the edge of an array of pillars and touches the flat surface at $t = t_1$. Middle: the first row is filled at $t = t_2$. Right: the liquid is moving in between the pillars from the third to the fourth row at $t = t_3$. The liquid slows down significantly when reaching the edge of the drop base.

same material and gap size the velocity decreases with increasing pillar height h. For a given geometry the velocity is reduced as the material displays a larger contact angle θ. As mentioned in §. 8.3, a critical point for front propagation can be defined by balancing the energy equations. The values for the critical gap size a_c for the different patterns described here can be calculated using

$$a_c = \frac{2h}{\cos\theta + 1} - 2h \quad , \tag{8.5}$$

which is Eq. 8.2 in rewritten form. When $a > a_c$, front propagation is energetically favored, whereas for $a < a_c$ any front will stop. These values, below which no front propagation takes place, can also be obtained experimentally from the data (gap size at zero front velocity) in Fig. 8.11. In the next sections, we describe the scaling of front velocities with geometrical (a and h) and material (θ) parameters.

8.5.1 Unitary cell approach

Based on the knowledge that there are two limiting cases with different characteristics (zipping and non-zipping), the presence of multiple scaling arguments is expected, each valid for its own regime. The unit cell is characterized by the sum of the volume between two pillars (volume A in Fig. 8.12) and the volume beyond the pillars (volume B). The difference in surface energies before and after wetting volume A and B can be written as
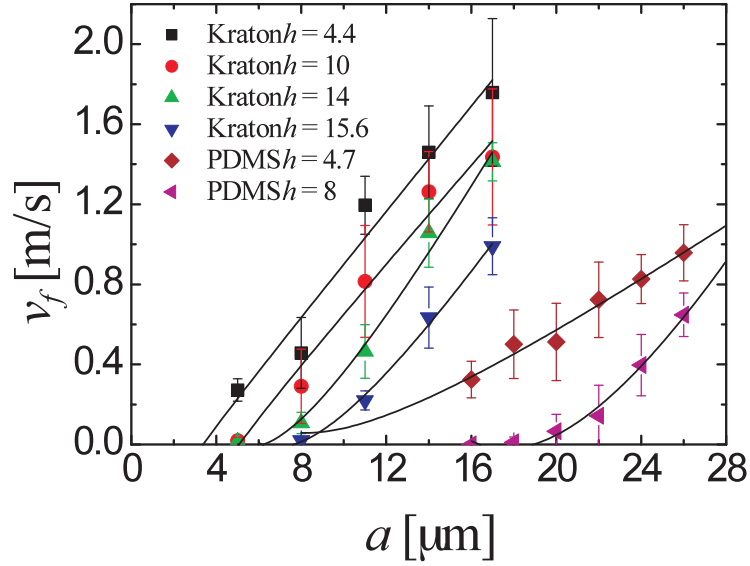
Figure 8.11: Front velocity v_f versus gap size a for Kraton ($\theta \sim 100°$) and PDMS ($\theta \simeq 120°$) at different pillar heights h (given in μm, see legend). In order to estimate the critical gap size a_c from these experimental data, each data set is fitted by some spline-type function and the fits (solid lines) are then extrapolated to $v_f = 0$ m/s. The obtained values of a_c are shown in Table 8.2 and compared with the theoretical expectations.

Material	h (μm)	a_c (Eq. 8.5) (μm)	a_c (exp) (μm)
Kraton	4.4	1.9	3.4
	10	4.2	5.1
	14	5.9	6.2
	15.6	6.6	6.2
PDMS	4.7	9.4	8.2
	8	16.0	18.9

Table 8.2: Critical gap sizes a_c for different pillar heights h, obtained from equation 2 and from experimental fitting

$$\Delta E_s = \sigma_{LG}(d^2 - w^2) + (\sigma_{SG} - \sigma_{LS})(d^2 - w^2 + 4wh)$$

$$= \sigma(d^2 - w^2)\left(1 + \cos\theta\left(\frac{d^2 - w^2 + 4wh}{d^2 - w^2}\right)\right) \tag{8.6}$$

with σ the surface tension of the liquid-air interface. This energy gain has to be balanced with the viscous dissipation in the unit cell that we estimate with the volume integral of the velocity shear rate, estimated as v/l

$$\Delta E_d \simeq \int dV \eta \frac{v}{l} = h(d^2 - w^2)\eta \frac{v}{l} \tag{8.7}$$

with $h(d^2 - w^2)$ the volume of the unit cell, η the dynamical viscosity of the liquid, v a characteristic velocity and l a characteristic length scale. The definition of l is crucial to understand the way the front velocity scales as a function of geometry and material properties [24]. As reported in §8.3 and §8.4 the 3D filling dynamics is very complex, including strong spatial anisotropies. If the gap size a is larger than the pillar height h, the shear rate is expected to be dominated by the vertical direction ($l \sim h$). In the other limit ($a << h$) the shear rate is gap-dominated ($l \sim a$). Due to the presence of the critical point it is difficult to do experiments with gap sizes much smaller than the pillar height. The gap is usually larger than, or on the order of, the pillar height and therefore $l \sim h$ is introduced in Eq. 8.7. Balancing Eqs. 8.6 and 8.7 with $l \sim h$ leads to the front velocity as a function of geometry and wetting properties, which can be written as the dimensionless capillary number Ca

$$Ca = \frac{\eta v}{\sigma} \simeq 1 + \cos\theta\left(\frac{d^2 - w^2 + 4wh}{d^2 - w^2}\right) \quad . \tag{8.8}$$

This averaged capillary number is a measure of the averaged viscous forces per unit length (ηv) against the capillary forces per unit length (σ). This scaling argument is not generally valid though. A simple estimate of the viscous integral as in Eq. 8.7 does not take local variations in the velocity into account. The next section will address this point.

8.5.2   Two subcell approach

In the zipping regime ($a \sim a_c$), the overall front velocity v_f can actually include two time scales τ_1, τ_2 with τ_1 being much smaller than τ_2, see §8.4. τ_1 equals the time needed to propagate in between two pillars (fill volume A, figure 8.12) and τ_2 equals the time needed to fill up the next row (volume B, Fig. 8.12). In §8.3, only τ_1 was derived by matching surface energy with viscous dissipation between the pillars of subcell A
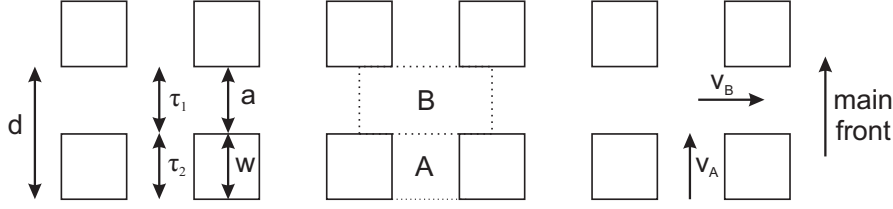
Figure 8.12: Illustration of the top view of twelve pillars with wavelength d (gap size a + pillar width w), timescales τ_1 and τ_2 and velocities v_A and v_B. The dotted lines mark the unit cell with subcells A and B.

$$\tau_1 = \frac{t_0}{1 - \frac{\cos\theta}{\cos\theta_c}} = \frac{\eta h}{\sigma\left(1 + \cos\theta\left(\frac{2h+a}{a}\right)\right)} \quad . \tag{8.9}$$

To obtain an overall front velocity, the residence time in both subcells has to be defined. For that a characteristic velocity is considered separately for each subcell (A and B). The in-plane velocity of the liquid in subcell A is defined as v_A and the liquid advances in the direction of the main front. The liquid in subcell B propagates in the direction perpendicular (in-plane) to the liquid in subcell A with a characteristic velocity v_B (Fig. 8.12). Reformulating the surface energy gain and balancing that with the relative energy dissipation separately, one obtains for subcell A:

$$awh\eta\frac{v_A}{h} = \sigma aw\left(1 + \cos\theta\left(\frac{2h+a}{a}\right)\right) \tag{8.10}$$

and for subcell B:

$$adh\eta\frac{v_B}{h} = \sigma ad\left(1 + \cos\theta\left(\frac{2wh+da}{da}\right)\right) \quad . \tag{8.11}$$

Hence there is a capillary number for each subcell:

$$Ca_A = \frac{\eta v_A}{\sigma} = 1 + \cos\theta\left(\frac{2h+a}{a}\right) \quad , \tag{8.12}$$

$$Ca_B = \frac{\eta v_B}{\sigma} = 1 + \cos\theta\left(\frac{2wh+da}{da}\right) \quad . \tag{8.13}$$

It can be shown that $Ca_A \leqslant Ca_B$ is generally valid for a hydrophobic substrate ($\cos\theta < 0$) since

$$\frac{2h+a}{a} \geqslant \frac{2wh+da}{da} \tag{8.14}$$

as $d \geqslant w$ because $d = a + w$. The conclusion is that filling up subcell B is never slower than filling up subcell A. In the zipping regime this difference in filling veloc-ity between the two subcells is clearly observed. Volume B is filled much faster than volume A. Near the critical point the front between the pillars (in volume A) almost stops. In this limiting case $\cos\theta \to \cos\theta_c$ and the capillary numbers become

$$Ca_A = 1 - \left(\frac{a}{2h+a}\right)\left(\frac{2h+a}{a}\right) = 0 \quad , \tag{8.15}$$

$$Ca_B = 1 - \left(\frac{a}{2h+a}\right)\left(\frac{2wh+da}{da}\right) > 0 \quad . \tag{8.16}$$

By treating the two subcells separately, scaling arguments can be identified. The front velocity is evaluated in a unidirectional way: the filling is followed along a line between two rows of micro-pillars in the main front direction (Fig. 8.12). The front velocity is thus defined in terms of distance that the front travels to fill up volume A and B, divided by the time it needs for that,

$$v_f = \frac{d}{\tau_1 + \tau_2} \simeq \frac{d}{\tau_A + \tau_B} \tag{8.17}$$

with τ_A the time scale corresponding to velocity v_A ($\tau_1 = \tau_A$) and τ_B to velocity v_B ($\tau_2 \simeq \tau_B$). From here on we distinguish between two limiting regimes. In the zipping regime ($a \simeq a_c$) time scale τ_A is much larger than time scale τ_B due to its divergence as stated before. The overall front velocity is therefore dominated by time scale τ_A (see appendix). This time scale can be described as $\tau_A = w/v_A$ and can be combined with Eq. 8.10 for subcell A. The resulting equation for the front velocity in the zipping regime is

$$v_z \simeq \frac{d}{\tau_A + \tau_B} \simeq \frac{d}{\tau_A} = \frac{\sigma}{\eta}\frac{d}{w}\left(1 + \cos\theta\left(\frac{2h+a}{a}\right)\right) \tag{8.18}$$

or rewritten in dimensionless terms as

$$Ca_z \simeq \frac{d}{w}\left(1 + \cos\theta\left(\frac{2h+a}{a}\right)\right) \quad . \tag{8.19}$$

In the non-zipping regime a is much larger than a_c and the large scale wetting pattern is more circular. This imposes that the velocities, v_A and v_B, are almost comparable, which gives

$$\frac{w}{\tau_a} \simeq \frac{a}{\tau_B} \quad . \tag{8.20}$$

Using the same approach as for the zipping regime, the overall non-zipping velocity becomes
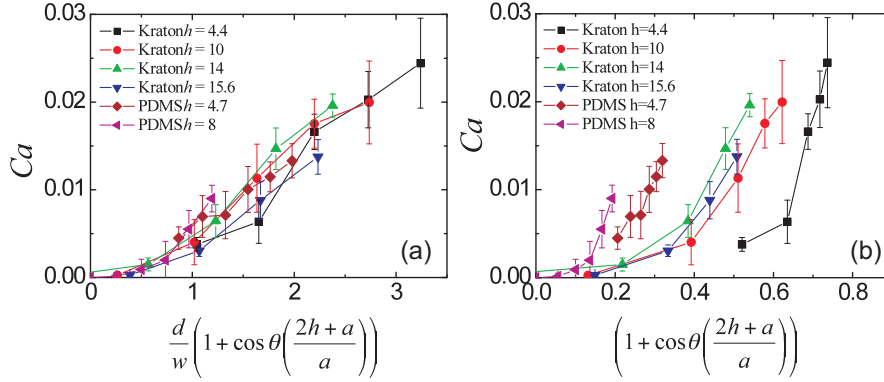
Figure 8.13: Same data as Fig. 8.11, but now plotted as Capillary number Ca versus the scaling factor suggested by Eq. 8.19 for the various materials and pillar heights h (given in µm). The data should give a universal curve in the zipping regime according to Eq. 8.19.

$$v_{nz} \simeq \frac{d}{\tau_A + \tau_B} \simeq \frac{d}{\tau_A + \frac{a}{w}\tau_A} = \frac{\sigma}{\eta}\left(1 + \cos\theta\left(\frac{2h+a}{a}\right)\right) \qquad (8.21)$$

and in dimensionless form

$$Ca_{nz} \simeq 1 + \cos\theta\left(\frac{2h+a}{a}\right) \qquad . \qquad (8.22)$$

Equations 8.19 and 8.22 express the core of this paragraph, predicting a scaling behavior for the capillary number as a function of the geometry (a and h) and wetting properties (θ). For both scaling relations it holds that an increase in a (for fixed h and θ with $\theta > 90°$) produces an increase in capillary number Ca (increased velocity). An increase in h (for fixed a and θ with $\theta > 90°$) results in a decrease in Ca. These observations match the trends in the experimental data (Fig. 8.11).

To assess the quantitative accuracy of Eqs. 8.19 and 8.22, the scaling arguments are applied to the experimental data. In Fig. 8.13a the rescaling for the zipping regime (Eq. 8.19) is displayed. An excellent degree of collapse is observed for small gap sizes, where the zipping mechanism is expected to dominate. Even for larger gap sizes, where the filling is expected to be less influenced by the zipping mechanism, the proposed scaling argument still provides a good data collapse. Equation 8.19 reveals that the relevant geometrical parameters influencing the front velocity are the non-dimensional ratios d/w and h/a.

Rescaling according to the non-zipping equation (Eq. 8.22) does not result in a collapse of the data (Fig. 8.13b). Indeed, at these gap sizes the wetted area still displays a step-like contour (Fig. 8.14), which indicates that the zipping motion is still present.
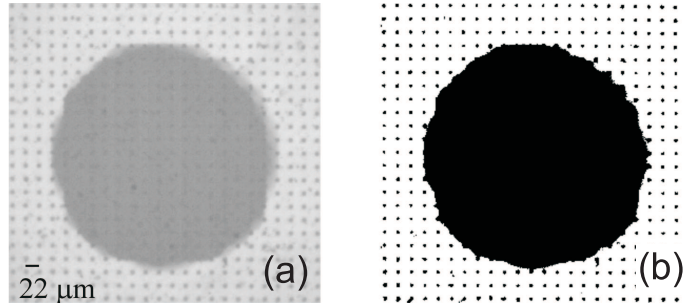
Figure 8.14: (a) Original image of one frame (exposure time 5 μs) during the wetting transition on a micro-patterned Kraton surface with d=22μm and h=10μm. The wetting front seems to be circular. (b) The same image with enhanced contrast. Now a step-like contour becomes visible at the liquid front.

A pure non-zipping regime is expected for patterns with even larger gap sizes, involving front velocities beyond our experimental recording capabilities (probably in the order of 10 m/s).

8.6   Conclusion

In conclusion, we have experimentally, numerically, and theoretically revealed the origin of zipping wetting behavior at the spontaneous breakdown of superhydrophobicity. We observed that the wetting process starts locally from a single point and then proceeds laterally, depending on a critical contact angle. The critical contact angle can be calculated from the geometrical properties of the micro-textured material and is consistent with our experimental and numerical findings. Close to this critical point the driving energy for the lateral filling reduces, the front propagation slows down through viscous effects and zipping wetting is observed. As a consequence, the front propagates in a stepwise manner and square-shaped [33] wetted areas emerge.

In the zipping regime, even if the pattern grows in a regular way (the front velocity V_f is almost constant), the zipping velocity V_z involved to fill a row undergoes a noticeable dispersion (from 25 to 125 mm/s in a typical experiment). This reveals the strong sensitivity of the dynamics to local wetting properties without prejudging the cause (roughness variation, geometrical imperfection, material inhomogeneity, dust deposit, . . .). Interested in getting further details at a smaller scale, we have performed high-speed submicron observations of the zipping-wetting dynamics. The dynamical details of the interface demonstrate the complexity of the invasion process, while being in very good agreement with numerical predictions for $z/h = 0.3$ (corresponding to $z = 3$μm in the experiment). Moreover, the numerical results shown

for $z/h = 0.5$ give a deeper insight of the complex 3d stretching experienced by the interface.

Finally, the geometry (pillar height and gap size) and material surface properties (water contact angle) of the surfaces has been varied extensively. The velocity of the wetting front increases with increasing gap size, decreasing pillar height or decreasing contact angle. The theoretically derived critical gap size, below which no transition occurs, is also observed in the experiments.

Balancing interfacial energy contributions with viscous dissipation yielded universal equations for the zipping and the transition dynamics. When using the height of the pillar as a characteristic length scale for the shear rate, good scaling is obtained with the argument for the zipping regime. Scaling arguments have also been derived to determine whether the assumption of a horizontal characteristic length scale for the shear rate ($l \simeq w$) could be correct. This did not lead to any scaling for the set of experimental data, neither for the zipping nor for the non-zipping regime. The relevant parameters driving the front velocity are therefore the non-dimensional ratios d/w and h/a. These scaling arguments provide design criteria to tune the liquid velocity precisely on a micro-scale level. Future work will be devoted to exploring its practical use in the field of microfluidics, in particular by experimenting with other geometries and arrays of decreasing gap sizes.

References

[1] P.-G. de Gennes, F. Brochard-Wyart, and D. Quéré, *Capillarity and Wetting Phenomena: Drops, Bubbles, Pearls, Waves* (Springer, New York) (2003).

[2] C. Neinhuis and W. Barthlott, "Characterization and distribution of water-repellent, self-cleaning plant surfaces", Ann. Bot. **79**, 667–677 (1997).

[3] J. Bico, C. Marzolin, and D. Quéré, "Pearl drops", Europhys. Lett. **47**, 220–226 (1999).

[4] D. Quéré, "Surface chemistry - fakir droplets", Nat. Mater. **1**, 14–15 (2003).

[5] A. Lafuma and D. Quéré, "Superhydrophobic states", Nat. Mater. **2**, 457–460 (2003).

[6] T. M. Squires and S. R. Quake, "Microfluidics: Fluid physics at the nanoliter scale", Rev. Mod. Phys. **77**, 977–1026 (2005).

[7] E. Lauga, M. P. Brenner, and H. A. Stone, *Handbook of Experimental Fluid Dynamics* (Springer, New York) (2005).

[8] A. Otten and S. Herminghaus, "How plants keep dry: A physicists point of view", Langmuir **20**, 2405–2408 (2004).

[9] A. B. D. Cassie and S. Baxter, "Wettability of porous surfaces", Trans. Faraday Soc. **40**, 546–551 (1944).

[10] V. Bergeron, D. Bonn, J. Martin, and L. Vovella, "Controlling droplet deposition with polymer additives", Nature **405**, 772–775 (2000).

[11] B. He, N. A. Patankar, and J. Lee, "Multiple equilibrium droplet shapes and design criterion for rough hydrophobic surfaces", Langmuir **19**, 4999–5003 (2003).

[12] R. N. Wenzel, "Resistance of solid surfaces to wetting by water", Ind. Eng. Chem. **28**, 988–994 (1936).

[13] L. Feng, S. Li, Y. Li, H. Li, L. Zhang, J. Zhai, Y. Song, B. Liu, L. Jiang, and D. Zhu, "Super-hydrophobic surfaces: From natural to artificial", Adv. Mater. **14**, 1857–1860 (2002).

[14] N. A. Patankar, "On the modeling of hydrophobic contact angles on rough surfaces", Langmuir **19**, 1249–1253 (2003).

[15] N. A. Patankar, "Transition between superhydrophobic states on rough surfaces", Langmuir **20**, 7097–7102 (2004).

[16] T. N. Krupenkin, J. A. Taylor, T. M. Schneider, and S. Yang, "From rolling ball to complete wetting: The dynamic tuning of liquids on nanostructured surfaces", Langmuir **20**, 3824–3827 (2004).

[17] L. Vogelaar, R. Lammertink, and M. Wessling, "Superhydrophobic surfaces having two-fold adjustable roughness prepared in a single step", Langmuir **22**, 3125–3130 (2006).

[18] T. S. Meiron, A. Marmur, and I. S. Saguy, "Contact angle measurement on rough surfaces", J. Colloid Interf. Sci. **274**, 637–644 (2004).

[19] R. Benzi, S. Succi, and M. Vergassola, "The lattice boltzmann equation: Theory and applications", Phys. Rep. **222**, 145–197 (1992).

[20] R. Benzi, L. Biferale, M. Sbragaglia, S. Succi, and F. Toschi, "Mesoscopic modeling of a two-phase flow in the presence of boundaries: The contact angle", Phys. Rev. E **74**, 021509 (2006).

[21] M. Sbragaglia, R. Benzi, L. Biferale, S. Succi, and F. Toschi, "Surface roughness-hydrophobicity coupling in microchannel and nanochannel flows", Phys. Rev. Lett. **97**, 204503 (2006).

[22] L. D. Landau and E. M. Lifschitz, eds., *Fluid Mechanics* (Pergamon, London) (1959).

[23] T. Cubaud and M. Fermigier, "Faceted drops on heterogeneous surfaces", Europhys. Lett. **55**, 239–245 (2001).

[24] C. Ishino, M. Reyssat, E. Reyssat, K. Okumura, and D. Quéré, "Wicking within forests of micropillars", Europhys Lett. **79**, 56005 (2007).

[25] E. W. Washburn, "The dynamics of capillary flow", Phys. Rev. **17**, 273–283 (1921).

[26] S. Succi, *The Lattice Boltzmann Equation* (Oxford University Press, Oxford) (2001).

[27] D. A. Wolf-Gladrow, *Lattice Gas Cellular Automata and Lattice Boltzmann Models* (Springer, Berlin) (2000).

[28] D. M. Anderson, G. B. McFadden, and A. A. Wheeler, "Diffuse-interface methods in fluid mechanics", Annu. Rev. Fluid Mech. **30**, 139–165 (1998).

[29] A. J. Briant, A. J. Wagner, and J. M. Yeomans, "Lattice boltzmann simulations of contact line motion. i. liquid-gas systems", Phys. Rev. E **69**, 031602 (2004).

[30] H. Kusumaatmaja, J. Leopoldes, A. Dupuis, and J. M. Yeomans, "Drop dynamics on chemically patterned surfaces", Europhys Lett. **73**, 740–746 (2006).

[31] A. Dupuis and J. M. Yeomans, "Modeling droplets on superhydrophobic surfaces: Equilibrium states and transitions", Langmuir **21**, 2624–2629 (2005).

[32] M. Sbragaglia, A. M. Peters, C. Pirat, B. M. Borkent, R. G. H. Lammertink, M. Wessling, and D. Lohse, "Spontaneous breakdown of superhydrophobicity", Phys. Rev. Lett. **99**, 156001 (2007).

[33] G. Wulff, Z. Kristallogr. **34**, 449 (1901).

9

Conclusion & Outlook

In this thesis interfacial properties of water in contact with hydrophobic surfaces on the scale of nm to µm have been explored by means of experiment, theory and numerical simulations. We have focussed on three systems with increasing surface roughness and increasing length scales: 1) surface nanobubbles present in between water and smooth hydrophobic surfaces ($10 - 100$ nm); 2) nucleation of gas bubbles trapped in (sub)microscopic surface defects ($100 - 1000$ nm); 3) microscopic wetting characteristics during the breakdown of superhydrophobicity ($1 - 10$ µm).

A detailed study of the contact angle θ of surface nanobubbles with the substrate (through the water) revealed that θ neither depends on the size of the bubble, nor on intrinsic cantilever properties (Chapter 2). The parameter which crucially changes θ is the apparent roughness of the substrate, which could be correlated to contamination originating most likely from the cantilever chip. Relatively rough substrates contained nanobubbles with $\theta \sim 140° - 160°$, while apparently smooth surfaces yielded $\theta \sim 120°$. This drastic change in contact angle, however, cannot be explained merely by the effect of the roughness - which is in the contaminated cases still relatively small - but should be understood in terms of interfacial energies which are modified by the surface-active contamination. In future studies this interpretation could be tested quantitatively by determining the contamination dependent elasticity (i.e. surface tension) of surface nanobubbles, for instance with the use of the novel HarmoniX system [1]. Such an experiment would also show in how far our 'clean' cases were still contaminated, and ultimately, whether the mystery of surface nanobubbles can be fully understood by the stabilizing effect of surface-active molecules, as suggested recently [2].

Another characteristic of surface nanobubbles is their preference in size (Chapter 3),

which shows up in dense nanobubble populations created by droplet deposition or ethanol-water exchange. It is a robust finding, which also shows up when the 'clean' cases of Chapter 2 are analyzed, despite differences in number densities and surface wetting properties. If number densities are large enough, surface nanobubbles also show local ordering. Both effects could be relevant ingredients to understand how nanobubbles are formed and/or stabilized.

When exposed to a huge negative pressure in standard shock wave experiments, surface nanobubbles do not grow to visible size in contrast with the expectation (Chapter 4). In fact, the bubbles are still present on the surface *after* passage of the shockwave, i.e. they somehow have survived the huge negative liquid pressure, which we denote as "superstability" of surface nanobubbles.

In contrast, bubbles of similar nanoscopic size *do* act as nucleation sites, provided that the gas is trapped in a surface defect (Chapter 5-7). This has been shown using smooth surfaces patterned with well-defined cylindrical pits down to 100 nm in diameter. The high spatial control of our nuclei down to nm length scales allowed us to quantitatively compare the minimum pressure required to nucleate the entrapped gas pockets with the theoretical predictions developed in the framework of the crevice model by Atchley & Prosperetti in 1989 [3], yielding a perfect match between theory and experiment. Thus, we have demonstrated that cavitation inception studies - which were usually associated with irreproducibility and a poor nuclei characterization - can in principal be controlled and understood completely. The key to this achievement is the golden rule of any cavitation experiment, anticipated by Robert Apfel in 1984 [4]: "know thy liquid" (including the nanometer sized characteristics of the nuclei), "know thy sound field", and "know when something happens". Even in the more practical situation of sub-microscopic gas pockets present on freely floating microparticles suspended in a liquid, we have demonstrated that cavitation experiments can still be fully reproducible (Chapter 7).

Usually, cavitation nuclei become used up once they have emitted a bubble once (Chapter 5 and 7). This phenomenon could be explained with the help of numerical simulations as the result of diffusion and an aspherical high-speed liquid jet upon bubble collapse. In addition, we have been able to design nuclei with a superhydrophobic bottom, with the advantage that they are able to nucleate cavitation bubbles hundreds of times without the need to re-activate the nuclei. This and the aforementioned results are of potential great value in situations where absolute control on the presence, nucleation threshold, and activation of surface entrapped gas pockets is desired, as in marine engineering or sonochemistry studies.

In addition, we have revealed both experimentally, theoretically and numerically the origin of the huge acceleration which microparticles can achieve due to cavitation inception originating on their surfaces (Chapter 6). We found that particles acquire translational momentum (allowing them to reach velocities of > 10 m/s) as a result

of a pressure gradient over the particle surface during the initial growth phase of the bubble (i.e. when the liquid pressure is lower than the vapor pressure). A future study could be dedicated to the question whether this phenomenon is responsible for additional surface erosion in particle-laden flows, which could be important for e.g. the dredging ship industry. Another future line of work could focus on a medical application, i.e. in-vivo injection of microparticles (containing drugs) from a liquid phase into (human) tissue. We have demonstrated the feasibility of this idea using a gelatine sample. One could even think of designing micro-particles to optimize this process.

Finally, the spontaneous infiltration of a water droplet into a superhydrophobic substrate has been studied through experiments, numerics and theory (Chapter 8). We have shown that the timescale which the liquid needs to proceed horizontally in between two posts (in the radial outward direction) diverges when the contact angle of the substrate is close to a critical contact angle. As a consequence, the front propagates in a stepwise manner and square-shaped wetted areas emerge, in agreement with experimental and numerical results. We found that 3d lattice Boltzmann simulations are a powerful tool to study the complex 3d filling process and it deserves further use in microfluidics. At last, scaling arguments have been derived to describe the velocity of the wetting front as a function of water contact angle and geometry. Our findings can provide design criteria to tune the liquid velocity precisely on a micro-scale level, which is useful for e.g. the membrane filtration or lab-on-a-chip industry.

All together, we can conclude that the world of micro- and nanofluidics comprises numerous fascinating phenomena, ranging from surface nanobubbles (which are so small that they can only be studied with atomic force microscopy) to cavitation bubbles or advancing wetting fronts (which are so dynamic that they can only be observed through high-speed imaging). In all these studies, we have experienced that the smallest experimental details (literally) matter: the presence of tiny amounts of contamination in surface nanobubble experiments; nanoscopic gas pockets in cavitation inception studies; and local microscopic surface imperfections in the breakdown of superhydrophobicity. The experimental challenge is to eliminate, to control, or to use them.

References

[1] O. Sahin, S. Magonov, C. Su, C. F. Quate, and O. Solgaard, "An atomic force microscope tip designed to measure time-varying nanomechanical forces", Nature Nanotech. **2**, 507–514 (2007).

[2] W. Ducker, "Contact angle and stability of interfacial nanobubbles", preprint (2009).

[3] A. A. Atchley and A. Prosperetti, "The crevice model of bubble nucleation", J. Acoust. Soc. Am. **86**, 1065–1084 (1989).

[4] R. E. Apfel, "Acoustic cavitation inception", Ultrasonics **22**, 167–173 (1984).

Summary

Water droplets on certain plant leaves (like the Lotus leaf) are almost perfectly spherical and can roll off easily. The plant leave is extremely water-repellent ("superhydrophobic") and consequently self-cleaning in nature. We can only understand this macroscopic phenomenon, which may be exploited to prevent fouling of window glasses, only if we zoom in to microscopic details of the surface of the plant leave. Similarly, some microscopic phenomena, like the emerge of vapor bubbles in water under tension ("cavitation"), we can only understand completely if we consider the submicroscopic characteristics of water, i.e the world of nanometers where things are smaller than typically $1\,\mu$m, but larger than the typical size of individual molecules ($1\,$nm$= 0.001\,\mu$m $= 0.000001\,$mm*). Fluid physics at these small length scales is called micro- and nanofluidics and is governed by forces which are less dominant at macroscopic scales. Some of these forces originate from or at interfaces (like the liquid-air or liquid-solid interface), and require a thorough understanding in order to understand the sometimes large scale phenomena which they can lead to, as illustrated by the example of cavitation bubble or extreme water repellency. Fundamental insight, which is gained through such research, can be of great potential value in areas where micro- and nanofluidics are utilized: membrane- and filtration technology, cavitation inception research, megasonic cleaning, inkjet printing, etc.

In this thesis, we have studied water in contact with a hydrophobic surface. The thesis covers three interfacial phenomena which can occur in such a system: I - spherically cap-shaped gas bubbles residing on atomically smooth surfaces ($10-100\,$nm); II - gas pockets, trapped in extremely small surface defects, growing to micrometer sized vapor bubbles ("cavitation") ($100-1000\,$nm); III - wetting a rough, superhydrophobic surface ($1-10\,\mu$m). Typical lateral length scales are increasing each step by a factor of 10, as indicated by the numbers in between brackets. Likewise, the roughness of the solid surface of interest increases each time: atomically smooth (part I), a little pit here and there (part II), surfaces decorated with pillars (part III). A third distinction is that part I studies a static situation, while part II and III are concerned with dynamic phenomena. A schematic overview can be found in Table 1.1 of Chapter 1.

Spherical cap-shaped bubbles, studied in part I of this thesis, are usually called "sur-

---

*A human hair is approximately 80000 nm in diameter and grows about 5 nm per second.

face nanobubbles", since they are residing at smooth surfaces in contact with water and have typical lateral dimensions below 100 nm. The existence of these little bubbles is remarkable: since the radius of curvature of the bubbles is extremely small, the resulting surface tension pressure in the bubble is extremely large and should lead to rapid dissolution of the bubbles within milliseconds, but this doesn't happen. Hence, the central question is why surface nanobubbles are stable. Another issue is how to explain the large contact angles (measured through the water) which deviate tens of degrees with the macroscopically measured values.

Chapter 2 describes an experiment which aims at measuring nanobubble dimensions as accurate as possible, using an atomic force microscope. We find that the observed nanobubble shape does not depend on intrinsic cantilever properties, used in detecting the bubbles. Furthermore, we find that the nanoscopic contact angle (measured through the water) does not depend on the nanobubble radius and is much smaller ($\sim 120°$) than has hitherto been reported ($\sim 160°$). Contamination is the most likely candidate to explain the latter observation.

In addition, we have analyzed properties of surface nanobubble populations, which is only possible when a sufficient amount of nanobubbles is detected. This study, as described in Chapter 3, yields that nanobubbles show a preference in size. When number densities are sufficiently large, a local structuring effect shows up as well.

The central question in Chapter 4 is what happens with surface nanobubbles when they are hit by a shockwave containing a huge negative pressure phase. The result is remarkable: nothing. We had expected nanobubbles to be nucleation sites for cavitation bubbles, but this appears not to be the case. After passage of the shockwave, surface nanobubbles were still present on the substrate, which we denote as "super-stability".

Since cavitation bubbles can emerge from micro-sized pits entrapping gas, but apparently not from surface nanobubbles, we study the situation in between these two cases in Chapter 5 (part II): cavitation bubbles emerging from nano-sized pits filled with gas. We find that these extremely little gas pockets indeed serve as nucleation sites when the liquid pressure is lowered sufficiently and cavitation bubbles occur. The minimum pressure which is needed to nucleate the bubbles is inversely proportional to the pit radius and is in excellent agreement with the crevice model theory as developed in 1989. Hence, the origin of cavitation inception can be controlled and understood down to submicroscopic dimensions.

In practice, cavitation usually starts from nuclei (submicroscopic gas pockets) present on microparticles, which are abundantly present and freely floating around in (unfiltered) water. In this process the cavitation bubble accelerates the microparticle (from which it emerged originally) to velocities up to tens of m/s. This spectacular phenomenon is studied in Chapter 6 using an extreme high-speed camera coupled with

a microscope. Experimental observations perfectly match an analytical model based on the pressure gradient over the particle surface as the main driving force. Numerical simulations confirm this view.

Reproducibility is most often a serious concern in cavitation inception studies, since even the smallest contaminative particles in the water can already contain nanoscopic cavitation nuclei. Yet it is possible to perform reproducible cavitation inception studies. Chapter 7 describes an experiment which demonstrates this claim.

Superhydrophobic surfaces, which are useful in various applications, are studied in part III of the thesis. Such surfaces can be prepared easily by decorating a hydrophobic surface (e.g. polymer material) with physical roughness (e.g. pillars). A water droplet in contact with a superhydrophobic surface of this kind rests on the top of the pillars, like a Fakir on a bed of nails. Since the droplet just touches the apex of the pillars, it is essentially in contact with the air in between the pillars, which makes the droplet completely spherical and enables it to move around freely. However, it may be energetically more favorable for the droplet to wet the structure completely. The reason that this does not occur spontaneously, is due to an energy barrier which is faced upon wetting the structure in the vertical direction. Chapter 8 describes an experiment where the droplet overcomes the energy barrier, either by a local defect in the micro-structure, or by sideways pulling the droplet into the structure. Subsequently, an energy barrier dictates whether the droplet will wet the micro-structure or not. The velocity of the wetting front diverges as the dimensions of the structure approach a critical value, with square-shaped wetted areas as a direct result.

Samenvatting

Waterdruppels op het blad van bepaalde planten (zoals de Lotus plant) zijn bijna perfect rond en kunnen er vaak makkelijk vanaf rollen. Het blad is extreem waterafstotend ("superhydrofoob") en daarom ook zelf-reinigend van aard. Dit macroscopische verschijnsel, dat ons op termijn wellicht het wassen van ruiten kan besparen, kunnen we pas begrijpen als we inzoomen op de microscopische details van het blad oppervlak. Evenzo zijn er microscopische verschijnselen waarneembaar, zoals het ontstaan van waterdamp belletjes in water dat onder een onderdruk staat ("cavitatie"), die we pas volledig kunnen begrijpen als we nog verder inzoomen. We belanden dan in de wereld die kleiner is dan de micrometer, maar nog wel groter is dan de lengte van individuele moleculen: het regime van de nanometer (1 nm= $0.001\,\mu$m = $0.000001\,\text{mm}^{\dagger}$). De vloeistoffysica op deze kleine lengteschalen wordt *micro- en nanofluidics* genoemd en wordt geregeerd door krachten die op de macro-schaal minder dominant zijn. Sommige van die krachten vinden hun oorsprong bij grensvlakken (zoals het grensvlak water-lucht of water-vaste wand). Daarom is een grondige kennis van de details van deze grensvlakken en bijbehorende krachten van cruciaal belang om de verschijnselen te begrijpen die zij uiteindelijk kunnen veroorzaken, zoals het ontstaan van belletjes of extreme waterafstotendheid. De fundamentele kennis die we hier uit opdoen, kan worden gebruikt in diverse gebieden waar kennis van vloeistoffen op kleine schaal wordt toegepast: membraan- en filtratietechnologie, cavitatie-onderzoek, megasone reiniging van oppervlakken, inkjet-printers, etc.

In dit proefschrift hebben we water bestudeerd dat in contact is met een waterafstotend oppervlak. Het proefschrift bestudeerd drie grensvlakverschijnselen die hier kunnen optreden: I - sferische luchtbelletjes op een atomisch glad oppervlak ($10-100\,\text{nm}$); II - luchtbelletjes, ingesloten in een extreem klein putje, die uitgroeien tot micrometers grote waterdampbelletjes ("cavitatie") ($100-1000\,\text{nm}$); III - de bevochtiging van een ruw, extreem waterafstotend oppervlak ($1-10\,\mu$m). De typische laterale lengteschaal, zoals deze vermeld is tussen de haakjes, neemt steeds een factor 10 toe in elk onderdeel. Ook neemt de ruwheid van het waterafstotende oppervlak toe: van atomisch glad (deel I), via hier en daar een putje (deel II), naar een oppervlak dat volledig is bedekt met pilaren (deel III). Een derde onderscheid is dat deel I een statische situatie bestudeerd, terwijl deel II en III beiden een dynamisch verschijnsel onderzoeken. Een schematisch overzicht van de drie onderdelen is ook te vinden in

---

†Een menselijke haar is ongeveer 80000 nm dik en groeit zo'n 5 nm per seconde.

Tabel 1.1 van Hoofdstuk 1.

De sferische luchtbelletjes die we bestuderen in deel I van dit proefschrift worden
"oppervlakte nanobellen" genoemd, omdat ze aanwezig zijn op het oppervlak van een
gladde wand dat in contact is met water en omdat de typische afmetingen $< 100\,\text{nm}$
zijn. Het bestaan van deze belletjes is opmerkelijk: Omdat de kromtestraal van de
belletjes extreem klein is, zou de druk in de bel als gevolg van de oppervlaktespanning
extreem groot moeten zijn en de bel zou binnen een seconde moeten oplossen in het
water, maar dit gebeurt niet. De vraag is dus waarom deze bellen stabiel zijn. Een an-
dere vraag is hoe we de contacthoek van de bel met het oppervlak kunnen verklaren,
aangezien deze totaal niet in overeenstemming is met wat we zouden verwachten.
Hoofdstuk 2 beschrijft een experiment waarbij we de vorm van de nanobel heel
nauwkeurig meten met een atomische kracht miscroscoop. Het blijkt dat de dimen-
sies van de nanobel niet afhangen van de intrinsieke eigenschappen van het naaldje
waarmee de bel wordt gemeten. Verder vinden we dat de contacthoek die de nanobel
maakt met het oppervlak (gemeten door het water) niet afhangt van de straal van de
bel en heel wat lager is ($\sim 120°$) dan voorheen altijd was vastgesteld ($\sim 160°$). Con-
taminatie is zeer waarschijnlijk verantwoordelijk voor dit laatste.
Als we voldoende nanobellen hebben, kunnen we ook eigenschappen van nanobel
populaties analyseren, hetgeen wordt beschreven in Hoofdstuk 3. Dit onderzoek
levert op dat nanobelletjes een statistische variatie rondom een voorkeursafmeting
hebben en bij voldoende hoge dichtheden zelfs lokale ordening vertonen.
In Hoofdstuk 4 kijken we wat er gebeurt als een oppervlak vol met nanobelletjes
wordt getroffen door een passerende schokgolf met een enorme negatieve druk. Het
resultaat is opmerkelijk: niets. We hadden verwacht dat nanobelletjes de kernen zijn
van waaruit cavitatiebellen kunnen groeien, maar dit blijkt in dit experiment niet het
geval te zijn. De belletjes zijn nog aanwezig op het oppervlak, zelfs na het passeren
van de schokgolf, hetgeen we aanduiden met de term "superstabiliteit".

Uit eerder onderzoek weten we dat cavitatiebellen wèl kunnen ontstaan als de gas-
belletjes ingesloten zitten in micro-putjes aanwezig op een verder glad oppervlak.
Daarom gaan we in Hoofdstuk 5 (deel II) de situatie tussen de micro-putjes en de
oppervlakte nanobellen in bestuderen: cavitatie uit nano-putjes gevuld met lucht. Uit
deze extreem kleine putjes, die zeer nauwkeurig ge-etst zijn in silicium, kunnen we
met behulp van een schokgolf cavitatiebelletjes laten ontstaan, waarbij we vinden
dat de negatieve druk die hiervoor minimaal nodig is omgekeerd evenredig is met de
straal van het putje. Dit klopt precies met de theorie zoals die in 1989 door Atchley
& Prosperetti werd gepubliceerd. De oorsprong van cavitatie uit submicroscopische
luchtbelletjes is hiermee kwantitatief gecontroleerd en begrepen.
In de praktijk ontstaan cavitatiebellen vaak uit ingesloten luchtbelletjes die aanwezig

zijn op microdeeltjes, die in (ongefilterd) water volop aanwezig zijn en los rond-zweven. Als we dit verschijnsel onder de microscoop bekijken met behulp van een extreme hogesnelheidscamera vinden we dat het cavitatiebelletje in staat is om het microdeeltje (van waaruit het zelf ontstaat) weg te schieten met snelheden tot enkele tientallen m/s. Dit spectaculaire fenomeen hebben we in Hoofdstuk 6 bestudeerd en verklaard. De experimentele resultaten kunnen theoretisch goed beschreven worden door de drukgradient over het microdeeltje verantwoordelijk te stellen voor de ver-snelling van het deeltje. Numerieke simulaties bevestigen dit beeld.

In cavitatie-onderzoek is reproduceerbaarheid vaak lastig te bereiken, omdat de klein-ste verontreinigingen in het water al een nanoscopische cavitatie-kern kunnen bevat-ten. Toch is het mogelijk om op reproduceerbare wijze cavitatie-onderzoek in suspen-sies te doen en Hoofdstuk 7 beschrijft een experiment waarin dit wordt aangetoond.

In deel III van dit proefschrift staan extreem waterafstotende oppervlakken centraal, die van nut kunnen zijn in allerlei toepassingen. Een dergelijk oppervlak is te prepa-reren door een waterafstotend materiaal (bijvoorbeeld een polymeer) ruw te maken (bijvoorbeeld door het met pilaren te bedekken). Een waterdruppel dat in contact komt met zo'n oppervlak zal op de toppen van de pilaren rusten, als een fakir op een spijkerbed. Omdat de druppel alleen de toppen van de pilaren aanraakt, is hij voornamelijk in contact met de lucht tussen de pilaren, zodat de druppel volkomen rond wordt en vrij is om te bewegen over het oppervlak. Energetisch kan het voor de druppel echter voordeliger zijn om de structuur volledig te bevochtigen. Dat dit niet spontaan gebeurt is te wijten aan een energiebarrière: de druppel moet eerst de wanden van de pilaren bevochtigen (dit kost energie) voordat het de bodem van de structuur raakt (dit levert energie op). Omdat de druppel niet "weet" waar de bodem is, blijft de druppel in een meta-stabiele toestand boven op de pilaren zitten. Hoofd-stuk 8 beschrijft een experiment waarbij de druppel de locatie van de bodem wel weet, ofwel door een lokaal defect in de structuur, ofwel door de druppel zijwaarts in de structuur te slepen. Een energiebalans dicteert vervolgens of de druppel de structuur zal bevochtigen. De snelheid waarmee het water tussen twee pilaren doorstroomt divergeert naarmate de structuur een bepaalde kritische dimensie bereikt, zodat in uitzonderlijke gevallen de druppel in vierkante vlekken uitspreidt.

Acknowledgements

*Something completed is better
than something just begun;
patience is better
than too much pride.*
The Bible, Ecclesiastes 7:8

After completing this thesis it is time to reflect on the past four years. During this period I have never been able to foresee how the final thesis would look like. This is a natural consequence of working in fundamental physics, where the typical timescale to perform and analyze a decent experiment varies between a few weeks and a few months (or even years). Only after each experiment, if successful at all, I knew what to do next. In the beginning, this process made me quite nervous: The result of the first experimental cycles was that there was no result and extrapolating this observational fact to infinity I started to doubt seriously on my whole PhD project. I still remember the words Christophe Pirat spoke to me at that time (December 2005): "Just continue! It's all about getting new ideas. You should worry when you don't have new ideas anymore. Otherwise, just continue!" These words inspired me. Gradually nervousness became patience. After all, these three nutrients - imagination, patience, and support from colleagues - have fed the research part of my life which in the end yielded various fruits, of which this thesis is just one.

I would like to spend a few more words on the last nutrient, support from colleagues. In the first place, I would like to thank my supervisor and promotor Detlef Lohse for being my scientific inspirator. I am grateful for his long term guidance, scientific input, wording lessons, stimulus to make use of a parental leave, and all the other support he gave me. Claus-Dieter Ohl, Manish Arora, Stephan Dammer, Christophe Pirat, and Mauro Sbragaglia have been extremely stimulating and helpful PoF colleagues for me, in particular during the first part of my PhD project, while Shangjiong Yang, Jacco Snoeijer, Peichun Amy Tsai, Chao Sun, James Seddon, Joost Weijs, and Hanneke Gelderblom, took over in the second part. It has always been a pleasure to discuss and carry out research with all of them. Special thanks goes to Rory Dijkink for being a perfect lab mate during the years and for designing the cover of this thesis. How to do an experiment without the technical and practical infrastructure provided by Gert-Wim Bruggert, Martin Bos, Bas Benschop, and Joanita Leferink? I am

185

thankful for their flexibility and problem solving attitude. I acknowledge intern Daan Benschop for designing and preparing the clamp which held the valuable chips with nanopits.

The benefit of a large research group is that there is always someone in for a cup of coffee, a chat, a lunch break or a Friday afternoon experiment. Thanks to all PoF members the time I have spent in various labs and offices was diverting.

A multidisciplinary research approach, as demonstrated in this thesis, forces the postmodern, individualistic researcher to become a social, networking scientist. The list of co-authors involved in the papers constituting this thesis counts 22 people from 9 different research groups, while the number of people who contributed to some extent is probably twice as large. The first successful collaboration was set up with Holger Schönherr (at that time associated with the Materials Science and Technology of Polymers (MTP) group, UT) already during my Master's project and is still continuing today. I am still amazed by Holger's unconditional willingness to get involved in the nanobubble research and I thank him for his work and great contributions during the years. Also Clemens Padberg, Szczepan Zapotoczny and Julius Vancso are acknowledged for their support. Another fruitful collaboration was established with the Physics of Complex Fluids group. I want to thank Helmut Rathgen for his help in various experimental issues, in particular his effort to build a coating device is acknowledged, since it allowed us to produce high-quality hydrophobic coatings in a reproducible fashion. In addition, I want to thank Sissi de Beer for her enthusiasm to study nanobubbles with AFM. Her AFM-pictures are always impressive. I am grateful to Frieder Mugele for various useful discussions and for being able to collaborate with his group. Another collaboration which I have enjoyed very much was together with the Membrane Science and Technology group, headed by Prof. Matthias Wessling. The work together with him, Rob Lammertink and Alisia Peters was as spontaneous as the breakdown of superhydrophobicity itself. I still remember with pleasure the Friday afternoon experiment in which the first zipping wetting recordings were obtained using the Photron camera by Alisia and me, and the days afterwards in which we were suddenly completely occupied by this topic. Next, I want to express my gratitude towards Harold Zandvliet and Stephan Kooij of the Solid State Physics group, with whom I share good memories on various nanobubble meetings. Another group to acknowledge here is the BIOS group, headed by Prof. Albert van den Berg. The Captain of the Nanofluidics Flagship always asked one or the other good question during NanoNed meetings, which stimulated further research. I am grateful for the opportunity he gave me to make use of cleanroom expertise available in his group. I am extremely grateful to Johan Bomer and Ton Jenneboer (now cleanroom staff) who carried out lots of hard cleanroom work. The cleanroom staff should also be mentioned: they have always been very helpful. During the years I have been in touch with a few other groups, which I want to thank in

this way too: Catalytic Processes and Materials (Leon Lefferts), Mesoscale Chemical Systems (Han Gardeniers), and Molecular Nanofabrication (Jurriaan Huskens). I believe that each meeting, each talk, each experiment brought this project to a higher level. In addition, I want to acknowledge colleagues from abroad: Evert Klaseboer, Boo Cheong Khoo, and Knud Aage Mørch for their work in the shooting particle project (Chapter 6), and Gérard Le Caër and Benjamin Dollet for their ideas and work in the statistical analysis of nanobubbles (Chapter 3).

Besides colleagues, several friends have been very inspiring during the years as well. I was happy to have lunch walks with Albertus Laan each week with nice bird sightings every now and then. I thank him and Bram Rosenbrand for being my paranymphs during the PhD defense.

Let me finish by showing gratitude to the most important nutrients feeding the tree of my life, of which research is just a branch: the love and support of my parents and, above all, Karien.

Bram Borkent
Sept 1st, 2009

About the author

Bram Matthias Borkent was born on July 1, 1981, in Apeldoorn, where he lived the first eighteen years of his life. He graduated from high school 'Greydanus College' in Zwolle in May 1999. Three months later he moved to Enschede to study Applied Physics at the University of Twente (UT). He participated in various student activities and was freelance reporter of UT-Nieuws, the university news paper, from 2000 till 2004. In 2004 he went to Japan for a research internship at the Netherlands Office of Science and Technology located at the Dutch Embassy in Tokyo. The resulting state-of-the-art report, entitled 'Nanotechnology based drug delivery systems in Japan', was distributed in The Netherlands and later in other countries through an international publisher. Bram conducted his Master project on cavitation inception in the Physics of Fluids group (Prof. Dr. Detlef Lohse) under guidance of Dr. Claus-Dieter Ohl. After his Master thesis defense in August 2005, he continued research on micro- and nanoscale interfacial phenomena as a PhD student.

Bram is married with Karien Huisman and together they have two kids: Koen (2007) and Luuk (2008). In his free time, Bram is an enthusiastic bird-watcher with a special interest in bird migration and local rarities. During a lunch walk with Albertus Laan in early 2008, he discovered a new territory of the rare Middle Spotted Woodpecker in the park next to the UT, while in 2009 he found a new territory of the rare Central European Treecreeper (Certhia familiaris macrodactyla) just north of the UT.